Probing valley and magnetic photoexcitations in 2D crystals and their heterostructures

Kyle Lee Seyler

A dissertation
submitted in partial fulfillment of the
requirements for the degree of

Doctor of Philosophy

University of Washington

2018

Reading Committee:

Xiaodong Xu, Chair

David Cobden

Boris Spivak

Program Authorized to Offer Degree:
Physics

University of Washington

Abstract

Probing valley and magnetic photoexcitations in 2D crystals and their heterostructures

Kyle Lee Seyler

Chair of the Supervisory Committee:
Associate Professor Xiaodong Xu
Physics

Layered materials are excellent systems for investigating physics in two dimensions. Understanding the optical response of 2D layered materials and their heterostructures at the atomically thin limit is an important aspect of this field. Photoexcitations, such as excitons, critically impact future optoelectronic technologies, such as next-generation solar cells, light-emitting diodes, lasers, and single-photon sources. Moreover, they can provide deep insights into the rich electronic properties of the host crystals, especially in two dimensions, where stronger electron confinement, symmetry changes, and interfacial effects are often very influential. The 2D semiconducting transition metal dichalcogenides, for example, have garnered tremendous excitement for their strong light-matter interactions, which involve tightly bound excitons with intriguing spin-valley physics. Furthermore, newly discovered 2D magnets are unlocking new opportunities to explore magnetic photoexcitations in the atomically thin limit.

This dissertation presents optical spectroscopy experiments that probe the fundamental photoexcitations within 2D semiconducting transition metal dichalcogenides, magnetic chromium triiodide (CrI_3), and their van der Waals heterostructures. First, we show how second-harmonic generation spectroscopy serves as a powerful probe of excitons and trions in monolayer WSe_2 and demonstrate an electrical exciton-based second-harmonic generation switch. We then add $MoSe_2$ to the picture, forming $MoSe_2/WSe_2$ heterobilayers in which we reveal the valley-contrasting physics of long-lived free and trapped interlayer excitons. Next, we introduce atomically thin CrI_3 and describe our observation of spontaneous circularly polarized photoluminescence. We also unravel its ligand-field and charge-transfer-dominated photoresponse, which broadens the landscape of 2D material photoexcitations beyond exci-

tons. Finally, we combine ultrathin layers of CrI_3 with monolayer WSe_2, where we discover unprecedented control of valley excitons in monolayer WSe_2 by magnetic proximity to CrI_3.

TABLE OF CONTENTS

LIST OF FIGURES

ABBREVIATIONS

2D: Two-dimensional

PL: Photoluminescence

SHG: Second-harmonic generation

TMD: Transistion metal dichalcogenide

H-BN: Hexagonal boron nitride

CCD: Charge-coupled device

CW: Continuous-wave

FWHM: Full-width at half-maximum

IX: Interlayer exciton

RT: Room temperature

ACKNOWLEDGMENTS

First and foremost, it is difficult to overstate my gratitude towards my advisor, Xiaodong Xu. From the very beginning, he has been extraordinarily supportive. His relentless work ethic, combined with intellectual curiosity and conscientiousness, have created a wonderful and productive research environment. The path to a PhD can be a rollercoaster ride of emotions. Xiaodong has a gift for injecting inspiration, confidence, and lightheartedness at just the right moments, which kept life and science consistently enjoyable and hopeful. I feel so lucky to have worked with Xiaodong, and I will miss it!

I would also like to acknowledge my other committee members, David Cobden and Boris Spivak. Dave has been very supportive over the years. It has been a pleasure to be around his scientific insight, deep curiosity, and good humor. Without the active collaboration between Dave and Xiaodong, the work in this dissertation would have been much more difficult.

Thanks to all the collaborators that have contributed to this work. From UW, Kai-Mei Fu, Xiayu Linpeng, and Emma Schmidgall generously offered time and expertise on their magnet cryostat that helped get our magnetic heterostructure projects off the ground. Daniel Gamelin and Xiaosong Li and his students have been helpful in our attempts to understand the 2D magnets. Outside UW, Wang Yao, Di Xiao, and Hongyi Yu have been a consistent source of enlightenment. Wang and Hongyi are responsible for the theory of interlayer excitons, and Di and his students, Ran Cheng, Nikhil Sivadas, and Xiaoou Zhang, have given invaluable insight on 2D magnets. We benefited from Li Yang and Shiyuan Gao's expertise at WUSTL on the CrI_3 photoexcitation project. The scientists at Oak Ridge National Laboratory (David Mandrus, Jiaqiang Yan, Nirmal Ghimire, and Michael McGuire) and NIMS (Takashi Taniguchi and Kenji Watanabe) generously grew most of the high-quality bulk crystals used in this work. Pablo Jarillo-Herrero, Dahlia Klein, and Efrén Navarro-Moratalla contributed vital fabrication support for the atomically thin CrI_3 projects.

I am deeply grateful to all the labmates, past and present, for making my PhD experience enjoyable. Thanks so much to John Schaibley, Aaron M. Jones, Grant Aivazian, Sanfeng Wu, Jason Ross, Helin Cao, Pasqual Rivera, and Gen Clark for welcoming me into the lab,

making the transition to grad school smooth, and their great camaraderie over the years. I consider myself lucky to have crossed paths with John, who was there to offer moral support and optical advice when I needed it most. And thanks to Pasqual for insightful discussions about science and life, commiserating with me over problem sets, and being a genuinely outstanding colleague. He has put in a tremendous amount of excellent work on the interlayer exciton projects, and it has been wonderful collaborating with him. Thanks to Ding Zhong for graciously welcoming me onto the magnetic heterostructure projects. Thanks to Nathan Wilson for being a great deskmate over the past few years and keeping the lab (mostly) in order. I have learned a great deal from his insights about optics, design, and machining. Thanks to Bevin Huang for teaching me about magnets and providing comic relief. Thanks to all the other postdocs and visiting scientists that have been through the lab: Qi Zhang, Chang-Hua Liu, Harold Cai, Colin Chow, Zaiyao Fei, Dmitry Ovchinnikov, Fucai Liu, Essance Ray, and Cheng Zhang. Thanks and good luck to all the up-and-coming students: Tiancheng Song, Chenfeng Du, Minhao He, and John Cenker. Thanks to Frank Wise, Tobias Hanrath, Liangfeng Sun, and Byung-Ryool Hyun for their kind mentorship as I tried to find my way into science during undergrad. Thanks to everyone else from the labs of David Cobden, Kai-Mei Fu, Arka Majumdar, and Jiun-Haw Chu for making experimental condensed matter physics at UW a friendly and collaborative environment.

Lastly, words cannot express how grateful I am to my family for their love and support. The time away from the lab spent with you all has been so invaluable for keeping me healthy, happy, and productive. Thanks to my brother, whose curiosity, thoughtfulness, and skepticism always inspire me to become a better person and scientist. Thanks to my father, for taking an active interest in my research and who is always available to offer precious scientific and life advice. Thanks to my mother for her boundless energy and good cheer, which never fails to brighten my day. Thanks to the Hsia family for graciously welcoming me into their home and feeding me delicious food during the holidays. Thanks to Allison for her unwavering support and for being a steady source of happiness. It's been a long journey, but she has been there every day, keeping me energized and excited for the future. I am so grateful and fortunate to have such a bright, funny, and caring person in my life. And finally, thanks to Darcy for always greeting me during video chats and reminding us there's more to life than work.

DEDICATION

To my family

Chapter 1

INTRODUCTION TO THE WORLD OF 2D MATERIALS

Take a moment to appreciate the materials that surround you. Wood, stone, metal, glass, plastic, and much more. Consider their forms, their compositions, and their functionalities. What would happen if you removed a particular material from your life? We take much of this for granted nowadays, but our mastery of different materials has powered human progress since our earliest beginnings and it continues to shape our future. For example, think about the billions of precisely engineered field-effect transistors and magnetic storage elements that lie beyond the black mirror of your computer and cell phone. They ultimately owe their seamless operation to an impressive body of solid-state physics that scientists and engineers have developed over the past century. By poking and prodding different materials, we not only discover how nature works, but we also encounter useful physical phenomena that we can then exploit to help humanity flourish in new ways.

The quest to create, understand, and control solid-state materials and phenomena has pushed many avenues of research to the nanoscale. When materials are shrunk down to the length scale of several atoms (in any of the three dimensions), their properties often differ dramatically from their bulk form. Quantum mechanical effects are inescapable, and interfacial interactions become influential. As a result, the nanoscale is a rewarding place for discovering new and weird phenomena. Moreover, with humanity's insatiable hunger for faster, cheaper, and lighter technologies, the effects of the nanoscale on everyday devices are increasingly important.

A particularly promising group of nanoscale materials for science and technology are the layered van der Waals crystals. These materials consist of strongly bound two-dimensional (2D) layers held together in a stack by weak van der Waals interactions, which can be cleaved down from large bulk crystals to single monolayer sheets using mechanical exfoliation with tape (Fig. 1.1A). With thickness on the order of 1 nm and lateral dimensions of several microns, 2D materials are like atomically thin sheets of paper (Fig. 1.1B). Unlike paper, however, the 2D materials are typically single crystals that can consist of a wide variety of chemical elements, which endows the 2D material family with a great diversity of electronic,

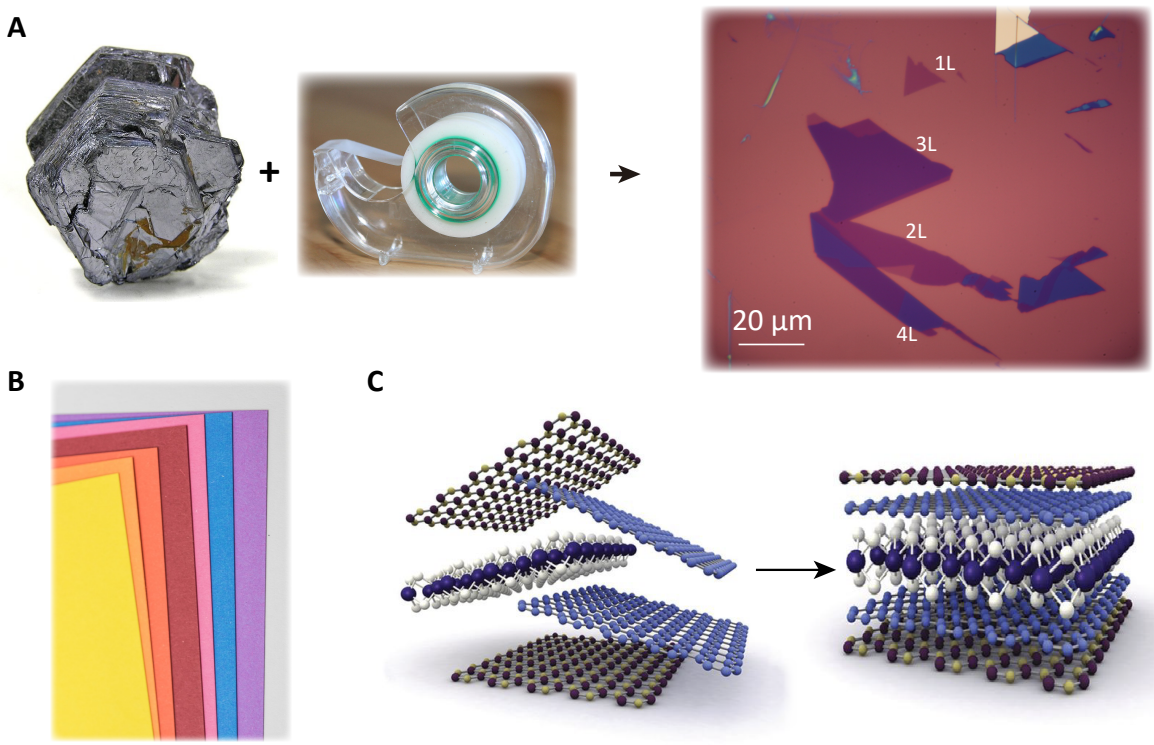

Figure 1.1: Layered materials and van der Waals heterostructures. (A) Using adhesive tape, a bulk van der Waals crystal can be exfoliated down to atomically thin sheets. The optical microscope image on the right shows monolayer (1L) and few-layer thickness crystals. [MoS_2 bulk crystal photo credit: Rob Lavinsky, iRocks.com CC-BY-SA-3.0.] (B) Colored paper, an analogy to van der Waals "2D paper" crystals. (C) Schematic of van der Waals heterostructure assembly. [From [1]. Reprinted with permission from AAAS.]

magnetic, mechanical, and optical properties. The van der Waals bonding between the monolayer sheets further enables their layer-by-layer reassembly into custom heterostructures [1, 2] (1.1C), which host unique phenomena absent from the individual layers. As Richard Feynman presciently wondered nearly 60 years ago [3], "What could we do with layered structures with just the right layers?" With the mastery of van der Waals crystals, there will be extraordinary opportunities to create nanoscale designer quantum materials.

One area in which layered materials may have a significant impact is in optoelectronics. Many of the 2D materials are known to interact strongly with light, and their photoresponses extend across the electromagnetic spectrum, from the ultraviolet, through the visible and infrared, and to the microwave regime (Fig. 1.2). 2D materials are thus very promising for photonic devices, such as light-emitting diodes, solar cells, lasers, sensors, and more.

However, we are just beginning to explore what is possible with light-matter interactions in 2D materials and heterostructures, and thus, basic research into their optical properties is still needed. Fortunately, as we will see in this dissertation, the path towards understanding 2D material optical properties is intertwined with many other exciting fields, including spintronics, nanophotonics, topological matter, and quantum information.

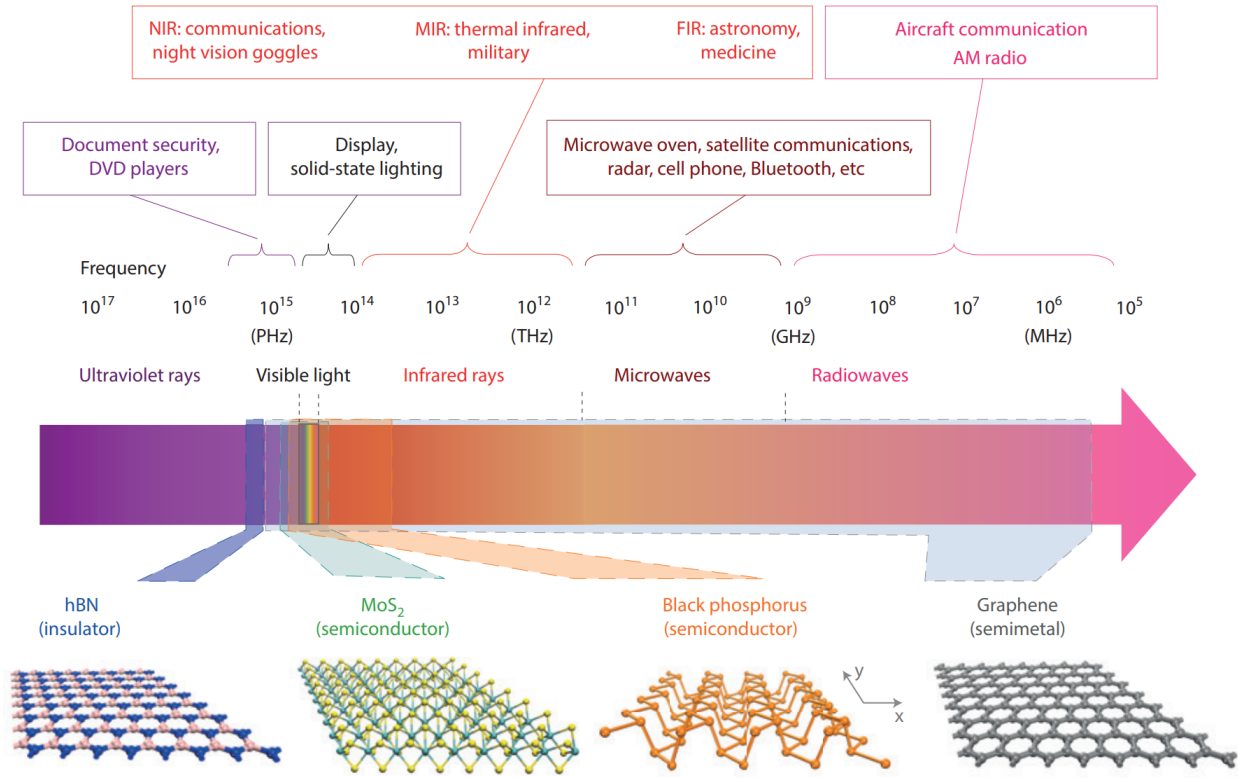

Figure 1.2: 2D materials and the electromagnetic spectrum The diversity of electronic properties within the 2D material family enables light-matter interactions across a wide range of the electromagnetic spectrum, which are highly relevant to many optoelectronic technologies. [Reprinted by permission from [4]: Nature Photonics, Copyright 2014.]

1.1 Overview of dissertation

In this dissertation, we explore the photoresponse of 2D crystals and their heterostructures. Our focus is on the monolayer semiconductors, WSe_2 and $MoSe_2$, in addition to the magnetic insulator, CrI_3. Several questions drive this research. What are the fundamental light-matter

interactions in different 2D materials? How does the optoelectronic response change in the 2D limit? What new phenomena emerge in 2D materials and their heterostructures due to crystal symmetry, quantum confinement, exchange interactions, Berry phase, interfacial coupling, and more? How can we create, understand, and control these phenomena using photons? In each chapter, we will learn how optical spectroscopy, in concert with nanoscale device design, provides simple yet powerful tools to answer to these questions.

We begin in Chapter 2 by introducing the monolayer transition metal dichalcogenide (TMD) semiconductors, including their crystal structure, electronic band structure, spin-valley physics, and 2D excitonic properties. The results described here are foundational for all of the following chapters.

Chapter 3 explores second-harmonic generation (SHG) in monolayer WSe_2. We first briefly overview the relevant nonlinear optics concepts and acknowledge prior attempts to electrically control SHG in other material systems. The bulk of the chapter details our studies of exciton- and trion-enhanced SHG in monolayer WSe_2 and our realization of a novel electrically tunable SHG transistor. We also describe the two-photon valley optical selection rules in monolayer TMDs, which follow naturally from our discussions in the previous chapter.

Chapter 4 considers how the excitonic properties change when we interfacially couple two different monolayer semiconductors ($MoSe_2$ and WSe_2) to form a heterobilayer. The introductory subsections survey previous foundational work on indirect excitons in coupled quantum wells in addition to recent experimental and theoretical studies of TMD heterobilayers. We then describe our photoluminescence (PL) spectroscopy studies on the valley physics of interlayer excitons, in which we realize valley polarization of interlayer excitons, demonstrate their exceptionally long valley lifetime (relative to monolayer excitons), and observe signatures of valley-dependent exciton drift.

Chapter 5 describes our observations of a new class of interlayer excitons in high-quality $MoSe_2/WSe_2$ heterobilayers, which are trapped in a quantum-dot-like confinement potential. We compare and contrast them to the free interlayer excitons of the previous chapter, as well as the single-photon emitters in the monolayer case, and we argue that the confining potentials arise from the naturally formed moiré superlattice.

Chapter 6 introduces atomically thin CrI_3 as a new platform for investigating light-matter interactions in 2D magnetic materials. We discover that the PL helicity possesses a clear fingerprint of its intrinsic long-range magnetic order. In addition, we explore the nature of photoexcitations in CrI_3, which turn out to be highly localized ligand-field and charge-

transfer excitations, in contrast to the ubiquitous Wannier-Mott excitons in all previously studied 2D semiconductors and insulators.

Chapter 7 explores the optical response of the first van der Waals magnetic semiconductor heterostructure, which is composed of monolayer WSe_2 and ultrathin CrI_3. In the process, we draw upon much of our understanding from the earlier chapters. We first survey prior attempts to manipulate the valley physics in monolayer TMDs, and then propose van der Waals magnetic heterostructures as a unique platform for tunable spin- and valleytronics. Our experimental results establish unprecedented control of the spin-valley physics in WSe_2 via interfacial coupling with CrI_3, via strong exchange coupling and ultrafast spin transfer.

Chapter 8 expands the WSe_2/CrI_3 heterostructure studies of the previous chapter by demonstrating how small changes in the laser excitation power can widely tune the valley polarization and valley Zeeman splitting. These results show an exciting route towards optically controllable magnetic phenomena in van der Waals heterostructures.

Finally, Chapter 9 provides a short conclusion and outlook to the dissertation.

Chapter 2

MONOLAYER SEMICONDUCTORS

In this chapter, we overview important theoretical and experimental work on the group-6 transition metal dichalcogenides (TMD) semiconductors.

2.1 Transition metal dichalcogenide semiconductors

The TMDs possess the chemical formula MX_2, where M is a transition metal and X is a chalcogen (S, Se, or Te) (see periodic table in Fig. 2.1). Ancient civilizations were aware of the mineral molybdenite (MoS_2), one of the most common TMDs, but humans often confused it with the similarly slippery graphite or the shiny gray mineral galena (PbS). The first correct identification dates back to around 1800, along with the discovery of the element molybdenum [5]. However, detailed studies into the rich properties of the TMD family did not begin until the mid-1900s, after the development of quantum mechanics and solid-state theory.

There are around 40 layered TMD compounds, which exhibit a great diversity of electronic properties [6]. For example, MoS_2 is a semiconductor, WTe_2 is semi-metallic, and $NbSe_2$ is metallic, or superconducting at low-enough temperatures [7]. Our focus is on the group-6 TMD semiconductors, such as WS_2, MoS_2, WSe_2, and $MoSe_2$, and hereafter we use the shorthand "MX_2" to refer specifically to this group. They typically crystallize in the 2H form, where individual monolayer sheets consist of a hexagonal pattern of alternating M and two X atoms, arranged in a trigonal prismatic coordination (Fig. 2.2C) [8]. The 2H bulk crystal contains stacked monolayers with a 180° rotation between neighboring layers (Fig. 2.2D). While the in-plane bonding is covalent, the interlayer attraction is due to weak van der Waals forces, which rapidly vanish at large interlayer distances ($\sim 1/r^6$), allowing for easy exfoliation. Ultrathin crystals composed of an even number of layers have D_{3d} symmetry, while bulk crystals possess D_{6h} symmetry. Both are centrosymmetric, due to the presence of an inversion center in between the neighboring planes (Fig. 2.2D). On the other hand, for an isolated monolayer, the inversion symmetry is broken (D_{3h} point group). The hexagonal crystal symmetry leads to a hexagonal Brillouin zone, which is shown in Fig. 2.2E

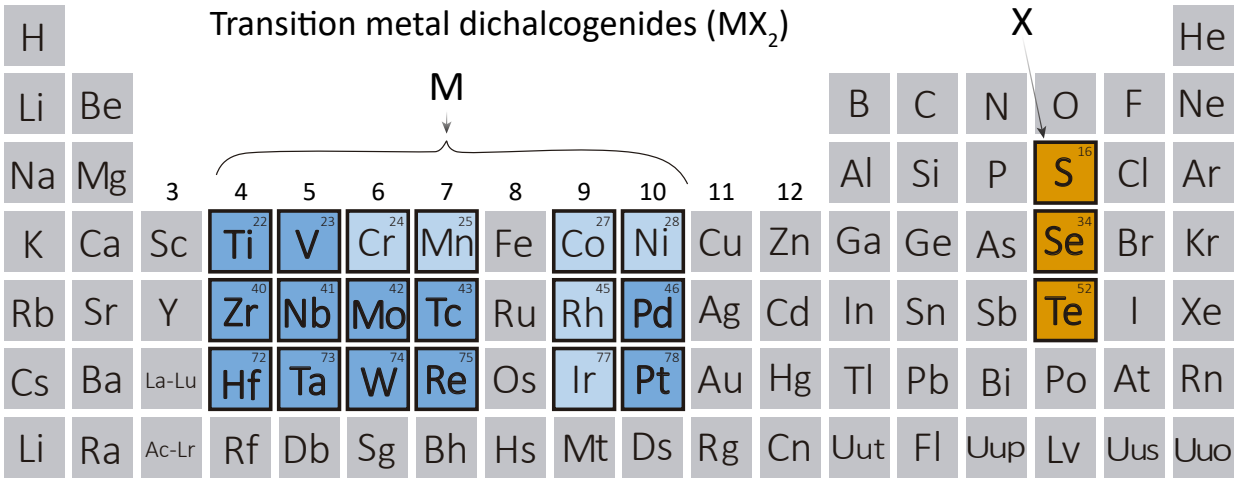

Figure 2.1: Transition metal dichalcogenides. Periodic table highlighting the numerous possible layered TMD compounds. The lighter shading in the transition metal group designate the atoms that sometimes form dichalcogenides with a 3D (non-layered) form. Based on the specific metal and chalcogen, the resulting symmetry (either trigonal prismatic or octahedral (possibly distorted)) and metal d-electron count play key roles in establishing the basic electronic properties.

with several important high-symmetry points labeled.

Although the bulk forms of MX_2 semiconductors were first studied in the 1960s and 1970s [11], interest was reignited in 2010 with the isolation of MoS_2 to the atomically thin limit and the discovery of bright photoluminescence (PL) [9, 10]. When moving from bilayer to monolayer MoS_2, there is a drastic increase in the PL intensity, as shown in the PL image in Fig. 2.3A, which originates from an indirect-to-direct bandgap transition from bilayer to monolayer. Bright PL at different wavelengths is also observable in monolayer WS_2, $MoSe_2$, and WSe_2 (Fig. 2.4). For all MX_2 of bilayer thickness and above, the valence band edge is at Γ, while the conduction band edge lies at the Q point (halfway between Γ and K), as shown in Fig. 2.3B. Since the photon momentum is $\sim 10^{-3}K$, phonon or defect scattering is required to satisfy momentum conservation during radiative recombination at this indirect bandgap, which implies weak PL intensity. In the monolayer, however, the valence band at Γ shifts down significantly, and the Q point shifts up, leaving the largely unchanged K point extrema as the new bandgap (Fig. 2.3B) [10]. The K direct gap naturally allows for bright PL emission. The indirect-to-direct gap transition can be understood by considering the orbital contributions to the K, Q, and Γ points, which are shown for a monolayer in

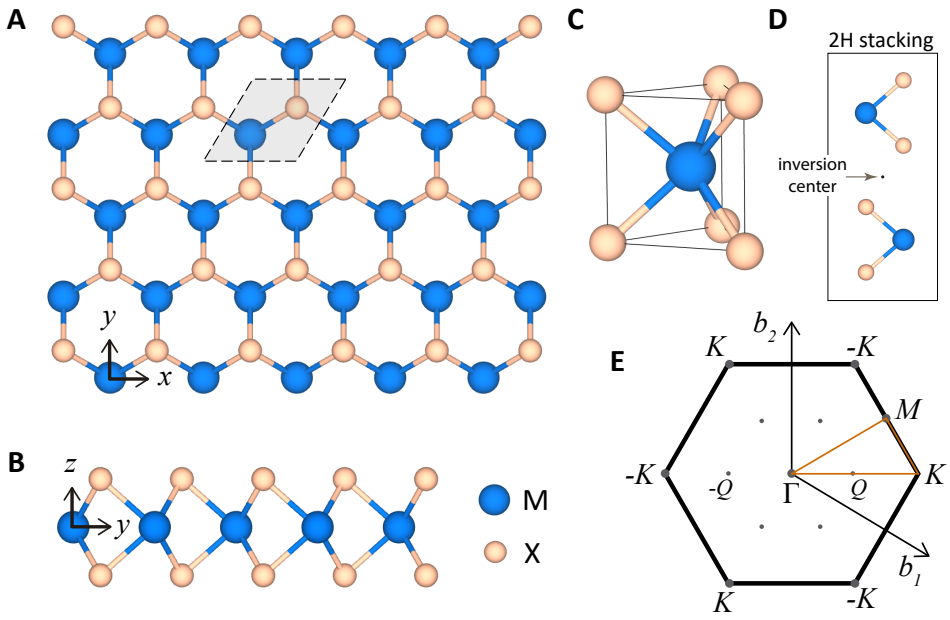

Figure 2.2: Group-6 TMD crystal structure. (A) Top view of monolayer MX_2 crystal structure. The diamond shows the unit cell. (B) Side view of monolayer crystal structure, as viewed along the zigzag edge direction. (C) Trigonal prismatic coordination of the M atom. (D) Side view of 2H-stacked bilayer unit cell. The inversion center is shown by the black dot. (E) First Brillouin zone with high-symmetry points labeled. The bandstructures shown later in this section are drawn along the orange path. b_1 and b_2 are the reciprocal lattice vectors.

Fig. 2.5. The K points predominantly consist of d orbitals, which are located in the metal atom plane away from the adjacent layers, while the Γ and Q points contain significant p_z orbital contribution from the chalcogen atom. The spatial overlap between the p_z orbitals at Γ and Q in adjacent layers is significant, which naturally explains their significant energetic shift in the monolayer when the interlayer interaction is removed.

In the monolayer limit, we can therefore understand the basic optical properties by considering the electronic structure at the $\pm K$ points [13]. However, the bandstructures given in Figs. 2.3 and 2.5 are missing an important ingredient: spin-orbit coupling. For bulk MX_2, spin-up and spin-down electrons at any k point are energetically degenerate ($E_\uparrow(k) = E_\downarrow(k)$) because there exist both time-reversal symmetry ($E_\uparrow(k) = E_\downarrow(-k)$) and inversion symmetry ($E_\uparrow(k) = E_\uparrow(-k)$). Monolayers have no inversion symmetry, on the other hand, and therefore a spin splitting can develop at finite k [14]. Furthermore, the presence of a mirror plane, σ_h, along the metal atom plane (Fig. 2.2B) constrains the spins (and spin splitting) to the

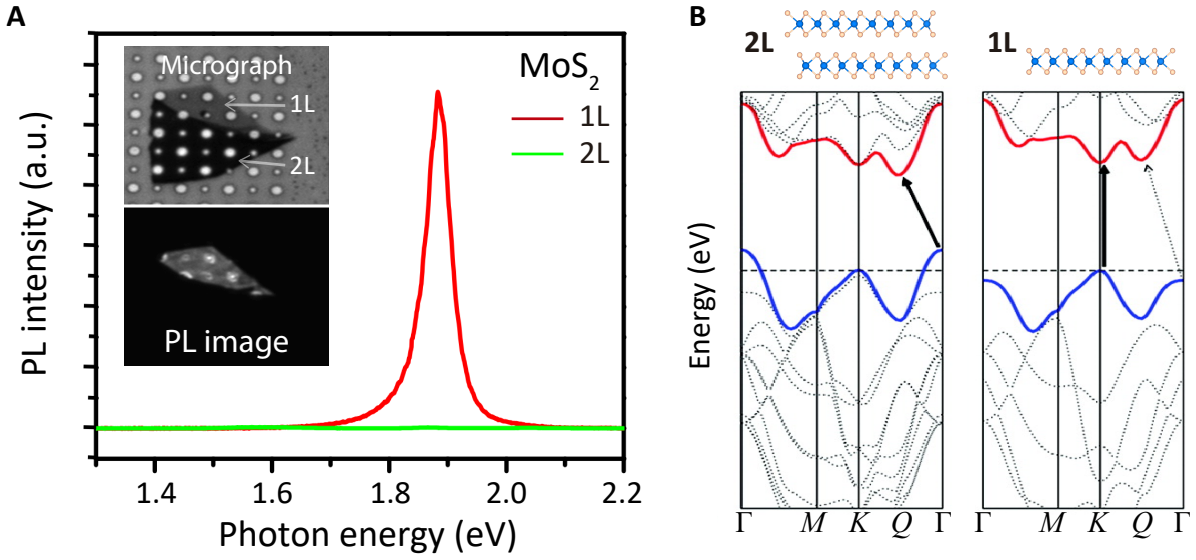

Figure 2.3: Indirect-to-direct gap transition. (A) Photoluminescence (PL) spectrum of monolayer (1L) and bilayer (2L) MoS_2 at room temperature. Inset: optical micrograph and PL image of an MoS_2 flake with 1L and 2L areas. [Adapted with permission from [9]. Copyright 2010 by the American Physical Society.] (B) Bandstructure of 1L and 2L MoS_2 calculated by density functional theory. The dark arrows show the lowest energy transition, which changes to a direct-gap transition at K in the 1L case. [Adapted with permission from [10]. Copyright 2010 American Chemical Society.]

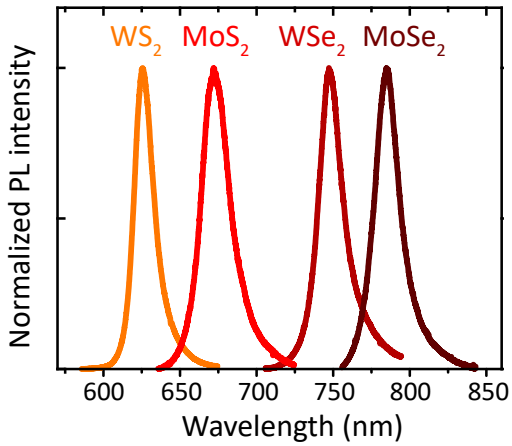

Figure 2.4: Photoluminescence of group-6 MX_2. Typical PL spectra for WS_2, MoS_2, WSe_2, and $MoSe_2$, taken at room temperature.

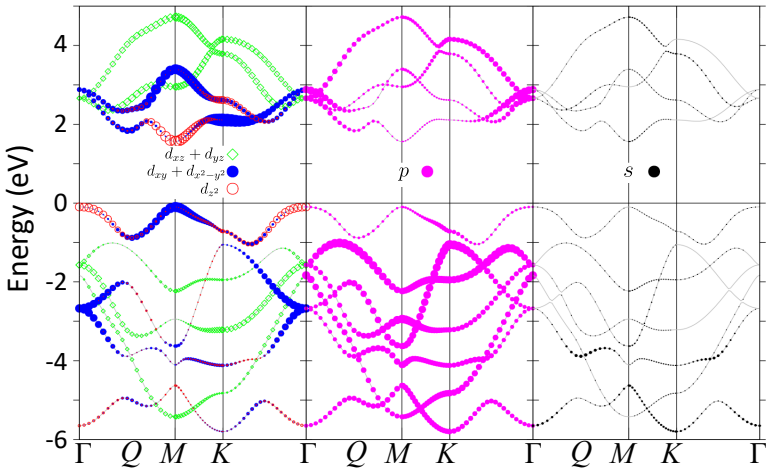

Figure 2.5: Orbital-projected bandstructure for MX_2. The symbols denote the different orbitals that contribute to the bandstructure, and their size is proportional to the population of the state. [[12] - Reproduced by permission of The Royal Society of Chemistry.]

out-of-plane direction. In-plane spins are forbidden because they flip to the opposite orientation under σ_h reflection, while out-of-plane spins map to themselves. As seen in Fig. 2.2A, in-plane inversion symmetry is absent in the y direction (and its C_3 counterparts), which generates a crystal electric field. Electrons travelling perpendicular to these directions (e.g. with momentum along k_x) experience the electric field as an effective magnetic field in the out-of-plane direction. Consequently, spin splittings develop along the Γ-K direction [14]. The magnitude of the spin-orbit coupling ($\lambda \mathbf{L} \cdot \mathbf{S}$) depends on the orbital contributions. For $\pm K$ point valence bands, there is a large spin splitting from the $d_{x^2-y^2} + d_{xy}$ states, which is significantly larger for the heavier W compounds than Mo [14]. In conduction band, the spin splitting is signficantly lower because the dominant orbital contribution is d_{z^2}, which has $L_z = 0$. The finite splitting arises from a balance between chalcogen $p_x \pm ip_y$ influence and second-order effects from coupling to $d_{xz} \pm id_{yz}$ conduction bands [12]. Finally, because time-reversal symmetry remains, the spin splitting is equally strong but opposite in sign at $+K$ and $-K$ [13]. The bandstructure at $\pm K$ is shown in Fig. 2.6 for $MoSe_2$ and WSe_2, with the bandgap (E_g), valence band splitting (Δ^v_{SOC}) and conduction band splitting (Δ^c_{SOC}) splittings labeled. We will revisit the MX_2 electronic structure in context of valley physics in section 2.3 after a brief detour on 2D exciton physics.

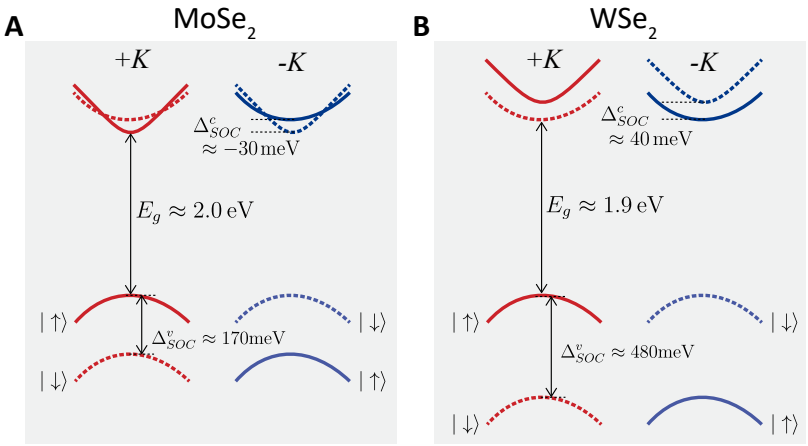

Figure 2.6: K-point bandstructure energies. Schematic of the bandstructure at the $\pm K$ points for $MoSe_2$ (left) and WSe_2 (right) with spin up (down) states marked by solid (dashed) lines. Energies for the band gap (E_g) and spin-orbit splitting (Δ^c_{SOC} for the conduction band and Δ^v_{SOC} for the valence band) are marked on each panel. The quantities are estimates based on various calculations, optical measurements, and scanning tunneling microscopy studies (see references in [15]).

2.2 2D excitons

The optical properties of MX_2 are dramatically influenced by strong Coulomb interactions between photoexcited electrons and holes, which lead to the formation of tightly bound excitons. For a 2D semiconductor in the absence of Coulomb interactions, the absorption edge is given by a step function due to the constant joint density of states. However, as shown by the absorption spectra for different MX_2 monolayers in Fig. 2.7A [16], this is not the case in practice. There are prominent excitonic absorption peaks at low energy, labeled A and B, which correspond to spin-allowed transitions from the spin-split valence band to the conduction band at the K points. Furthermore, Coulomb effects, in addition to several higher-energy interband transitions, enhance the higher-energy absorption and cause it to deviate from a simple band edge. One should notice that the A exciton absorption (e.g. $\sim$1.7 eV for WSe_2) is substantially lower energy than the bandgap given in Fig. 2.6 ($\sim$2 eV). The exciton binding energy is, therefore, several hundred meV in MX_2 [15], which is an order of magnitude larger than both bulk MX_2 semiconductors [17] and quasi-2D quantum well systems [18].

The strong exciton binding energy (E_b) arises from dimensionality and screening effects,

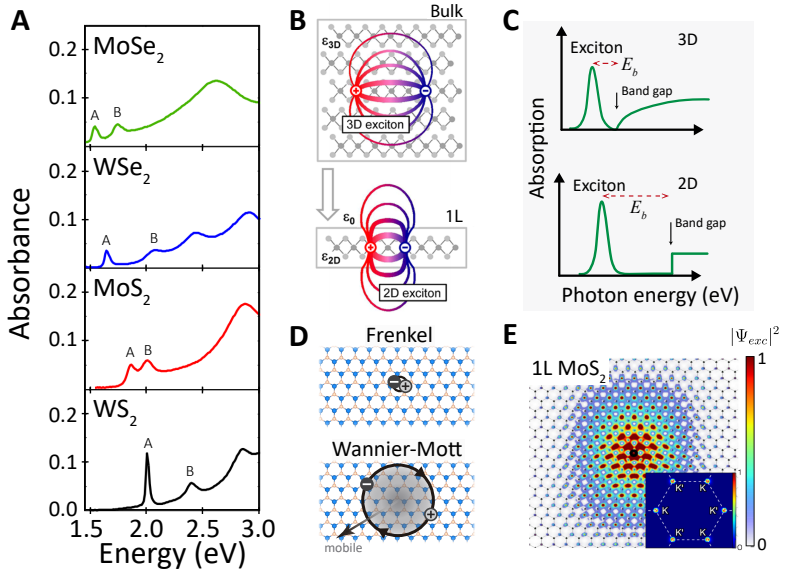

Figure 2.7: Excitonic properties of MX_2. (A) Absorbance of different monolayer MX_2 with A and B excitonic resonances labeled. [Adapted with permission from [16]. Copyright 2014 by the American Physical Society.] (B) Schematic of an exciton in monolayer versus bulk, with the electron and hole electric field lines. The Coulomb interaction is enhanced in the 2D limit since there is less screening from the surrounding media. [Adapted with permission from [19]. Copyright 2014 by the American Physical Society.] (C) Schematic absorption spectrum of an exciton in 2D vs 3D, where the binding energy (E_b) is significantly higher in 2D. [Adapted with permission from [19]. Copyright 2014 by the American Physical Society.] (D) Schematic of a Frenkel and Wannier-Mott exciton. The Wannier-Mott exciton has considerably larger Bohr radius and is free to move throughout the crystal, but its binding energy is generally much lower. (E) Calculated real-space and momentum-space (inset) exciton wavefunction. The plots show the electron spatial probability density with hole position fixed. [Adapted with permission from [20]. Copyright 2013 by the American Physical Society.]

in addition to large effective electron and hole masses [15]. Considering the electron and hole of the exciton as a simple hydrogenic system, the 3D binding energy $E_b^{(3D)} = R_y^*/n^2$, while for the 2D case, it is modified to $E_b^{(2D)} = R_y^*/(n-1/2)^2$. Therefore, the binding energy should be four times stronger in 2D compared to 3D for the lowest exciton state. In addition, the effective Ryberg energy $R_y^* \propto \mu/\epsilon_{\text{eff}}^2$, where μ the reduced mass (μ) of the electron-hole system and ϵ_{eff} is the effective dielectric constant of the surrounding media. The effective masses at the K band edges are $\sim 0.5m_0$, where m_0 is the free electron mass, implying $\mu \approx \sim 0.25m_0$. These is well above other semiconductor systems like GaAs ($\mu \approx 0.06m_0$)

and further enhances the binding energy in MX_2. Moreover, unlike in traditional quantum wells, the MX_2 are often supported by a low-permittivity substrate (such as SiO_2) with only vacuum or air above, thus lowering ϵ_{eff} and increasing E_b. A schematic of the enhanced Coulomb interactions and binding energy for 2D materials are shown in Fig. 2.7B and C. The effect of screening by the surrounding dielectric also strongly depends on the electron-hole separation [19]. At large separations (r), the potential follows the usual $1/r$ dependence. But for smaller separations, screening from the 2D material dielectric constant itself becomes relevant, and the potential goes like $\log(r)$. Since the exciton Bohr radius (a_B) increases with increasing principal quantum number n, the energetic spacing of the various ground and excited exciton states deviates from the hydrogenic series. This situation was described analytically by Keldysh in 1979 [21] with the potential:

$$V(r) = -\frac{e^2}{8\epsilon_0 r_0}\Big[H_0(\frac{\kappa r}{r_0}) - Y_0(\frac{\kappa r}{r_0})\Big], \tag{2.1}$$

where r_0 is a characteristic screening length (related to the polarizability), and Y_0 and H_0 are Neumann and Struve functions. Several experiments using linear and nonlinear optical spectropscopy have confirmed this non-hydrogenic excitonic series. A more detailed discussion of the experiments and theory may be found in the review article by Wang et al. [15] and references therein.

The excitons in MX_2 monolayers lie at an interesting intermediate region between traditional Wannier-Mott and Frenkel excitons [22]. Frenkel excitons typically correspond to charge-transfer excitations between adjacent atomic sites (Fig. 2.7D), so the electron-hole separation is comparable to the lattice spacing, and they have large binding energies ($\sim$1 eV). Wannier-Mott excitons, in contrast, are at the other limit with large exciton Bohr radius and consequently much lower binding energy ($<$0.1 eV). For MX_2 monolayers, the Bohr radius $a_B \sim 1$ nm, so excitons extend over several unit cells (lattice constant $\sim$0.3 nm), and they possess binding energies $\sim$0.5 eV. The calculated $1s$ real-space and momentum-space exciton wavefunction for MoS_2 is shown in Fig. 2.7E [20]. Since the monolayer excitons are generally well-described by effective-mass theory, they are in practice considered to be "tightly bound Wannier-Mott excitons". A direct consequence of the small Bohr radius is large electron-hole wavefunction overlap, which implies large exciton oscillator strength. Furthermore, the strong Coulomb interactions permit the formation of other multi-particle excitonic states.

In particular, an additional electron or hole can bind to an exciton to form a negative

or positive trion. The binding energy of the extra electron or hole in monolayer MX_2 is typically $\sim$30 meV; therefore trion effects are not only prominent at low temperatures but can also influence room-temperature optical properties. Extensive experiments have been performed on electrostatically gated samples (Fig. 2.8A), where positive or negative gate voltages (V_g) dope electrons or holes into the monolayer MX_2 [23, 24]. Figure 2.8B shows a typical PL spectrum of monolayer $MoSe_2$ at 30 K at zero gate voltage [24]. The higher energy peak at $\sim$1.66 eV is the neutral exciton and the peak $\sim$30 meV lower in energy is the negative trion state. To definitively assign the charged excitonic states, one can sweep the gate voltage and monitor the PL spectrum. The results are shown in the PL intensity map of Fig. 2.8C, from [24], where there are clear transitions from the neutral exciton state to positive trion (X^+) and negative trion (X^-) away from zero gate voltage. The electrical control of excitonic states is illustrated schematically in Fig. 2.8D. Often, other emission features (apart from the neutral exciton and trions) can emerge depending on the sample or under particular experimental conditions. These include defect-bound exciton states, excited exciton states, biexcitons, exciton-trion complexes, phonon-related sidebands, momentum-indirect transitions, and more. One example is seen in Fig. 2.8C near zero doping, labeled X', which may be due to defect-bound excitons. The playground of exciton physics in 2D materials is extraordinarily rich, and it remains an active area of research full of debates and surprises [15]. In the next section, we move on to explore one of the most intriguing aspects of the electronic structure and optical properties of monolayer MX_2 semiconductors.

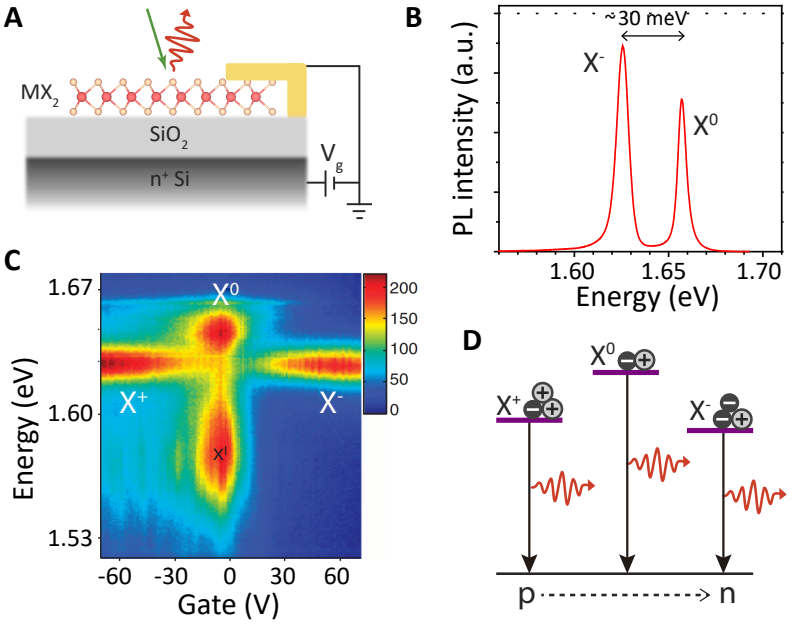

Figure 2.8: Neutral and charged excitons (trions) in MX_2. (A) Schematic of a field-effect transistor with monolayer MX_2. The heavily doped Si serves as a backgate, and the SiO_2 is the dielectric. A positive (negative) gate voltage, V_g, causes electrons (holes) to enter the monolayer from the metallic contact. (B) Low-temperature PL spectrum of monolayer $MoSe_2$, with exciton (X^0) and negative trion (X^-) states separated by a ~30 meV binding energy. (C) PL spectra versus applied gate voltage ("gate map") with excitonic species labeled. (D) Schematic of the gate-dependent excitonic states. [For Panels B-D. Reprinted by permission from [24]: Nature Communications, Copyright 2013.]

2.3 Valley physics in 2D semiconductors

The periodic crystal structure of semiconductors often leads to the formation of multiple valleys, which are local maxima in the valence band and local minima in the conduction band. In some semiconductors, the valleys are located at high symmetry points away from the Brillouin zone center (Γ), meaning there is more than one energetically degenerate valley. Electrons may thus possess a valley degree of freedom, in addition to charge and spin, which is potentially controllable through external stimuli for information processing and storage. For example, in AlAs, strain [25] and magnetic fields [26] have been used to break the valley degeneracy and create valley polarization. However, in general, the valley index is much less accessible than the electron spin, which makes it very difficult to construct useful valleytronic devices. Monolayer MX_2, on the other hand, possesses a highly accessible valley pseudospin

degree of freedom.

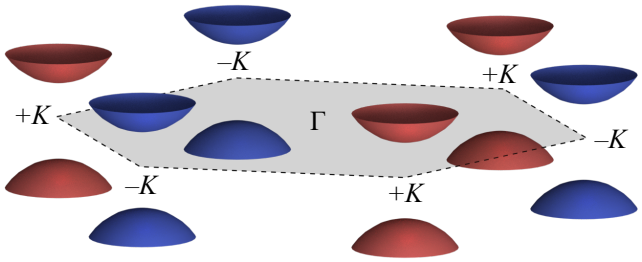

Figure 2.9: Low-energy bandstructure in first Brillouin zone. Schematic bandstructure of monolayer MX_2 with inequivalent $+K$ and $-K$ valleys labeled.

As we introduced in section 2.1, the low-energy bandstructure consists of direct gaps at the $\pm K$ points at the corners of the hexagonal Brillouin zone (Fig. 2.9) [13]. While the $\pm K$ valleys are degenerate, they are related by time reversal and are thus not equivalent. It is therefore in principle possible to distinguish between the valley states by addressing physical quantities that have odd parity under time reversal, such as a pseudovector like the magnetic moment ($\mathbf{m}(-\mathbf{k}) = -\mathbf{m}(\mathbf{k})$). However, under the spatial inversion operation, the momentum changes sign while a pseudovector does not ($\mathbf{m}(-\mathbf{k}) = \mathbf{m}(\mathbf{k})$). As a result, it is necessary to break inversion symmetry to achieve valley-contrasting phenomena [27, 28]. The broken inversion symmetry in monolayer MX_2 leads to the formation of a valley-contrasting Berry curvature ($\mathbf{\Omega}(\mathbf{k})$) and magnetic moment $\mathbf{m}$ [13].

2.3.1 Berry curvature

The Berry curvature and Berry phase are fundamental geometric properties of a quantum mechanical wavefunction in a parameter space [29, 30]. We refer the interested reader to the excellent review by Xiao, Chang, and Niu [31] for a detailed treatment on Berry phase effect in solids and an extensive list of references showing the ubiquity of Berry phase effects throughout physics. Here we will briefly overview some of the most relevant concepts, closely following [31], with the aim of giving some rough physical intuition for the relevance of Berry phase in monolayer MX_2.

Consider a quantum mechanical system that depends on a time-varying parameter $\mathbf{R}(t)$. Its Hamiltonian is $H(\mathbf{R})$ and the eigenstates are given by $H(\mathbf{R})|n(\mathbf{R})\rangle = E_n(\mathbf{R})|n(\mathbf{R})\rangle$. If the system begins in an eigenstate $|n(\mathbf{R}(t_i))\rangle$ at an initial time t_i, it will remain in that

eigenstate at a later time under adiabatic evolution, apart from a phase factor:

$$|\psi(t_f)\rangle = e^{-\frac{i}{\hbar}\int_{t_i}^{t_f} E_n(t')dt'} e^{i\phi_B} |n(\mathbf{R}(t_i))\rangle. \tag{2.2}$$

The first phase is the standard dynamical phase from time evolution, while the second one, ϕ_B, is the Berry phase. One might think that the Berry phase can be removed by simply adjusting the phase of the eigenbasis $|n(\mathbf{R})\rangle$ and thus it cannot be physically relevant. However, it turns out that this phase need not necessarily return to its original value after a cyclic evolution in the parameter $\mathbf{R}$. The situation is analogous to the general geometrical concept of parallel transport of a vector along a curved surface. During parallel transport, a vector moves along the surface without rotating about the local surface normal. For curved surfaces, the vector can acquire a rotation after being transported around a closed path. Adiabatic evolution is the quantum mechanical analog of parallel transport, and the Berry phase is the vector rotation. To determine the form of ϕ_B, we plug Eq. 2.2 into the time-dependent Schrödinger equation

$$i\hbar\frac{\partial}{\partial t}|\psi(t)\rangle = H(t)|\psi(t)\rangle \tag{2.3}$$

from which one can derive the form of the Berry phase

$$\phi_B = \int_{C_\mathbf{R}} d\mathbf{R} \cdot \langle n(\mathbf{R})|i\boldsymbol{\nabla}_\mathbf{R}|n(\mathbf{R})\rangle, \tag{2.4}$$

where $C_\mathbf{R}$ is a path in $\mathbf{R}$-space from $\mathbf{R}(t_i)$ to $\mathbf{R}(t_f)$. The Berry phase depends only upon the path in parameter space and not on the time taken. The integrand, $\mathbf{A} = \langle n(\mathbf{R})|i\boldsymbol{\nabla}_\mathbf{R}|n(\mathbf{R})\rangle$, is known as the Berry connection. We can also define the quantity $\boldsymbol{\Omega}(\mathbf{R}) = \boldsymbol{\nabla} \times \mathbf{A}(\mathbf{R})$, which is our Berry curvature. There is important insight to be gained from noting the mathematical similarities to electromagnetism. If one performs a gauge transformation $|n(\mathbf{R})\rangle \to e^{i\chi(\mathbf{R})}|n(\mathbf{R})\rangle$, then the Berry connection transforms as $\mathbf{A}(\mathbf{R}) \to \mathbf{A}(\mathbf{R}) - \boldsymbol{\nabla}_\mathbf{R}\chi(\mathbf{R})$. We see that the Berry connection behaves like the vector potential in electromagnetism, except the parameter space $\mathbf{R}$ need not be real space. Moreover, the gauge-invariant Berry curvature $\boldsymbol{\Omega}(\mathbf{R})$ acts like a magnetic field in $\mathbf{R}$-space.

How do these concepts translate to the physics of electrons in crystalline solids? The relevant parameter is the crystal momentum $\mathbf{k}$ across the space of the Brillouin zone. The eigenstates in a periodic Hamiltonian are Bloch wavefunctions, $\psi_{n\mathbf{k}}(\mathbf{r}) = e^{i\mathbf{k}\cdot\mathbf{r}}u_{n\mathbf{k}}(\mathbf{r})$, where

n is the band index and $u_{n\mathbf{k}}(\mathbf{r})$ is a cell-periodic function obeying the boundary condition $u_{n\mathbf{k}}(\mathbf{r}) = u_{n\mathbf{k}}(\mathbf{r}+\mathbf{a})$ (with $\mathbf{a}$ the lattice vector). The Schrödinger equation is recast into the $\mathbf{k}$-dependent form $H_{\mathbf{k}}|u_{n\mathbf{k}}\rangle = E_{n\mathbf{k}}|u_{n\mathbf{k}}\rangle$. The Bloch state can then acquire a Berry phase by tracing out a closed path in momentum space,

$$\phi_n = \int_{C_{\mathbf{k}}} d\mathbf{k} \cdot \langle u_n(\mathbf{k})|i\boldsymbol{\nabla}_{\mathbf{k}}|u_n(\mathbf{k})\rangle. \tag{2.5}$$

Furthermore, the Berry curvature in a solid can be now expressed as

$$\boldsymbol{\Omega}_n(\mathbf{k}) = \boldsymbol{\nabla}_{\mathbf{k}} \times \langle u_n(\mathbf{k})|i\boldsymbol{\nabla}_{\mathbf{k}}|u_n(\mathbf{k})\rangle. \tag{2.6}$$

Unlike the Berry connection and phase, the Berry curvature is uniquely defined across the Brillouin zone and is an intrinsic property of the band n. Two important consequences of a nonzero Berry curvature are anomalous Hall effects [32] and orbital magnetic moments [33–36]. A magnetic field affects the electron transport through the Lorentz force $-e\dot{\mathbf{r}} \times \mathbf{B}$ to give a semiclassical equation of motion:

$$\hbar\dot{\mathbf{k}} = -e\mathbf{E} - e\dot{\mathbf{r}} \times \mathbf{B}. \tag{2.7}$$

The Berry curvature serves as an analogous role to the magnetic field, but in momentum space, and affects the velocity

$$\dot{\mathbf{r}} = \frac{1}{\hbar}\frac{\partial E_{n\mathbf{k}}}{\partial \mathbf{k}} - \dot{\mathbf{k}} \times \boldsymbol{\Omega}_{n,\mathbf{k}}. \tag{2.8}$$

The final term here generates an perpendicular velocity to the electric field $\mathbf{E}$, leading to an anomalous Hall effect (even in the absence of a magnetic field). Furthermore, an electron wavepacket in a Bloch band with nonzero Berry curvature in general rotates about its center of mass, which generates an orbital magnetic moment $\mathbf{m}_n(\mathbf{k})$. The orbital magnetic moment is given by

$$\mathbf{m}_n(\mathbf{k}) = -i\frac{e}{\hbar}\langle \boldsymbol{\nabla}_{\mathbf{k}} u_n(\mathbf{k})| \times [H_{\mathbf{k}} - E_{n\mathbf{k}}]|\boldsymbol{\nabla}_{\mathbf{k}} u_n(\mathbf{k})\rangle, \tag{2.9}$$

which modifies the electron energy to $\tilde{E}_{n\mathbf{k}} = E_{n\mathbf{k}} - \mathbf{m}_n(\mathbf{k}) \cdot \mathbf{B}$.

2.3.2 Monolayer electronic structure

We qualitatively explored the bandstructure of monolayer MX_2 in section 2.1, but now let us dive deeper and synthesize our understanding and consider the role Berry curvature and orbital magnetic moments. Near the $\pm K$ points, monolayer MX_2 is commonly described by the massive Dirac fermion Hamiltonian with spin-orbit coupling [13]:

$$\hat{H} = at(\tau_z k_x \hat{\sigma}_x + k_y \hat{\sigma}_y) + \frac{\Delta}{2}\hat{\sigma}_z + \lambda\tau_z \frac{\hat{\sigma}_z - 1}{2} s_z \tag{2.10}$$

$$= \begin{bmatrix} \Delta/2 & at(\tau_z k_x - ik_y) \\ at(\tau_z k_x + ik_y) & -\Delta/2 + \lambda\tau_z s_z \end{bmatrix}. \tag{2.11}$$

The C_{3h} symmetry-adapted basis functions at $\pm K$ are $d_c = d_0 = d_{z^2}$ for the conduction band and $d_v = d_{2\tau_z} = \frac{1}{\sqrt{2}}(d_{x^2-y^2} + i\tau_z d_{xy})$ for the valence band. They have even parity under reflection about the mirror plane σ_h, allowing them to hybridize and open a bandgap Δ. In Eq. 2.10, $\hat{\sigma}$ are the Pauli matrices for these basis functions, $\tau_z = \pm 1$ is the valley index for $\pm K$, t is the nearest-neighbor hopping integral, and a is the lattice constant. The final term gives the spin-splitting ($s_z = \pm 1$ is spin up/down) at the valence band, 2λ, which arises from the spin-orbit interaction $\lambda \mathbf{L} \cdot \mathbf{S}$. We note that the wavevector ($\mathbf{k}$) in this $\mathbf{k} \cdot \mathbf{p}$ Hamiltonian is measured from $\pm K$.

The Berry curvature and the orbital magnetic moment for the massive Dirac fermion model are [13]

$$\boldsymbol{\Omega}_c(\mathbf{k}) = -\tau_z \frac{2a^2t^2\Delta}{(4a^2t^2k^2 + \Delta^2)^{3/2}}\hat{\mathbf{z}} \tag{2.12}$$

$$\boldsymbol{\Omega}_v(\mathbf{k}) = -\boldsymbol{\Omega}_c(\mathbf{k}) \tag{2.13}$$

and

$$\mathbf{m}(\mathbf{k}) = \tau_z \frac{2a^2t^2\Delta}{4a^2t^2k^2 + \Delta^2}\frac{e}{2\hbar}\hat{\mathbf{z}}. \tag{2.14}$$

As expected from our earlier considerations of time-reversal symmetry and broken inversion symmetry, both $\boldsymbol{\Omega}$ and $\mathbf{m}$ are nonzero at the $\pm K$ points with opposite signs. Exactly at the $\pm K$ points, the magnetic moment simply becomes $\mathbf{m} = \tau_z \mu_B^* \hat{\mathbf{z}}$, where $\mu_B^* = e\hbar/2m^*$ is the Bohr magneton with electron effective mass m^*. First-principles calculations of the Berry curvature are shown in Fig. 2.10A and B, confirming finite value and valley contrast

at $\pm K$ [37]. Due to this valley-contrasting Berry curvature, electrons in $+K$ will move in the opposite direction to those in $-K$ under an applied in-plane electric field, thus leading to a valley Hall effect [38, 39]. In Fig. 2.10C, we schematically show the magnetic moments of Bloch wavepackets near $\pm K$ [40]. In addition to the self-rotation contribution to the orbital magnetic moment described above, there are two additional magnetic moments. The d atomic orbitals themselves give a magnetic moment of $2\tau_z \mu_B \hat{\mathbf{z}}$ (0) in the valence (conduction) band. Lastly, the spin magnetic moment, which is locked to valley index due to the spin-orbit splitting (Fig. 2.6), contributes $s_z \mu_B \hat{\mathbf{z}}$.

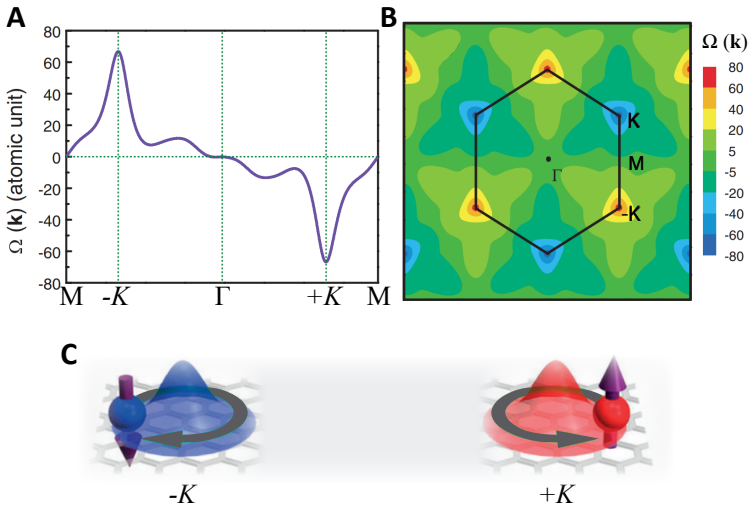

Figure 2.10: Berry curvature and magnetic moment in monolayer TMDs. Calculated Berry curvature in the conduction band shown along high-symmetry points (A) and across the Brillouin zone (B). The Berry curvature in the valence band has the opposite sign. [Reprinted with permission from [37]. Copyright 2012 by the American Physical Society.] (C) Schematic of the electron wavepackets at the $\pm K$ valleys showing their magnetic moments. The gray arrow represents the self-rotation of the wavepackets that gives rise to an orbital magnetic moment. The electrons also possess magnetic moments from the atomic orbitals (depicted by the arrows) and spin (depicted by red and blue color). [Reprinted by permission from [40]: Nature Physics, Copyright 2015.]

2.3.3 Valley optical selection rules

An important consequence of the valley-contrasting orbital magnetic moment is valley-dependent optical selection rules [13]. In other words, σ^+ light polarization couples to the

$+K$ valley, while σ^- couples to $-K$. The degree of circular polarization near $\pm K$ is related to the magnetic moment by

$$\eta(\mathbf{k}) \equiv \frac{|P_+(\mathbf{k})|^2 - |P_-(\mathbf{k})|^2}{|P_+(\mathbf{k})|^2 + |P_-(\mathbf{k})|^2} = \frac{\mathbf{m}(\mathbf{k}) \cdot \hat{\mathbf{z}}}{\mu_B^*(\mathbf{k})}, \tag{2.15}$$

where $|P_\pm(\mathbf{k})|^2$ is the oscillator strength for $\sigma^\pm$ light [13]. At $\pm K$ exactly, there is complete circular dichroism, with $\eta = \tau_z$. These valley optical selection rules are shown in Fig. 2.11. Since spin-orbit coupling locks the valley to the spin direction, the circular selection rules are also spin-selective: in the spin-conserving optical transitions shown in Fig. 2.11, spin up (down) electrons are excited in $+K$ $(-K)$.

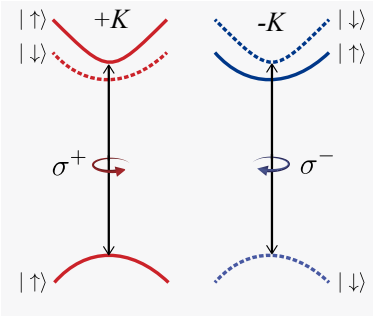

Figure 2.11: Valley optical selection rules. Optical transitions in the $+K$ $(-K)$ valley are allowed for only σ^+ (σ^-) light. Due to the large spin-splitting in the valence band (only uppermost band shown), the lowest energy spin-conserved optical transitions are necessarily spin-selective.

Due to the centrality of the valley optical selection rules to monolayer TMD physics, it is worthwhile to understand them in more detail. First, let us gain some intuition. The valley selection rule implies that the change in angular momentum between conduction and valence band states is $\pm\hbar$, since $\sigma^\pm$ photons carry $\pm\hbar$ angular momentum. From looking at the relevant atomic orbitals, $m_v = 2\tau_z$ and $m_c = 0$, it is not immediately obvious how this can be satisfied. It turns out the missing ingredient is the C_3 rotational symmetry at $\pm K$ points, which effectively relaxes the requirement for angular momentum conservation to modulo $3\hbar$ and thus permits $\sigma^\pm$ transitions at $\pm K$.

We can make this more rigorous by exploring the impact of C_3 rotation on the Bloch states and then considering the effects on the interband optical matrix element. The Bloch

states are expressed as [41]

$$\psi_\alpha^{\tau_z}(\mathbf{r}) = \frac{1}{N}\sum_{\mathbf{a}} e^{i\tau_z \mathbf{K}\cdot(\mathbf{r}+\boldsymbol{\delta})} d_\alpha(\mathbf{r}-\mathbf{a}-\boldsymbol{\delta}), \tag{2.16}$$

where N is the unit cell number, $\mathbf{a}$ is the lattice vector, δ is the metal atom position within the unit cell, and $\alpha = c, v$. The effect of C_3 on $\psi_\alpha^{\tau_z}(\mathbf{r})$ was derived in [41]:

$$C_3\psi_\alpha^{\tau_z}(\mathbf{r}) = \gamma_{d_\alpha} e^{i\tau_z \mathbf{K}\cdot(C_3^{-1}\boldsymbol{\delta}-\boldsymbol{\delta})}\psi_\alpha^{\tau_z}(\mathbf{r}). \tag{2.17}$$

The eigenvalue of C_3, $\gamma_\alpha^{\tau_z}$, has two components: γ_{d_α} and $e^{i\tau_z \mathbf{K}\cdot(C_3^{-1}\boldsymbol{\delta}-\boldsymbol{\delta})}$. The first is due to the rotation of the atomic orbitals about their center, which transform as $C_3 d_0 = d_0$ in the conduction band and $C_3 d_{2\tau_z} = e^{i\tau_z 2\pi/3} d_{2\tau_z}$ in the valence band. The second arises from the change in planewave phase factor $e^{i\tau_z \mathbf{K}\cdot\mathbf{r}}$ after C_3 rotation. This lattice contribution depends on $\boldsymbol{\delta}$ and thus changes for different rotation centers, which can be chosen as the metal atom, chalcogen atom, or center of the hexagon. The total eigenvalues and their dependence on rotation center has been tabulated in [42]. If we choose the metal atom as our rotation center, $\boldsymbol{\delta} = 0$, so there is no change in lattice phase factor, and we are left with $\gamma_c^{\tau_z} = 1$ and $\gamma_v^{\tau_z} = e^{i\tau_z 2\pi/3}$. These eigenvalues enable us to extract the optical selection rule. Following [42], we write the interband optical transition matrix element

$$\begin{aligned}
\langle\psi_f|\hat{P}_\pm|\psi_i\rangle &= \langle\psi_f|C_3^{-1}C_3\hat{P}_\pm C_3^{-1}C_3|\psi_i\rangle \\
&= \langle C_3\psi_f|C_3\hat{P}_\pm C_3^{-1}|C_3\psi_i\rangle \\
&= e^{-i\frac{2\pi}{3}(m_f - m_i \pm 1)}\langle\psi_f|\hat{P}_\pm|\psi_i\rangle,
\end{aligned} \tag{2.18}$$

where the m_f and m_i are determined by the C_3 eigenvalues according to $C_3\psi_f = e^{i\frac{2\pi m_f}{3}}\psi_f$ and $C_3\psi_i = e^{i\frac{2\pi m_i}{3}}\psi_i$, and $\hat{P}_\pm = \hat{P}_x \pm i\hat{P}_y$ is the momentum operator, which transforms as $C_3\hat{P}_\pm C_3^{-1} = e^{-i\frac{2\pi}{3}}\hat{P}_\pm$. For the matrix element to be nonzero, $e^{-i\frac{2\pi}{3}(m_f - m_i \pm 1)} = 1$, therefore the selection rule can be written as $\text{modulo}(m_f - m_i \pm 1, 3) = 0$ for $\sigma^\pm$. Using our Bloch state C_3 eigenvalues with the metal atom as the rotation center, $m_f = 0$ and $m_i = \tau_z$, therefore confirming once again that only σ^+ (σ^-) optical transitions are allowed at $+K$ ($-K$). If we choose a different rotation center, the C_3 eigenvalues of ψ_c and ψ_v change, but the eigenvalue of the electron-hole pair $\psi_c\psi_v^*$ does not (i.e. $\text{modulo}(m_f - m_i, 3)$ is constant) is independent of rotation center), so the selection rule is unaffected.

The same optical selection rules can also be derived by directly considering the irreducible

representations of the initial and final states at $\pm K$ under the C_{3h} point group. This more traditional approach is detailed in [43, 44]. Finally, we note that the inherent chirality of the basis functions at $\pm K$ in two dimensions was acknowledged as early as 1972 by Yoffe and co-workers [45]. They observed that at the K points, "...the optical selection rules do not depend on the linear polarization of the light, but on the sense of circular polarization. Unfortunately, this unusual situation will only occur in very thin crystals, approximating the single layer model...".

2.3.4 Valley polarization and Zeeman effect

Soon after the isolation of MX_2 to their monolayer forms, the valley optical selection rules were confirmed experimentally through PL measurements [46–49]. Optical excitation with σ^+ light exclusively creates electron-hole pairs in the $+K$ valley, which bind via the Coulomb interaction to form $+K$ valley excitons. Assuming the excitons do not scatter to $-K$, the PL emitted after recombination should be σ^+ polarized. The same process occurs with σ^- polarization in the $-K$ valley. As a result, co-circularly polarized PL is the signature of optically generated exciton valley polarization. In Fig. 2.12A and C, we show the PL of a typical monolayer WSe_2 at 30 K from [46], where significant valley polarization is detected in both the exciton and trion species. In addition to creating valley polarization, one can also generate exciton valley coherence [46] by exciting the system with linearly polarized light, which is a superposition of σ^+ and σ^- light. This creates a coherent superposition of $+K$ and $-K$ valley pseudospin states. If the valley exciton superposition maintains coherence before recombination, the emitted PL should be linearly polarized along the same direction as the excitation. The detection of valley coherence for the WSe_2 monolayer is shown in the PL spectra of Fig. 2.12B [46], where under vertical linear excitation, the vertically polarized PL component is much stronger than horizontally polarized PL. One can further confirm the coherence by rotating the angle of linear polarization (which changes the phase relation between σ^+ and σ^-), and the emitted PL linear polarization will follow that of the excitation. Note that there is no valley coherence in the trion state due to the orthogonality of the leftover charged particle between the two valleys after electron-hole recombination, which prohibits linear superpositions of σ^+ and σ^- in the emission. Similar to a spin-1/2 system, we can represent the two-level valley state space with a Bloch sphere (Fig. 2.12D), where $+K$ and $-K$ states are at the north and south poles, and the equator represents the coherent valley superposition states. The creation and manipulation of states in the valley Bloch sphere lie

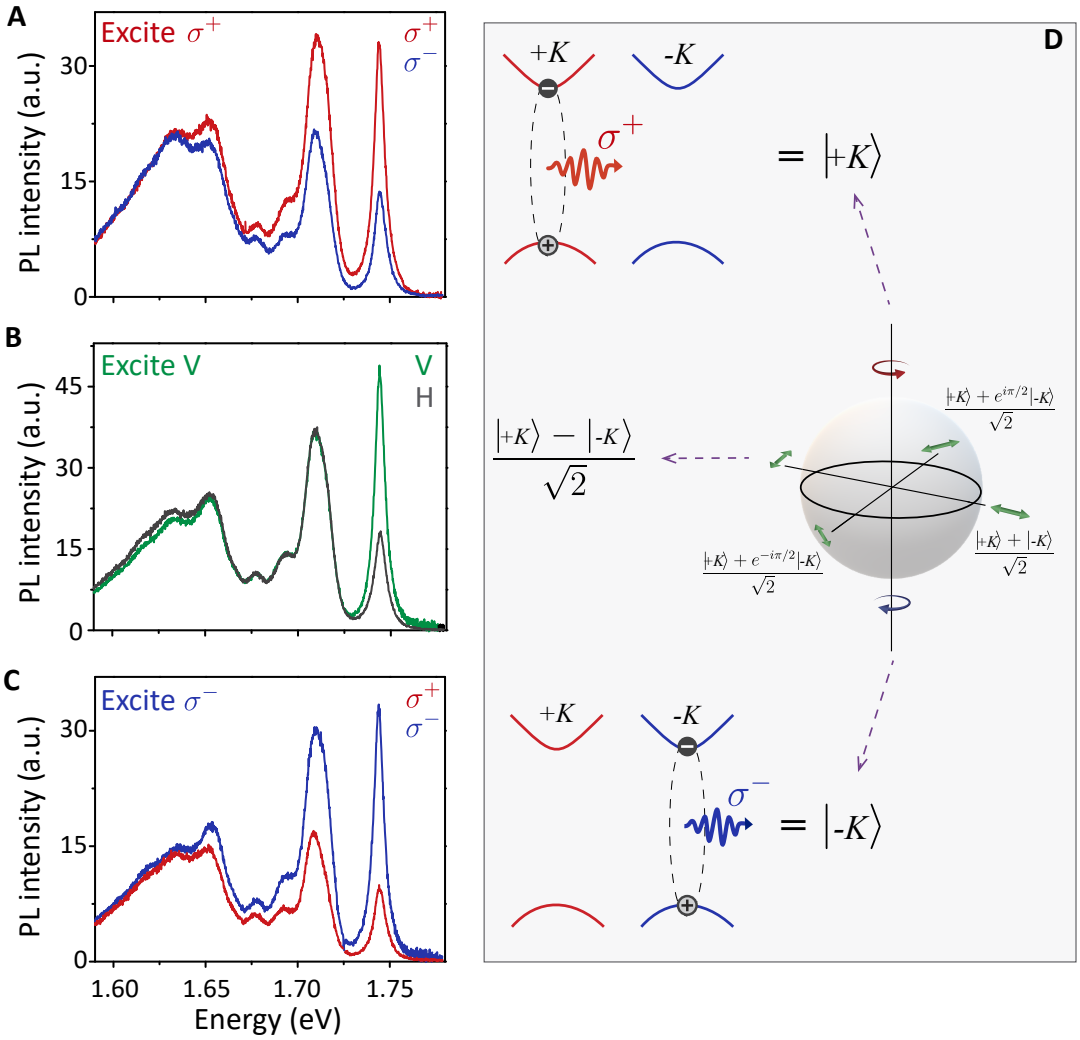

Figure 2.12: Valley polarization and coherence. σ^+ (red) and σ^- (blue) PL spectra in monolayer WSe_2 under σ^+ (A) or σ^- (C) laser excitation. There is strong co-circular polarization in each case. The data are taken at 30 K. (B) PL spectrum under linear excitation (V, green) with co-linear (V) or cross-linear (black) detection. The polarization on the exciton peak is valley coherence. (D) Representation of the valley polarization and coherence using the Bloch sphere. [Adapted by permission from [46]: Nature Nanotechnology, Copyright 2013.

at the heart of valleytronics.

Due to the valley-contrasting magnetic moment, a simple method to manipulate the valley pseudospin is to apply a magnetic field [40, 51–56]. The magnetic moments are entirely out-

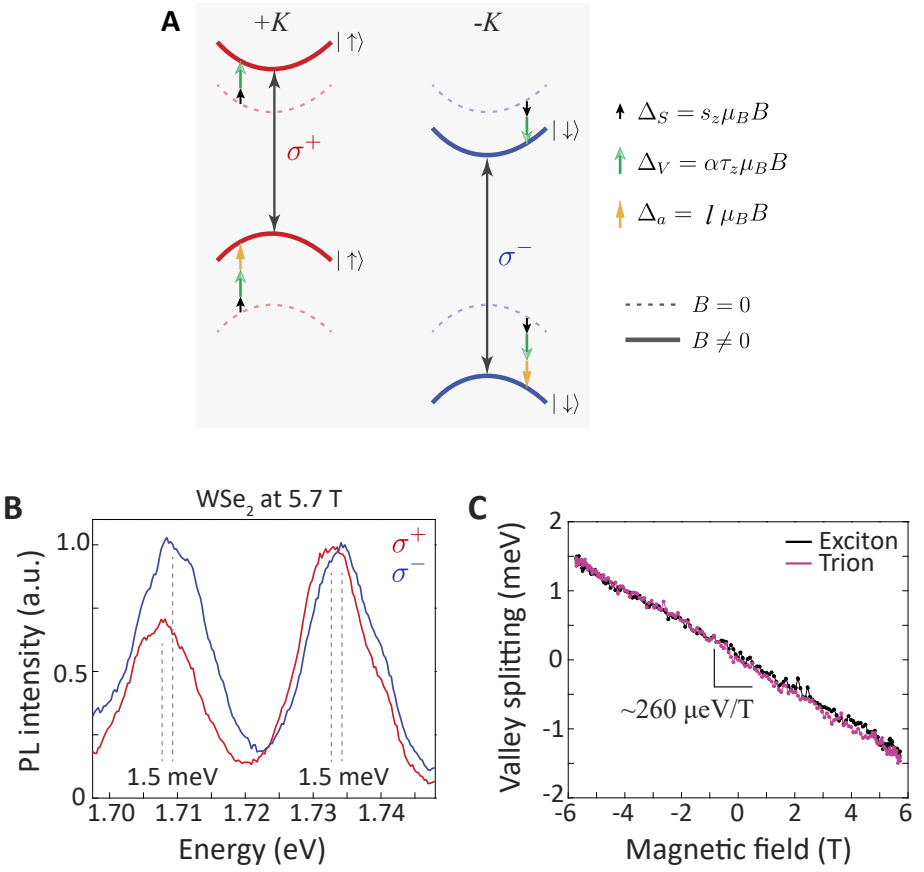

Figure 2.13: Valley Zeeman effect. (A) Energy levels of the $\pm K$ valleys under a magnetic field out of the sample plane. The different arrows denote the Zeeman effect from the magnetic moment contributions of spin (S), valley (V), and the atomic orbitals (a). Note that only one spin-split conduction band state is shown, which is most relevant to the spin-conserving optical transition. [Panels B and C are reprinted with permission from [50] under CC BY-NC 4.0.]

of-plane, so a perpendicular magnetic field breaks the degeneracy between the $+K$ and $-K$ valleys through the Zeeman effect, $E = E_0 - m_{\tau_z} B_z$. As we described earlier, the magnetic moment has spin (S), valley (V), and atomic orbital (a) contributions, which are listed in Fig. 2.13A along with their effect on the bands. The Zeeman splitting between $+K$ and $-K$

energy gaps are given by

$$\begin{aligned}\Delta_{Zeeman} &= 2[(\Delta_{S,c} - \Delta_{S,v}) + (\Delta_{V,c} - \Delta_{V,v}) + (\Delta_{a,c} - \Delta_{a,v})] \\ &= 2(2S_{z,c} - 2S_{z,v} + \alpha_c - \alpha_v - 2)\mu_B B \\ &= g_{\text{eff}}\mu_B B.\end{aligned} \tag{2.19}$$

The relevant optical transitions conserve spin ($S_{z,v} = S_{z,c}$), so the spin contribution drops out. The atomic orbital contribution is $4\mu_B B$ ($l = \pm 2$ in the valence band and $l = 0$ in the conduction band). Finally, the valley contribution is $2(\alpha_c - \alpha_v)\mu_B B$, where $\alpha = m_0/m^*$. Figure. 2.13B shows circularly polarized PL spectra of WSe_2 monolayer at 5.7 T magnetic field [50]. There is a clear energy splitting between σ^+ ($+K$) and σ^- ($-K$) emission. The splitting is tracked as a function of magnetic field in Fig. 2.13C, which yields a linear trend with a slope of $\sim$260 μeV T^{-1}. Since $\mu_B \approx 58$ μeV T^{-1}, the effective g-factor is ~ -4.5. It is thus largely determined by the atomic orbital magnetic moments, with small differences due to electron-hole asymmetry from effective mass between conduction and valence band, which may account for the remaining valley contribution. We will return to these foundational results in future chapters when we explore the excitons in 2D heterostructures.

Chapter 3

ELECTRICALLY TUNABLE EXCITONIC SECOND-HARMONIC GENERATION IN WSE_2

3.1 Introduction

In this chapter, we explore the electrical control of exciton-enhanced optical second-harmonic generation (SHG) in monolayer WSe_2. We touch upon several techniques and concepts that are foundational to 2D material optics and later sections of this thesis, such as PL spectroscopy, SHG, electrostatic doping, 2D excitons, and valleytronics. First, we review the basics of nonlinear optics and overview its importance to studies of crystallographic symmetries in 2D materials. To motivate our work, we survey prior attempts to control nonlinear optics through electrical means.

Following this introductory discussion and a presentation of the experimental methods, we describe our studies of WSe_2 SHG, reprinted from the published study, **Kyle L. Seyler**, John R. Schaibley, Pu Gong, Pasqual Rivera, Aaron M. Jones, Sanfeng Wu, Jiaqiang Yan, David G. Mandrus, Wang Yao, and Xiaodong Xu. *Electrical control of second-harmonic generation in a WSe_2 monolayer transistor.* Nature Nanotechnology 10, 407411 (2015) [57]. Our central finding is that the intensity of SHG at the A-exciton resonance is tunable by over an order of magnitude at low temperature and nearly fourfold at room temperature through electrostatic doping in a field-effect transistor. The large tunability arises from the pronounced exciton charging effects in monolayer semiconductors, which allow for exceptional control over the oscillator strengths at the exciton and trion resonances. Furthermore, the excitonic SHG is counter-circularly polarized to the excitation laser, which arises from the combination of the two-photon and one-photon valley optical selection rules that have opposite helicity in the monolayer. These studies reveal new opportunities for chip-scale, electrically tunable nonlinear optical devices based on 2D semiconductors.

3.1.1 Nonlinear optics of 2D materials

Matter behaves in fascinating ways when subjected to strong electromagnetic fields. The field of nonlinear optics studies light-matter interactions when the light is sufficiently intense to affect the material response in a nonlinear fashion. In turn, the material nonlinearly modifies the optical fields. Perhaps the most well-known nonlinear optical process is SHG, in which light interacts with a medium to produce light with double the frequency. The process is used to create lasers with different frequencies and is ubiquitous in modern photonic systems. This chapter deals with SHG from an atomically thin semiconductor. We overview some of the relevant background concepts in this section [58, 59].

The starting point for describing the propagation of light in a medium is Maxwell's equations:

$$\begin{aligned} \nabla \cdot \mathbf{D} &= \rho_f \\ \nabla \cdot \mathbf{B} &= 0 \\ \nabla \times \mathbf{E} &= -\frac{\partial \mathbf{B}}{\partial t} \\ \nabla \times \mathbf{H} &= \frac{\partial \mathbf{D}}{\partial t} + \mathbf{J}_f \end{aligned} \tag{3.1}$$

We assume that there are no free charges and currents, so $\rho_f = 0$ and $\mathbf{J}_f = 0$, and the material is nonmagnetic ($\mathbf{B} = \mu_0 \mathbf{H}$). Nonlinearity enters the picture since $\mathbf{D} = \epsilon_0 \mathbf{E} + \mathbf{P}$, and $\mathbf{P}$ may relate to $\mathbf{E}$ in a nonlinear way as we will see shortly. A wave equation is derived by taking the curl of Faraday's law, inserting Ampere's law, and substituting in the constitutive relation for $\mathbf{D}$ to give

$$\nabla \times \nabla \times \mathbf{E} + \frac{1}{c^2} \frac{\partial^2 \mathbf{E}}{\partial t^2} = -\mu_0 \frac{\partial^2 \mathbf{P}}{\partial t^2}. \tag{3.2}$$

An oscillating optical field $\mathbf{E}(t)$ generates an oscillating electric polarization in the material, which then radiates. In general, the polarization can depend nonlinearly on the applied field, with $P(t) = \epsilon_0[\chi^{(1)}E(t) + \chi^{(2)}E^2(t) + \chi^{(3)}E^3(t) + ...]$, where $\chi^{(2)}$ and $\chi^{(3)}$ are the second- and third-order electric susceptibilities. Therefore, for example, given an input electric field $E(t) = E(\omega_1)e^{-i\omega_1 t} + E(\omega_2)e^{-i\omega_2 t}$, the quadratic term leads to polarization components at the second harmonics ($2\omega_1$, $2\omega_2$), as well as the sum ($\omega_1 + \omega_2$) and difference ($\omega_1 - \omega_2$) frequencies.

In this chapter, we are concerned with the simplest case of a single optical field at ω and its second harmonic (2ω) in the electric-dipole approximation, where

$$P_i(2\omega) = \epsilon_0 \chi^{(2)}_{ijk} E_j(\omega) E_k(\omega). \tag{3.3}$$

Because $\chi^{(2)}_{ijk}$ is a third-rank tensor, it is a powerful probe of crystallographic symmetries. Neumann's principle states that any physical property tensor is invariant under every point group symmetry operation of the crystal [60]. In other words, if T_{ip} is a permissible symmetry operation and $X_{ijk...n}$ is a polar property tensor, then

$$X_{ijk...n} = T_{ip} T_{jq} T_{kr} ... T_{mn} X_{pqr...m}. \tag{3.4}$$

Consider, for example, the fundamental operation of inversion, where

$$T = \begin{bmatrix} -1 & 0 & 0 \\ 0 & -1 & 0 \\ 0 & 0 & -1 \end{bmatrix}. \tag{3.5}$$

If $X_{ijk...n}$ is of odd rank, Equation 3.4 reduces to $X_{ijk...n} = -X_{ijk...n}$ and therefore $X_{ijk...n} = 0$. This means that a crystal must have broken inversion symmetry to have a non-zero second-order electric susceptibility.

For SHG, the susceptibility is often written in the notation $d_{ijk} = \frac{1}{2}\chi^{(2)}_{ijk}$ and since the last two indices are indistinguishable (both at frequency ω), a contracted matrix d_{il} is typically used [59]. The jk indices translate into the l index using the following convention ($jk \rightarrow l$): $11 \rightarrow 1$; $22 \rightarrow 2$; $33 \rightarrow 3$; 32 or $23 \rightarrow 4$; 13 or $31 \rightarrow 5$; 12 or $21 \rightarrow 6$. We can then write the full second-harmonic polarization response as [59]

$$\begin{bmatrix} P_{x,2\omega} \\ P_{y,2\omega} \\ P_{z,2\omega} \end{bmatrix} = 2\epsilon_0 \begin{bmatrix} d_{11} & d_{12} & d_{13} & d_{14} & d_{15} & d_{16} \\ d_{21} & d_{22} & d_{23} & d_{24} & d_{25} & d_{26} \\ d_{31} & d_{32} & d_{33} & d_{34} & d_{35} & d_{36} \end{bmatrix} \begin{bmatrix} E^2_{x,\omega} \\ E^2_{y,\omega} \\ E^2_{z,\omega} \\ 2E_{y,\omega}E_{z,\omega} \\ 2E_{x,\omega}E_{z,\omega} \\ 2E_{x,\omega}E_{y,\omega} \end{bmatrix}. \tag{3.6}$$

One can further narrow down the possible point group symmetries by resolving the sus-

ceptibility tensor components through SHG rotational anisotropy measurements, in which the fundamental and second-harmonic components are resolved as function of excitation and detection angles. We saw in Chapter 2 that monolayer semiconducting MX_2 possess D_{3h} symmetry, which implies that the only nonzero $\chi^{(2)}$ elements are $\chi^{(2)}_{yyy} = -\chi^{(2)}_{yxx} = -\chi^{(2)}_{xxy} = -\chi^{(2)}_{xyx}$ (y along armchair direction) [59]. This greatly simplifies the susceptibility tensor to

$$\begin{bmatrix} 0 & 0 & 0 & 0 & 0 & -d_{22} \\ d_{22} & -d_{22} & 0 & 0 & 0 & 0 \\ 0 & 0 & 0 & 0 & 0 & 0 \end{bmatrix}, \tag{3.7}$$

where 1, 2, and 3 are taken along x, y, and z [59] (see Fig. 2.2). The second-harmonic polarization in Cartesian coordinates is therefore

$$\begin{bmatrix} P_{x,2\omega} \\ P_{y,2\omega} \\ P_{z,2\omega} \end{bmatrix} = 2\epsilon_0 d_{22} \begin{bmatrix} E^2_{x,\omega} - E^2_{y,\omega} \\ -2E_{x,\omega}E_{y,\omega} \\ 0 \end{bmatrix}. \tag{3.8}$$

For example, consider the case where the armchair axis of an MX_2 monolayer is along the y direction. Suppose we rotate our excitation laser polarization about an angle ϕ from the y-axis, so $\mathbf{E}_\omega(\phi) = E_0(\hat{x}\cos\phi + \hat{y}\sin\phi)$. The nonlinear polarization then becomes

$$\begin{bmatrix} P_{x,2\omega} \\ P_{y,2\omega} \\ P_{z,2\omega} \end{bmatrix} = 2\epsilon_0 d_{22} \begin{bmatrix} \cos(2\phi) \\ -\sin(2\phi) \\ 0 \end{bmatrix}. \tag{3.9}$$

If we collect the SHG components that are co-linear (along $\hat{e}_{co} = \hat{x}\cos\phi + \hat{y}\sin\phi$) and cross-linear (along $\hat{e}_{cross} = \hat{x}\sin\phi - \hat{y}\cos\phi$) to the excitation laser, the SHG intensity has a six-fold dependence on the excitation angle:

$$\begin{aligned} I_{co,2\omega} &\propto d^2_{22}E^4_0(\cos 2\phi\cos\phi - \sin 2\phi\sin\phi)^2 = d^2_{22}E^4_0\cos^2(3\phi) \\ I_{cross,2\omega} &\propto d^2_{22}E^4_0(\cos 2\phi\sin\phi + \sin 2\phi\cos\phi)^2 = d^2_{22}E^4_0\sin^2(3\phi) \end{aligned}. \tag{3.10}$$

Nonlinear optics has developed into an important subfield of 2D materials research. In 2013, strong SHG was discovered in 2D MX_2 crystals with an odd number of layers, contrasting with the vanishing SHG in the centrosymmetric even-numbered layers (D_{3d} symmetry) and bulk crystals (D_{6h} symmetry) [61–64]. In addition, the characteristic sixfold rotational

anisotropy described in Eq. 3.10 was confirmed [61–63, 65], which opened the door to using SHG as a probe of the crystal orientation of exfoliated layers for heterostructure fabrication (see Chapter 4) and studies of piezoelectricity [66, 67] and domains within polycrystalline films [68, 69]. Other early works showed that PL through two-photon absorption (a $\chi^{(3)}$ process) could be used to detect excited exciton states and allow extrapolation of the large exciton binding energy in monolayers [70–73]. Real electronic states also enhance the SHG process if their energies coincide with the fundamental or second-harmonic photons [73, 74]. A general form of the second-order electric susceptibility is

$$\chi^{(2)}_{ijk} \propto \sum_{v} \frac{\langle 0|\hat{V}_{i,2\omega}|\psi_{exc}\rangle\langle\psi_{exc}|\hat{V}_{j,\omega}|\psi_v\rangle\langle\psi_v|\hat{V}_{k,\omega}|0\rangle}{(E_{exc} - 2\hbar\omega - i\Gamma_{exc})(E_v - \hbar\omega)}, \tag{3.11}$$

where $|\psi_{exc}\rangle$ is the exciton state, $|\psi_v\rangle$ are virtual intermediate states, $|0\rangle$ is the zero-energy ground state, Γ_{exc} is the exciton damping constant, and the electron-photon interaction is given by $\hat{V} = (e)/(mc)\mathbf{A}\cdot\mathbf{p} = \hat{\mathbf{p}}\cdot\mathbf{E}$ in the electric dipole approximation. Significant enhancement in the SHG process can thus occur when $E_{exc} \approx 2\omega$. Our work in this chapter utilizes the strong resonances from 2D excitons and trion for electrical SHG control.

3.1.2 Electrically controlled nonlinear optics

Electrical control of light plays a crucial role in photonic devices for optical switching and communications. For example, electro-optic modulators are widely used table-top laser systems and have also been proposed for chip-scale optical interconnects [75]. Typically, these devices tune the refractive index of a material by an electric field or free carrier injection, and offer a simple and robust approach to tune the light intensity. One may imagine that it is also possible to electrically control nonlinear optical properties. For example, by modulating the second-order electric susceptibility, $\chi^{(2)}$, it is possible to control the fundamental processes of SHG and optical parametric amplification, which are ubiquitous in laser systems.

In the past several decades, there have been several efforts to create systems where the SHG is electrically controllable. Electrically tunable SHG was first demonstrated over 50 years ago, soon after the invention of the laser and the first demonstrations of SHG. In 1962, Terhune and colleagues showed that by applying a strong electric field to a centrosymmetric material (calcite, in this case), one could effectively break the inversion symmetry and enable SHG [76]. This phenomenon of electric-field-induced second-harmonic (EFISH) generation is a $\chi^{(3)}$ process, where the DC electric field acts as one of the driving fields ($\omega + \omega + 0 \rightarrow$

2ω, or $\chi^{(3)}E = \chi^{(2)}_{eff}$). Unfortunately, in the case of calcite, high voltages (a few hundred kilovolts) are required to produce a significant field-induced SHG response, so the effect is not practical for applications. However, the effect has been observed in a variety of other systems, including charged metallic surfaces in electrolytic solutions [77], the depletion regions of silicon structures [78], and most recently, plasmonic [79] and metamaterial devices [80]. These latter nanostructure examples are exciting because the effects are significantly enhanced through finely tuned resonances. A few other methods to control SHG, beyond EFISH, include current-induced SHG [81], charge-assisted SHG tuning in a nanostructured plasmonic device [82], and resonant Stark tuning of intersubband transitions in coupled quantum wells [83]. Despite this progress, dynamic control of optical nonlinearities has not achieved practical applications outside of research labs since the effects are generally quite weak, so new approaches are always welcome. This chapter demonstrates a novel technique to electrically tune SHG using excitons.

3.2 Experimental methods

Monolayer WSe_2 crystals were produced by mechanical exfoliation onto 300 nm SiO_2 on n^+-doped Si and the thickness was confirmed by optical contrast. Electrical contacts of V/Au (5/50 nm) were created through standard electron beam lithography and evaporation. The sample was housed in a dual in-line package chip carrier, to which the electrical contacts were wire-bonded. The device was measured in a Janis ST-500 continuous flow cryostat, which enabled studies at low temperature. Figure 3.1A shows a schematic of the device and Fig. 3.1B provides an optical microscope image of one of our devices. Gate voltages (V_g) were applied to the Si back-gate, and the contact to the WSe_2 was grounded.

The optical setup for the SHG experiments is shown in Fig. 3.1A. An amplified mode-locked Ti:sapphire laser (RegA 9000) pumped an optical parametric amplifier (Coherent OPA 9800), which sent ~200 fs pulses from 0.5 eV to 1 eV with ~25 meV bandwidth at 250 kHz into the setup. We used 40 µW of average power unless otherwise specified, which was below the sample damage threshold, as determined by deviations from the quadratic power dependence of the SHG. The laser was focused to 2 μm^2 by a 50X near-IR objective lens (Olympus) and the back-scattered SHG signal was reflected off a long-pass dichroic beamsplitter (Semrock) and sent into a spectrometer and CCD for analysis. For linear polarization measurements, a half- and quarter-wave Fresnel rhomb produced circularly polarized light from the OPA before the beamsplitter. We mounted a linear polarizer (P_2) in the excitation

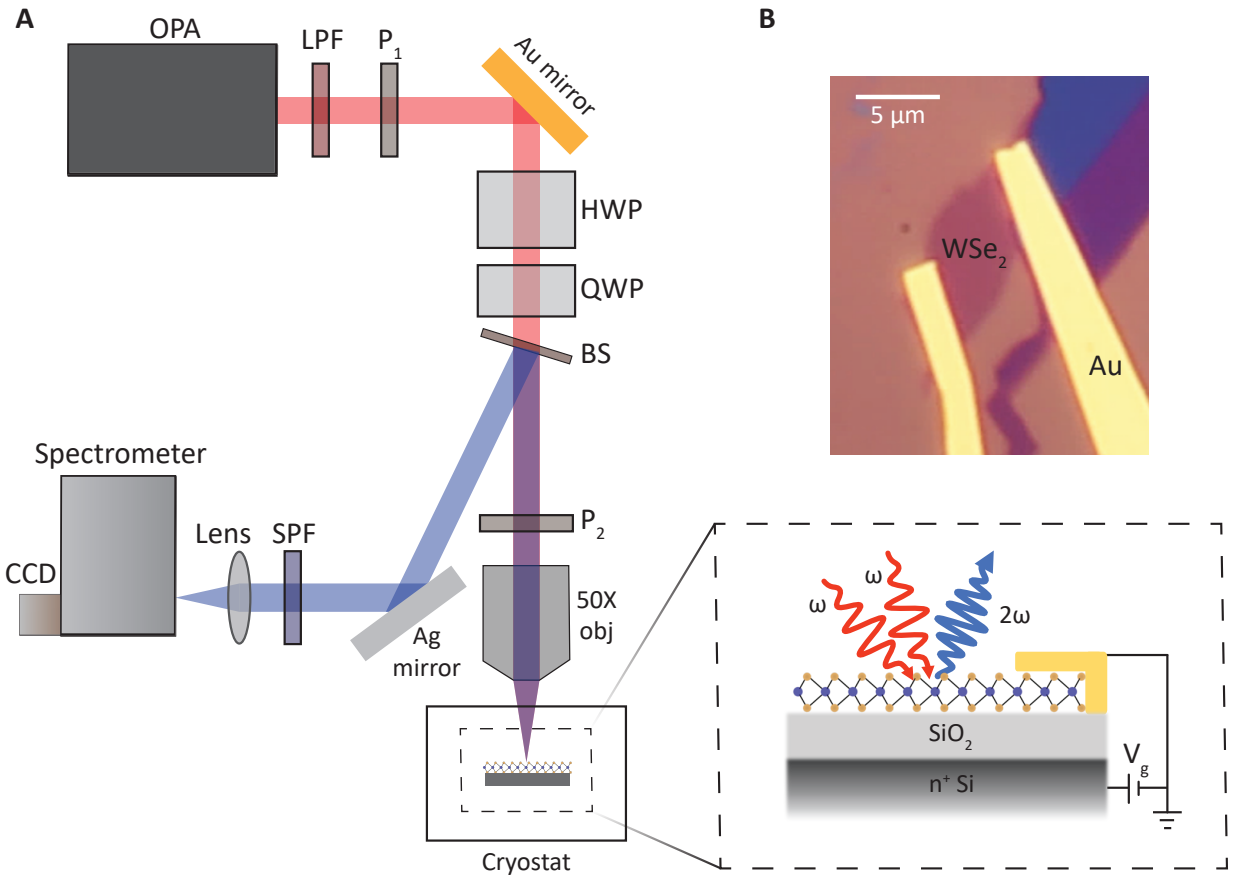

Figure 3.1: Schematic of SHG setup and device. (A) Schematic of SHG setup and gating scheme. OPA, optical parametric amplifier. LPF, 1 µm long-pass filter. P, linear polarizer. HWP, half-wave Fresnel rhomb. QWP, quarter-wave Fresnel rhomb. BS, long-pass dichroic beamspitter. SPF, 1 µm short-pass filter. (B) Optical microscope image of WSe_2 monolayer transistor.

and detection path on an automatic rotation mount, which maintains a constant excitation intensity during rotation and selects for the co-linearly polarized SHG component. The spectrometer grating diffraction efficiency was approximately equal for *s*- and *p*- polarization at our wavelengths of interest. For circular polarization measurements, the half- and quarter-wave Fresnel rhomb were moved to after the beamsplitter, and polarizer P_2 was removed from the setup. The back-reflected signal went through the same Fresnel rhombs, off the beamsplitter, and through an achromatic half-wave plate and a linear polarizer for analysis. PL measurements were performed in a similar setup, but with a 50:50 beamsplitter, 20 µW CW excitation from a 655 nm (1.89 eV) diode laser, and appropriate filters.

To determine the second-order susceptibility, SHG from monolayer WSe_2 exfoliated onto

fused quartz was measured and compared to SHG from the front surface of a bulk crystal of z-cut α-quartz following the procedures in ref. [62, 63]. The expression for the second-harmonic electric field amplitude reflected from the surface of a bulk nonlinear crystal was derived by Pershan and Bloembergen [84], and for normal incidence excitation in vacuum, it is given by

$$E_{2\omega,\alpha} = -\frac{P_\alpha^{(2)}}{\epsilon_0[n(\omega)+1][1+n(2\omega)]}, \tag{3.12}$$

where $P_\alpha^{(2)} = \epsilon_0 \chi_\alpha^{(2)} E(\omega)^2$ is the second-order polarization of the α-quartz and n is its refractive index. On the other hand, for a polarization sheet on a centrosymmetric dielectric substrate, as in the case of monolayer WSe_2 on fused quartz, the electric field is

$$E_{2\omega,s} = \frac{2\omega i P_s^{(2)}}{c[n(\omega)+1]}, \tag{3.13}$$

where $P_s^{(2)} = \epsilon_0 \chi_s^{(2)} E(\omega)^2$ is the nonlinear sheet polarization of WSe_2 and n is the refractive index of fused quartz (which is nearly equal to that of α-quartz). By taking the ratio of the square of Eq. 3.13 to Eq. 3.12, we can then determine $\chi_s^{(2)}$ by comparing the relative SHG intensities of α-quartz and WSe_2:

$$\chi_s^{(2)} = \frac{c}{4\omega[n(\omega)+n(2\omega)]}\sqrt{\frac{I_{2\omega,s}}{I_{2\omega,\alpha}}}\chi_\alpha^{(2)}, \tag{3.14}$$

as given in Ref. [62]. For monolayer WSe_2, we thus determined the modulus of the only nonzero second-order sheet susceptibility element: $\chi_s^{(2)} = \chi_{s,yyy}^{(2)} = \chi_{s,yxx}^{(2)} = \chi_{s,xxy}^{(2)} = \chi_{s,xyx}^{(2)}$, where y is along the armchair direction). We used $\chi_\alpha^{(2)} = 2d_{22} = 0.6\,\mathrm{pm\,V^{-1}}$ for α-quartz and took it as a constant in our wavelength range (1400 nm to 1600 nm). To obtain the effective volume second-order susceptibility, we divided the calculated second-order sheet susceptibility, $|\chi_s^{(2)}|$, by the monolayer WSe_2 thickness of 0.7 nm. Our estimation of the SHG conversion efficiency assumed our standard excitation condition of 40 µW average power with 200 fs pulses at 250 kHz focused to a spot size of 2 µm, corresponding to a peak pulse $\sim$24 GW cm^{-2}. The calibration measurements were performed at room temperature.

3.3 Second-harmonic generation in monolayer WSe_2

At room temperature, under 0.88 eV (∼1.41 µm) excitation, we observe a clear SHG signal at double the laser frequency (1.76 eV) in addition to a broader asymmetric emission peak near 1.74 eV (black curve, Fig. 3.2A). The broad peak is PL from radiative recombination of the 1s state of the WSe_2 A exciton after two-photon absorption (2-P PL). These two nonlinear optical processes are illustrated in the leftmost energy level diagram in Fig. 3.2B. When we tune the laser energy to half the exciton energy (blue curve), there is only a single peak at 1.66 eV (∼750 nm) with an intensity that scales quadratically with excitation power (Fig. 3.2B). Since the excitation is two-photon resonant with the exciton energy, SHG and 2-P PL are degenerate (Fig. 3.2C). However, the laser-like line shape of the emission suggests that SHG dominates, and the polarization dependence rules out the possibility of 2-P PL further. Figure 3.2D shows the emission intensity parallel to the incident laser polarization as a function of crystal orientation, which exhibits the characteristic six-fold pattern of SHG in monolayer TMDs [61–63, 65, 85]. If the emission were 2-P PL, the intensity of the co-linearly polarized emission should be independent of crystal orientation, due to loss of phase coherence from nonradiative relaxation processes. For the 2-P PL signal in Fig. 3.2A, we observe clear angle-independent intensity (Fig. 3.2D). The polarization dependence for resonant excitation, in contrast, shows an intensity contrast of 40 between the maxima and minima of the lobes, which establishes the dominance of the coherent nonlinear optical response on the excitonic resonance.

By scanning the excitation laser energy and monitoring the SHG signal, we observe a $15\times$ enhancement of the intensity on the two-photon resonance at the 1s exciton energy (Fig. 3.3A). This corresponds to a second-order susceptibility contrast of ∼4 (Fig. 3.3B). We estimate an effective volume second-order susceptibility of $\sim 60\,\mathrm{pm\,V^{-1}}$ on resonance, which is equivalent to sheet second-order susceptibility $\sim 0.04\,\mathrm{nm^2\,V^{-1}}$ (see experimental methods). The SHG conversion efficiency is $\sim 4 \times 10^{-10}$ under our experimental conditions, which is an order of magnitude larger than what one would achieve if standard transparent nonlinear crystals could be scaled to the same thickness [58]. The excitonic WSe_2 SHG is comparable to reports of SHG in monolayer MoS_2 under higher energy excitation, which is itself enhanced by interband electronic transitions [62, 63].

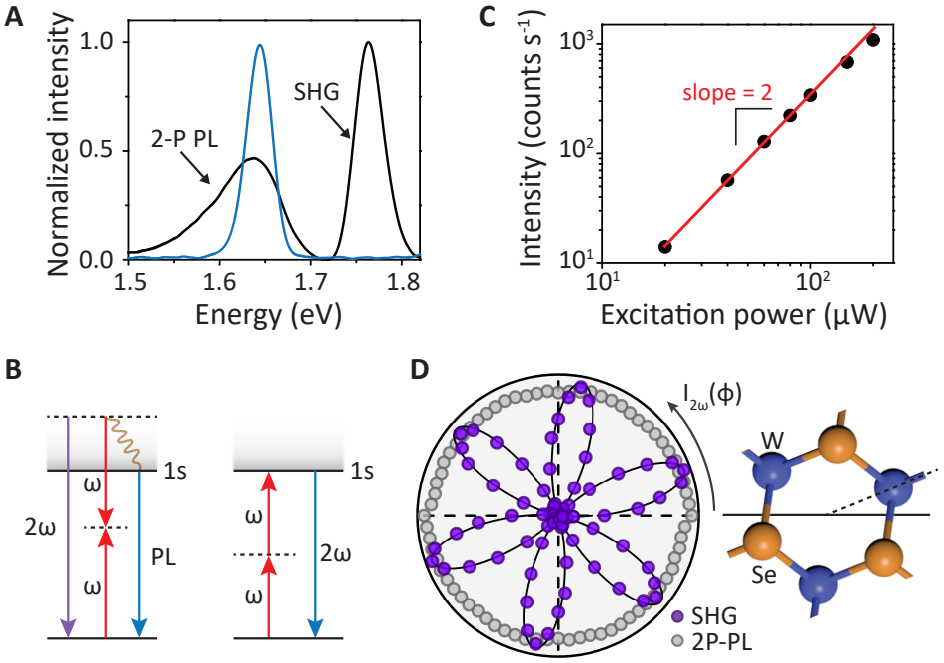

Figure 3.2: Characterization of SHG in monolayer WSe_2. (A) Emission spectrum for excitation at 0.83 eV (black curve) dominated by SHG, and 0.88 eV (blue curve), showing SHG at 1.76 eV and two-photon-induced PL (2-P PL) from the WSe_2 A-exciton. (B) Energy level diagrams for emission processes in fig. A. Left: Under two-photon excitation above the 1s exciton state, both SHG at 2ω and PL at lower energy are observed. The PL is due to two-photon absorption, nonradiative relaxation into the exciton state, and radiative recombination of the exciton. Right: Under resonant two-photon excitation of the exciton, only SHG is observed. (C) Power dependence of SHG peak intensity for two-photon-resonant excitation of the A exciton, where the red line shows the expected quadratic dependence. (D) Left: Intensity of SHG and 2-P PL (under non-resonant excitation at 0.88 eV) parallel to the incident laser polarization as a function of the crystal angle ϕ, with the black line showing the expected SHG polarization dependence. Right: Top view of monolayer TMD crystal structure showing possible corresponding orientation based on the SHG rotational anisotropy, where the angle between the armchair axis (dotted line) and horizontal is $\sim 20°$. [Adapted from [57].]

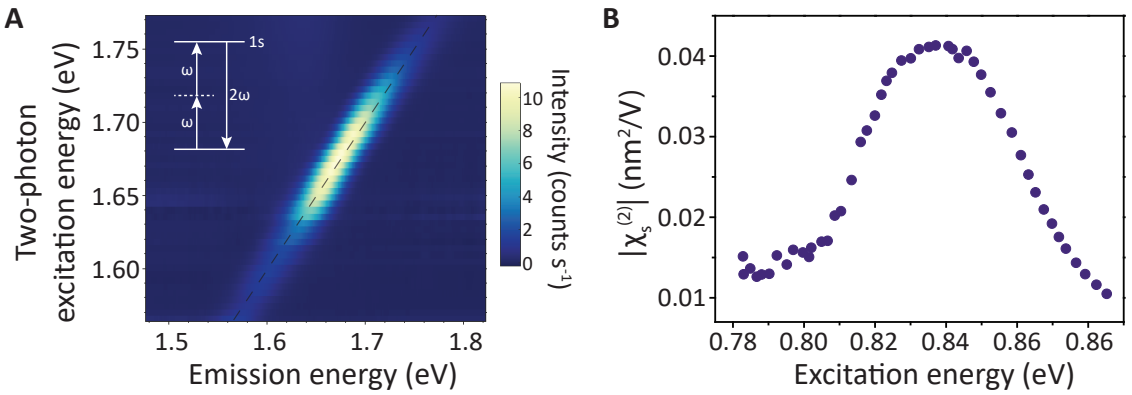

Figure 3.3: Resonant enhancement of room-temperature SHG. (A) Two-photon excitation map showing the strong SHG resonance and negligible two-photon PL near the 1s A exciton energy. The dashed line is a guide to the eye with unit slope. (B) Measured sheet second-order susceptibility as a function of excitation energy. [Adapted from [57].]

3.4 Gate-tunable SHG

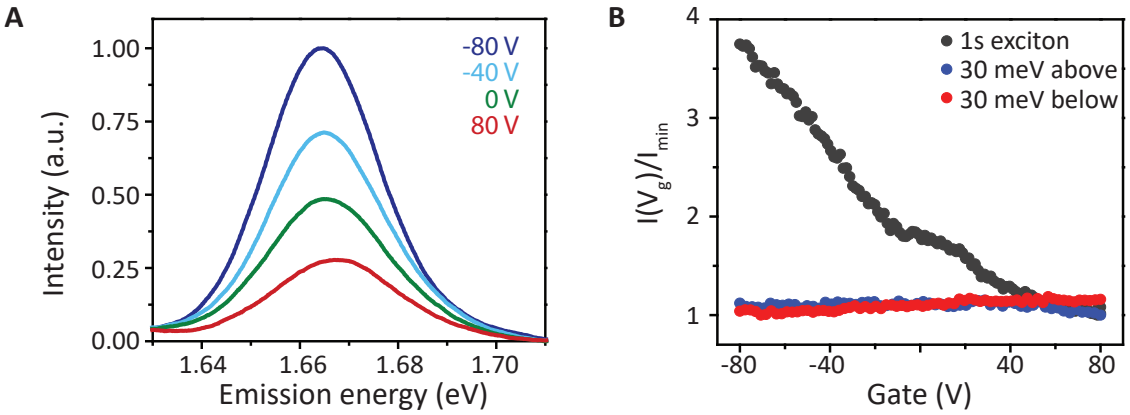

Figure 3.4: Gate tunability of room-temperature SHG. (A) Resonant SHG spectra at selected gate voltages. (B) SHG intensity as a function of gate voltage with two-photon excitation energy above, below, and resonant with 1s exciton. The intensity is normalized by the minimum of each dataset. [Adapted from [57].]

The resonant SHG tunable via electrostatic doping. As the DC gate voltage (V_g) is swept from $-80\,\mathrm{V}$ to $80\,\mathrm{V}$ (Fig. 3.4A and B), the resonant SHG intensity drops by nearly a factor of 4. The data resemble the effect of electrostatic doping on the PL intensity (Fig. A.1), which decreases with increased electron doping. Off the exciton resonance, V_g has a negligible effect on the SHG (Fig. 3.4B), which supports the idea that the SHG modulation stems from tuning the exciton oscillator strength.

At low temperatures, the SHG gate tunability substantially increases. Figure 3.5A displays a sequence of SHG intensity maps as the two-photon excitation energy changes from $0.85\,\mathrm{eV}$ to $0.875\,\mathrm{eV}$ at $30\,\mathrm{K}$, with the corresponding excitation laser spectrum shown on top. In each map, for V_g near $-40\,\mathrm{V}$, there is a peak around $1.74\,\mathrm{eV}$. Toward higher positive V_g, the feature is suppressed and a new peak appears around $1.71\,\mathrm{eV}$ for the two left maps. For negative V_g, the SHG peak shifts to lower energy. These spectral features are similar to the gate-dependent PL for WSe_2 monolayers [46]. By comparing to the gate-dependent PL intensity plot in Fig. 3.5B, we assign neutral exciton (X^0) for the peak at $1.74\,\mathrm{eV}$ for V_g near $-40\,\mathrm{V}$, negatively charged excitons (negative trions, X^-) near $1.71\,\mathrm{eV}$ at small positive V_g, and positive trions (X^+) at lower energy for high negative V_g. The strong presence of X^0 at negative voltages shows the sample is intrinsically electron-doped. The broad spectrum

of the pulsed laser (∼25 meV full width at half maximum) allows us to excite both X^0 and the trions at once. However, SHG over X^0 energy dominates, even when the excitation is not centered on X^0, due to the large oscillator strength at the exciton resonance relative to at the trion resonance.

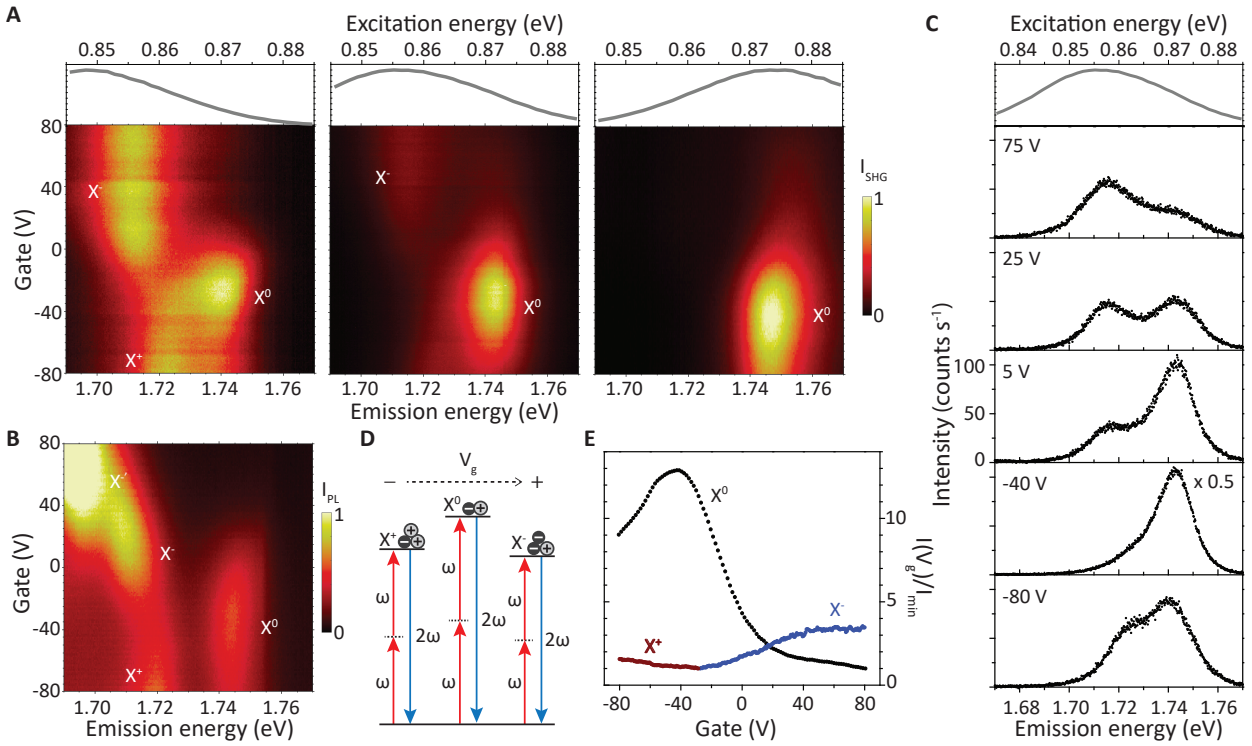

Figure 3.5: Electrical control of PL and SHG at 30 K. (A) SHG spectra maps as a function of gate voltage. The spectrum of the excitation laser for each dataset is shown on top. The plots correspond to two-photon excitation centered on $X^{-'}$ (left), the negative trion X^- (center), and the exciton X^0 (right). Each map is individually normalized. (B) PL spectra map as a function of gate voltage showing the neutral and charged excitonic states. (C) SHG spectra at selected gate voltages. The laser spectrum is shown on top. (D) Illustration of the energy levels for gate-dependent exciton- and trion-enhanced SHG. (E) Normalized peak intensity of exciton and trion SHG as a function of gate voltage. The excitation laser is fixed at the corresponding resonance. [Adapted from [57].]

The spectra in Fig. 3.5C illustrate the tunability of the SHG by gate bias. In analogy to an FET where an electrical current is modulated by a gate voltage, here we demonstrate a monolayer SHG transistor. The electrostatic doping tunes the strength of the neutral and charged excitonic resonances, and thus the strength and frequencies of the SHG response

(Fig. 3.5D). In particular, the X^0 SHG decreases by over an order of magnitude from $-30\,\mathrm{V}$ to $70\,\mathrm{V}$ (Fig. 3.5E). For the approximately linear regime from $20\,\mathrm{V}$ to $0\,\mathrm{V}$, the modulation is over $10\,\%\,\mathrm{V}^{-1}$, comparable to plasmonic electric-field-induced SHG devices [79]. For the trions, the SHG tunes opposite to the exciton signal, as expected. We find similar tunability curves under different excitation energies (Fig. A.2) and the observations are reproducible between different devices (Fig. A.3). The strong SHG modulation with gate illustrates the important influence that the exciton species have on the second-order susceptibility.

Microscopically, the exciton or trion plays the role of a resonant intermediate state for the photon scattering process (Fig. 3.5D). When the sample is electrostatically doped, the eigenenergy spectrum of these intermediate states changes due to the Coulomb interaction. At zero doping, X^0 is the eigenstate of Coulomb interaction. At very large doping, an electron-hole pair will find an additional carrier in its proximity; thus the trion becomes the eigenstate of the Coulomb interaction. At moderate doping, exciton and trion coexist. Therefore, with doping, the joint density of states (and hence the optical oscillator strength) shifts from the exciton resonance to the trion resonance, which results in the observed electrostatic tuning of the SHG efficiency at a given energy. At large electron doping, the X^- PL resonance redshifts appreciably due to the presence of the formation of another excitonic state, $X^{-'}$ [86]. There is currently no consensus in the literature as to the nature of this lower energy trion-like state; however, it is clear from our data that it does not efficiently enhance the SHG.

We have shown that monolayer TMD field-effect transistors represent a new class of electrically tunable nonlinear optical devices, with strong SHG around the 1s A exciton energy, allowing for efficient optical frequency doubling. Improved device engineering, including better gating schemes and waveguide integration, will enable enhanced tunability. Furthermore, bandgap engineering through alloying [87–89] and heterostructures means that a wide range of wavelengths is potentially accessible, including SHG of the telecom wavelengths. These complementary metal-oxide-semiconductor (CMOS)-compatible monolayer SHG transistors extend the versatility of 2D semiconductors for controllable nonlinear photonics.

3.5 Valley-optical selection rules for one- and two-photon excitations

Finally, we remark on the intriguing two-photon optical selection rules of the exciton-enhanced SHG. Figure 3.6 depicts how two σ^- photons at the fundamental frequency (ω) generate a single σ^+ photon at the second-harmonic frequency (2ω) with near unity polariza-

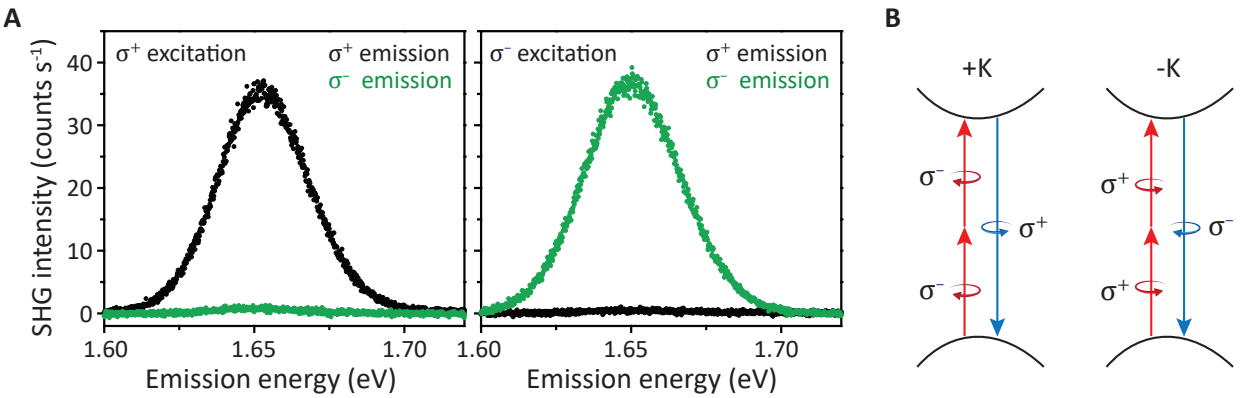

Figure 3.6: SHG valley optical selection rules. (A) Circular polarization-resolved SHG spectra showing the generation counter-circular SHG. (B) Interband valley optical selection rules for SHG. [Figure adapted from [57].]

tion, and the opposite holds for σ^+ excitation. This is the expected SHG selection rule from D_{3h} crystal symmetry. The production of a counter-rotating second harmonic is a general feature of materials with both broken inversion and threefold rotational symmetry, where the lattice supplies the angular momentum mismatch of the absorbed and emitted photons [90]. However, given the valley-contrasting physics in monolayer TMDs, it is also interesting to examine the microscopic origin of the SHG selection rule.

For monolayer TMDs, one-photon band-edge transitions at the $+K$ ($-K$) valley are only allowed for σ^+ (σ^-) polarized light, as reported previously [13, 47–49] (see 2.3). Two-photon interband transitions between the top valence band and lowest conduction band are characterized by the product of matrix elements, $\langle\psi_c|\hat{P}_\pm|\psi_j\rangle\langle\psi_j|\hat{P}_\pm|\psi_v\rangle$, where the ψ give the Bloch states at $\pm K$ for lowest conduction band (c), highest valence band (v), and virtual intermediate states (j). $\hat{P}$ is the momentum operator and $\hat{P}_\pm = \hat{P}_x + i\hat{P}_y$. Under the operation of $\hat{C}_3$, a $2\pi/3$ rotation about the z-axis, the Bloch states transform as $\hat{C}_3|\psi_j\rangle = e^{-i\frac{2\pi}{3}l_\alpha}|\psi_j\rangle$, where $\alpha = c, v, j$, and l_α is an integer. For rotations about the W atom, l_α is the magnetic quantum number of the local atomic orbitals. The 3-fold rotational symmetry then constrains the two-photon transition matrix elements:

$$\begin{aligned}\langle\psi_c|\hat{P}_\pm|\psi_i\rangle\langle\psi_i|\hat{P}_\pm|\psi_v\rangle &= \langle\psi_c|\hat{C}_3^{-1}\hat{C}_3\hat{P}_\pm\hat{C}_3^{-1}\hat{C}_3|\psi_j\rangle\langle\psi_j|\hat{C}_3^{-1}\hat{C}_3\hat{P}_\pm\hat{C}_3^{-1}\hat{C}_3|\psi_v\rangle \\ &= \langle\hat{C}_3\psi_c|\hat{C}_3\hat{P}_\pm\hat{C}_3^{-1}|\hat{C}_3\psi_j\rangle\langle\hat{C}_3\psi_j|\hat{C}_3\hat{P}_\pm\hat{C}_3^{-1}|\hat{C}_3\psi_v\rangle \\ &= e^{i\frac{2\pi}{3}(l_c - l_j \mp 1)}\langle\psi_c|\hat{P}_\pm|\psi_j\rangle e^{i\frac{2\pi}{3}(l_j - l_v \mp 1)}\langle\psi_j|\hat{P}_\pm|\psi_v\rangle,\end{aligned} \tag{3.15}$$

where we used $\hat{C}_3\hat{P}_\pm\hat{C}_3^{-1} = e^{\mp i\frac{2\pi}{3}}\hat{P}_\pm$. For transitions with two σ^+ or two σ^- photons, we need $e^{i\frac{2\pi}{3}(l_c-l_v\mp 2)} = 1$, or in other words, $l_c - l_v \mp 2 = 3n$,where n is an integer. At $+K$ $(-K)$, we have $l_c = 0$ and $l_v = +2$ (-2), allowing transitions for two σ^- (σ^+) photons. Thus the valley-contrasting optical selection rule extends to two-photon interband transitions, but with a flip in the helicity allowed for each valley. For SHG at $+K$ $(-K)$, two-photon absorption of two σ^- (σ^+) photons is accompanied by immediate emission of a single σ^+ (σ^-) photon of twice the energy. This leads to the prediction of cross-circularly polarized SHG, consistent with the macroscopic approach. In principle, it is possible to deviate from this selection rule in the presence of an electronic state with a different symmetry. However, under the C_3 rotation, the 1s exciton wavefunction transforms the same as the product of the electron and hole Bloch states at the K points. Therefore, the above selection rule also holds for SHG at the 1s exciton resonance, which agrees with experimental findings. This exercise further illustrates the initimate relation between the crystal symmetries and the microscopic valley-contrasting physics, which the excitons inherit.

Although the nearly instantaneous nature of SHG limits its direct utility in valley-based information processing, the two-photon absorption process is beneficial because it allows for efficient initialization of valley exciton coherence by minimizing the pathways for non-excitonic absorption [73]. In addition, it has been theoretically shown that when both fundamental and second-harmonic driving fields are present, it is possible to inject charge, spin and valley currents through quantum interference effects [91]. Monolayer TMDs may thus become a new platform for electrically controllable nonlinear valley optics.

Chapter 4

INTERLAYER VALLEY EXCITONS IN $MOSE_2/WSE_2$ HETEROSTRUCTURES

4.1 Introduction

This chapter adds a new layer to our story of 2D exciton physics with the addition of monolayer $MoSe_2$ stacked together with monolayer WSe_2. These heterobilayers of different monolayer semiconductors are attractive for both fundamental science and device technologies, such as in the emerging fields of valleytronics and nanophotonics. In the introductory sections, we first pay homage to prior foundational work on indirect excitons in coupled quantum wells in addition to the recent studies of TMD heterobilayers. We then describe the unique valley physics of twisted TMD heterobilayers.

The bulk of the chapter describes our optical spectroscopy studies on the valley physics of interlayer excitons in $MoSe_2/WSe_2$ vertical heterobilayers, reprinted from the published study, Pasqual Rivera*, **Kyle L. Seyler***, Hongyi Yu, John R. Schaibley, Jiaqiang Yan, David G. Mandrus, Wang Yao, and Xiaodong Xu. *Valley-polarized exciton dynamics in a 2D semiconductor heterostructure*. Science 351, 688691 (2016). [92]. We demonstrate the generation of interlayer exciton spin-valley polarization by circularly polarized optical pumping and determine a valley lifetime of $\sim$40 ns nanoseconds. By spatially resolving the PL, we observed significant spatial drift and diffusion of the exciton population and detected the formation of a spatial ring of valley polarization at high exciton densities, which is evidence of the interplay of dipolar and valley exchange interactions. These studies introduce 2D semiconductor heterobilayers as an intriguing setting in which to study valley exciton physics.

4.1.1 Indirect excitons in coupled quantum wells

Before detailing our studies of interlayer excitons in 2D semiconductor heterobilayers, it is important to acknowledge the important precursors studied in quantum wells. Indeed, the interlayer excitonic properties overlap significantly with the well-known indirect excitons,

which have been extensively studied in both type-II AlAs/GaAs superlattices [93–97] and coupled III-V quantum wells (Fig. 4.1A) [98–101] since the late 1980s. This section briefly overviews the most basic properties of the indirect excitons to clarify the similarity and contrast between these systems.

The essential property of the indirect excitons is that the electron and hole are spatially separated in the out-of-plane direction. In the coupled quantum well system, this occurs through the application of an out-of-plane electric field, so that holes and electrons preferentially occupy opposite wells (Fig. 4.1B). The spatial separation reduces the overlap between the electron and hole wave function, which suppresses the magnitude of exciton oscillator strength and the electron-hole exchange interaction. This is crucial for the exciton dynamics since the oscillator strength controls the radiative lifetime and the electron-hole exchange interaction is responsible for exciton spin depolarization. As a result, indirect excitons possess greatly enhanced population [96] and spin lifetimes [102] compared to their direct exciton cousins.

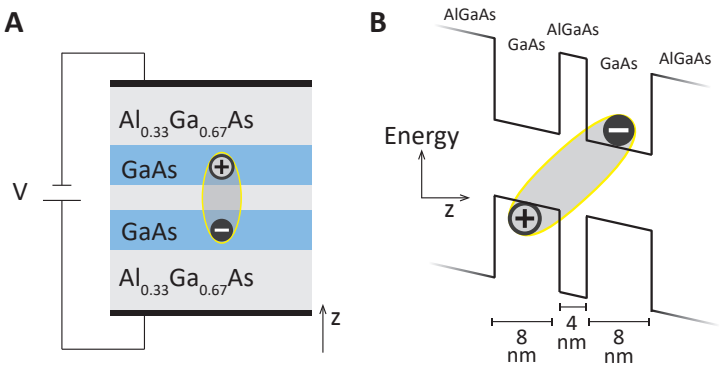

Figure 4.1: Indirect excitons in coupled quantum wells. (A) Schematic of GaAs/AlGaAs coupled quantum well under applied voltage V. (B) Energy level diagram of coupled quantum well. An electric field shifts the band alignments and allows for the formation of spatially indirect excitons.

The long indirect exciton population lifetime, combined with their repulsive dipolar interactions, allows them travel over significant distances (>1 µm) before relaxing [103–105]. In addition, the indirect excitons can also thermally equilibrate before recombining, which unlocks the possibility of realizing superfluidity and Bose-Einstein condensation within this composite boson system [106]. Much of the scientific interest on indirect excitons has been geared towards exploring the signatures of indirect exciton quantum degeneracy [107]. Re-

garding applications, researchers have proposed the use of indirect excitons in photonic switches [108], in which the excitons act as an intermediary between optical signal communication and electronic signal processing. Due to the built-in electric dipole moment of indirect excitons, an electric field perpendicular to the confinement plane (E_z) can change their energy by $\delta U = edE_z$, where d is the electron-hole (layer) separation. Spatial patterning of electrodes to control the electric field landscape can thus create traps [109–112] and conveyers [113–115] for indirect exciton spatial manipulation.

While these features should in principle translate to the interlayer exciton system, there remains significant experimental work to bring the 2D heterobilayer system up to speed. For example, evidence for exciton condensation and demonstrations of electrical spatial control have yet to be realized. On the other hand, interlayer excitons are distinct from quantum well systems in several important ways; as we overview prior work on 2D MX_2 heterostructures in the following sections, we will highlight what makes them unique.

4.1.2 Prior work on TMD heterobilayers

Soon after the first studies on group-VI monolayer TMDs (MoS_2, WS_2, WSe_2, $MoSe_2$), several groups considered the implications of creating MoX_2/WX_2 (X = S or Se) heterobilayers (Fig. 4.2A). Electronic structure calculations determined that many of the heterobilayer combinations should possess a type-II band alignment, where the conduction band minimum is in MoX_2 and the valence band maximum is in WX_2 (Fig. 4.2B) [116–119]. As a result, electrons and holes preferentially occupy opposite layers (Fig. 4.2A and B), thus forming an atomically thin p-n junction. This was shortly thereafter confirmed by device studies showing current rectification, enhanced photocurrent generation, and electroluminescence [120–122] characterstic of a p-n junction. Direct measurements of the band offsets through combined X-ray photoelectron spectroscopy and scanning tunning microscopy measurements verified and quantified the type-II alignment [123]. There is now significant interest in using these type-II heterojunctions for ultrathin, lightweight photovoltaics [124].

After photoexcitation, the electrons and holes transfer between layers on ultrafast timescales, as shown by several groups using non-degenerate optical pump-probe measurements [126–131]. Once localized to opposite layers, they bind with one another through Coulomb interactions to form interlayer excitons (IX, Fig. 4.2B). The signature of IX is PL emission at lower energy than the MoX_2 or WX_2 intralayer excitons [125, 132], as determined by the reduced bandgap. Meanwhile, the intralayer exciton PL is often significantly quenched on

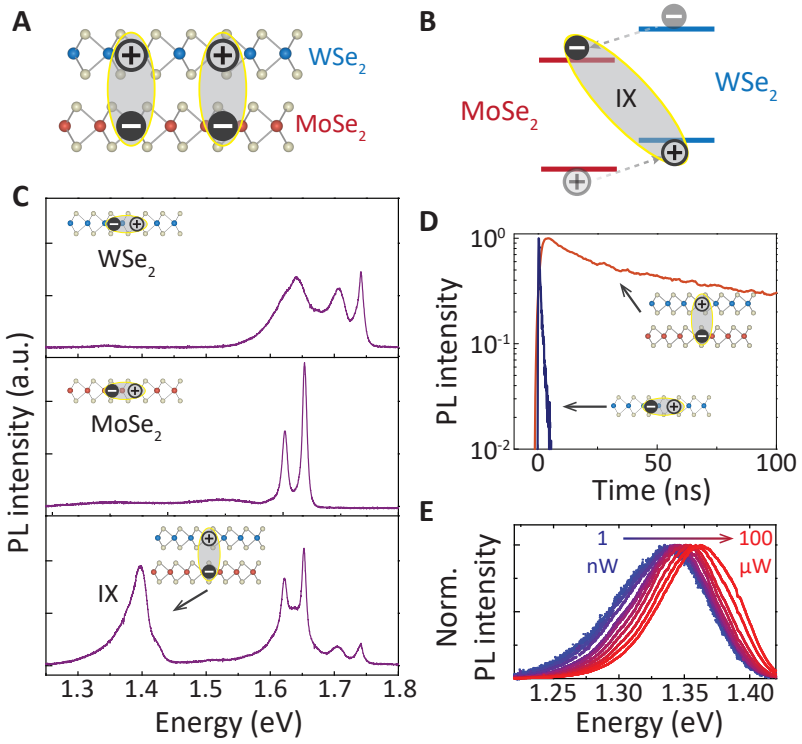

Figure 4.2: Basic properties of interlayer exciton. (A) Cartoon of interlayer excitons in $MoSe_2/WSe_2$. (B) Type-II band alignment of $MoSe_2/WSe_2$ heterojunction. Electrons (holes) transfer to $MoSe_2$ (WSe_2) on ultrafast timescales and bind via Coulomb interactions to form an interlayer exciton. (C) Low-temperature PL spectra of monolayer WSe_2 (top), monolayer $MoSe_2$, and an $MoSe_2/WSe_2$ heterobilayer with strong interlayer exciton PL. In other samples, the intralayer PL peaks are often more strongly quenched than this sample and interlayer PL dominates. [Reprinted with permission from [125].] (D) Comparison of the PL dynamics for interlayer and intralayer excitons. The interlayer exciton lifetime is orders of magnitude longer. (E) Power-dependent PL spectra showing the strong blueshift with power due to strong dipole-dipole interactions between the excitons.

the heterostructure due to the charge transfer [125, 126]. An example of a PL spectrum for the $MoSe_2/WSe_2$ heterobilayer is displayed in Fig. 4.2C, where the emergence of low-energy PL emission $\sim$1.3 eV to 1.4 eV is clearly seen (bottom panel, from ref. [125]). Similar to indirect excitons in coupled quantum wells, the interlayer exciton lifetime is typically $\sim$100 ns due to the increased electron-hole separation [125], vastly longer than picosecond scale lifetimes of intralayer excitons (see Fig. 4.2D for comparison) [133]. The long lifetime allows the creation of high exciton densities, and due to repulsive dipole-dipole interactions between ex-

citons, the PL energy can blueshift significantly with increasing excitation power (Fig. 4.2E) [125]. Furthermore, the permanent out-of-plane dipole gives rise to significant energy shifts with gate voltage due to the quantum-confined Stark effect [125], as with coupled quantum wells. Since the oscillator strength is reduced for interlayer excitons, it is difficult to excite them directly and typically they are created through charge transfer after intralayer exciton or interband absorption within the monolayers. PL spectroscopy is thus a crucial tool for studying the interlayer exciton properties. Recent experiments have shown that it is possible to achieve a small photocurrent response due to resonant interlayer exciton excitation; these measurements reveal an interlayer exciton oscillator strength about two orders of magnitude weaker compared to that of intralayer excitons [134].

Distinct from quantum well systems, MX_2 heterostructures possess several unique features. In monolayer MX_2, the exciton binding energy is $\sim$300 meV, due to the strong confinement of charges to the 2D plane and reduced dielectric screening from the surrounding media [19, 56, 70–72]. This is over an order of magnitude larger than in quantum wells [135]. The same ideas also apply to the interlayer excitons, which were shown to have a binding energy $>$200 meV and are thus observable at room temperature [136]. The unique features of the interlayer excitons stem from spin-valley physics of monolayer TMDs. In the next section, we dive into the valley properties of interlayer excitons.

4.1.3 Theory of valley physics in TMD heterobilayers

As we learned in Chapter 2, the monolayer valence and conduction band edges are located at doubly degenerate corners of the hexagonal Brillouin zone. Therefore, IX has an internal degree of freedom specified by the combination of electron and hole valley indices. Moreover, van der Waals heterostructures overcome the strict lattice matching requirements in traditional heterostructures. It is thus possible to introduce a relative twist between the crystal orientations of the constituent monolayers. The twist (and inherent $\sim$0.1 % lattice mismatch between the layers) leads to a displacement of the conduction and valence band edges in momentum space, which makes the IX momentum indirect at its minimum energy and direct only at finite center-of-mass velocities. The location of the IX light cones will also depend on the twist angle, affecting optoelectronic properties such as the dipole strength and interlayer exciton lifetime. Most importantly, the valley-contrasting physical properties of the constituent MX_2 monolayers, such as spin-valley locking, optical selection rules, and Berry curvature, are expected to impact the interlayer exciton optical and transport prop-

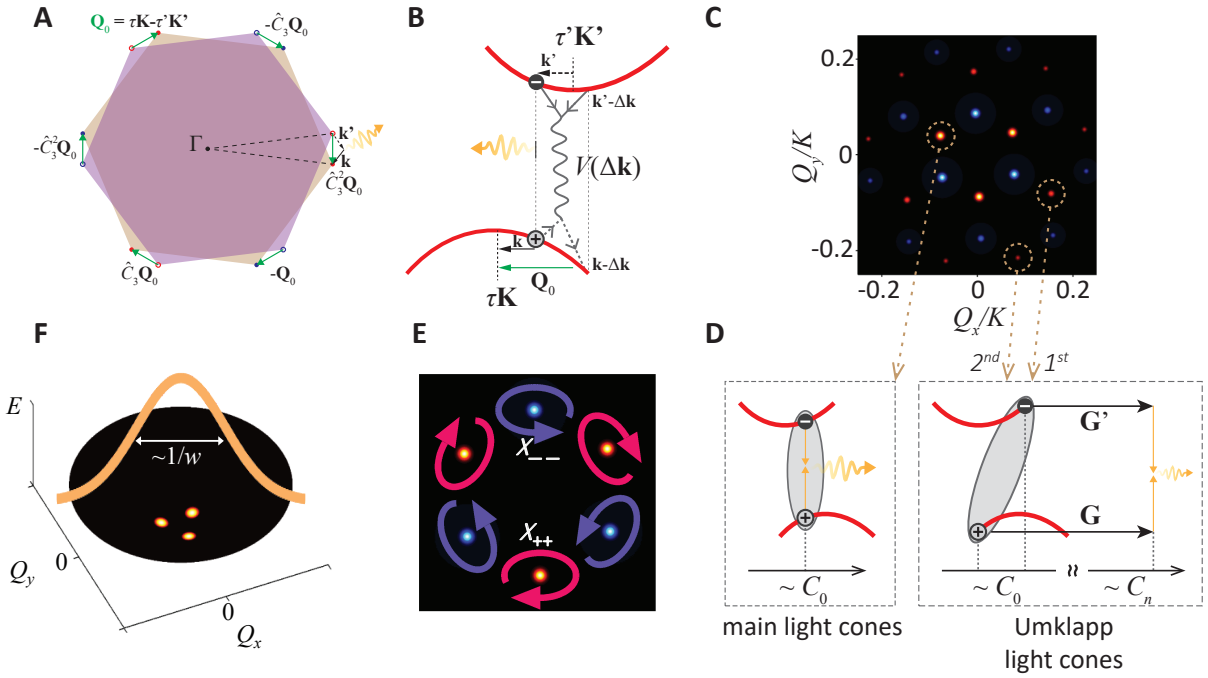

Figure 4.3: Interlayer valley exciton theory. (A) First Brillouin zone of $MoSe_2$ ($\tau' K'$, open dots) and WSe_2 (τK, closed dots) layers with a relative twist. Radiative recombination is allowed if the sum of electron and hole momentum ($\mathbf{k}' + \mathbf{k}$) add up to K-point momentum offset ($\mathbf{Q}_0$). (B) Bright interlayer exciton at finite velocity, with Coloumb interaction conserving the momentum sum. (C) Finite velocity light cones in Q-space. Brightness corresponds to transition dipole strength. (D) Schematic of exciton state at each of the main brightest light cones (left) and the Umklapp light cones (right). (E) Elliptical polarization at the main light cones. [For Panels A-E. Reprinted by permission from [137]. Copyright 2015 by the American Physical Society.] (F) Depiction of momentum-space wavepacket for interlayer exciton. Its width ($\sim 1/w$, w is the real-space width) covers the main light cones. [Reprinted with permission from [138] under CC BY-NC 4.0.]

erties dramatically. In this section, we outline some of the relevant theoretical background for interlayer valley excitons (see [137] and [138] for further details).

The twisted Brillouin zone of the heterobilayer system is shown in Fig. 4.3A, where the low-energy electrons in the $MoSe_2$ $\pm K'$ valleys are displaced from the low-energy holes in WSe_2 $\pm K$ valleys. Therefore, the heterobilayer forms a twist-angle-dependent, momentum-indirect bandgap system. Despite the indirect bandgap, the recombination between interlayer electron-hole pairs is allowed a finite exciton kinematic momentum $\mathbf{Q} \equiv \mathbf{k} + \mathbf{k}'$ (which the Coulomb interaction conserves, Fig. 4.3B) or phonon scattering. Specifically, momentum

conservation is satisfied when $\mathbf{Q}_0 = \tau\mathbf{K} - \tau'\mathbf{k}'$ and its C_3 rotations, which are the main light cones where direct IX recombination is allowed. The Q-space light cones are depicted in Fig. 4.3C and D, with the central 6 points forming the main light cones. The other bright regions are Umklapp-type light cones, where the momentum mismatch is compensated by the reciprocal lattice vectors from the two layers; the dipole strength in these light cones are typically at least a few orders of magnitude weaker than the main light cones (Fig. 4.3D). Let us now consider the interlayer exciton optical properties.

In the absence of interlayer hopping, the interlayer exciton wavefunction is written as

$$|X^{(0)}_{\tau'\tau,\mathbf{Q}}\rangle = \sum_{\Delta\mathbf{Q}} \Phi_I(\Delta\mathbf{Q})|e_{\tau',\frac{m_e\mathbf{Q}}{M_0}+\Delta\mathbf{Q}}\rangle|h_{\tau,\frac{m_h\mathbf{Q}}{M_0}-\Delta\mathbf{Q}}\rangle, \tag{4.1}$$

where $|e_{\tau',\mathbf{k}'}\rangle$ ($|h_{\tau,\mathbf{k}}\rangle$) is the electron (hole) Bloch state from $\tau'\mathbf{K}'$ ($\tau\mathbf{K}$) in $MoSe_2$ (WSe_2). The electron-hole relative motion is captured by $\Phi_I(\Delta\mathbf{Q})$, with $\Delta\mathbf{Q} \equiv (m_h\mathbf{k}' - m_e\mathbf{k})/M_0$, and $M_0 \equiv m_e + m_h$. The eigenenergy is $E_I(\mathbf{Q}) = (\hbar^2Q^2/2M_0) + \Delta_g - E_b$, where Δ_g is the bandgap and E_b is the binding energy. Finite interlayer hopping between the layers perturbs the waveunction and hybridizes it with intralayer excitons. This gives rise the transition dipole:

$$\begin{aligned}\boldsymbol{D}_{\tau'\tau,\mathbf{Q}} = \langle 0|\hat{\mathbf{D}}|X^{(0)}_{\tau'\tau,\mathbf{Q}}\rangle + \langle 0|\hat{\mathbf{D}}|X^{(0)}_{\tau'}\rangle\frac{\langle X_{\tau'}|\hat{H}_T|X^{(0)}_{\tau'\tau,\mathbf{Q}}\rangle}{E_I(\mathbf{Q}) - E_M} \\ +\langle 0|\hat{\mathbf{D}}|X^{(0)}_{\tau}\rangle\frac{\langle X_{\tau}|\hat{H}_T|X^{(0)}_{\tau'\tau,\mathbf{Q}}\rangle}{E_I(\mathbf{Q}) - E_W}.\end{aligned} \tag{4.2}$$

The three terms correspond to the transition dipole between electron and hole, light coupling mediated by a bright $MoSe_2$ intralayer exciton ($X_{\tau'}$ with energy E_M), and light coupling mediated by a bright WSe_2 intralayer exciton (X_τ with energy E_W). As shown in Fig. 4.3C, the emission polarization at each light cone is elliptical, with opposite ellipticity for between X_{++} and X_{--} time-reversal pairs. However, the interlayer exciton should really be considered in its wavepacket form [138]:

$$\chi_{\tau\tau',\mathbf{R}} = \sum_{\mathbf{Q}} e^{-i(\mathbf{Q}+\mathbf{K}-\mathbf{K}')\cdot\mathbf{R}}W(\mathbf{Q})X_{\tau'\tau,\mathbf{Q}}, \tag{4.3}$$

where $\mathbf{R}$ is the center of the wavepacket and $W(\mathbf{Q})$ is an envelope function. The twisted heterobilayer forms a moiré pattern, with periodicity $b \approx a/\sqrt{\theta^2+\delta^2}$ determined by the twist

angle θ and $\delta = a'/a - 1$. For small enough twist angles, where IX is bright, the wavepacket spatial extent w is much smaller than b and therefore covers a Q-space region larger than Q_0 (Fig. 4.3). As a result, the emission dipole strength and polarization is determined by the coherent superposition of the three main light cones.

Because the phase factor $e^{-i(\mathbf{Q}+\mathbf{K}-\mathbf{K}')\cdot\mathbf{R}}$ depends on the wavepacket location $\mathbf{R}$, the light coupling varies spatially across the moiré unit cell. Figure 4.4 summarizes the basic optical properties of moiré excitons in AA-stacked (R-type) MoS_2/WSe_2 heterobilayer. The moiré supercell is shown in Fig. 4.4A with the three regions that possess C_3 symmetry marked as A, B, and C. At these locations, the polarization is circular, as dictated by the C_3 eigenvalue of the electron-hole pair ($\psi_c\psi_v^*$). Unlike in the monolayer case (see section 2.3.3), the rotation can differ between electron and hole and thus, the σ^+ and σ^- light coupling varies spatially as shown in Fig. 4.4B and C. Furthermore, the spatially varying relative interlayer translation causes a potential energy modulation throughout the moiré pattern. In the case of AA stacking, the energy minimum is at the A site, where a co-circular selection rule is expected. We refer the reader to refs. [138], [139], and [140] for more details on moiré excitons. This new theoretical understanding of the interlayer excitons came after the experimental studies described later in this chapter, so we do not draw upon it directly in trying to understand the results and instead leave the original theoretical analysis intact. In fact, the disorder from the underlying SiO_2 substrate is strong enough that the interlayer excitons may be considered as free interlayer excitons distributed throughout the moiré supercells. At the present time, while there is evidence of strong moiré effects in scanning tunnel microscopy measurements [141], solid experimental evidence for moiré excitons via optical spectroscopy is difficult to achieve since the moiré periodicity is $\sim$100 nm or less, smaller than the diffraction-limited laser beam ($\sim$1 µm). However, it is useful to keep this theoretical picture is mind as it will play an important role in future studies that use high-quality heterobilayers with BN encapsulation. For example, in Chapter 5, we present signatures of trapped interlayer excitons, where the moiré potential is a likely cause of the exciton localization.

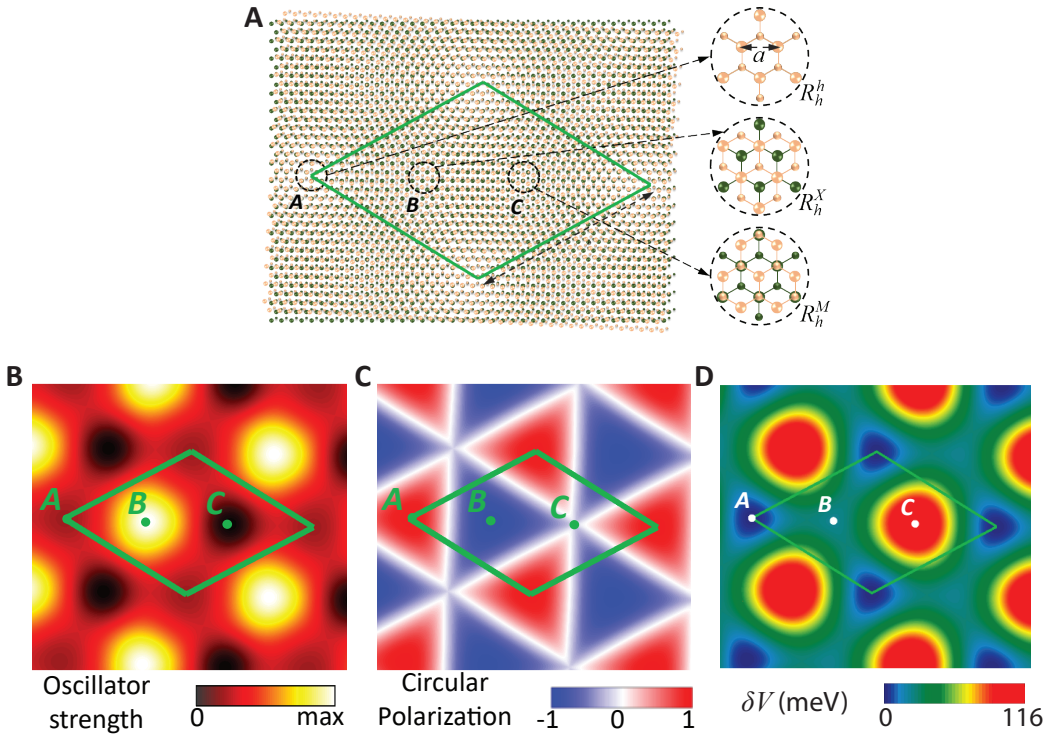

Figure 4.4: Moiré exciton optical properties. (A) Top view of twisted heterobilayer crystal, showing the moiré supercell and points with C_3 symmetry. The calculated oscillator strength (B), circular polarization (C), and potential modulation (D) across the superlattice are shown for WSe_2/MoS_2 heterobilayer. [Reprinted with permission from [138] under CC BY-NC 4.0.]

4.2 Experimental methods

In this section, we outline the details of heterobilayer fabrication. After exfoliating the monolayers of WSe_2 and $MoSe_2$ separately, we identified their crystal axes using linear-polarization-resolved SHG. To do this, we measured the intensity of the co-linearly polarized SHG as a function of crystal orientation using the techniques developed in Chapter 3 (see Fig. 3.1). The orientation of the armchair edges was determined by fitting the SHG intensity angular dependence to the equation, $I = I_0 \cos^2(3\phi)$, where I_0 is the maximum SHG intensity and ϕ is the angle between the laser linear polarization and the armchair axis (see section 3.1.1 for details). Because this technique measures the intensity of SHG, phase information is lost and the crystal axes are only resolved up to a 60° rotation (i.e. the specific direction along an armchair axis is not known). We refer the interested reader to Appendix C to learn about a

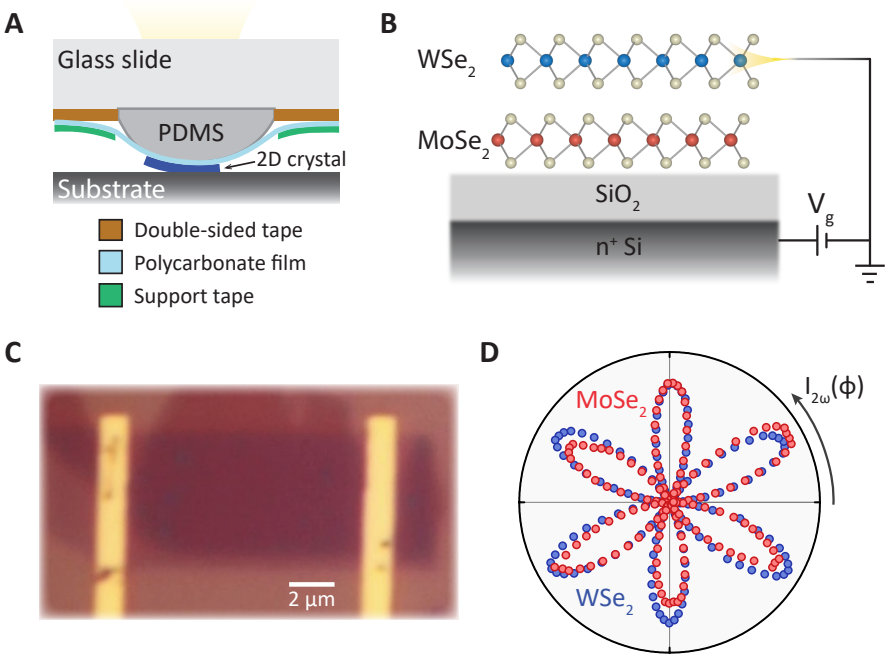

Figure 4.5: Heterobilayer fabrication. (A) Illustration of polymer stamp transfer process. (B) Schematic of heterobilayer FET device. (C) Microscope image of heterobilayer sample. (D) Polarization-resolved SHG pattern for WSe_2 and $MoSe_2$ on the device in fig. C.

phase-resolved SHG technique to determine the exact orientation of heterobilayers; however, this process was developed after the studies in this chapter [142] and thus was not used.

After characterizing the individual monolayers, they were stacked together using a dry-transfer technique (Fig. 4.5A), based on Ref. [143]. A side view of our transfer stamp is shown in Fig. 4.5A, which consists of a thin polycarbonate film stretched over a PDMS slab. The 2D crystals adhere to the polycarbonate film and other 2D crystals more strongly than to the SiO_2 substrate, allowing repeated pickups of any number of crystals onto the stamp, which can then be melted off onto the desired substrate. We oriented the monolayers under the transfer microscope to align their armchair axes to within $\sim 2°$, thus allowing the creation of heterobilayers with twist angles near $0°$ or $60°$. Electrical contacts of V/Au (6/60 nm) were patterned by electron beam lithography and deposited by electron beam evaporation. Similar to the monolayer WSe_2 SHG studies from Chapter 3, the Si substrate acts as a global backgate to the heterostructure (Fig. 4.5B). Figure 4.5C shows an optical microscope image of a representative heterobilayer device. Because this sample had isolated WSe_2 and $MoSe_2$ monolayers, we confirmed the accuracy of the stacking process after device

fabrication (Fig. 4.5D). Furthermore, by comparing Fig. 4.5C and D, we see that the long straight edges of the monolayers coincide with the zigzag crystal direction, as determined by the SHG pattern. We have found this to be true of many exfoliated WSe_2 and $MoSe_2$ monolayers, so the edges serve as a useful reference when aligning the monolayer samples under the microscope prior to stacking.

We performed PL measurements in reflection geometry with a home-built setup, with the device housed in a closed-cycle optical cryostat (Montana Instruments Cryostation) at 30 K. The PL was collected and analyzed by a grating spectrometer (Andor SR-500i) and CCD (Andor Newton CCD). For CW excitation, we used a power-stabilized and frequency-tunable narrow-band (<50 kHz) Ti:sapphire laser (M^2 Solstis) at 1.72 eV (720 nm). Pulsed excitation was performed with a supercontinuum laser (∼10 ps pulse duration) centered at 1.72 eV. The laser spot size was ∼700 nm (FWHM), with a single-mode Gaussian beam profile.

For time-resolved PL measurements, we spectrally filtered the interlayer exciton PL through the spectrometer, out the exit port, and focused onto a single-photon counting module (PicoQuant τ-SPAD or Excelitas SPCM-AQRH). This detector was connected to a picosecond event timer (PicoQuant PicoHarp 300) for time-correlated single photon counting. The instrument response of ∼400 ps is significantly shorter than the observed interlayer exciton decay times. To accommodate long lifetimes, we operated at 100 kHz repetition rate.

To measure the spatially resolved PL, we magnified the PL through a telescope and set the spectrometer grating to its zero order to image the emission on the CCD. We used a long-pass dichroic beamsplitter and an interference longpass filter to extinguish the laser reflection and intralayer PL, ensuring that only interlayer exciton PL was collected.

4.3 Observation of valley-polarized interlayer excitons

We first investigated the IX PL at zero gate voltage ($V_g = 0$ V). Under either σ^+ (Fig. 4.6A) or σ^- (Fig. 4.6B) excitation, the XI PL is clearly co-circularly polarized with the excitation laser. Defining the degree of circular polarization by $\eta = \frac{I_+ - I_-}{I_+ + I_-}$, where $I_\pm$ is the intensity of the $\sigma^\pm$ PL components, the data show $|\eta_{max}| > 0.3$. Our observations have been reproduced across several additional samples (Fig. C.1), though η is seen to vary between samples. We also performed measurements in a linear basis, where we excited the samples with linearly polarized laser and detected the linear PL components, but no appreciable polarization was observed (Fig. C.2).

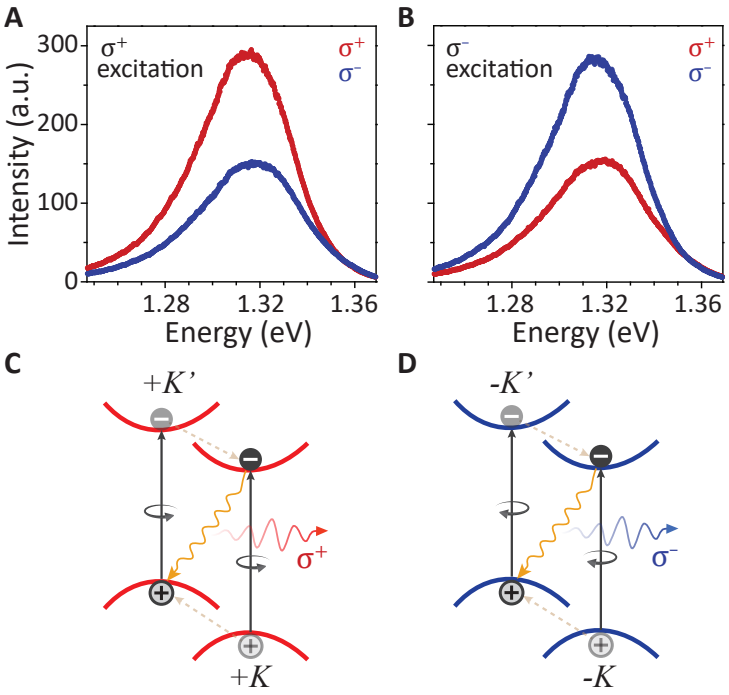

Figure 4.6: Generation and detection of interlayer excitation valley polarization. (A) Circular polarizationresolved interlayer exciton PL spectra showing the generation of strong valley polarization under σ^+ excitation. (B) Same as A, but for σ^- excitation. (C) Schematic of the interlayer exciton in the $+K$ valley. σ^+ circularly polarized light (gray lines) excites intralayer excitons in the $+K'$ and $+K$ valleys. Fast interlayer charge hopping (tan dashed lines) forms the interlayer exciton in the $+K$ valley. The optical selection rules for transitions between the $+K$ and $+K'$ valleys produce co-polarized PL. (D) Same as C but for $-K$ valley. [Adapted from [92].]

The observation of circularly polarized PL demonstrates that the IX can retain memory of the excitation light helicity, similar to monolayer TMD samples [13, 47–49]. However, due to extra complexity of the heterobilayers, the generation of interlayer exciton valley polarization is less straightforward than the case of intralayer excitons in monolayers. Here, we discuss the optical creation of valley polarization for heterostructures close to AA stacking (twist angle near 0°, illustrated in Fig. 4.6B). Similar conclusions can be drawn for heterostructures near AB-like stacking (twist angle near 60°, Fig. C.3) and we provide details in Appendix D. The valley configuration of IX is specified by the valley indices of its electron and hole. With the spin-valley locking in monolayer MX_2, a universal assignment of the valley index is applicable in the twisted heterostructures, and herein we denote the valley with electron

spin up (down) as $+K$ ($-K$) in both layers. First, σ^+ excitation creates valley-polarized intralayer excitons in the $+K$ valley in WSe_2 and $+K'$ valley in $MoSe_2$. Next, charge carriers relax to the heterostructure band edges through interlayer charge transfer on sub-picosecond timescales to form IX. Because of the large momentum difference, interlayer hopping between $+K$ and $-K'$ valleys is strongly suppressed. Conversely, the $+K$ and $+K'$ valleys have small momentum mismatch and the spin-conserving interlayer hopping between these valleys becomes the dominant relaxation channel. Therefore, the σ^+ excitation leads to valley-polarized IX, as illustrated in Fig. 4.6B. The situation for σ^- excitation can be obtained by time reversal (Fig. 4.6C and D). The radiative recombination of the valley-polarized IX is facilitated by the interlayer coupling, which allows emission of photons that are co-polarized with the excitation source [137].

4.4 Gate tunability and valley dynamics

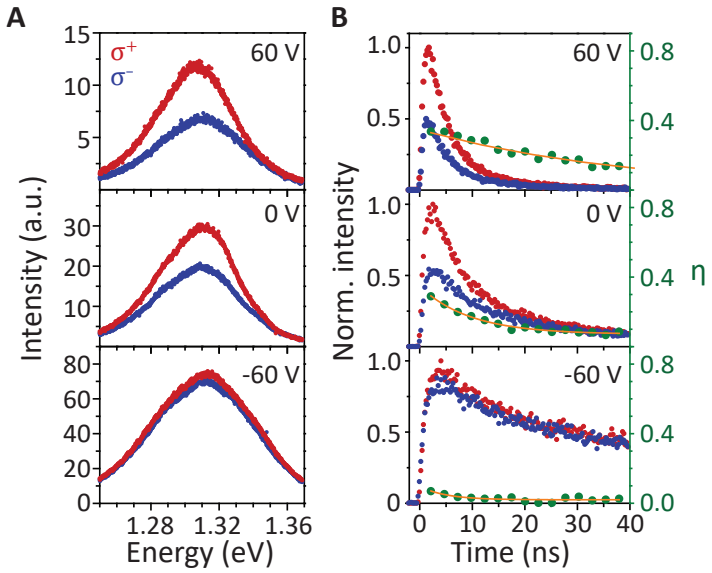

Figure 4.7: Gate-tunable interlayer exciton valley polarization and lifetime. All plots are for σ^+ pulsed laser excitation with co-polarized and cross-polarized PL shown in red and blue, respectively. (A) Polarization-resolved interlayer exciton PL at selected gate voltages. (B) Time-resolved interlayer exciton PL at selected gate voltages. The blue curve (right axis) shows the decay of valley polarization. Solid lines are single exponential fits to valley polarization decay, with lifetimes of 39(2) ns, 10(1) ns and 5(2) ns for gate voltages of 60 V, 0 V and −60 V, respectively. [Adapted from [92].]

The degree of IX valley polarization is electrically controllable by a gate voltage. Figure 4.7A shows polarization-resolved PL spectra at selected V_g under σ^+ excitation with 50 ps laser pulses. There is a strong gate dependence of the valley polarization, which is greatest at 60 V and highly suppressed at -60 V. In Fig. 4.7B, we show the decay of co-polarized (black) and cross-polarized (red) interlayer exciton PL, as well as the degree of polarization (blue), at the same V_g values as in Fig. 2A (see Fig. C.6 for the full data set). The valley polarization lifetime increases with V_g, reaching 39(2) ns at 60 V, as determined by fitting a single exponential decay. Long valley lifetimes were also measured in heterostructures with the opposite stacking order (i.e. $MoSe_2$ on WSe_2, Fig. C.6).

These measurements imply a strong suppression of intervalley scattering for the IX and a valley lifetime several orders of magnitude longer than that of intralayer excitons in monolayers, where valley depolarization occurs on picosecond timescales [133, 144–146]. Our measurement also shows that the initial PL polarization of IX is about 40 % at 60 V. The imperfect initial valley polarization of IX is likely due to valley depolarization of intralayer excitons in the constituent monolayers, which mediate the IX formation. We note that because the IX is dark at the minimum of the energy dispersion, due to the finite twisting angle and slight lattice mismatch between the two layers, it effectively provides a reservoir from which the IX are scattered into the light cones and luminesce. This complicated exciton-light coupling is likely responsible for the subtle but intriguing features in Fig. 4.7B, such as the increase of PL lifetime accompanying the decrease of valley polarization lifetime. However, future studies are required to gain a clear understanding of the microscopic mechanism for the observed gate-dependent PL dynamics of the IX.

4.5 Detection of valley-polarized drift-diffusion

The long valley lifetime of the IX allows visualization of their lateral drift and diffusion. Figure 4.8 displays a sequence of spatial maps at different excitation powers for the IX σ^+ and σ^- intensity, as well as the valley polarization. In this experiment, we used σ^+ pulsed excitation (40 MHz repetition rate) at $V_g = 60$ V, where there was strong valley polarization. We first notice the significant increase in spatial extent for the PL intensity at higher excitation powers. Moreover, we observe the evolution of a ring in the spatial pattern of η, which increases in diameter with excitation intensity. The pattern of polarization stands in contrast to the spatial distribution of the emission intensity, which decreases monotonically away from the excitation spot on average. For direct comparison of the different spatial

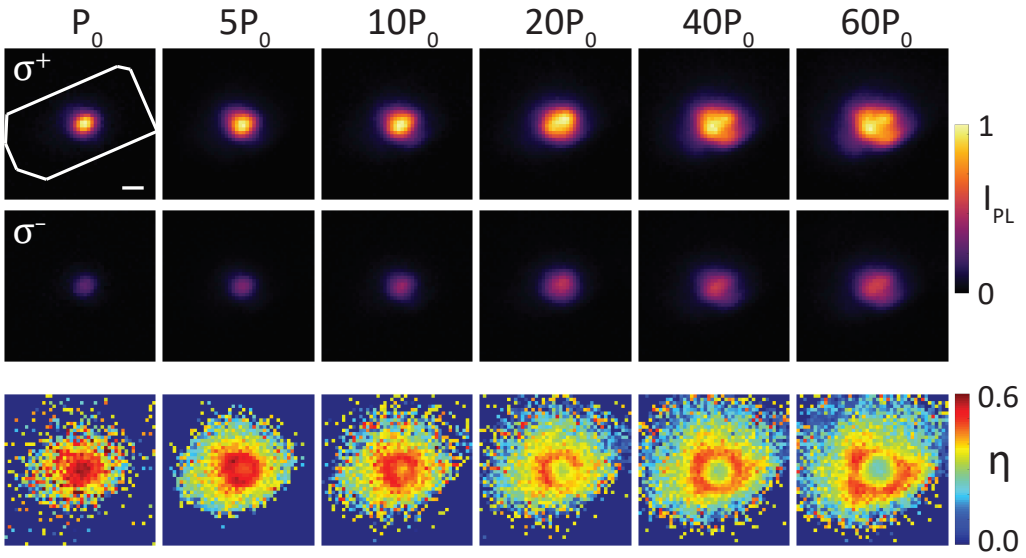

Figure 4.8: Drift-diffusion of valley-polarized interlayer exciton gas. Excitation is *sigma*$^+$ polarized. The top, middle, and bottom horizontal panels show the σ^+ PL intensity, σ^- PL intensity, and valley polarization as a function of excitation power. The white outline shows the heterobilayer area (scale bar, 2 µm). $P_0 = 1$ µW. [Adapted from [92].]

profiles, Fig. 4.9A gives the average PL intensity and η as a function of the distance from the beam center for the 40 µW case. The data reveal the drift-diffusion of σ^+ (red) and σ^- (blue) polarized excitons away from the laser spot (0.7 µm FWHM, dashed) as well as the increasing ring of η (green), demonstrating the striking difference between the spatial distribution of polarization and the total density of IX.

One possible explanation for the observed polarization ring is density-dependent intervalley scattering. However, consideration of the valley polarization as a function of excitation intensity suggests otherwise. Figure 4.9B shows the power dependence of valley polarization from the spatially integrated $I_{\pm}$, which decreases by about 25 % over a 60-fold increase in excitation power (corresponding to at least an order of magnitude increase in the exciton density). Yet, the radial dependence of η shows a decrease of nearly 40 % from its peak, at the radius of the ring of polarization, to its minimum at the excitation center (4.9A). This is a dramatic change in η considering that the exciton density drops by only a factor of two over this region (i.e., the corresponding PL intensity decreases by approximately 50 %). The weak dependence of the integrated valley polarization on excitation intensity, contrasted with the strong variation of η in the ring feature, implies that density-dependent intervalley

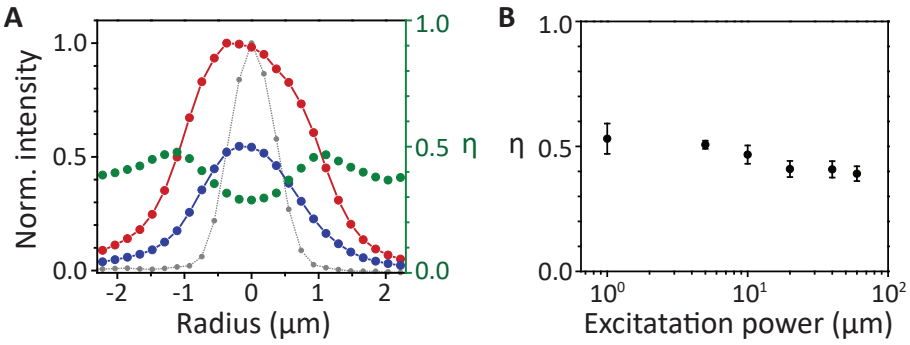

Figure 4.9: Spatial profile and power-dependent polarization of interlayer exciton. (A) Polarization-resolved spatial profiles of σ^+ (red) and σ^+ (blue) components of interlayer exciton PL under 40 μW excitation. The spatial distribution of valley polarization is shown in green, and the laser excitation profile is shown in gray. Line cuts are radially averaged through the excitation center, and curves are added as guides to the eye. (B) Power dependence of the co-polarized component of interlayer exciton PL intensity (under σ^+ pulsed excitation at 1.72 eV). [Adapted from [92].]

scattering is not the dominant mechanism in the ring formation.

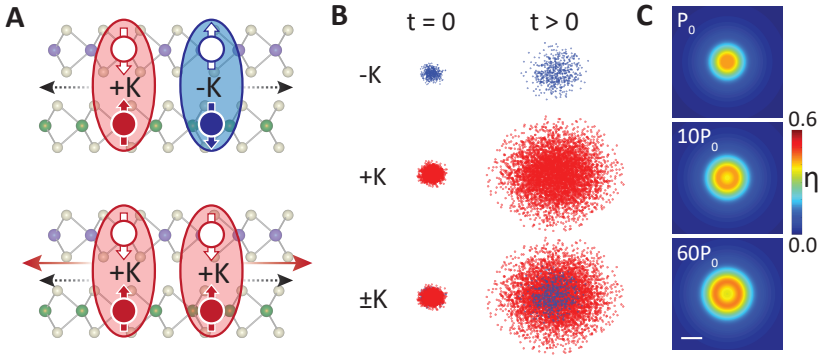

Figure 4.10: Valley ring formation. (A) Schematic of the valley-dependent repulsive interactions between interlayer excitons. Excitons in the same valley (top) experience repulsive forces due to the dipole-dipole interaction (short dotted arrows) as well as the exchange interaction (long solid arrows), whereas excitons in opposite valleys (bottom) only experience the dipole-dipole interaction. (B) Cartoon picture of the ring formation. [Adapted from [92].]

Instead, the observed spatial patterns in the valley polarization can be understood as manifestations of valley-dependent many-body interactions in the dense interlayer exciton

gas. For a heterostructure sample with spatially inhomogeneous X_{++} density $N_+(\mathbf{r})$ and X_{--} density $N_-(\mathbf{r})$, an X_{++} (X_{--}) wavepacket at position $\mathbf{R}$ will feel a mean potential from both the dipole-dipole ($\overline{V}_{dd}$) and exchange interactions ($\overline{V}_{ex}$),

$$\Delta E_\pm(\mathbf{R}) \approx N_\pm(\mathbf{R})\overline{V}_{ex} + \big(N_+(\mathbf{R}) + N_-(\mathbf{R})\big)\overline{V}_{dd}. \tag{4.4}$$

Both the exchange and dipole-dipole terms are repulsive (see Appendix C for further details). In addition, due to the small interlayer separation of about 7 Å, we estimate that the exchange interaction is stronger than the dipole-dipole repulsion. Because the exchange interactions are appreciable only between excitons of the same valley species, in a cloud of valley-polarized interlayer excitons, the majority valley excitons experience align stronger mutually repulsive force (4.10A), leading to more rapid expansion than the minority valley excitons. On the other hand, the density gradient of excitons will also give rise to diffusion, which is valley-independent and does not produce a ring pattern. Therefore, the relative strength of the diffusion and valley-dependent drift controls the pattern of the spatial polarization. If the interlayer exciton density is large enough that the valley-dependent repulsive interaction dominates the expansion of the exciton gas, higher valley polarization can appear away from the excitation center (4.10B). Indeed, a pronounced ring in the polarization is generated at sufficiently high excitation intensity, as seen in 4.8.

We simulate the valley-dependent IX expansion and PL using a phenomenological drift-diffusion model. It is similar to ref. [105], but also accounts for valley-dependent drift effects. The time-dependent spatial density of $\sigma^\pm$ interlayer valley excitons are denoted by $N_\pm(r,t)$ and the model takes the form

$$\frac{\partial N_\pm}{\partial t} = I_\pm + D\nabla^2 N_\pm + \nabla\cdot(N_\pm(\alpha_0\nabla N_\pm + \beta_0\nabla N_\mp)) - \frac{N_\pm}{\tau} - \frac{N_\pm - N_\mp}{\tau_v} \tag{4.5}$$

Here, I_+ and I_- denote the IX formation rate that are co- and cross-polarized with the optical pump, D is the diffusion coefficient, and τ and τ_v are the lifetimes of interlayer exciton and valley polarization, respectively. The third term on the right of each equation captures the effects of the valley-dependent repulsive interactions, by which the density gradient manifests as a driving force for the drift. The force from the same valley species (α_0 part) is from the sum of the dipole and exchange interactions, and the force from the different valley species (β_0 part) is from the dipole interaction only. This simple model captures the essential experimental features and simulations based on it show the formation of the ring pattern as

seen experimentally (Fig. 4.10C) (see Appendix C for additional theoretical details).

Chapter 5

SIGNATURES OF MOIRÉ-TRAPPED VALLEY EXCITONS IN $MOSE_2/WSE_2$ HETEROBILAYERS

5.1 Introduction

The creation of moiré patterns in crystalline solids is a powerful approach to manipulate their electronic properties, which are fundamentally influenced by periodic potential landscapes. In two-dimensional (2D) materials, a moiré pattern with a superlattice potential can form by vertically stacking two layered materials with a twist and/or finite lattice constant difference. This unique approach has led to emergent electronic phenomena, including the fractal quantum Hall effect [147–149], tunable Mott insulators [150, 151], and unconventional superconductivity [152]. Furthermore, theory predicts intriguing effects on optical excitations by a moiré potential in 2D valley semiconductors [137, 138, 140], but these signatures have yet to be experimentally detected. Here, we report experimental evidence of interlayer valley excitons trapped in a moiré potential in high-quality BN-encapsulated $MoSe_2/WSe_2$ heterobilayers. At low temperatures, we observe photoluminescence near the free interlayer exciton energy but with over 10 times narrower linewidths ($\sim$100 µeV). The emitter g-factors are homogeneous across the same sample and only take two values, -15.9 and 6.7, in samples with twisting angles near 60° and 0°, respectively. The g-factors match those of the free interlayer exciton, which is determined by one of two possible valley pairing configurations. At a twist angle near 20°, the emitters become two orders of magnitude dimmer, but remarkably, they possess the same g-factor as the heterobilayer near 60°. This is consistent with the Umklapp recombination of interlayer excitons near the commensurate 21.8° twist angle [137]. The emitters exhibit strong circular polarization, which implies the preservation of three-fold rotation symmetry by the trapping potential. Together with the power and excitation energy dependence, all evidence unambiguously points to their origin as interlayer excitons trapped in a smooth moiré potential with inherited valley-contrasting physics. Our results open opportunities for 2D moiré optics with twist angle as a unique control knob.

5.2 Experimental methods

The samples were fabricated by dry-transfer of monolayers obtained from the mechanical exfoliation from bulk crystals. The crystal orientation of the individual monolayers was determined by linear-polarization-resolved second-harmonic generation [92] prior to transfer. During the transfer process for device 1, a region of the WSe_2 monolayer tore off and twisted 18° relative to the original piece (see Fig. 5.1C). This yield heterobilayers with twist angle $\theta = 2°$ and 20°. Device 2 was fabricated from a large WSe_2 monolayer and an $MoSe_2$ piece with two overlapping monolayers (monolayer-bilayer-monolayer). The two $MoSe_2$ monolayer regions are formed from different layers of a 2H-bilayer, so they were oriented 180° relative to one another prior to transfer. Therefore, after transfer, device 2 possessed two heterobilayer regions, one with near 0° twist angle (6°) and another close to 60° (57°). The difference in twist angle between the two heterobilayer regions deviates from the expected 60° because one of the $MoSe_2$ monolayer regions rotated slightly during transfer. To verify the absolute stacking orientation, we used a phase-resolved second-harmonic generation technique, as described in Appendix B. This yielded a reference heterobilayer sample with 56° twist angle, on which we measured a g-factor near -15.9 (Fig. D.6). The two regions of device 2 were then measured to have a g-factor of 6.7 and -15.9, which confirmed their different stacking orientations as well as the general correspondence between samples with twist angle near 0° or 60° and their g-factor. The absolute twist angle for samples with near 0° or 60° was ultimately determined by the g-factor (close to 6.7 for 0° and close to -15.9 for 60°).

PL measurements were performed in a home-built confocal microscope in reflection geometry, with the sample mounted in an exchange-gas cooled cryostat equipped with a 9 T superconducting magnet in Faraday configuration. The sample temperature was kept at 1.6 K unless otherwise specified. A power-stabilized and frequency-tunable narrow-band continuous-wave Ti:sapphire laser (M^2 SolsTiS) was used to excite the sample, unless otherwise specified. The PL was spectrally filtered from the laser using a long-pass filter before being directed into a spectrometer, where the PL was dispersed by a diffraction grating (600 or 1200 grooves/mm) and detected on a Si charge-coupled-device. At the interlayer PL energies of ∼1.4 eV, the spectral resolution was ∼160 µeV for the 600 grooves/mm grating (Figs. 5.1D-E, 5.2B, 5.3B) and ∼80 µeV for 1200 grooves/mm (Figs. 5.1E inset, 5.2A, 5.2C, 5.3A, 5.3C). Polarization-resolved PL data were acquired using a combination of quarter-wave plates, half-wave plates, and linear polarizers for excitation and collection.

5.3 Trapped interlayer excitons

Heterobilayers formed by monolayer semiconducting transition metal dichalcogenides are a fascinating system for exploring nanoscale semiconductor optoelectronics with valley functionality [92, 153]. Vertically stacked $MoSe_2$ and WSe_2 monolayers, for example, exhibit an atomically sharp interface and type-II band alignment which hosts interlayer excitonsthe Coulomb bound state between electrons and holes located in different monolayers. Under circularly polarized optical pumping, electrons and holes preferentially populate the K valleys in the $MoSe_2$ conduction band and WSe_2 valence band, respectively. This allows for the formation of interlayer excitons with a plethora of appealing properties, such as valley-contrasting physics [92, 137, 138, 140, 154–156], long population and valley lifetimes [92, 125, 157, 158], high electrical tunability [92, 125, 134], and strong many-body interactions [92, 125, 157].

One enticing possibility, which has so far only been theoretically explored, is to harness the spatially periodic moiré superlattice potential for excitonic manipulation. Recent scanning tunneling microscopy/spectroscopy measurements have directly measured the moiré pattern of 2D semiconductor heterobilayers, showing a periodically varying interlayer separation and electronic band gap [141]. The periodicity of this moiré superlattice is determined by the lattice constant mismatch and twist angle (θ) between the layers (Fig. 5.1A). When the moiré period is larger than the interlayer exciton Bohr radius ($\sim$1 nm), the excitons will experience a spatially periodic potential modulation, forming a solid-state analog of a bosonic quantum gas in an optical lattice [159]. The moiré potential minima can function as a smooth quantum-dot-like confinement potential (Fig. 5.1B), and unique to these moiré-defined trapping sites is the preservation of three-fold rotational (C_3) symmetry8,9. Therefore, the moiré-trapped interlayer excitons should inherit valley-contrasting properties, a feature which distinguishes them from excitons bound to other randomly formed potential traps (e.g. defects, impurities, strain, etc.)

In this work, we report experimental signatures of interlayer excitons trapped in a moiré potential in $MoSe_2/WSe_2$ heterobilayers. The samples consist of exfoliated monolayers of $MoSe_2$ and WSe_2, stacked using a dry-transfer technique and aligned deterministically with 1o uncertainty, which are encapsulated between $\sim$10 nm to 30 nm hexagonal boron nitride to provide an atomically smooth substrate. Data from two devices are presented in the main text. Each device contains two heterobilayers that were simultaneously fabricated from the same pair of monolayers, but have regions with different θ (see Methods). This procedure

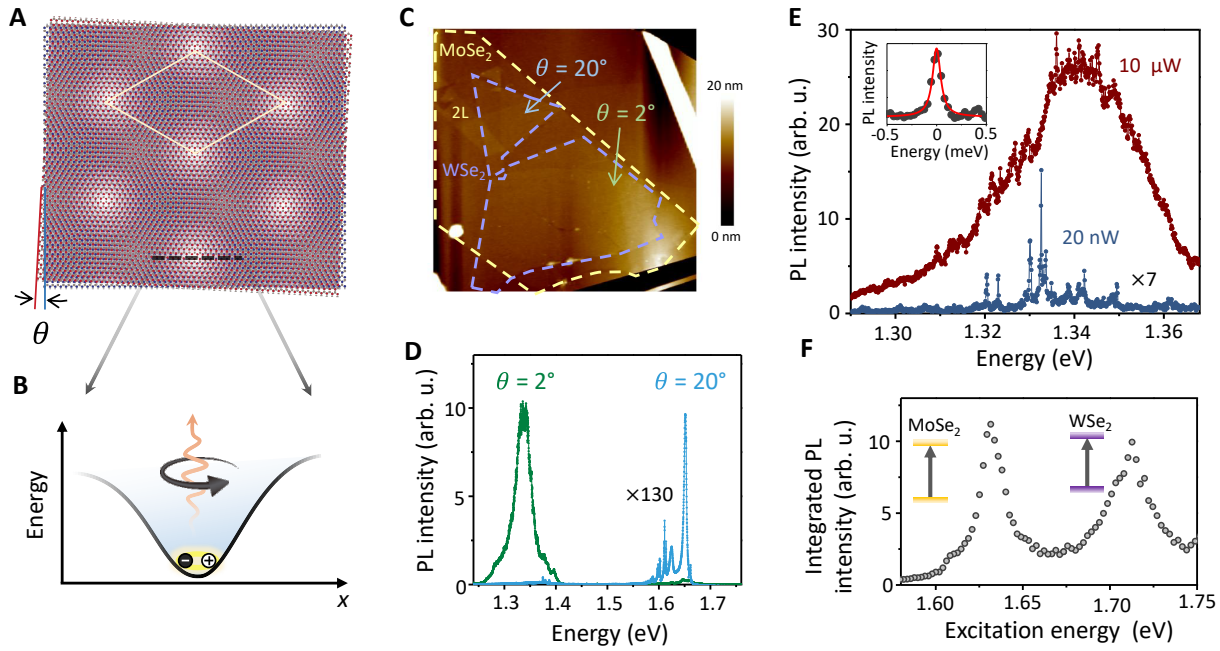

Figure 5.1: Moiré superlattice potential and observation of trapped interlayer excitons. (A) Illustration of the moiré superlattice formed in a heterobilayer with twist angle θ. (B) Cartoon of an exciton trapped in a moiré potential. (C) Topographical height map of $MoSe_2/WSe_2$ heterobilayers encapsulated by hexagonal boron nitride, obtained from an atomic force microscope. Orange and purple solid lines indicate the $MoSe_2$ and WSe_2 monolayers, respectively. The heterobilayers have different twist angles, as indicated. (D) PL spectra from the heterobilayer with 2° (green) and 20° (blue, intensity scaled by 130×) twist angle, at 5 μW excitation power. (E) Comparison of interlayer exciton PL from the 20° twist angle heterobilayer at 10 μW (orange) and 20 nW (purple, intensity scaled by 7×) excitation power. Inset, Lorentzian fit to a representative PL peak indicates a linewidth of ∼100 μeV (20 nW excitation power). (F) PL excitation intensity plot on a narrow PL peak showing two prominent resonances corresponding to the intralayer exciton states in the monolayers of $MoSe_2$ and WSe_2. The intensity is integrated over a single peak of the $\theta = 57°$ sample, but the results are qualitatively similar for all other emission lines on each sample.

minimizes the uncertainties when comparing the interlayer exciton properties at different twist angles. Device 1 contains heterobilayers with $\theta = 2°$ and 20° (Fig. 5.1C), while device 2 has regions with $\theta = 6°$ and 57°.

$MoSe_2/WSe_2$ heterobilayers with aligned crystallographic axes generally exhibit bright interlayer exciton photoluminescence (PL) around 1.3 eV to 1.4 eV with a typical linewidth less than ∼10 meV. Figure 5.1D shows PL spectra from the $\theta = 2°$ and 20° regions of device

1 under 5 µW 632.8 nm HeNe laser excitation (beam spot size $\sim$1 µm^2) at a temperature of 1.6 K. In both heterobilayer regions, the intralayer exciton PL near 1.65 eV is strongly quenched relative to PL from the isolated monolayers due to ultrafast interlayer charge transfer [126]. However, there is a stark contrast in the interlayer exciton PL intensity, with the 2° region being over two orders of magnitude brighter than the 20° region. This is due to the large mismatch of the first Brillouin zone corners between electrons and holes in 20° heterobilayer, which strongly suppresses the PL quantum yield compared to the nearly aligned 2° sample.

Under much lower excitation power (20 nW) near the monolayer WSe_2 A exciton resonance (1.72 eV), the broad interlayer PL develops into several narrow peaks near the free interlayer exciton energy around 1.33 eV (Fig. 5.1E and Fig. D.1), which fit well to Lorentzian curves (Fig. 5.1E, inset). The average linewidth of the observed peaks is about 100 µeV, which is comparable to the quantum emitters reported in monolayers of WSe_2 [160–163] and hexagonal boron nitride [164], and two orders of magnitude narrower than previous reports of interlayer exciton PL [92, 125, 154–158, 165, 166]. Narrow PL peaks and power broadening were also observed in the 57° and 20° sample (Fig. D.1).

The evolution of the broad interlayer PL peak into several narrow lines at low power suggests that the interlayer excitons are trapped in confinement potentials. The strong power saturation and broadening are characteristic of trapped excitons, where under high-power excitation, the traps are filled, and the emission becomes dominated by delocalized excitons that have broadened linewidth. Moreover, the narrow-line emission is suppressed above 30 K, after which the broader PL peaks dominate the spectrum (Fig. D.2). To substantiate the assignment of these features to interlayer excitons, we performed low-power PL excitation (PLE) spectroscopy, scanning a continuous-wave laser from 1.55 eV to 1.77 eV while monitoring the intensity of the narrow PL peaks. The PLE spectrum in Fig. 5.1F features two prominent resonances, consistent with the absorption of the $MoSe_2$ and WSe_2 intralayer excitons, which establishes the interlayer exciton character of the narrow PL lines.

5.4 Valley polarization

The trapped interlayer excitons exhibit strong valley polarization. Figure 5.2 shows circular polarization-resolved PL spectra under σ^+ excitation for heterobilayers with $\theta = 57°$, 20°, and 2°. Denoting the valley polarization $\eta = \frac{I_+ - I_-}{I_+ - I_-}$, where $I_\pm$ is the $\sigma^\pm$ PL intensity, the narrow peaks in the 57° and 20° heterobilayers display over 70 % valley polarization

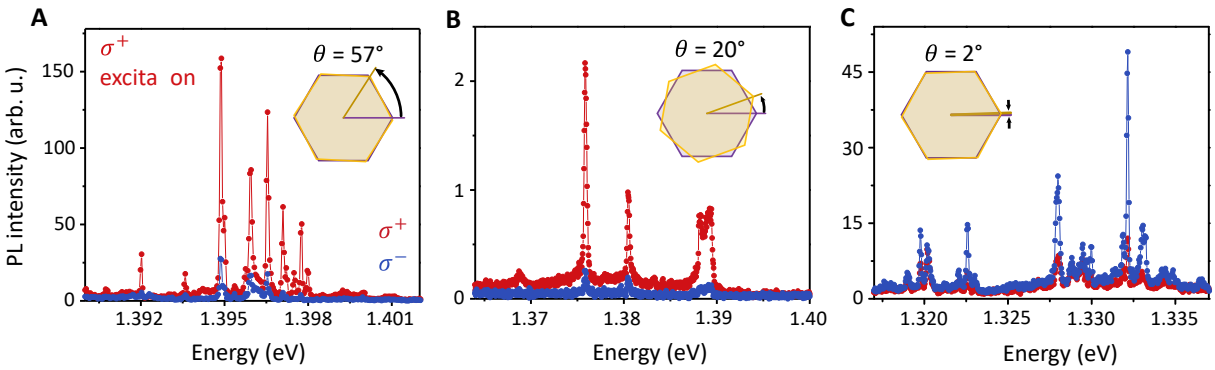

Figure 5.2: Valley polarization of trapped interlayer excitons. Helicity-resolved PL spectra of trapped interlayer excitons of $MoSe_2/WSe_2$ heterobilayers with twist angle of (A) 57°, (B) 20°, and (C) 2°. Insets illustrate the twist angle of the three samples. The samples are excited with σ^+-polarized light at 1.72 eV. The σ^+ and σ^- components of the PL are shown in red and blue, respectively. The PL from heterobilayers with twist angles of 57° and 20° are co-circularly polarized, while PL from the heterobilayer with twist angle of 2° is cross-circularly polarized.

(Figs. 5.2A and B). On the other hand, the selection rule is reversed for the 2° sample, with σ^-emission dominating under σ^+ excitation (i.e. $\eta < 0$, Fig. 5.2C). Using σ^- excitation, we confirmed the time-reversal process, establishing the observation of co-circularly polarized PL for 57° and 20° and cross-circularly polarized PL for 2° (Fig. D.3). Furthermore, under linearly polarized excitation, no significant linear PL polarization components were detected (Fig. D.4). Additional samples near 0° and 60° stacking show similar narrow PL features and polarization properties (Fig. D.3).

The circular polarization properties of the trapped interlayer excitons are distinct from the quantum emitters reported in monolayer materials, which exhibit either intrinsically linearly or un-polarized PL [160–163]. In those systems, high magnetic fields or trion formation under strong electron doping [167] are required to restore modest circularly polarized PL. Fine structure splitting observed in linearly polarized monolayer emitters implies anisotropy of the trapping potential, which breaks the three-fold rotational symmetry of the host lattice [160]. While the exact origin of the quantum emitters in monolayers is currently unclear, they are generally thought to arise from excitons bound to defects [168], impurities, or strain-induced potential traps [169, 170]. However, unlike the monolayer case, the strong circularly polarized PL from the trapped interlayer excitons implies that the confining potential must possess three-fold rotational symmetry. One possible origin for the observed exciton trapping

in the heterobilayer is the potential landscape resulting from the moiré superlattice, which naturally forms arrays of confinement centers with local atomic configurations that maintain C_3 symmetry [138, 140]. This preserves valley optical selection rules and generally allows for cross-circularly polarized emission by interlayer excitons [138–140, 156, 165] which will be discussed later.

5.5 Magnetic field dependence

To support the moiré potential assignment, we performed magneto-PL spectroscopy to determine the Landé g-factor of trapped interlayer excitons. In Figs. 5.3A-C, we show circularly polarized PL under linearly polarized excitation as a function of perpendicular magnetic field B for heterobilayers with $\theta = 57°$, 20°, and 2°, respectively. The linearly polarized excitation equally pumps the degenerate $\pm K$ valleys of the monolayers, resulting in equal intensity and energy for σ^+ and σ^- PL at 0 T. For nonzero magnetic fields, σ^+ and σ^- PL split strongly in energy due to the valley Zeeman effect [40, 51–55], but otherwise maintain the same peak structures, as illustrated by the spectra at 3 T (top row of Fig. 5.3). We visualize the full magnetic field dependence by plotting the total PL intensity versus the emission energy and B (middle row of Fig. 5.3). For a given twist angle, we observe that for all PL peaks, the energies of σ^+ and σ^- emission shift equally and oppositely to one another. Since several of the peaks are closely spaced in energy ($\sim$1 meV or less), the large energy shifts cause crossing points between the σ^+ and σ^- emission of different PL peaks at high magnetic fields.

The bottom row of Fig. 5.3 shows the energy difference between the $\sigma^\pm$ PL ($\Delta E_{\sigma^+} - E_{\sigma^-}$, where $E_{\sigma^\pm}$ is the peak energy of $\sigma^\pm$ polarized PL) of representative trapped interlayer excitons in each twisted heterobilayer. The extracted g-factor of 6.72(2) for $\theta = 2°$ heterobilayer is nearly the same as the free interlayer exciton in near 0° samples (Fig. D.5). For $\theta = 57°$, the effective g-factor is $-15.89(3)$, which is also very close to the g-factor of -15.1 reported for free interlayer excitons in 54° twisted heterobilayer [154]. We found that the g-factor is not only uniform between different trapped interlayer excitons in the same heterobilayer, but also nearly the same for different heterobilayers with similar twist angle (Fig. D.6).

The valley magnetic moment plays a central role in the distinct g-factors between nearly 0° and 60° heterobilayers. The Zeeman shift of carriers in the valley semiconductors has three contributions (Figs. 5.4A, B): spin ($\Delta_s = 2s_z\mu_B B$), atomic orbital ($\Delta_a = l_i\mu_B B$), and a valley contribution ($\Delta_v = \tau\alpha_i\mu_B B$) from the Berry phase effect [40, 51–53]. Here, $\tau = \pm 1$ is the valley index, $s_z = \pm 1/2$ is electron spin index, μ_B is Bohr magneton, α_i is valley

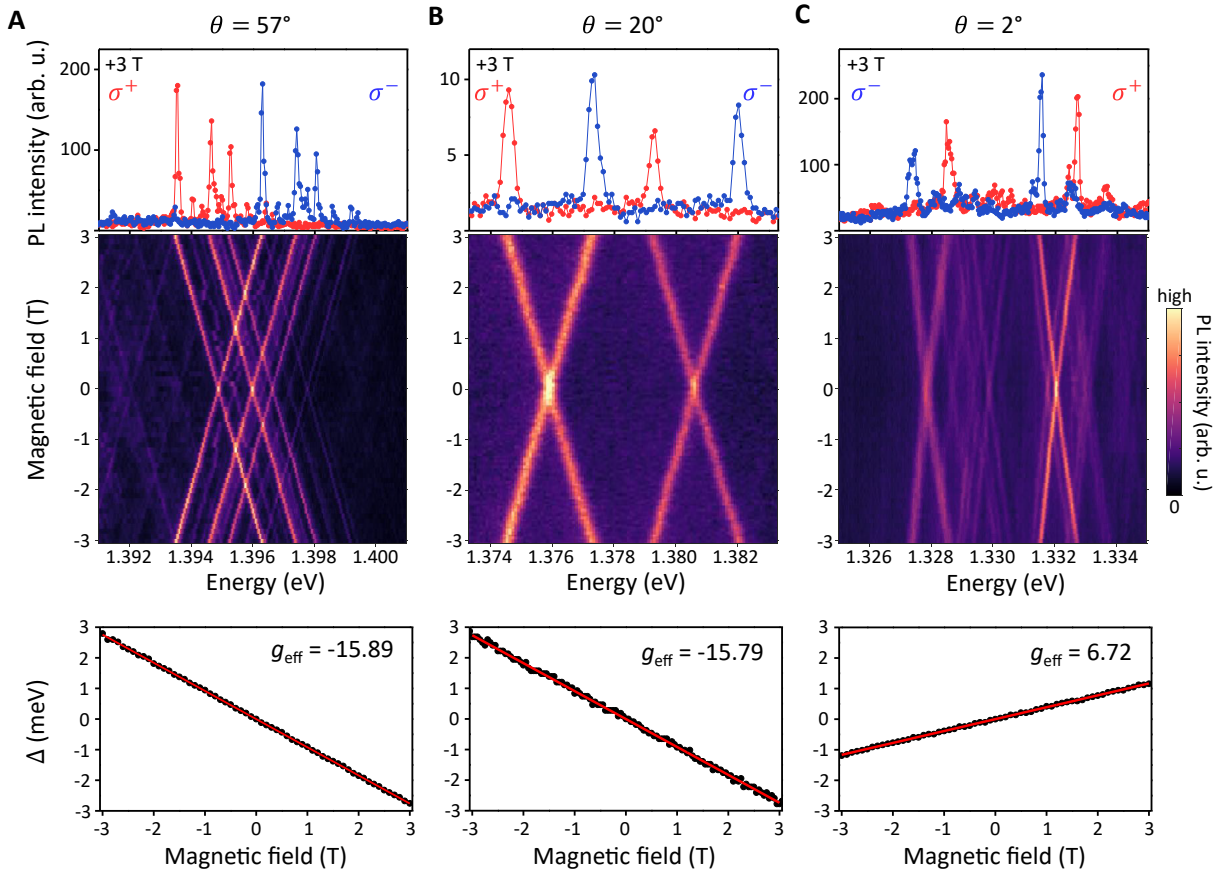

Figure 5.3: Twist-angle-dependent Zeeman splitting of trapped interlayer excitons. Magnetic-field-dependent PL from interlayer excitons in the $MoSe_2/WSe_2$ heterobilayer with twist angle of (A), 57°, (B), 20°, and (C) 2°. Top row: Helicity-resolved PL spectra at 3 T. The excitation is linearly polarized, and the σ^+ and σ^- components of the PL are shown in red and blue, respectively. Middle row: Total PL intensity plot as a function of magnetic field, showing a linear Zeeman shift of the σ^+ and σ^- polarized PL. Bottom row: Zeeman splitting of the polarization-resolved PL as a function of the applied magnetic field. The effective g-factors for the three samples ($-15.89(2)$, $-15.79(5)$, and $6.72(2)$ for (A), (B), and (C), respectively) are extracted from a linear fit of Δ versus B (red solid line).

g-factor for the conduction ($i = c$) or valence band ($i = v$), and l_i is the magnetic quantum number for band i ($l_c = 0$ and $l_v = 2\tau$). The Zeeman splitting of the interlayer exciton is then the difference between the Zeeman shifts of conduction band edge in $MoSe_2$ and valence band edge in WSe_2.

For interlayer excitons with spin-conserving optical transitions, spin does not contribute to the exciton Zeeman shift. Furthermore, the atomic orbital contribution to the Zeeman

splitting, $-4\mu_B B$, is independent of the twist angle. The major difference between nearly 0° and 60° stacking therefore lies in the valley magnetic moment contribution because of their distinct conduction-valence valley pairing. The bright interlayer exciton configuration can be uniquely specified by the valley index pair (τ_c, τ_v), which is $(+,+)$ or $(-,-)$ for nearly 0° stacking (Fig. 5.4A), and $(+,-)$ or $(-,+)$ for nearly 60° stacking (Fig. 5.4B). Consequently, for0° stacking, the excitonic Zeeman splitting is similar to monolayers and may be written as $\Delta_0 = -2(2 - \Delta\alpha)\mu_B B$, where the valley contribution $\Delta\alpha = \alpha_c - \alpha_v$. For the 60° stacking case, the valley contribution changes from a cancellation to a sum12, which gives rise to much larger Zeeman shift $\Delta_60 = -2(2 + \Sigma\alpha)\mu_B B$, where $\Sigma\alpha = \alpha_c + \alpha_v$ is the summation of valley g-factors, and thus larger effective interlayer g-factor than0° stacked heterobilayer (Appendix D).

From the above analysis, we see that interlayer exciton g-factor is a fingerprint of their valley configuration and valley magnetic moment. The defect-localized excitons in monolayers do not possess valley-contrasting properties [160–163] since the bulk crystal structure is not retained in the extent of the exciton wavefunction. Indeed, excitons bound to defects or strain-confined potentials observed in WSe_2 have distinct g-factors (a few times larger) compared to the free intralayer exciton counterparts, and often exhibit fine structure splitting and absence of circular polarization from the anisotropic quantum confinement [160–163]. Our observation that the trapped interlayer excitons have the same g-factors and twist angle dependence as the free ones demonstrates that the trapping potential must be smooth enough and three-fold rotational symmetric to allow the inheritance of the valley properties from the heterobilayer bulk. These findings strongly suggest that extrinsic factors (defects, impurities, strain) cannot be the origin of the trapping, whereas the moiré potential traps are the only known candidate.

5.6 Moiré excitons near 21.8° *twist angle*

Another remarkable finding which further supports the above picture is that the g-factor of interlayer excitons for $\theta = 20°$ is $-15.78(5)$ (bottom row, Fig. 5.3C), which is nearly the same as that of $\theta = 57°$ heterobilayer. This, at the first glance, is counterintuitive, as 20° is closer to0° than to 60°. The mystery is solved by noticing that 21.8° is a commensurate stacking angle7 that produces the shortest superlattice periodicity, with a supercell of size $\sqrt{7}a \times \sqrt{7}a$. Figure 5.4C shows the conduction (solid points) and valence band edges (open points) of heterobilayer in the extended Brillouin zone scheme, where red and blue denote $+K$ and

$-K$ valley respectively. For a random twist angle, the valleys from $MoSe_2$ and WSe_2 are in general not aligned in momentum space, and thus interlayer excitons are momentum-indirect and optically dark. At 21.8° twisting angle, the conduction and valence band $\pm K$ points are misaligned in the first Brillouin zone but overlap on the second Brillouin zone, with the $(+,-)$ and $(-,+)$ valley pairings. As a result, the interlayer exciton at this commensurate stacking can directly couple to light for radiative recombination, with the momentum mismatch from the twisting compensated by the reciprocal lattice vectors from the two layers (i.e. Umklapp recombination) [137]. Since the valley pairings of 21.8° are the same as for 60° twisted heterobilayers, they have the same g-factor. The optical dipole of the Umklapp recombination is expected to be very weak compared to that of the direct recombination at 0° and 60°. Indeed, our measurement reveals the PL intensity of the 2° sample is about 100 times stronger than that of the 20° sample (Fig. D.7).

Our heterobilayer of $\theta = 20°$ forms an interesting concatenated moiré pattern, as schematically shown in Fig. D.8. Close-up views of any local region resemble the commensurate moiré pattern of the 21.8° stacking, but the interlayer translation varies smoothly over a longer length scale with the periodicity $A = \frac{a}{\sqrt{7}\delta\theta}$. Here, $\delta\theta$ is the small deviation of the actual twisting angle from the commensurate angle of 21.8°, and $A \approx 4\,\text{nm}$ at $\theta = 20°$. In this concatenated moiré supercell, we can also identify three local regions that retain the three-fold rotational symmetry, which must correspond to either the minima or maxima of the moiré superlattice potential for the interlayer excitons (Appendix D). As with the $\theta = 2°$ and $\theta = 57°$ moiré pattern, interlayer excitons in our 20° heterobilayer trapped in such potential minima can retain circularly polarized valley optical selection rules, consistent with the high degree of PL polarization observed. The experimental observations of narrow-line emission, circular selection rules, and distinct binary g-factors at a variety of twisting angles are compelling evidence of interlayer excitons trapped in moiré superlattice potential.

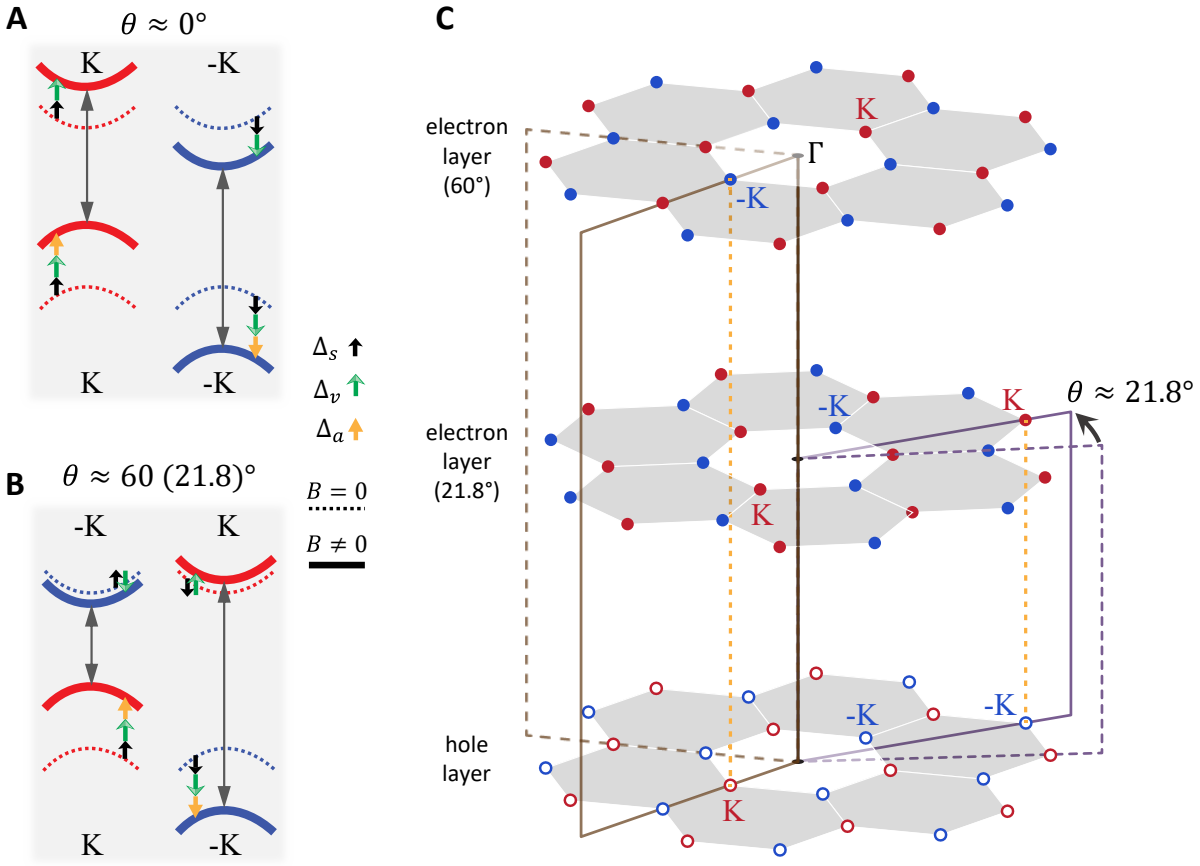

Figure 5.4: Twist-angle-dependent g-factors and Umklapp light coupling of interlayer excitons. (A), (B), Energy level diagram showing the contributions of the interlayer exciton Zeeman shift by the electron spin (Δ_s, in black), valley (Δ_v, in green), and atomic orbital (Δ_a, in orange) for the $MoSe_2/WSe_2$ heterobilayer with twist angle near 0° (A) and 60° (B). (C), Schematic of valley alignments in extended Brillouin zone for a twisted heterobilayer. The open and solid points represent the $+K$ (red) and $-K$ (blue) valleys in the hole and electron layers, respectively. Near 21.8° twist angle, the $\pm K$ and $\mp K$ valleys align in the second Brillouin zone, which has the same valley pairing as the 60 twisted heterolayer and thus the same g-factor. Light coupling at 21.8° is facilitated by an Umklapp-type process.

5.7 Discussion

Finally, we remark on some subtle features in the observed moiré-trapped interlayer excitons. The polarization of PL is determined by local crystal symmetry of moiré potential. Theory shows two high-symmetry points, A and B, in the moiré superlattice8,9. The former has

co-circular optical selection rules, while the latter has circular polarization reversal. Our experiment implies the moiré exciton is located at the B point of the moiré supercell for $\theta = 2°$, and the A point for $\theta = 20°$ and $\theta = 57°$. This also explains why the g-factor we measured was positive for $\theta = 2°$ but negative for $\theta = 20°$ and $\theta = 57°$, because the Zeeman splitting is defined as the energy difference between $\sigma^{\pm}$ PL (Appendix D).

The moiré-trapped interlayer excitons we observe are nonuniform in the number of emitters, their relative intensities, and their energies. We often detect several narrow PL peaks with sub-meV energy separation within the laser excitation spot. The intensities and valley polarization can also vary significantly between the peaks (Fig. D.9). These observations imply that the moiré superlattice potential has some inhomogeneity, which is not surprising because imperfections are expected during fabrication of the moiré superlattice. In fact, fabricating a homogenous moiré pattern by mechanical transfer is an open challenge in the community. On the other hand, different emitters for similar stacking configurations have a common g-factor, which is expected in a moiré potential trap but *not* in other extrinsic traps. As we mentioned, the g-factor of the moiré exciton is a property of the heterobilayer bulk determined by the valley pairing only, which is the same for every local region of a given moiré pattern. Lastly, considering that the energy spacing of several PL lines is on the same order as the repulsive interaction between proximate interlayer excitons, there is a possibility that some of the narrow PL peaks may originate from the cascaded emission of multi-exciton states in a single trap or several neighboring traps. All these possibilities require future studies with improved sample quality and possibly new scanning probe techniques, such as near-field scanning microscopy with sub-10 nm spatial resolution. Nevertheless, our observation of moiré excitons provides a promising starting point to explore several intriguing theoretical proposals related to quantum photonics, such as entangled photon sources, giant spin-orbit coupling [138], topological excitons [138, 171], and much more.

Chapter 6

OPTICAL PROPERTIES OF ATOMICALLY THIN MAGNETIC CRI_3

6.1 Introduction

In this chapter, we explore the fundamental photoexcitations of atomically thin magnetic CrI_3. While it is possible to generate excitonic populations in monolayer and heterostructure TMDs with net magnetic moments via valley-selective optical pumping, the semiconducting TMDs themselves are nonmagnetic. In contrast, CrI_3 intrinsically possesses long-range magnetic ordering and thus it offers a new platform for investigating light-matter interactions and magneto-optical phenomena in 2D materials. As an introduction, we first briefly overview the field of 2D magnetism and the development of isolated van der Waals monolayer magnets. We then discuss prior work on the photophysics of magnetic semiconductors and insulators.

The core of the chapter details our optical spectroscopy experiments on 2D CrI_3 and the nature of its optical response, reprinted from the published study **Kyle L. Seyler**, Ding Zhong, Dahlia R. Klein, Shiyuan Gao, Xiaoou Zhang, Bevin Huang, Efrén Navarro-Moratalla, Li Yang, David H. Cobden, Michael A. McGuire, Wang Yao, Di Xiao, Pablo Jarillo-Herrero and Xiaodong Xu. *Ligand-field helical luminescence in a 2D ferromagnetic insulator*. Nature Physics 14, 277-281 (2018) [172]. We first report spontaneous circularly polarized PL in monolayer CrI_3 under linearly polarized excitation, with helicity determined by the monolayer magnetization direction. In contrast, the bilayer CrI_3 PL exhibits vanishing circular polarization. Our absorption and layer-dependent PL measurements reveal the importance of ligand-field and charge-transfer transitions to the optoelectronic response of atomically thin CrI_3. These are distinct from the Wannier-Mott excitons that dominate the optical response in the 2D semiconductors like WSe_2. We assign the PL to a parity-forbidden *d-d* transition characteristic of Cr^{3+} complexes, which displays a large Stokes shift and broad linewidth due to strong vibronic coupling, as well as thickness-independent peak energy due to its localized molecular orbital nature. These results broaden and enrich the landscape of photo-physical phenomena in atomically thin van der Waals materials.

6.1.1 Atomically thin magnets

Experimental studies of 2D magnetism have a long history, motivated by ideas of low-dimensional phase transitions and critical phenomena. In 1966, Mermin and Wagner proved that long-range magnetic order is not possible at finite temperature in 1D or 2D for an isotropic Heisenberg model [173]. More generally, it is true that for systems with sufficently short-ranged interactions in $d \leq 2$ dimensions, it is impossible to spontaneously break continuous symmetries at finite temperature [174]. For a magnet, the basic idea is that spin waves generated by thermal fluctuations cost very little energy to excite in 1D and 2D isotropic Heisenberg magnets, and therefore long-range magnetic order is destroyed. However, this restriction is overcome by the presence of magnetic anisotropy. We can gain a rough intuition for these results by considering the number of magnon excitations in different dimensions [175]. The magnon excitations reduce the total magnetization, $M(T)$, from its zero temperature value, $M(0)$, by

$$\frac{M(T)}{M(0)} = 1 - \frac{1}{NS}\sum_k n_k, \tag{6.1}$$

where NS is the total spin saturation value and $\sum_k n_k$ is the total number of magnons, using the Bose-Einstein occupation factor of $n_k = 1/[\exp(\hbar\omega/k_BT) - 1]$. The total number of magnons may be written as

$$\sum_k n_k = \int_0^\infty \frac{g(\omega)d\omega}{e^{\hbar\omega/k_BT} - 1}. \tag{6.2}$$

With the magnon dispersion (for small k), $\omega \propto k^n$, the magnon density of states is $g(\omega)d\omega \propto \omega^{(d-n)/n}d\omega$. Using the substitution, $x = \hbar\omega/k_BT$, Eq. 6.1 then becomes

$$\sum_k n_k \propto T^{d/n}\int_0^\infty \frac{x^{(d-n)/n}dx}{e^x - 1}. \tag{6.3}$$

The integral is finite for $d = 3$ and proportional to $T^{3/2}$ but consider the case of a 2D Heisenberg ferromagnet ($n = 2$, $d = 2$), which has a constant the density of states. The

integral

$$\sum_k n_k \propto T \int_0^\infty \frac{dx}{e^x - 1} \tag{6.4}$$

clearly diverges and $M \to 0$ for $T > 0$. However, if there exists anisotropy in the system, it costs additional energy cost to rotate spins from the ground state ordering. A gap will open in the magnon spectrum at $k = 0$, raising the lower limit of integral to a finite value and thus stabilizing 2D ferromagnetism for $T > 0$.

Beginning in the 1960s and 1970s, extensive work was performed to synthesize and probe the magnetic behavior of bulk insulating layered compounds [176]. Because of the weak interlayer exchange interactions in the layered crystals, the magnetic behavior is quasi-2D in nature, so these experiments contributed deeply to our understanding of 2D magnetism, including the effects of anisotropy and different crystal structures [177]. In the late 1980s, the surface scientists started exploring magnetism in metallic films (Fe, Ni, Co) down to the monolayer limit [178–182]. This work drew upon and extended the understanding developed decades earlier. For the first time, for example, they were able to study the dimensionality crossover from 3D to 2D [183, 184]. However, surface science can be a messy business. Reports indicate how the magnetism in thin metallic films is highly sensitive to the substrate, film morphology, and crystallinity [184]. The magnetic properties of nominally identical films often varied significantly between different groups. Consequently, there has been great motivation to realize truly 2D magnetic crystals that do not interact strongly with the substrate, for both fundamental science and spintronic applications.

Fortunately, the 2D materials community has developed the necessary toolset for isolating layered van der Waals crystals to the atomically thin limit. It was realized that the layered magnetic crystals studied several decades ago, with their weak van der Waals interlayer bonding, are potentially excellent candidates to realize truly 2D magnets [185]. In 2017, the first isolated monolayer ferromagnet was experimentally discovered in CrI_3 (Fig. 6.1A). As shown Fig. 6.1B, the polar magneto-optical Kerr rotation, which is proportional to the out-of-plane magnetization, exhibits a clear hysteresis loop as a function of the perpendicular magnetic field. A strong magnetic anisotropy due to Cr−I−Cr 90° superexchange interactions stabilizes an out-of-plane ferromagnetic ordering, leading to the Ising-like hysteresis

behavior [186]. Based on [186], a model Hamiltonian of the CrI_3 spins is

$$H = -\Big(D\sum_i (S_i^z)^2 + \frac{J}{2}\sum_{i,i'} \mathbf{S}_i \cdot \mathbf{S}_{i'} + \frac{\lambda}{2}\sum_{i,i'} S_i^z S_{i'}^z\Big). \tag{6.5}$$

The first term represents the single-ion anisotropy along the easy axis ($D > 0$ for out-of-plane eaxy axis), the second term is the isotropic Heisenberg exchange term ($J > 0$ for ferromagnetic), and third term is the anisotropic symmetric exchange (λ relates to the spin-orbit coupling strength of iodine). Calculations show that $J > \lambda \gg D$, so the last term (superexchange) dominates the anisotropy energy, which means the XXZ model is an appropriate description. The Curie temperature (T_C) for monolayer is $\sim$45 K, only slightly lower than the bulk value of 61 K [185], which reinforces the weak interlayer coupling and minimal substrate influence. Fascinatingly, however, the interlayer exchange interaction was discovered to be weakly antiferromagnetic, so bilayer CrI_3 shows no net magnetization at zero magnetic field (Fig. 6.1B, bottom). At $\sim \pm 0.7$ T, the bilayer undergoes a metamagnetic transition to a fully spin-polarized state. These results highlight the layer-dependent properties characteristic of 2D materials and unlock interesting possibilities for exploring the detailed magnetic behavior of isolated 2D crystals. Furthermore, exciting opportunities are available to create van der Waals magnetic heterostructures, as we will demonstrate in Chapter 7.

We briefly mention that, in addition to CrI_3, researchers are actively exploring several other 2D magnets, including $FePS_3$ [188], $Cr_2Ge_2Te_6$ [189], Fe_3GeTe_2 [190, 191], VSe_2 [192], and MnSe [193], which exhibit a diversity of magnetic orderings and electronic structures. The 2D magnet playing field is certain to vastly expand in the coming years.

6.1.2 Photoexcitations in magnetic semiconductors and insulators

The exploration of magnetism in non-metallic bulk materials (e.g. magnetite) is as old as civilization, but it was not until the early to mid-1900s that scientists began to systematically characterize their properties. Studies examined the intrinsic ferromagnetic ordering of a variety of insulating and semiconducting materials, including for example, the ferrites and ferrospinels [194], Cr trihalides [195], Eu chalcogenides [196], and Cr spinels [197]. Later, with the introduction of magnetic dopants into nonmagnetic II-VI and III-V semiconductors, diluted magnetic semiconductors captured widespread attention [198], boosted by the discovery of ferromagnetism in Mn-doped InAs [199] and GaAs [200] in the 1990s. Central to progress in these fields, optical experiments have led to a deep understanding of elec-

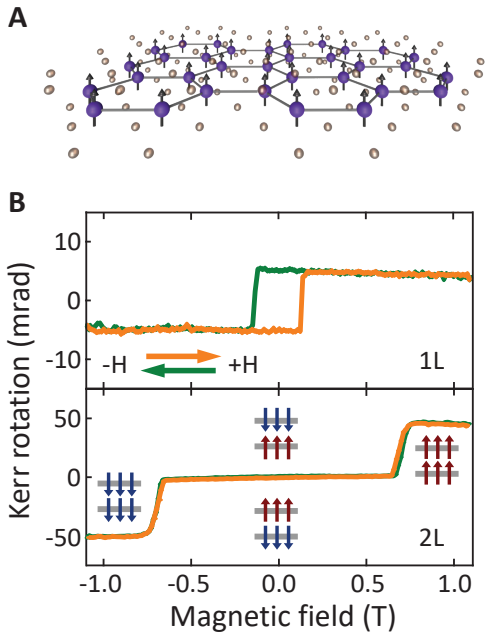

Figure 6.1: Magnetism in atomically thin CrI_3. (A) Crystal structure of CrI_3 magnetic monolayer. (B) Magneto-optical Kerr rotation as a function of applied magnetic field ($\mu_0 H$) for monolayer (top) and bilayer CrI_3. [Panel B adapted from [187].]

tronic structure, magnetization dynamics, and interactions between magnetism and light [196, 201–203]. While the fascinating physics in the quantum structures of diluted magnetic semiconductors has propelled spintronics research over the last few decades [204], there has been a comparative lack of non-metallic nanoscale materials hosting intrinsic magnetism. The recent arrival of monolayer magnetic insulators, such as CrI_3, now enables the study of novel 2D photo-physical phenomena and the interplay with underlying magnetic order.

Historically, the bulk chromium trihalides were found to behave as Mott insulators with an optical response governed by ligand-field and charge-transfer transitions, which are highly localized photo-excitations between molecular orbitals [201, 205–217]. Therefore, atomically thin chromium trihalides provide a new platform from which to study 2D optical physics under the influence of intrinsic magnetic ordering. In this chapter, we demonstrate magnetization-determined ligand-field transitions in 2D magnetic CrI_3 by magneto-PL and reflection spectroscopy. We will draw upon and further acknowledge this important foundational work as we describe our results in the following sections.

6.2 Experimental methods

Bulk CrI_3 crystals were grown by chemical vapor transport, as described in detail in [187] and [185]. Monolayer and bilayer CrI_3 samples were then obtained by mechanical exfoliation from bulk CrI_3 onto a 0.5 mm-thick *c*-plane sapphire substrate in an Ar-filled glovebox [218]. We also fabricated and measured samples on 285 nm SiO_2/Si (Fig. E.1 and Fig. 6.4D). We confirmed the optical contrast of bilayer CrI_3 on sapphire by transferring a bilayer from 285 nm SiO_2/Si (on which the optical contrast has been established2) to sapphire. Thus, we determined the optical contrast on sapphire to be ∼0.035 and ∼0.07 at 631 nm for monolayer and bilayer CrI_3, respectively. Samples were kept under inert atmosphere or vacuum during the entire fabrication and measurement process.

Low-temperature optical measurements were performed in a closed-cycle cryostat (Montana Instruments Cryostation) with a superconducting magnet with the axis directed out of the sample plane. For the PL measurements, the sample was excited by a HeNe laser (632.8 nm) focused to a ∼1 µm spot diameter. A low power of 10 µW was used to avoid sample heating and degradation. A dichroic beam splitter reflected the collected PL, which was then spatially filtered through a confocal pinhole (to avoid collecting nearby bulk CrI_3 PL), dispersed by a 1.2 µm blaze grating, and detected by a liquid-nitrogen-cooled InGaAs linear photodiode array (Princeton Instruments). The InGaAs detector was spectrally calibrated using Hg emission lines. The excitation and detection polarization were controlled using linear polarizers and achromatic near-infrared half- and quarter-wave plates. Peak intensities were calculated by averaging 100 points (∼30 meV) about the peak center.

For the white light differential reflection measurements, we spatially filtered a tungsten halogen lamp through a pinhole and focused the beam to a ∼3 µm spot size on the CrI_3. The reflected light was deflected with a beam splitter and detected by a spectrometer and Si CCD or InGaAs array, which enabled measurements from 1 eV to 3 eV. To obtain the differential reflectance, we subtracted and normalized the CrI_3 reflectance by the reflectance of the bare sapphire substrate. The $^4T_2$ absorbance was determined as [219]

$$\frac{1}{4}(n^2-1)\frac{\Delta R}{R}, \tag{6.6}$$

where $n \approx 1.76$ is the ordinary refractive index of sapphire at 1.5 eV [220].

6.3 *Magnetization-controlled PL in monolayer and bilayer CrI_3*

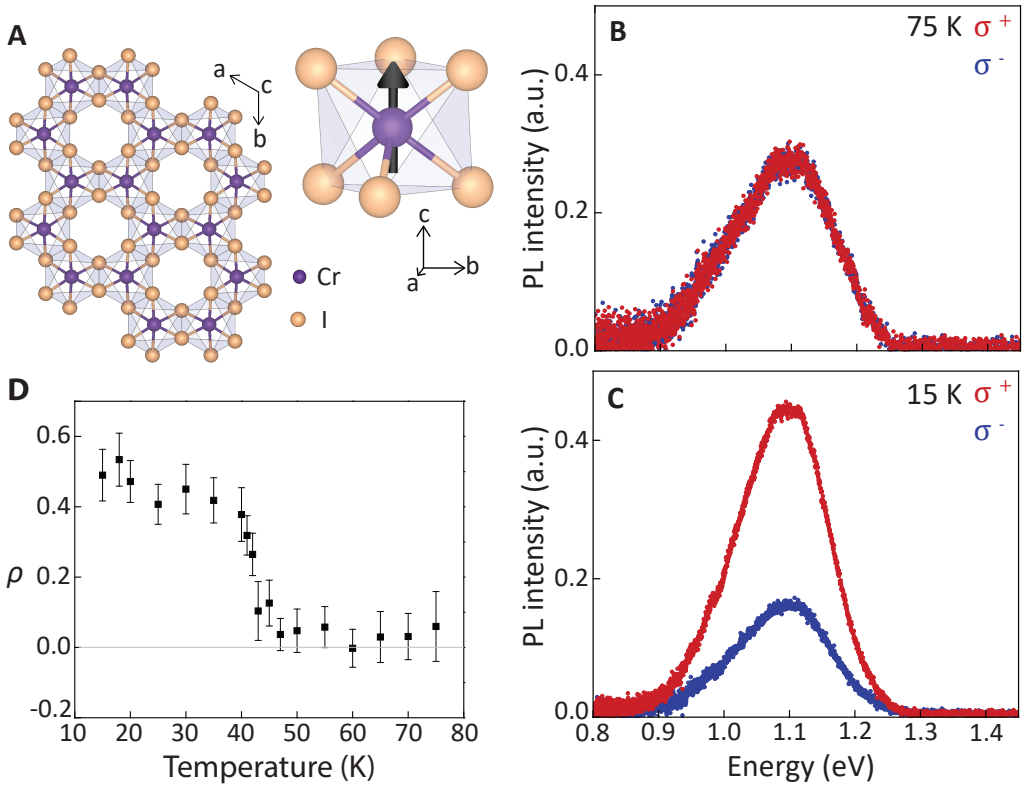

Figure 6.2: Spontaneous circularly polarized luminescence from monolayer CrI_3. (A) Top view of the crystal structure of CrI_3 (left) and side view (right) depicting single Cr site with an arrow representing its out-of-plane magnetic moment. (B) Photoluminescence (PL) spectrum for σ^+ (red) and σ^- (blue) circularly polarized PL from a monolayer at 75 K. The excitation is linearly polarized. (C) Same as fig. B, but at 15 K. (D) Temperature dependence of the degree of PL circular polarization (η) at 0 T from 75 K to 15 K. Error bars show the standard deviation of the polarization at the peak. No external magnetic field was applied while acquiring the data in this figure. [Adapted from [172].]

We first measured the monolayer CrI_3 PL at 75 K, above the Curie temperature (T_C) of 45 K [187], without applying magnetic field. As shown in Fig. 6.2B, there is a single broad emission feature centered at ∼1.1 eV with a full-width at half-maximum of about 180 meV. We observed no other PL features at higher energy. The red and blue spectra correspond to σ^+ and σ^- circularly polarized PL, respectively. The two components are indistinguishable, which is consistent with the absence of magnetic order above T_C.

Remarkably, upon cooling to 15 K (well below T_C) in the absence of a magnetic field, we observe that the σ^+ and σ^- PL diverge in intensity, with σ^+ much brighter than σ^- (Fig. 6.2C). Using our definition of the PL circular polarization, $\eta = (I_+ - I_-)/(I_+ + I_-)$, where I is the peak intensity of $\sigma^\pm$ PL, we find $\eta \approx 0.45$. Since the linearly polarized excitation does not break the time-reversal symmetry of the system, the observation of net circular emission demonstrates the appearance of spontaneous out-of-plane magnetic ordering in monolayer CrI_3. While the peak narrows slightly (∼10 %) on cooling from 75 K to 15 K, its position does not change. Any energy splitting between the two polarizations is smaller than ∼1 meV and unresolvable. The temperature dependence of η is shown in Fig. 6.2D. The onset of finite η at 45 K is consistent with T_C for a monolayer [187].

We next explore the effect of an applied out-of-plane magnetic field. Figure 6.3A shows the circularly polarized PL spectra at 0.5 T. Here the polarization is reversed relative to that shown in Fig. 6.2C (which was taken at zero field), due to a flip in the magnetization by the applied field. If the field is then lowered to 0 T, the spectra remain unchanged (Fig. 6.3V). When the opposite field, −0.5 T, is then applied, the magnetization is reversed again and the PL returns to its original state with a stronger σ^+ component than σ^-. This state is in turn preserved when the field is returned to zero (Fig. 6.3C, D). Additional data demonstrating this behavior for a monolayer on a SiO_2/Si substrate is presented in Fig. E.1. We show η over a cycle of the magnetic field in Fig. 6.3E, where the observed hysteresis loop is clearly the hallmark of ferromagnetic behavior. The saturation polarization is ±0.5, and the coercive field is ∼55 mT. Both circular polarization components show linear power dependence (Fig. E.1), leading to a power-independent η.

The field-dependent measurements unambiguously demonstrate that the helicity of the CrI_3 PL is determined by its magnetic ordering, and thus that measurement of PL helicity can be used as a simple probe of its magnetic phases. Figures 6.4A-C present the circular polarization-resolved PL from a bilayer of CrI_3 at 15 K, at magnetic fields 1 T, 0 T and −1 T respectively. We see strong circularly polarized PL at ±1 T (Figs. 6.4A, C), consistent with full spin polarization in bilayer CrI_3 at such high fields. In contrast with the monolayer, no net circular polarization is seen at zero field (Fig. 6.4B), which implies vanishing net out-of-plane magnetization. As shown in Fig. 6.4D, the polarization η is negligible between ±0.65 T and jumps abruptly to a value of −0.5 above 0.65 T and 0.5 below −0.65 T. This magnetic-field-dependent PL polarization forms a close parallel to the MOKE response in [187], which also vanishes in the same field range. The consistency of the results for these

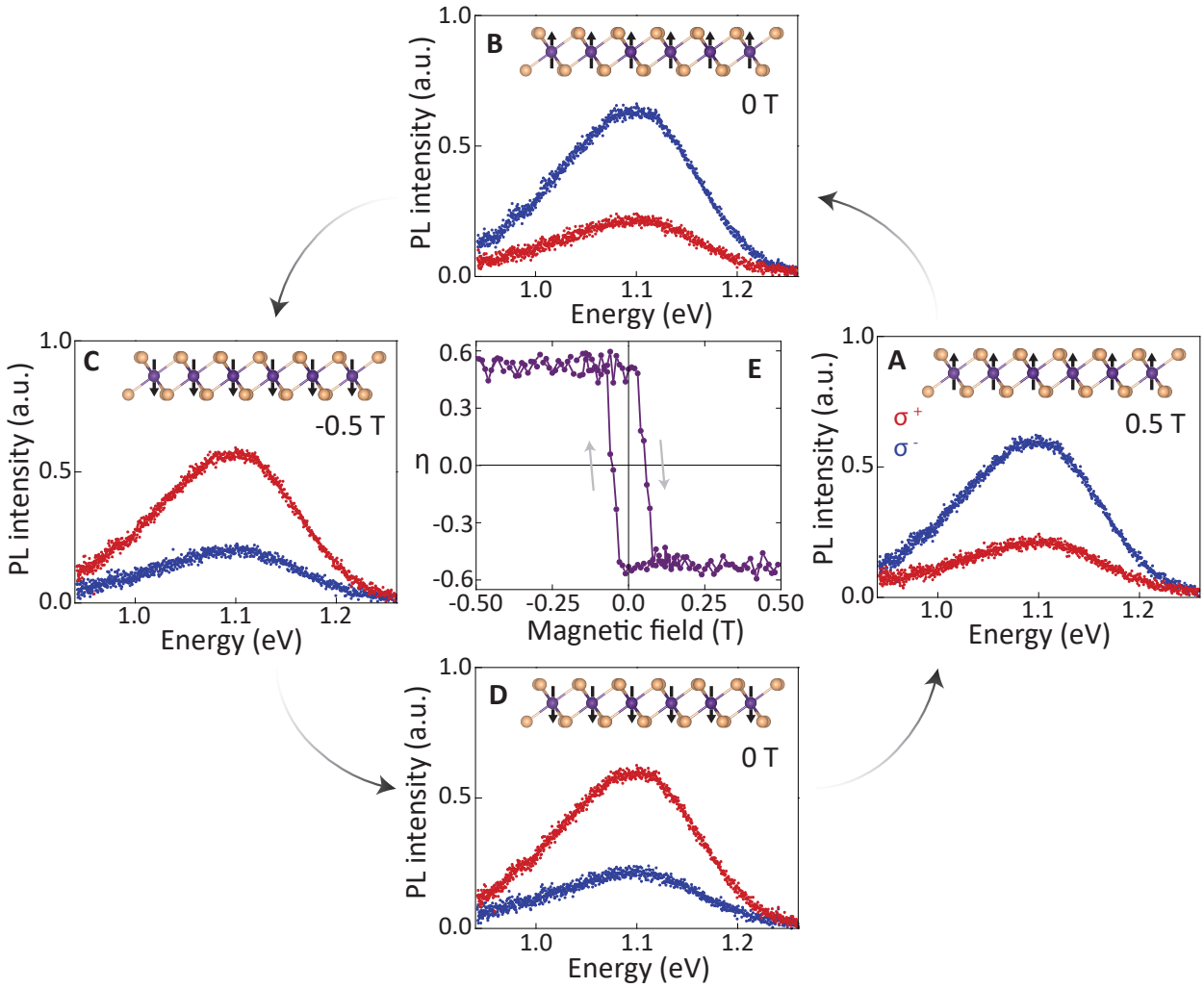

Figure 6.3: PL from monolayer CrI_3 in an applied magnetic field. Sequence of PL spectra for σ^+ (red) and σ^- (blue) circular polarization components, acquired at 15 K under linearly polarized excitation. (A) 0.5 T (increasing from 0 T), (B) 0 T (decreasing from 0.5 T), (C) −0.5 T (decreasing from 0 T), and (D) 0 T (increasing from −0.5 T). The curved arrows indicate the magnetic field sweep direction, and the insets depict the magnetization direction relative to the lattice. (E) Circular polarization (η) as a function of applied field over one full cycle. Gray arrows show the sweep direction of the applied field. [Adapted from [172].]

two distinct experimental probes reinforces the interpretation that at low fields, bilayer CrI_3 consists of two ferromagnetic monolayers that are antiferromagnetically coupled.

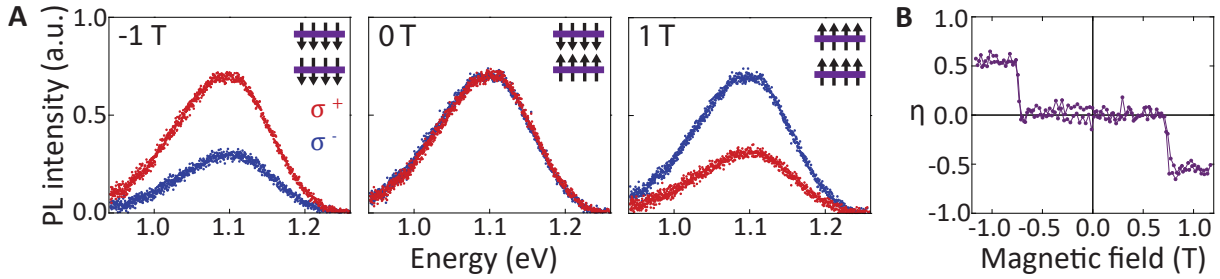

Figure 6.4: Bilayer CrI_3 PL reveals antiferromagnetic ground state. PL spectrum of a bilayer sample for σ^+ (red) and σ^- (blue) circular polarization and linearly polarized excitation acquired at 15 K at magnetic fields of -1 T, 0 T (B), and 1 T (C). The inset figures depict the inferred magnetization pattern of the bilayer. It should be noted that at 0 T the net magnetization is zero, but the exact spin orientation within each layer is unknown. (D) Circular polarization (η) as a function of magnetic field. Data points for increasing and decreasing magnetic field overlap to within uncertainty. The data in A-C are from a bilayer on sapphire while the data in D are from a bilayer on SiO_2. Their behavior is consistent. [Adapted from [172].]

6.4 Ligand-field theory for CrI_3

What is the origin of luminescence in atomically thin CrI_3? In well-studied 2D semiconductors, such as WSe_2, the photo-response can be described by band-to-band transitions with strong excitonic effects [221, 222]. Tightly bound Wannier-Mott excitons dominate the optical spectrum. In CrI_3, however, the $3d$ electrons are much more spatially localized, and thus to understand the optical response, a molecular orbital approach is more suitable. In fact, ligand field theory, which predicts intra-atomic d-d transitions and higher energy charge-transfer transitions within metal-ligand complexes [217], has previously been used to interpret the optical spectra of bulk transition metal halides [201, 205–216, 223, 224].

Fig. 6.5A shows a molecular orbital energy diagram for CrI_3, which shows the influence of the iodine octahedral ligand field on the 3 d electrons in Cr^{3+} [205, 208]. The bonding and non-bonding orbitals from $a_{1g}(\sigma^b)$ through $t_{1g}(\pi)$ are completely filled by the iodine electrons, leaving 3 spin-aligned electrons from Cr to occupy the $t_{2g}(\pi^*)$ level. The exchange interactions between these unpaired electrons on neighboring Cr sites gives rise to the ferromagnetic intralayer order and lead to a net magnetic moment of $\sim 3.1\mu_B$/Cr [185]. Even though $t_{2g}(\pi^*)$ is partially filled, CrI_3 forms an energy gap and becomes a Mott insulator due to the strong on-site repulsion [225]. Under optical excitation, it is possible to excite

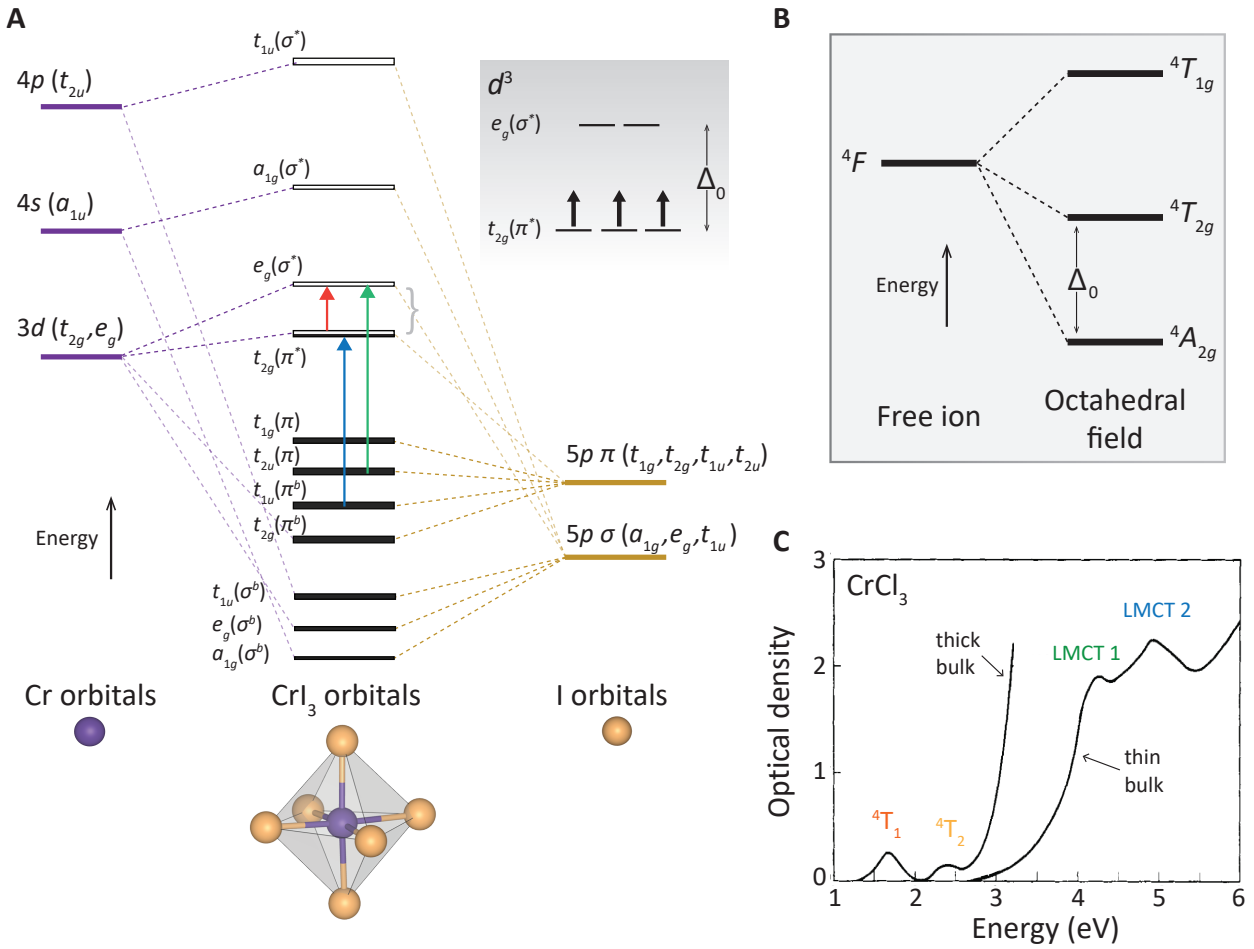

Figure 6.5: CrX_3 energy levels. (A) Molecular orbital energy diagram for CrI_3. The "b" superscripts and asterisks denote the bonding and anti-bonding orbitals, respectively. The orbitals from $a_{1g}(\sigma^b)$ through $t_{1g}(\pi)$ are completely filled by the iodine electrons. Three spin-aligned electrons occupy $t_{2g}(\pi^*)$ in the ground state (see inset diagram - ligand-field splitting Δ_0 is given by difference between $t_{2g}(\pi^*)$ and $e_g(\sigma^*)$). The effect of spin-orbit coupling is not included and the relative energy spacings are not quantitative. The red arrow shows a d-d transition. The green and blue arrows show two of the possible LMCT transitions, as noted in [223, 224]. Note that the transition to the $t_{2g}(\pi^*)$ involves an promotion of an electron with spin anti-parallel to the d^3 electrons. (B) Splitting of the free-ion term ^4F into its octahedral irreducible representations. (C) Example absorption spectrum for $CrCl_3$ showing the ligand-field (d-d) and ligand-to-metal charge transfer (LMCT) transitions. [Panel C adapted with permission from [209].]

electrons between the $t_{2g}(\pi^*)$ and $e_g(\sigma^*)$. These are known as ligand-field or d-d transitions,

as they have strong intra-atomic character.

To describe the optical excitations, we consider the symmetry of the full electronic configurations in the ground and excited states [226]. The available energy states are determined by the effect of octahedral symmetry reduction on the free-ion terms. For electron configurations in CrI_3 in the $t_{2g}(\pi^*)$ and $e_g(\sigma^*)$ levels with 3 electrons (see inset in Fig. 6.5A for ground state), the ^4F free-ion ground state splits into three levels, given by their irreducible representations: the $^4A_{2g}$ ground state, and the $^4T_{2g}$ and $^4T_{1g}$ excited state configurations (Fig. 6.5B, 4 is the spin multiplicity). Therefore, optical excitations are allowed between $^4A_{2g}$ to $^4T_{2g}$ or $^4T_{1g}$. Due to the octahedral symmetry, the configurations each have even parity (g subscript) and the d-d transitions are thus electric-dipole forbidden by the Laporte parity selection rule. However, as we will see, both lattice vibrations and the reduced crystal symmetry of the lattice can enable the transitions, making them weakly allowed. Because of this, we will leave off the parity subscript "g" in future references to these electron configurations.

It is also possible to photoexcite electrons from the iodine character bonding orbitals into the unoccupied Cr antibonding ordbitals (two possibilites are shown in Fig. 6.5A). These are known as ligand-to-metal charge transfer (LMCT) transitions, are parity-allowed, and thus they have much higher oscillator strength [226]. This picture will give a qualitative understanding of the different electronic transitions, but we emphasize that other important effects, such as spin-orbit coupling, Jahn-Teller distortions, and the Zeeman field, should be considered in future first-principles calculations for a fuller understanding [217].

While prior studies have focused on absorption/reflection in $CrCl_3$ (see Fig. 6.5C for an example spectrum from 1970 [209]) and $CrBr_3$, there are few reports on the optical properties of CrI_3 [201, 208, 227], and none examining the PL. Furthermore, all previous work was limited to bulk crystals containing thousands of layers. In the following section, we present evidence that these intrinsic localized photo-excitations dominate in 2D CrI_3.

6.5 Origin of PL and absorption

We first reiterate that the monolayer PL intensity is linear in excitation power, as illustrated in Fig. E.1. Taken together with the tight link between the PL helicity and layer-dependent magnetic phases, this rules out the possibility that the dominant PL contribution is from defect-bound excitons, which tend towards saturation at higher excitation intensity and are often seen in the low-energy PL spectra of other 2D semiconductors. To investigate the electronic response more broadly, we measured the differential reflectance of monolayer CrI_3

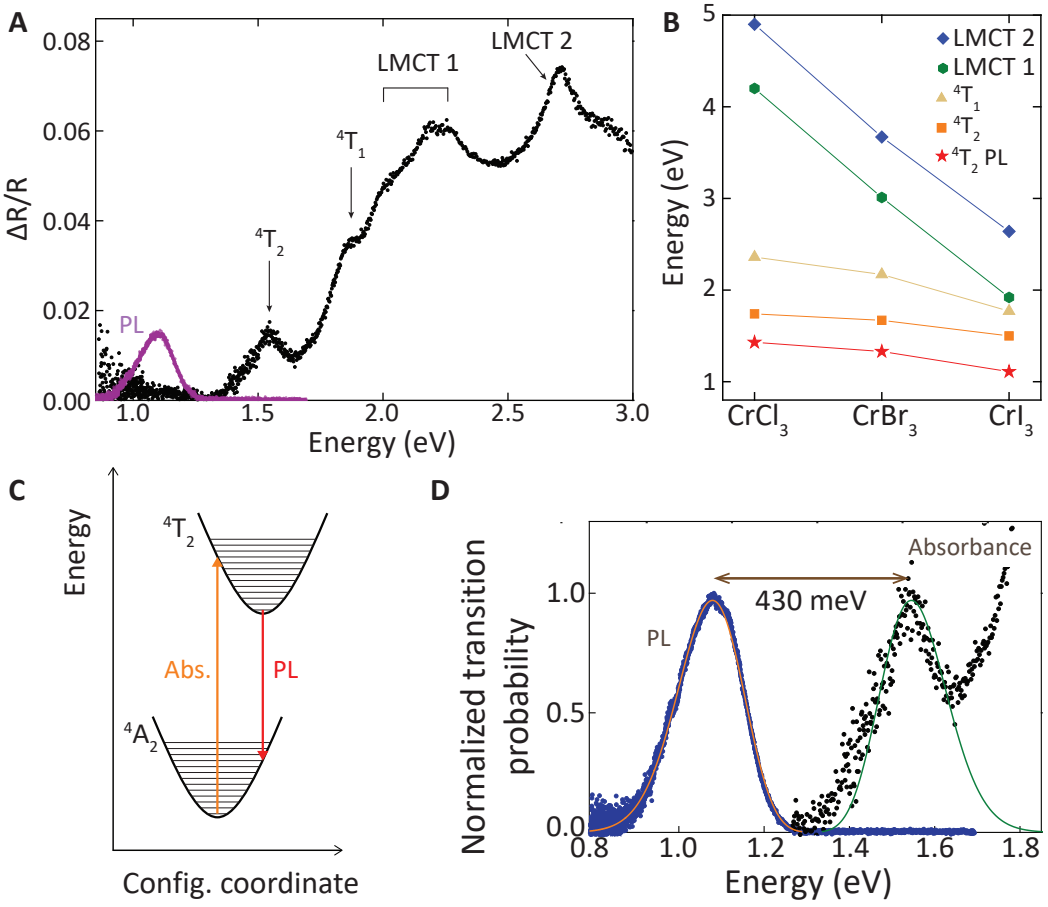

Figure 6.6: CrI_3 reflection and peak assigments. (A) Differential reflection spectrum of monolayer CrI_3 (black) and overlaid PL spectrum (purple). See text for discussion of labelled peak assignments. (B) Energies of the corresponding peaks in bulk $CrCl_3$, $CrBr_3$, and CrI_3. The CrI_3 data are from the sample in Fig. E.3, while the data for $CrBr_3$ and $CrCl_3$ are compiled from Refs. [201, 208, 209, 212]. (C) Stokes shift of monolayer CrI_3. (D) Configurational coordinate diagram in the harmonic approximation for the observed ligand-field $^4T_2$ absorption and PL. The horizontal lines represent vibrational levels. The calculated Huang-Rhys factor is ∼10. [Adapted from [172].]

on sapphire (Fig. 6.6A), which is proportional to its absorbance. There is a weak peak near 1.5 eV along with stronger features around 2 eV and 2.7 eV. Using the ligand-field framework, we can attribute the 2.7 eV peak as well as the strongest two peaks near 2 eV to dipole-allowed LMCT transitions between the iodine $5p$ orbitals and Cr^{3+} $3d$ orbitals. The 1.5 eV transition has not been discussed much before in the literature. As described in the previous section,

the approximate octahedral symmetry of the iodine ligands around each Cr^{3+} site splits the d^3 configuration (^4F term) into $^4A_2$ ground state and $^4T_2$ and $^4A_1$ excited states. We assign the 1.5 eV peak to the lowest energy transition between these levels, from $^4A_2$ to $^4T_2$. Despite being electric-dipole forbidden by the parity selection rule, *d-d* transitions can become weakly allowed by mixing with odd parity states, such as produced by phonons. In addition, the trigonal field of the nearest-neighbor Cr atoms (Fig. 6.2A) eliminates the local inversion symmetry of each Cr site, providing a static odd-parity field to allow the *d-d* transitions. We deduce that the absorbance of the $^4T_2$ transition is about 0.7 % for monolayer CrI_3 (see Methods), which is an order of magnitude lower than the absorbance for the A and B excitonic resonances in monolayer semiconducting transition metal dichalcogenides, such as MoS_2. The weak absorption underscores the weakly allowed parity-forbidden nature of the *d-d* transition.

Our assignment of the reflection features is consistent with the results of prior experiments and recent calculations on bulk $CrCl_3$ and $CrBr_3$ [223, 224]. To connect these with CrI_3, in Fig. 6.6B, we plot the absorption peak energies of bulk CrI_3 that we measured (Fig. E.3) against those of $CrCl_3$ (see e.g. Fig. 6.5C) and $CrBr_3$ from previous studies [201, 208, 209, 212]. The relationship between the optical spectra of the Cr trihalides then becomes clear. The large energetic shift of the two high-energy peaks between different ligand species confirms their charge transfer origin. On the other hand, the *d-d* transitions exhibit weaker dependence on the ligand. Interestingly, in view of the decreased ligand-field strength of I^- in CrI_3, we expect the lowest LMCT transition to overlap the highest *d-d* transition ($^4A_2$ to $^4T_1$). This suggests that the origin of the low-energy shoulder at 1.8 eV is absorption to the $^4T_1$ level, enhanced by its energetic proximity to the strong charge transfer transitions near 2 eV. Thus, it is likely that both LMCT and *d-d* transitions play a role in the recently observed magneto-optical Kerr response [187] near 2 eV in few-layer CrI_3.

We can now begin to understand the origin of PL in atomically thin CrI_3. The clear correlation between the three Cr trihalide compounds in the energies of the lowest absorption peak and PL (Fig. 6.6A) implies that the monolayer CrI_3 PL arises from the $^4T_2$ to $^4A_2$ *d-d* transition. The ∼430 meV Stokes shift between the PL and 1.5 eV reflection peak is a consequence of the Franck-Condon principle and strong electron-lattice coupling. In Fig. 6.6C, we display a fit to the low-temperature monolayer PL spectrum based on the simple, single configurational coordinate model in the harmonic approximation (Fig. 6.6D) and Franck-Condon principle [226]. The emission at energy E can be approximated by the

following:

$$I(E) = \frac{e^{-S}S^p}{p!}\left(1 + S^2\frac{e^{-\hbar\omega/kT}}{p+1}\right), p = \frac{E_0 - E}{\hbar\omega}. \tag{6.7}$$

Here, S is the Huang-Rhys parameter, $\hbar\omega$ is the effective phonon energy involved in the emission process, k is the Boltzmann constant, T is the temperature, and E_0 is the energy of the zero-phonon line. The measured PL and absorbance are first converted to the transition probability by dividing by a factor of E^3 and E respectively [226]. Using $T = 15\,\mathrm{K}$ and $E_0 = 1.312\,\mathrm{eV}$ in Eq. 6.7, we achieve a good fit to the PL spectrum (Fig. 6.6C) with $S \approx 10$ and $\hbar\omega \approx 24\,\mathrm{meV}$. The asymmetry and linewidth of the PL spectrum are captured well in this simple model. Because the tail of the 2 eV absorption features overlaps with the weak 1.53 eV peak, a careful fit of the absorption is not possible. However, if we plot the corresponding absorption line shape using the same parameters found from the PL fit, we find reasonable overlap with the experimental peak. The similarity between the PL and absorption shapes is further evidence of the shared origin of these optical transitions, namely between the $^4A_2$ ground and $^4T_2$ excited state configurations. A large Stokes shift is reasonable for the $^4T_2$ transition in Cr^{3+} octahedral complexes [226, 228]. In crystals with $CrCl_6^{3-}$ and $CrBr_6^{3-}$ complexes, Huang-Rhys parameters of 3.6 and 6.7, respectively, have been reported [228]. Since larger metal-ligand distance typically increases the Huang-Rhys parameter, we expect a high Huang-Rhys parameter in CrI_3 due to the comparatively large Cr-I bond lengths [229].

The extracted ~1.3 eV $^4T_2$ zero-phonon energy corresponds to the ligand-field splitting. This energy is determined by the relative strength of σ and π bonding for Cr-I and can be estimated as

$$\Delta_0 = 3e_\sigma - 4e_\pi, \tag{6.8}$$

where e_σ and e_π are the angular overlap model parameters for σ and π bonding [217]. For Cr-I bonds in an octahedral geometry [230], $e_\sigma = 4100\,\mathrm{cm}^{-1}$ and $e_\pi = 670\,\mathrm{cm}^{-1}$, which gives a ligand-field splitting of ~1.2 eV. The good agreement lends further evidence to the assignment of PL and absorption to the $^4T_2$ state.

The *d-d* transitions become allowed by mixing with odd parity states. For O_h symmetry, the phonon modes that can enable the *d-d* transitions are t_{1u} and t_{2u}. The even parity a_{1g}, e_g, and t_{2g} modes may then contribute to the broadening and structure of the bands [228].

This strong vibronic mixing precludes the formation of well-resolved phonon sidebands in the spectra. In the Cr trihalides, the trigonal (D_3) arrangement of nearest neighbor chromium atoms distorts the octahedral field and thus provide an additional static mechanism through which to intensify the *d*-*d* transitions, which is similar to what has been suggested for $CrCl_3$ and $CrBr_3$ [209, 212]. Future experiments and calculations will be needed to elucidate the details of the phonon modes and intensities, as well as other potentially relevant phenomena, such as excited state Jahn-Teller distortions, spin-orbit coupling, and impurity or substrate broadening.

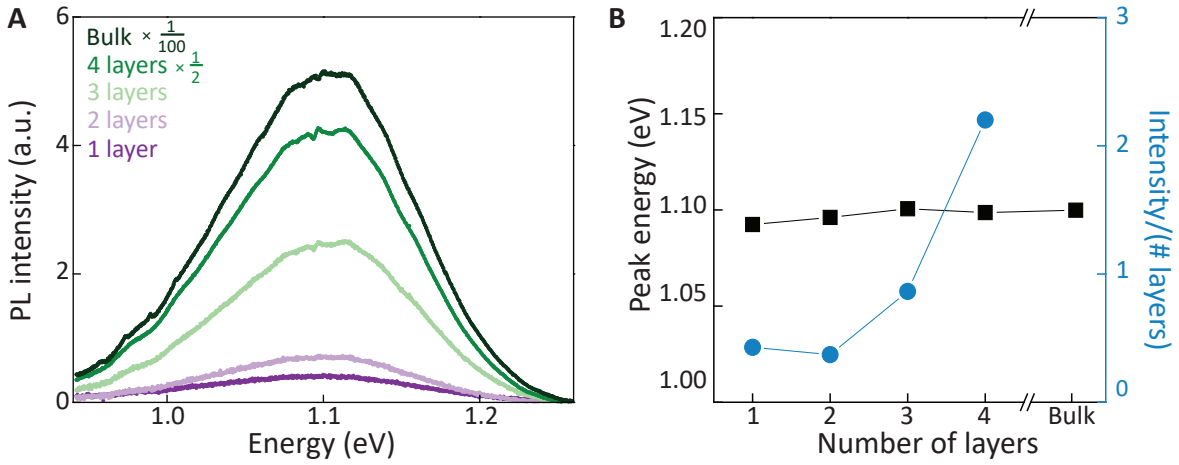

Figure 6.7: Thickness-dependent CrI_3 PL. (A) Layer dependence of the PL spectra at 15 K and zero magnetic field. Note that the 4-layer-thick and bulk spectra have been divided by a factor of 2 and 100 respectively. The small features near 1.08 eV are due to a slight artefact of the grating which could not be corrected. (B) Peak energy (black) and PL intensity normalized by number of layers (blue) for different thicknesses. The peak energy is calculated by weighted average. [Adapted from [172].]

Finally, we performed a layer-dependent PL study, as displayed in Fig. 6.7A, which demonstrates that the PL peak energy is independent of the thickness of CrI_3. The result highlights the localized nature of the ligand-field excitation, whose energy is not significantly affected by neighboring layers. However, because the *d*-*d* transition is parity-forbidden, the observed PL intensity will sensitively depend on the origins of local symmetry breaking, such as from odd-parity phonons and trigonal distortion, and on the interactions with excited states, spin-orbit coupling, and substrate disorder. In fact, we observe that the PL intensity per layer (i.e. normalized by the number of layers) increases with increasing thick-

ness (Fig. 6.7B), suggesting that the *d*-*d* relaxation processes may be affected by interlayer or substrate interactions. Determining the strengths of these interactions will be essential for understanding not only the layer-dependence, but also the relative intensity of the PL helicities observed when CrI_3 is ferromagnetically ordered.

6.6 Conclusions

The above measurements establish the prominence of highly localized optical excitations in atomically thin CrI_3. While transport measurements will be necessary to confirm its electrical properties, mono- and few-layer CrI_3 are likely to be relatively good insulators, judging from the localized optical response and the large bulk resistivity. The ligand-field luminescence helicity displays clear signatures of the underlying magnetic order, suggesting that the optical spectra will serve as an important probe of magnetic order in atomically thin CrI_3. Our results enlarge the landscape of light-matter interactions in 2D materials, and suggest new opportunities to study and control ligand-field spectra in the 2D limit in the presence of magnetic ordering. Further magneto-optical studies on the thickness and polarization dependence of the charge-transfer and ligand-field transitions may shed light on the nature of the intralayer and interlayer exchange interactions. Beyond this, our work previews exciting possibilities to use CrI_3 as an atomically thin magnetic insulator in van der Waals heterostructures. Complementary to the popular non-magnetic layered insulator hexagonal boron nitride, 2D CrI_3 will serve as a substrate, interfacial layer, and tunnel barrier for engineering magnetic proximity effects, exploring spin-dependent tunneling phenomena and designing novel magneto-optoelectronic devices with spontaneous helical light emission.

Chapter 7

VALLEYTRONICS IN WSE_2/CRI_3 MAGNETIC SEMICONDUCTOR HETEROSTRUCTURES

7.1 Introduction

In this chapter, we investigate CrI_3/WSe_2 heterostructures, drawing upon much of our knowledge of the exciton, valley, and 2D magnet physics from prior chapters. We begin by overviewing previous efforts to externally manipulate the valley physics in monolayer TMDs, which is a central goal of valleytronics. We then briefly survey prior work on magnetic heterostructures and propose their van der Waals analogs as a powerful system for spin- and valleytronics. As we will show, CrI_3 and WSe_2 are very well-suited to one another, since the out-of-plane valley-contrasting magnetic moments of WSe_2 can couple to the strong out-of-plane magnetic order in CrI_3.

The experiments presented in the body of this chapter are reprinted from the published study, Ding Zhong*, **Kyle L. Seyler***, Xiayu Linpeng, Ran Cheng, Nikhil Sivadas, Bevin Huang, Emma Schmidgall, Takashi Taniguchi, Kenji Watanabe, Michael A. McGuire, Wang Yao, Di Xiao, Kai-Mei C. Fu, Xiaodong Xu. *Van der Waals engineering of ferromagnetic semiconductor heterostructures for spin and valleytronics.* Science Advances 3, e1603113 (2017) [50]. Our experimental results establish unprecedented control of the spin-valley physics in WSe_2 via interfacial coupling with CrI_3. We detected a large magnetic exchange field of nearly 13 T and rapid switching of the WSe_2 valley splitting and polarization via flipping of the CrI_3 magnetization. We also demonstrate that the WSe_2 PL intensity strongly depends on the relative alignment between photo-excited spins in WSe_2 and the CrI_3 magnetization, due to ultrafast spin-dependent charge hopping across the heterostructure interface. The PL detection of valley pseudospin provides a simple and sensitive method to probe the intriguing domain dynamics in the ultrathin magnet. As an extension of this work, we show that the opticaσ^- excitation power can impact the interfacial CrI_3 magnetic order and the resulting magnetic proximity effect with WSe_2. This reveals a convenient new path towards optical control of valley pseudospins and van der Waals magnetic heterostructures.

7.1.1 Control of valley physics in monolayer TMDs

As we have seen from the previous chapters, the field of valleytronics has flourished with the study of atomically thin transition metal dichalcogenide semiconductors such as WSe_2. Valley pseudospin is straightforwardly initialized in exciton population and free carrier populations through circularly polarized optical pumping and read out through PL or Kerr rotation spectroscopies. For valleytronics to succeed practically, however, one must be able to manipulate valley pseudospin states. Lifting the valley energy degeneracy through time-reversal symmetry breaking is vital for valley control. For example, the exciton valley splitting, polarization, and coherence are tunable via the Zeeman effect with high magnetic fields [40, 51–55] (see also Chapter 5 for interlayer exciton Zeeman splitting). In addition, in the valley optical Stark effect, intense circularly polarized optical pulses can coherently break the valley degeneracy [231, 232] and manipulate the phase relation of a valley superposition state [233]. These effective magnetic fields are likely essential for valleytronic devices as well as proposed topological effects unique to monolayer valley semiconductors [171]. However, sweeping large magnetic fields is impractical for devices, and the pseudo-magnetic fields of the valley Stark effect are only effective in the presence of high intensity, ultrafast laser pulses. As we will see in this chapter, the emergence of 2D van der Waals magnetic materials expands and enhances the possibilities for valley manipulation via heterostructure engineering.

7.1.2 Magnetic heterostructures

Manipulating exchange interactions in magnetic heterostructures has proven to be an effective way to engineer highly functional materials. For example, control of the interlayer exchange coupling [234] and exchange bias [235] has enabled widely used magnetic storage technologies such as giant magnetoresistance [236, 237] and magnetic tunnel junctions [238]. Currently, there is an intense focus to expand the class of functional materials that can utilize magnetism via proximity exchange effects. Heterostructures of magnetic material integrated with superconductors [239], topological insulators [240, 241], and semiconductors [242] have been proposed and investigated. The integration of magnetic material with semiconductors has been particularly fertile ground for fundamental science as well as of great practical interest toward the seamless integration of information processing and storage [243, 244]. For example, exchange interactions between the ferromagnet spins and semiconductor charge carriers lead to a tunable spin polarization [245–248].

The use of 2D materials to form magnetic heterostructures has the advantage that the

proximity-induced exchange interaction, usually considered as a perturbative effect for bulk materials, can fundamentally alter the electronic structure of the 2D material. Theoretical work has predicted strong exchange effects [249–251] and emergent phenomena [252–256] in systems that integrate 2D materials with bulk, 3D magnets. Proximity-induced exchange effects have been experimentally demonstrated in graphene/EuS heterostructures [257, 258] and recently, valley-polarized electroluminescence from 2D semiconductors has been achieved [259, 260]. In this latter case, the degree of polarization remains modest and the effect of exchange fields has not been observed. Furthermore, due to the polycrystalline nature and small grain size of the 3D magnets in these devices, external magnetic fields are required to polarize the ferromagnets for any observable magnetic functionality.

Compared to the approach of interfacing 2D materials with 3D magnets, a van der Waals heterostructure has several advantages [1, 2, 261]. Lattice mismatch is not an issue, thus minimizing chemical modification and interfacial damage, which is desirable for engineering a clean interface for optimal interactions. Since single crystals are used, the twist angle and stacking order between constituent 2D materials becomes a potentially powerful control knob, enabling, for instance, the ability to engineer and study magnetic multilayer van der Waals stacks with unique spin textures. The flexibility of the layer stacking process also facilitates the creation of van der Waals heterostructures between layered ferromagnets and a diverse set of other 2D materials, such as graphene, Weyl semimetals (WTe_2), superconductors ($NbSe_2$), and beyond.

7.2 Experimental methods

Figure 7.1A displays the heterostructure architecture, where vertically stacked monolayer WSe_2 and $\sim$10 nm CrI_3 are sandwiched by thin (10 nm to 20 nm) h-BN flakes to prevent sample degradation. Bulk crystals of WSe_2, CrI_3, and h-BN were first exfoliated onto 90 nm SiO_2 on Si. Due to the instability of CrI_3 in air, we performed exfoliation in a glovebox with O_2 and H_2O levels below 0.5 ppm. Immediately after finding the CrI_3 sample, we assembled the heterostructure stack using the polycarbonate-based transfer technique in a glovebox. The chloroform rinse was performed in an ambient environment for 2 minutes. We note that bare CrI_3 flakes readily hydrate in air, decomposing within seconds. There were no signs of degradation in the h-BN sandwiched sample in ambient conditions for at least an hour, allowing us to transport and mount the sample for measurement.

The samples were measured in a continuous helium flow cryostat with a 7 T supercon-

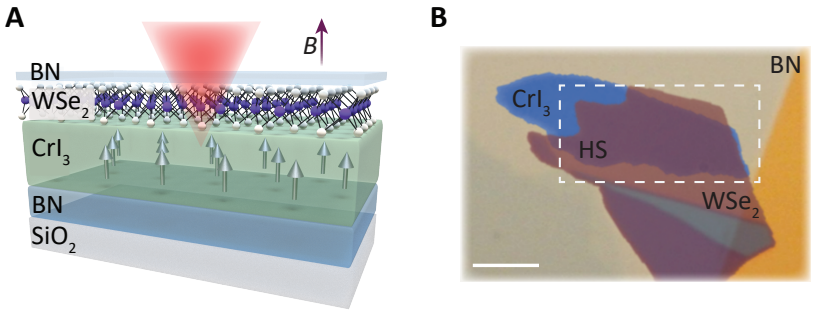

Figure 7.1: Ultrathin WSe_2/CrI_3 heterostructure schematic and image. (A) Schematic of van der Waals heterostructure formed by monolayer WSe_2 and ferromagnetic-layered semiconductor CrI_3 and encapsulated by h-BN. (B) Optical microscope image of device 2. The WSe_2/CrI_3 heterostructure is sandwiched by optically transparent h-BN. Scale bar, 5 µm. [Adapted from [50].]

ducting magnet, which can operate in both Faraday (Fig. 7.1A) and Voigt geometry. PL measurements were performed in reflection geometry using continuous-wave excitation from a HeNe laser (1.96 eV) that was power-stabilized (30 µW) and focused to ∼1 µm with an aspheric lens. The back-reflected PL was collected by the same lens and detected using a spectrometer and Si CCD. Samples were measured at 1 K and in Faraday geometry unless otherwise specified. For the magnetic-field-dependent measurements, we continuously scanned the magnetic field and collected a full hysteresis sweep (up and down in an applied magnetic field) for each polarization configuration before switching to the next polarization. Good overlap at saturation magnetic fields indicated the stability of the measurement and allowed comparison of magnetic-field-dependent data between different polarizations.

A two-axis piezoelectric scanning mirror was employed to scan the laser spot over the sample for spatially resolved measurements. Liquid crystal variable waveplates were used to allow repeatable and quick (< 100 ms) switching between different circular polarizations foσ^+ excitation and collection. Thus, we took both I_{++} and I_{--} polarization configurations (see definitions in text) at each pixel (1 s integration for each polarization) before moving the laser, which rules out sample drift effects in our data. For magnetic-field-dependent data at selected sample positions, we took I_{++} data and time-reversed it to get the expected I_{--} data, then compared them to determine the expected ρ.

7.3 Magnetic substrate control of valley excitons

We present results from two devices (12 nm and 9 nm thick CrI_3), which show similar behavior. A top view of device 2 is shown in Fig. 7.1B. In our design, we use monolayer semiconducting WSe_2 due to its well-established spin and valley pseudospin properties, including circularly polarized valley optical selection rules [13], spin-valley locking effects [262], and valley Zeeman splitting of $\sim$0.22 meV T^{-1} [40, 51–53, 263] (see Chapter 2). Bulk CrI_3 crystal exhibits a Curie temperature (T_C) of 61 K, a saturation magnetization of 3.1 μ_B per Cr, and an out-of-plane easy axis [185]. The last feature is important because in WSe_2 the spin quantization axis is also out-of-plane, with opposite orientations in opposite valleys due to the spin-valley locking effect. Thus, only perpendicular effective magnetic fields can lift the valley degeneracy.

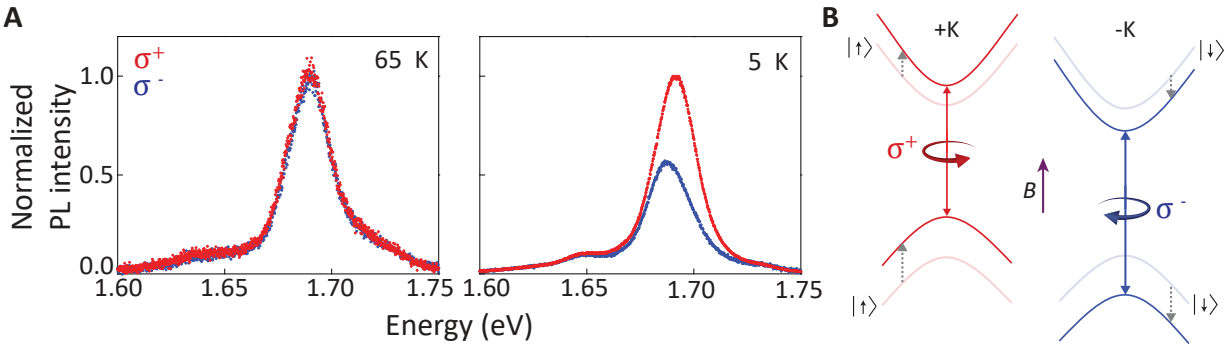

Figure 7.2: Observation of spontaneous magnetization. (A) Circularly polarized PL spectra above T_C (65 K, left) and below T_C (5 K, right) in the absence of an applied magnetic field. It is evident that the valley degeneracy is lifted at 5 K because of the magnetic proximity effect. [Reprinted from [50].]

Figure 7.2A (left panel) displays a typical PL spectrum (device 1) at a temperature of 65 K, above the T_C of CrI_3. We attribute the PL to a positively charged trion state in WSe_2 due to an expected type-II band alignment, with the CrI_3 conduction band lying below that of WSe_2 (see DFT calculation in F). Recent gate-dependent PL results have also confirmed the intrinsic p-doping in the WSe_2 layer when in contact with CrI_3. We denote the circularly polarization spectra as $I_{p1,p2}$, where p1 (p2) represent the excitation (detection) light helicity. The I_{++} and I_{--} spectra are nearly identical at 65 K, as expected from time-reversal symmetry between the valleys in WSe_2 and paramagnetic order in CrI_3.

Upon cooling below the T_C of CrI_3, the valley degeneracy is lifted. Figure 7.2B (right

panel) shows a representative spectrum taken at 5 K. The I_{++} spectrum exhibits both a larger peak intensity and energy than I_{--}. The extracted valley splitting between I_{++} and I_{--} spectra is about 3.5 meV (see Fig. F.3 for fitting details), equivalent to an effective magnetic field of about 13 T (using the monolayer WSe_2 g-factor of -4.5). Further measurements reveal that the magnitude of the valley splitting is independent of the excitation power (Fig. F.4), which rules out carrier density effects as a dominant mechanism for the valley splitting. Thus, we attribute the energy splitting to a strong magnetic exchange field between the CrI_3 spins and WSe_2 excitons. We emphasize that since the optical transition is determined by the energy difference between the conduction and valence bands, the observed valley splitting reflects the distinct coupling of the exchange field with the conduction and valence bands (Fig. 7.2B, solid lines). This is due to the different orbital character of the conduction and valence band edges [40, 254, 255].

We further study the polarized PL while sweeping an applied magnetic field B perpendicular to the sample plane (Faraday geometry, B parallel to easy-axis, Fig. 7.1A). In Fig. 7.3A, the total PL intensity for σ^- excitation ($I_{--} + I_{-+}$) and σ^- excitation ($I_{++} + I_{+-}$) is plotted as a function of applied magnetic field and emission energy for device 1. Six distinct regimes are denoted by the arrows, with three sharp jumps in PL intensity and peak energy near 0 T and ± 0.85 T, and two smaller jumps near ± 1.85 T. figure 7.2B illustrates the overlaid I_{++} and I_{--} spectra at the six selected magnetic fields corresponding to each regime, highlighting the multiple jumps in peak energy and intensity. In Fig. 7.3C and C, we display the valley splitting and the normalized difference between I_{++} and I_{--} intensities, $\rho = (I_{++} - I_{--})/(I_{++} + I_{--})$, as a function of increasing (orange curve) and decreasing (green curve) applied magnetic field. Hysteresis loops, a hallmark of ferromagnetic effects, are observed at $B = \pm 0.85$ T and $B = 0$ T. The widths of the observed hysteresis loops are around 50 mT. Similar measurements in Voigt geometry (B parallel to the sample plane) demonstrate a rotation of the magnetization from in-plane to out-of-plane as the applied magnetic field is reduced to zero, confirming the out-of-plane easy axis in ultrathin CrI_3 (Fig. F.5). In the following discussions, we ignore the direct influence of the applied magnetic field on WSe_2 PL intensity and energy due to the valley Zeeman effect, since the exchange field is much stronger than the applied field (typically ≤ 1 T).

A notable observation in Fig. 7.3A is that at a fixed applied magnetic field, the total PL intensity depends strongly on the excitation helicity. To understand this phenomenon, we focus on the regime with $B > 0.9$ T, where the CrI_3 magnetization M is nearly aligned with

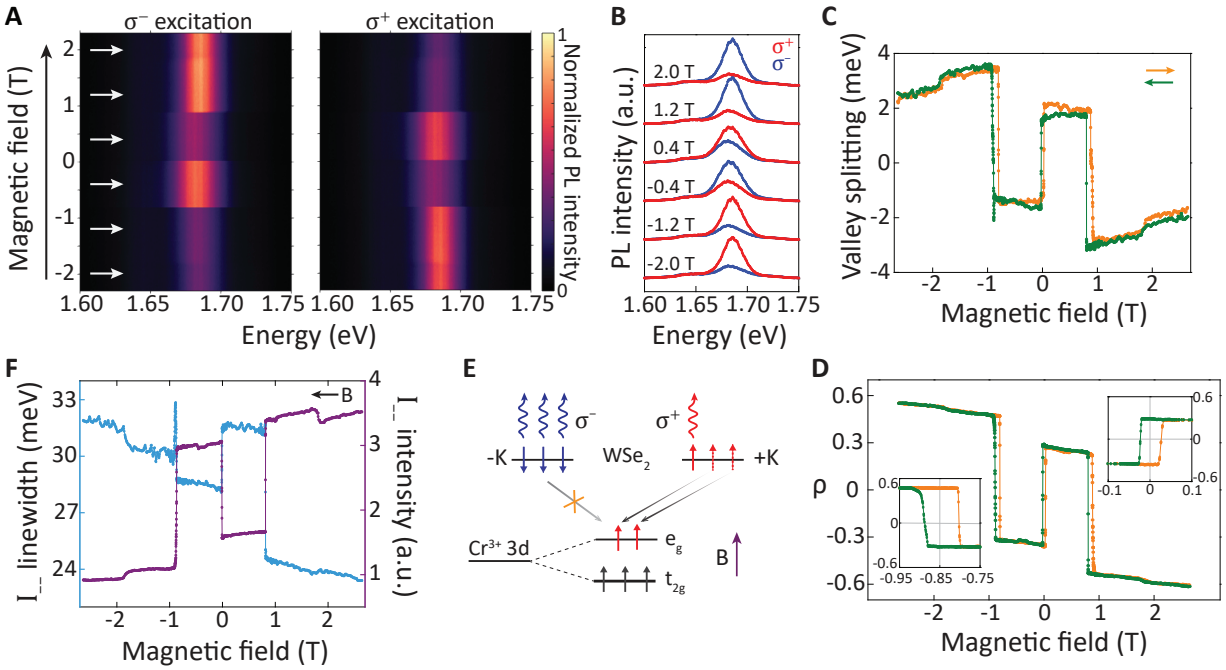

Figure 7.3: Ferromagnetic substrate control of spin and valley pseudospin dynamics. (A) Maps of the total PL intensity as a function of emission energy and applied magnetic field for σ^- and σ^+ excitation. The black arrow indicates the applied magnetic field sweeping direction. (B) I_{++} and I_{--} spectra at selected magnetic fields, which are indicated by the white arrows in fig. A. (C) Valley splitting and (D) normalized PL intensity difference between I_{++} and I_{--} (r) as a function of applied magnetic field sweeping up (orange) and down (green). Insets in fig. D are zoomed-in plots of hysteresis curves. (E) Schematic depicting the spin orientationdependent charge hopping between WSe_2 and CrI_3, which leads to the excitation helicity-dependent PL intensity in fig. A. See text for detailed description. (F) PL spectral linewidth (blue) and intensity (purple) versus applied magnetic field (sweeping from positive to negative) for the I_{--} condition. Broad width is always associated with weak PL intensity. [Reprinted from [50].]

B. As shown in Fig. 7.2B, σ^+ and σ^- excitation create $|+K,\uparrow\rangle$ and $|-K,\downarrow\rangle$ electrons, respectively, where $\uparrow$ ($\downarrow$) represents the electron spin orientation. In CrI_3, the lowest energy unoccupied conduction bands are mainly composed of the Cr atoms spin-polarized eg orbitals, with spin orientation parallel to the ground state spin (Fig. F.1). Therefore, electron hopping from WSe_2 to CrI_3 is only allowed for the aligned spin $|+K,\uparrow\rangle$ (Fig. 7.3E). Under the condition that optical absorption at 1.96 eV is independent of light helicity (Fig. F.6), the electron spins created by σ^+ excitation have an extra non-radiative relaxation channel

compared to σ^- excitation. This results in strongly quenched PL, as well as a broader spectral linewidth, compared to σ^- excitation. The helicity-dependent PL is similar to that observed recently in an epitaxially grown ferromagnet/quantum well heterostructure [247], but the PL polarization and intensity modulation is an order of magnitude stronger in our system with an order of magnitude smaller applied magnetic field range (Fig. F.7).

In Fig. 7.3F, we plot the extracted linewidth and PL intensity of the I_{--} spectrum versus applied magnetic field. The general trend is that the linewidth broadens whenever the PL intensity decreases, and vice versa. This is further evidence supporting the proposed physical picture that in the spin-aligned configuration, the allowed charge hopping opens up an additional non-radiative relaxation channel. We can estimate the hopping rate by the difference in spectral width between I_{++} and I_{--} conditions. For $B = 1\,\mathrm{T}$, the difference is $\sim$5 meV, implying a spin-dependent charge hopping rate on the order of $\hbar/(5\,\mathrm{meV}) \approx 130\,\mathrm{fs}$, where $\hbar$ is the reduced Planck constant. Moreover, the spectral widths vary with the applied magnetic field (Fig. F.8), suggesting that the hopping rate can be tuned by controlling the CrI_3 magnetization.

Another outstanding feature inFig. 7.3C and D is the sharp change of the valley splitting and ρ near $B = \pm 0.85\,\mathrm{T}$ and $0\,\mathrm{T}$. For example, when sweeping the applied magnetic field down through the transition near $B = -0.85\,\mathrm{T}$, the valley splitting changes from $-1.3\,\mathrm{meV}$ to $3.4\,\mathrm{meV}$ in a span of about $30\,\mathrm{mT}$ (Fig. 7.3C). This corresponds to a valley splitting rate of over $150\,\mathrm{meV\,T^{-1}}$, nearly three orders of magnitude larger than can be achieved by the Zeeman effect in bare WSe_2. Moreover, when sweeping through $-0.8\,\mathrm{T}$ in the other direction and also near zero field, the switching is even faster, occurring within a $\leq$6 mT span (Fig. F.9). We also note that the critical fields are independent of the sweep rate (Fig. F.10). The sign change of the valley splitting and ρ implies a flip of the CrI_3 magnetization. This behavior is expected for a ferromagnet when the applied magnetic field crosses zero. However, the sign change near $\pm 0.85\,\mathrm{T}$ is intriguing since the field has not changed direction. This complicated magnetic field dependence implies rich magnetization dynamics in the ultrathin CrI_3 substrate. By comparison, bulk CrI_3 exhibits the expected magnetization loop at zero magnetic field with small remanence and coercivity [185].

7.4 Imaging magnetic domain structures using valley excitons

Since both the valley splitting and ρ are tightly connected to the CrI_3 magnetization, spatial maps of these parameters should reveal the underlying magnetic domain structure. Inspired

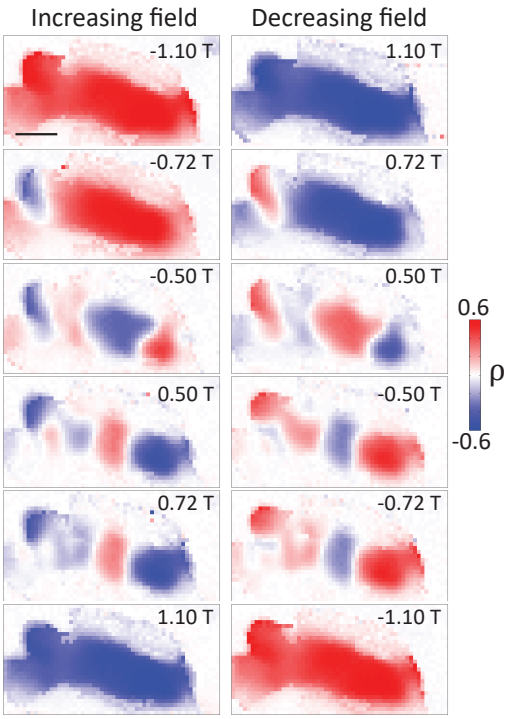

Figure 7.4: Polarization-resolved micro-PL imaging of domain structures. Each panel is a spatial map of ρ (see text for definition) at the indicated applied magnetic field. Left and right columns are arranged in a time-reversal manner corresponding to increasing (left) and decreasing (right) applied magnetic field, respectively. The blue arrow indicates a domain in which the sign of ρ flips three times by sweeping the field, whereas the red arrow points to a domain that flips the sign of ρ only once. Scale bar, 3 mm. [Adapted from [50].]

by this idea, we performed spatially resolved, polarized PL measurements as a function of applied magnetic field on device 2 (boxed region in Fig. 7.1B). Figure 7.4 displays spatial maps of ρ as a function of magnetic field sweeping direction, which are ordered to highlight time-reversal pairs (see Fig. F.11 for valley splitting maps). The time-reversal pair consists of two maps acquired at opposite applied magnetic field while sweeping in opposite direction. We find that each time reversal pair shows excellent consistency in their pattern except for the opposite sign, validating the stability of the system. The domain structure and ρ disappear above $\sim$60 K (Fig. F.12), indicating that T_C is similar to bulk CrI_3.

These maps reveal the evolution of the domain structure between 1.1 T to -1.1 T in the ultrathin CrI_3. When the applied magnetic field is larger than the coercive field, the uniform color across the entire heterostructure indicates full magnetization of CrI_3. When

the applied magnetic field is set at an intermediate value, a multi-domain structure appears with a domain size on the order of a few microns. We define domains that only switch signs with the reversal of the applied field as strong domains (indicated by the red arrow in $B = -0.5\,\mathrm{T}$ map), while those that flip without switching the applied field as weak domains (indicated by the blue arrow). Unlike the strong domains, the weak domains flip three times within one sweep. Therefore, if the laser spot is on a weak domain, the corresponding valley splitting and ρ will also flip three times within one sweep, which is consistent with the observation in Figs. 7.3C and D.

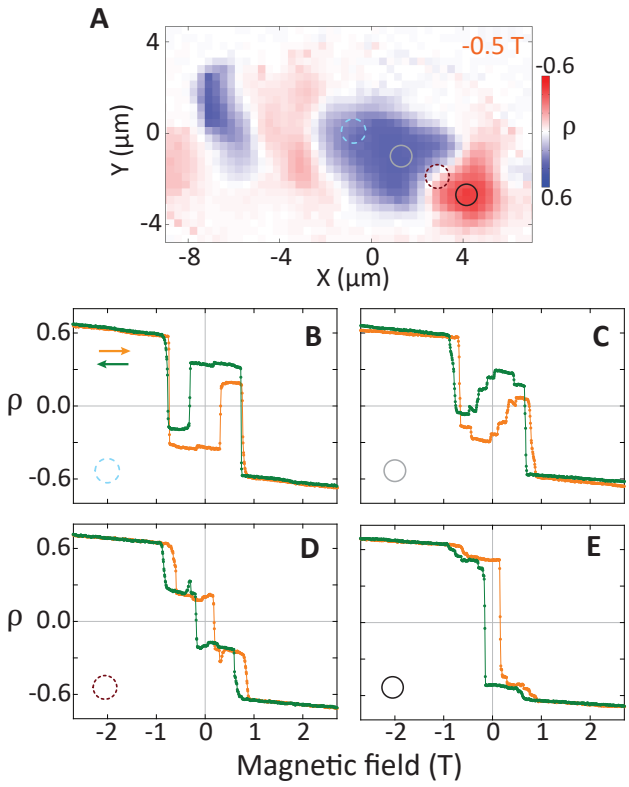

Figure 7.5: Position-sensitive ferromagnetic domain dynamics. (A) Spatial map of ρ from Fig. 7.4 ($-0.5\,\mathrm{T}$, sweep down) with blue, gray, brown, and black circles indicating the spots of selected magnetic field sweeps of ρ in (B), (C), (D), and (E). [Reprinted from [50].]

Measurement of the valley-polarized exciton PL in WSe_2 additionally provides a new local probe to investigate spin and domain dynamics in adjacent ferromagnets through van der Waals engineering. Figure 4 shows multiple distinct ρ-B curves at different sample posi-

tions. As expected from the spatial maps in Fig. 7.4, if the laser is focused on a weak domain (Fig. 7.5B and C), the magnetization can flip without changing the applied magnetic field direction, while in a strong domain (Fig. 7.5E), there is only one hysteresis loop centered at zero field. In addition to coarse changes in magnetization, fine structure is also observed. For instance, in Fig. 7.5C we observe fine steps of ρ as the applied magnetic field varies. At first glance, the observation is an echo of the Barkhausen effect due to the rapid change of the domain size in ferromagnets. However, the laser spot is towards the center of the weak domain, which is less likely to be affected by changes in domain size. Furthermore, the ρ-B curves near the domain boundary do not exhibit these fine steps, as seen in Fig. 7.5D. One possibility to consider is whether the magnetization in thin CrI_3 can flip layer by layer, as in certain types of layered antiferromagnets [264, 265]. Detailed CrI_3 thickness dependence will be crucial to help understand the electronic and magnetic coupling beyond the heterostructure interface. Further interesting topics include unraveling the origin of the slow jumps at $\pm 1.85\,\mathrm{T}$, which manifest themselves as an opposite trend between Fig. 7.3C and D, and may indicate a different origin from the other jumps at lower fields.

These intriguing phenomena will require additional study to elucidate the underlying mechanisms. It is already evident, however, that this probe is highly sensitive to spin interactions and magnetization dynamics, providing a powerful addition to conventional techniques such as magneto-optical Kerr rotation in studying magnetism in thin films. In addition, the integration of van der Waals magnetic materials into other heterostructures should empower researchers to harness exchange interactions and interfacial effects for exploring novel physical phenomena and spintronics at the atomically thin limit.

Chapter 8

VALLEY MANIPULATION BY OPTICALLY TUNING THE MAGNETIC PROXIMITY EFFECT IN WSE_2/CRI_3

8.1 Introduction

In this chapter, we extend the results of the previous chapter on heterostructures of monolayer WSe_2 and 2D magnetic CrI_3 by exploring the power-dependent excitonic properties. The text and figures are reprinted from the published study, **Kyle L. Seyler**, Ding Zhong, Bevin Huang, Xiayu Linpeng, Nathan P. Wilson, Takashi Taniguchi, Kenji Watanabe, Wang Yao, Di Xiao, Michael A. McGuire, Kai-Mei C. Fu, Xiaodong Xu. *Valley Manipulation by Optically Tuning the Magnetic Proximity Effect in WSe_2/CrI_3 Heterostructures.* Nano Letters 18, 38233828 (2018) [266]. We demonstrate wide continuous tuning of the valley polarization and valley Zeeman splitting with small changes in the laser excitation power. The valley manipulation is realized via optical control of the CrI_3 magnetization, which tunes the magnetic exchange field over a range of 20 T. Our results reveal a convenient new path towards optical control of valley pseudospins and van der Waals magnetic heterostructures.

8.2 Experimental methods

The samples consisted of monolayer WSe_2 and ∼10 nm CrI_3 protectively encapsulated by ∼10 nm to 20 nm hexagonal boron nitride (Fig. 8.1A and B), and were fabricated using the techniques describe in Chapter 7. They were measured in reflection geometry using a dry cryostat equipped with a 9 T superconducting magnet in Faraday configuration. The sample temperature was 1.6 K, unless otherwise noted. CW excitation from a power-stabilized laser at 1.96 eV was focused to $\sim 1\,\mu m^2$ with an aspheric lens, and the collected PL was detected with a spectrometer and Si CCD. The excitation polarization and power, as well as the detection polarization, were controlled by liquid-crystal variable waveplates and linear polarizers. For the excitation power sweeps, an integration time of 1 s was used for each polarization, and subsequent power data points were acquired within 2 s of each other. For the magnetic field sweeps, the sweep rate was $\sim 7\,mT\,s^{-1}$ and the PL integration time was 2 s for the

1 µW curves and 1 s for all other curves. Spatially resolved measurements were performed by scanning the sample position using a piezoelectric stage. The PL peak intensity and energy were extracted from a double pseudo-Voigt function fit to the trion and defect peaks. The effective magnetic field was calculated from the valley splitting, assuming a g-factor of -4.5 [50]. RMCD was measured using the same laser with a photoelastic modulator as detailed in Ref. [267].

8.3 Sample characterization

Below its Curie temperature (T_C) of 61 K, CrI_3 establishes long-range magnetic ordering. The coupling between the out-of-plane CrI_3 magnetization and the WSe_2 valley pseudospin (Fig. 8.1A, right) is measurable from the circularly polarized WSe_2 trion PL. Figure 8.1C is a spatial map of the WSe_2 PL intensity, which was acquired by rastering the laser over the boxed region in Fig. 8.1B. By resolving the PL into its circularly polarized components, we can determine the polarization, $\rho = (I_+ - I_-)/(I_+ + I_-)$, where $I_\pm$ is the $\sigma^\pm$ PL peak intensity excited by $\sigma^\pm$ polarized laser. Under time-reversal symmetry, the $\pm K$ valleys are degenerate and ρ is zero. In proximity to magnetic CrI_3, ρ becomes finite and its sign directly correlates with the underlying CrI_3 magnetization direction. Spatial maps of ρ thus reveal magnetic domain structure in CrI_3. For instance, ρ is spatially uniform and negative (Fig. 8.1D, right) at 1 T, with representative spectra shown in Fig. 8.1E. This implies uniform positive magnetization at the interface. However, upon decreasing to 0.7 T (Fig. 8.1D, left), a large region of the heterostructure flips to positive ρ, signifying a change in the magnetization state of the underlying CrI_3. We label this region as domain 1, where ρ flips sign three times in a single magnetic field sweep, as shown in Fig. 8.1F. For the remaining top region (which we label as domain 2), in contrast, the sign of ρ only flips once (see Fig. G.1).

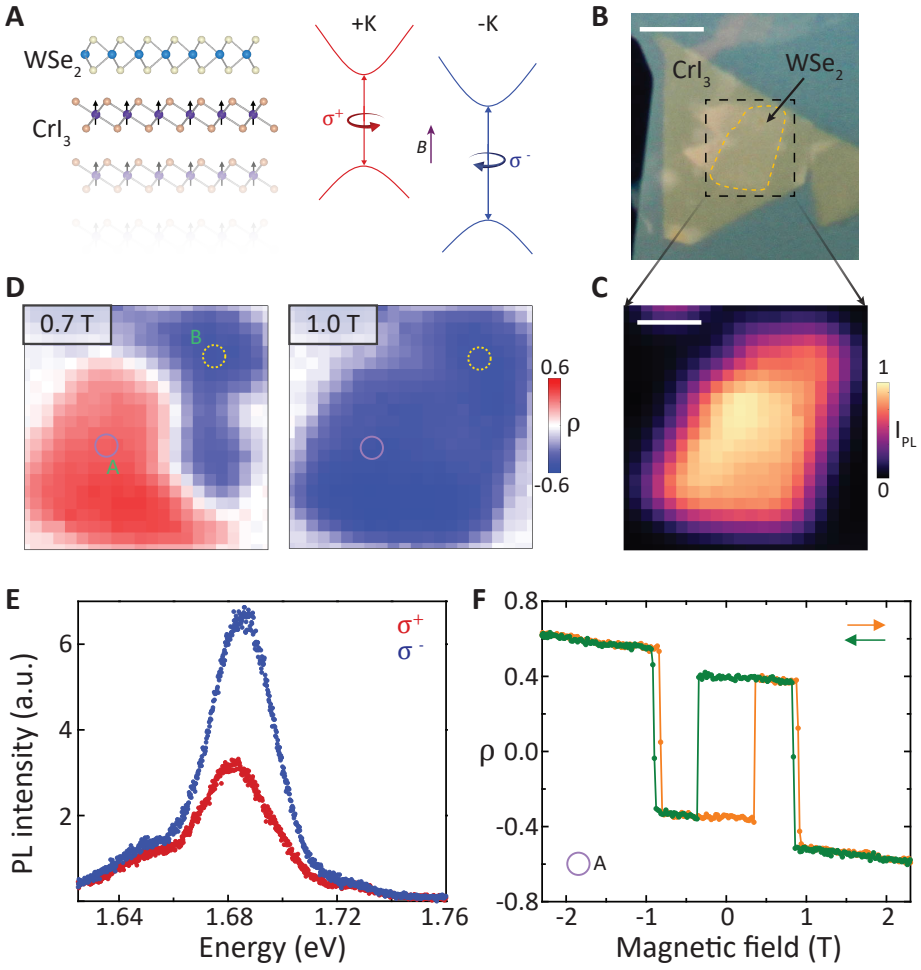

Figure 8.1: Basic characterization and domains of WSe_2/CrI_3 heterostructure. (A) Schematic of WSe_2/CrI_3 heterostructure (left). Valley energy level diagram and optical selection rules of monolayer WSe_2 with magnetic exchange field coupling (right). h-BN encapsulation layers are not shown. (B) Optical microscope image of heterostructure. Dashed box region shows the laser scanning area and the dotted yellow curve outlines the WSe_2 monolayer region. Scale bar, 5 µm. (C) Spatial map of total photoluminescence (PL) intensity within the boxed region of fig. B. Scale bar, 2 µm. (D) Spatial maps of the polarization parameter ρ (see text for definition) at 1 T (right) and 0.7 T (left) applied magnetic field. Same spatial scale as fig. C. (E) Spectra of σ^+ (σ^-) PL under σ^+ (σ^-) laser excitation taken at 1 T applied magnetic field, shown in red (blue). (F) Magnetic field dependence of ρ for up (orange) and down (green) field sweep directions. The data was taken on domain 1 at the location marked by the solid purple circle in fig. D. The corresponding data for domain 2 (marked by dashed yellow circle) is in Fig. G.1. [Reprinted from [266].]

8.4 Power-dependent hysteresis and valley switching

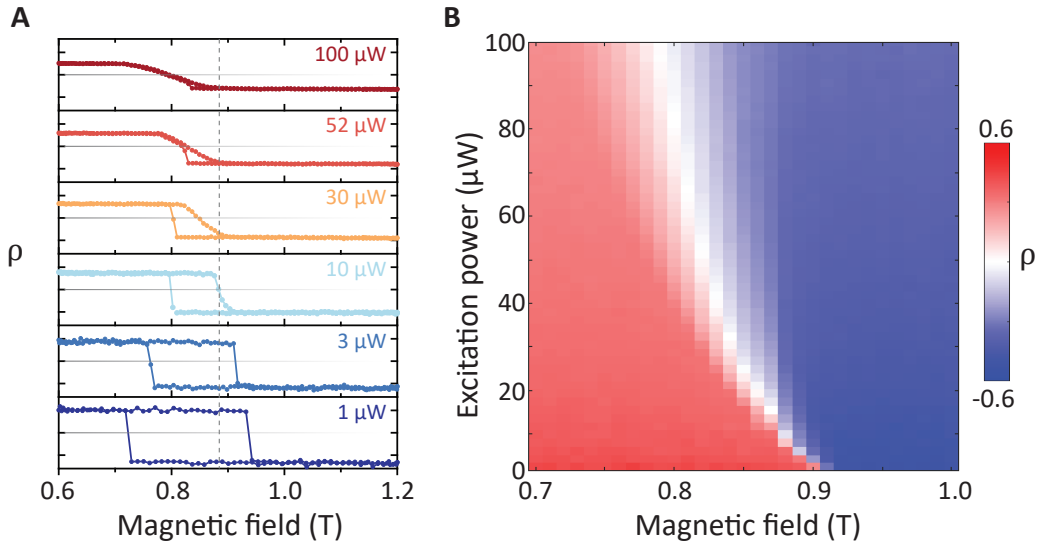

Figure 8.2: Power-dependent hysteresis and valley switching. (A) Magnetic field sweeps of ρ from 0.6 to 1.2 to 0.6 T (highlighted region in Fig. 8.1F) at different excitation powers. Gray horizontal lines indicate $\rho = 0$ and the neighboring tick marks on the y-axis are ± 0.5. Sweep directions are shown by the black arrows. (B) Map of the power dependence of ρ taken at different applied magnetic fields. The magnetic field was first initialized by sweeping up to 0.7 T. A power dependence was then performed from 1 µW to 100 µW at the different fixed magnetic fields from 0.7 T to 1 T. [Reprinted from [266].]

Our main finding is that the outer hysteresis loop of domain 1 near 0.8 T (highlighted in Fig. 8.1F) strongly depends on the photo-excitation power. In Fig. 8.2A, ρ is plotted as the magnetic field sweeps from 0.6 T to 1.2 T and then back to 0.6 T at selected excitation powers. The hysteresis loop gradually evolves from wide and square at 1 µW to narrow and sloped at 100 µW. This photoinduced change in the coercivity has dramatic consequences for the optical control of valley properties at fixed magnetic fields near the hysteresis loop. We performed power-dependent measurements of ρ at fixed magnetic fields from 0.7 T to 1 T as shown in the 2D plot of ρ in Fig. 8.2B. The magnetic field was first initialized by sweeping up from 0.6 T. Below $\sim$0.75 T and above $\sim$0.92 T, ρ decreases in magnitude slightly with increasing power, but its sign remains the same. In striking contrast, at intermediate fields, the sign of ρ flips at high powers. The curved white area shows that the critical power decreases at higher magnetic fields, consistent with the power dependence of the hysteresis

loop coercivity in Fig. 8.2A. The vertical line in Fig. 8.2A shows how the power-dependent coercivity can cause the sign flip in ρ at a fixed magnetic field. We also find similar power dependence and switching behavior for the valley Zeeman splitting (Δ), which was extracted by the energy difference between $\sigma^{\pm}$ PL peaks (Fig. G.2).

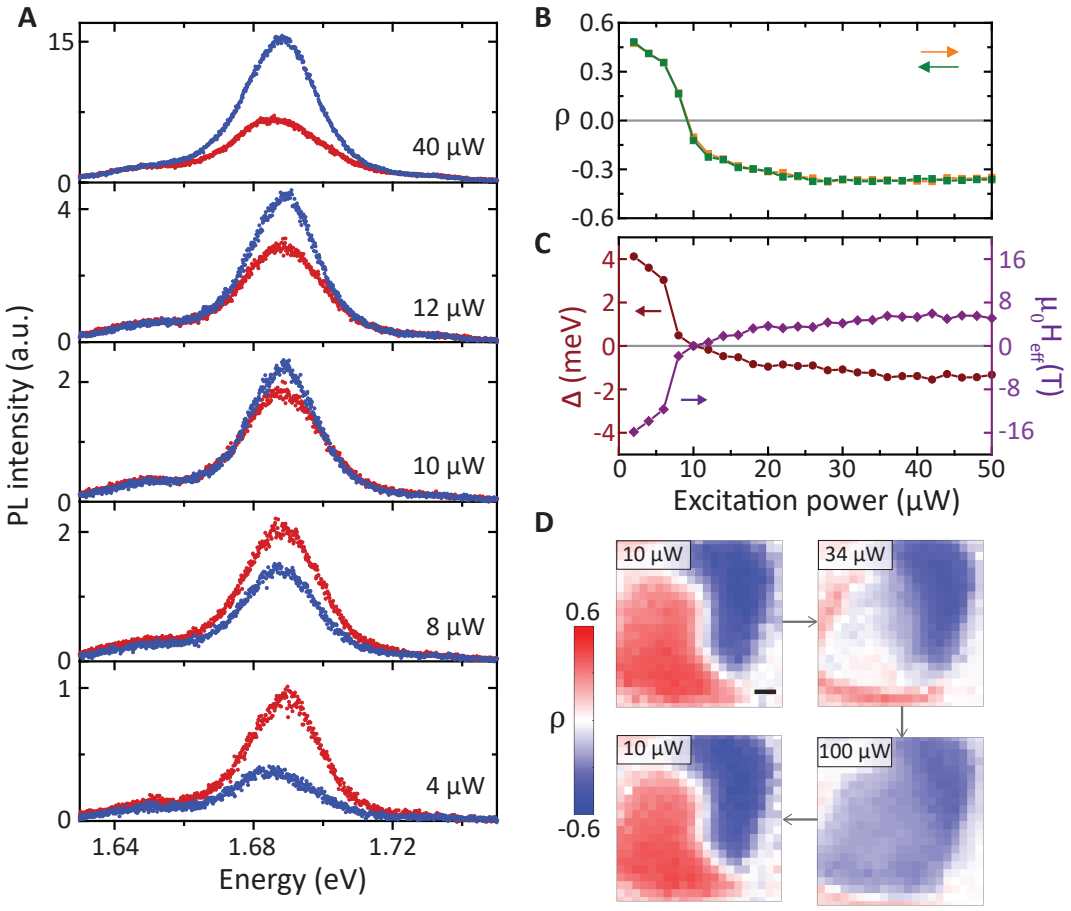

Figure 8.3: Manipulation of valley polarization and splitting via optical excitation power. (A) Circularly polarized PL spectra at selected excitation powers. The applied magnetic field was initialized to 0.88 T from 0.6 T. (B) Power dependence of ρ at 0.88 T with increasing (orange) and decreasing (green) power. (C) Power dependence at 0.88 T of the valley splitting (Δ, left) and the corresponding effective magnetic field ($\mu_0 H_{eff}$, right). Fig. G.3 contains the full dataset for Fig. 8.3B and C. (D) Spatial maps of ρ at 10 μW, 34 μW, 100 μW and 10 μW, in that order. The black scale bar represents the laser beam diameter (1 μm), which is much smaller than the domain size. [Reprinted from [266].]

The power-switchable valley properties are clearly illustrated in the PL spectra in Fig. 8.3A

taken at 0.88 T. At low excitation powers, I+ (red curve) is more intense and has higher energy than I- (blue curve). With increasing power, however, I_+ and $-$ become degenerate and eventually they switch in their relative intensity and energy. From 4 µW to 40 µW, ρ continuously changes from 0.41 to -0.37 (Fig. 8.3B) and Δ from 3.7 meV to -1.3 meV (Fig. 8.3A, also Fig. G.3). To produce comparable switching of the valley splitting with a bare WSe_2 monolayer would require sweeping an external magnetic field between -15 T and 5 T. These results are consistent with a second heterostructure sample (Fig. G.4). We provide additional power dependences for ρ and Δ at different magnetic field values in Fig. G.5. The valley switching effects were observed for both circular and linear excitation polarization, and therefore only the total optical excitation power matters (Fig. G.6). We also find that the power dependence is identical with both increasing and decreasing power, which indicates the effects are fully reversible with no hysteresis (Fig. 8.3B, Fig. G.7). These results demonstrate reversible optical control of the valley polarization (between about 40) and magnetic exchange field (Fig. 8.3C), by varying the excitation power within an order of magnitude.

As revealed by the power-dependent spatial maps of ρ in Fig. 8.3C, the reversible valley switching occurs on all areas of domain 1. The arrows denote the acquisition order of the maps, which were all taken at 0.84 T. At low laser excitation power, there are two areas of opposite polarization (see 10 µW plot in Fig. 8.3C), which correspond to the two magnetic domains as discussed. When the excitation power increases to 100 µW, the domain of positive polarization (A) completely reverses, which implies that optical excitation can flip all areas of domain 1. After the excitation power is lowered back to 10 µW, the original domain pattern recovers.

8.5 Discussion of underlying mechanisms for power dependence

The valley switching effect arises from optical control of the CrI_3 magnetization and hence the resulting magnetic proximity effects. To further unravel the connection, we directly probed the CrI_3 magnetization via reflection magnetic circular dichroism (RMCD) on domain 1. RMCD measures the difference in reflection between right and left circularly polarized light and is proportional to the total out-of-plane magnetization in the CrI_3. In Fig. 8.4A, we show the magnetic field dependence of the RMCD signal at different excitation powers, which should be compared to the study for ρ from Fig. 8.2A. The RMCD exhibits a very similar power-dependent hysteresis loop behavior to ρ; the full-width of the RMCD loop decreases

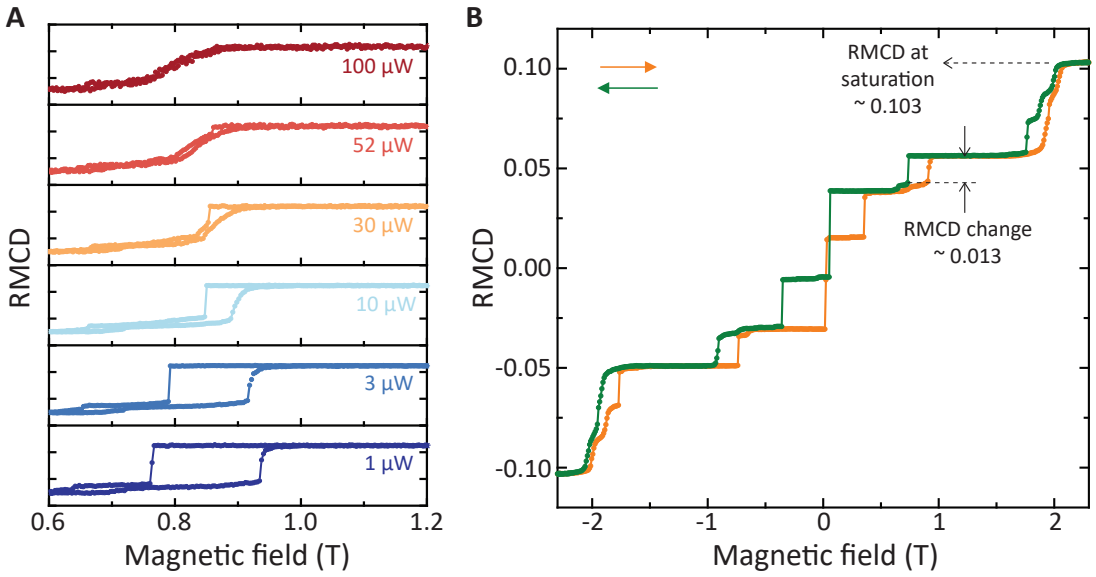

Figure 8.4: CrI_3 magnetization and temperature dependence of hysteresis loop. (A) Magnetic field dependence of the RMCD from 0.6 to 1.2 to 0.6 T at selected excitation powers. The RMCD range in each box is from 0.03 to 0.06 and the tick marks are separated by 0.01. (B) Magnetic field dependence of RMCD sweeping up (orange curve) and down (green curve) on domain 1 at 10 μW optical excitation power. [Reprinted from [266].]

and the loop slants with increasing power. However, unlike with ρ, the RMCD does not switch signs. Further differences are revealed in Fig. 8.4B, where the RMCD is tracked over a wider magnetic field range. In contrast to ρ, which flips three times in a magnetic field sweep (Fig. 8.1F), the RMCD signal contains many step-like jumps and is monotonic with the magnetic field (Fig. 8.4B). While there are changes in the RMCD signal where ρ and Δ flip sign (near ± 0.8 T), the additional jumps near 0 T and ± 1.9 T do not appear in the behavior of ρ. The RMCD data thus reveal that the CrI_3 magnetization changes discretely in several steps, unlike a typical ferromagnet.

We can understand this behavior if we assume that the magnetic proximity effect in WSe_2 is most strongly influenced by the top CrI_3 layer. This assumption is reasonable since the exchange coupling is short-ranged, so the magnetic interactions between WSe_2 and deeper CrI_3 layers are suppressed. In fact, the size of the RMCD steps near 0.8 T ($\sim$0.013) are about 1/8 of the saturation value at 2.3 T ($\sim$0.103), which indicates that the magnetization changes by the same fraction. If we assume that the step corresponds to a magnetization flip within a single CrI_3 layer, it indicates that the CrI_3 is 16 layers thick, or $\sim$10.6 nm ($\sim$0.66 nm

per layer)23. This is consistent with the ∼10 nm CrI_3 thickness that we measured by atomic force microscopy. The measurements thus imply that the valley switching originates from the photoinduced flipping of a single interfacial layer of CrI_3 magnetization. In addition, the other step-like jumps in the RMCD sweeps (Fig. 8.4B) must arise from magnetization changes within deeper layers and do not impact the WSe_2 to the same extent. We can also now refine our understanding of the differences between domains 1 and 2. In a magnetic field sweep, the topmost CrI_3 layer flips three times in domain 1, but only once in domain 2 (G.1). Near 0.8 T in domain 2, only deeper layers away from the WSe_2 interface are susceptible to flipping, which explains the negligible power-dependent PL polarization.

Since the top CrI_3 layer predominantly impacts the WSe_2, one might expect that the magnetic exchange field should be equal and opposite after flipping the top CrI_3 layer. However, from Fig. 8.3C, the magnitude of the effective exchange field at high powers (∼5 T) is less than the magnitude at the lowest powers (∼15 T). The origin of this discrepancy is currently unclear. One possibility is due to CrI_3 demagnetization at high powers, since small magnetization changes in the topmost CrI_3 layer can have an outsized impact on the WSe_2 layer. Another possibility is that the photoexcited excitons and free carriers at higher powers influence the valley depolarization in WSe_2. Future studies should consider pump-probe measurements, with pump light below the WSe_2 optical gap to control CrI_3 and weak above-gap excitation to measure the WSe_2 PL. Such experiments will provide insight into the excitation energy dependence of the opto-magnetic effects and help to disentangle the WSe_2 and CrI_3 power dependences.

Another essential topic for further study is the underlying mechanism for the photoinduced changes in the CrI_3 layer magnetization. While optically controlled magnetism is a vast field of research, the optical control of magnetic coercivity using relatively low-power continuous-wave excitation has only been observed in a few magnetic semiconductor systems, such as (Ga,Mn)As [268], Ni/GaAs [269], and (In,Mn)As/GaSb [270]. In these samples, photoexcited carriers reduce the coercivity by enhancing the carrier-mediated exchange interactions, which lower the domain wall energies. For CrI_3, our preliminary measurements show that width of the 0.8 T hysteresis loop is very sensitive to temperature, which suggests that laser heating of the lattice may be an important factor (Fig. G.8). We also observe that outermost RMCD hysteresis loops at ±1.9 T are sensitive to power (Fig. G.9). Therefore, excitation power also impacts deeper CrI_3 layers, and the photo-induced layer flipping effect can likely occur in CrI_3 in the absence of WSe_2. We emphasize that further theoretical

studies and detailed experiments, such as gate dependence, CrI_3 thickness dependence, and time-resolved studies, will be required to fully understand the opto-magnetic effects in CrI_3, which are beyond the scope this work.

In conclusion, we have demonstrated a new route to manipulate the WSe_2 valley pseudospins by optical control of the magnetic proximity effect. Using small changes in laser power, we can reversibly flip the top CrI_3 layer magnetization, which tunes the magnetic exchange field over a range of 20 T and thus controls the valley polarization and Zeeman splitting without changing the external magnetic field. These observations are uniquely enabled by the ability to fabricate a high-quality van der Waals heterostructure between a 2D magnetic insulator with large domain size and a non-magnetic monolayer valley semiconductor. A clean heterostructure interface, together with optically sensitive magnetic properties, is challenging to realize using conventional magnetic insulators. The optically tunable magnetic exchange field demonstrated here should be generalizable to a wide variety of CrI_3 -based van der Waals heterostructures, which may be a powerful tool in the study of physical phenomena requiring time-reversal symmetry breaking.

Chapter 9

OUTLOOK

This dissertation has focused on optical spectroscopic investigations of 2D crystals and their heterostructures. In the introduction, we posed several guiding questions. Here we summarize some answers, drawing upon what we have learned from the research in this dissertation.

What are the fundamental light-matter interactions in different 2D materials? It is clear that tightly bound excitons dominate the optical response of the 2D TMD semiconductors. We have explored both the intralayer excitons in monolayers as well as the free and trapped interlayer excitons that form in heterobilayers. On the other hand, in the 2D magnetic insulator CrI_3, we discovered that the main photoexcitations are from localized *d-d* and charge-transfer optical transitions.

How does the optoelectronic response change in the 2D limit? For 2D semiconductors, quantum confinement and the resulting increased Coulomb interactions significantly enhance the exciton binding energy and oscillator strength. We were able to realize electrical control of SHG for the first time due to the strong excitonic effects in the 2D limit. A full understanding of the differences between the 3D and 2D limits for CrI_3 remains to be explored. There is important work to be done on how the interlayer exchange interactions vary in 2D and 3D magnets, and also to what extent interlayer coupling can affect the various photoexcitations.

What new phenomena emerge in 2D materials and their heterostructures due to crystal symmetry, quantum confinement, exchange interactions, Berry phase, interfacial coupling, and more? We have found many answers to this question throughout the dissertation. Berry phase effects and crystal symmetry underlie the valley physics that is so central to this work. By forming magnet-semiconductor heterostructures, we demonstrated magnetic exchange coupling and interfacial charge transfer between valley photoexcitations and 2D CrI_3. We also showed that by tuning the laser power, it is possible to control the magnetic order in CrI_3 and thus manipulate the magnetic exchange field felt by an interfacial WSe_2 monolayer. We realized a new route to valley-polarized quantum-confined emitter arrays by harnessing the moiré superlattice potential in $MoSe_2/WSe_2$ heterobilayers.

How can we create, understand, and control these phenomena using photons? This dissertation shows that optical spectroscopy is a powerful toolset for studying the physics of 2D crystals and their heterostructures.

Appendix A

SUPPLEMENTARY DATA FOR WSE_2 SHG EXPERIMENTS

The following figures provide supporting experimental data for Chapter 3 and are reprinted from the supplementary information of [57].

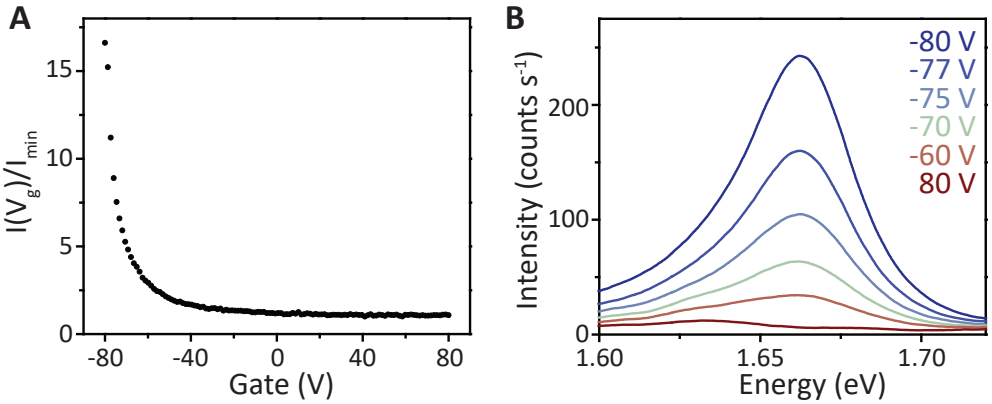

Figure A.1: Gate dependence of RT WSe_2 PL. (A) Peak intensity of PL as a function of gate voltage. (B) PL spectra at selected gate voltages. [Adapted from [57].]

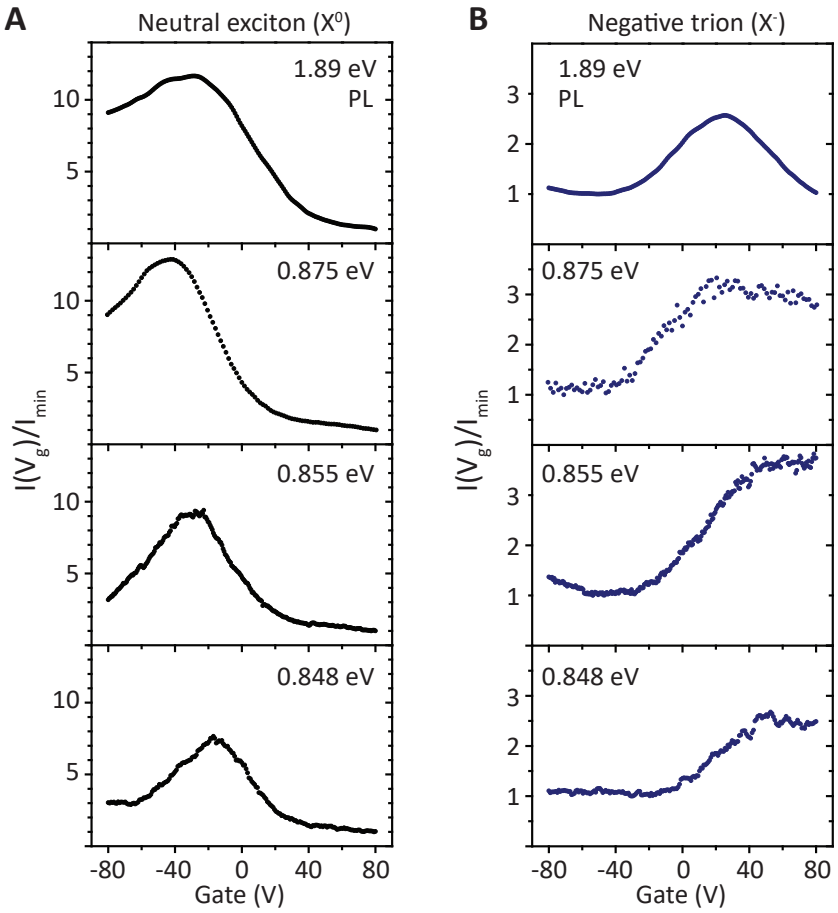

Figure A.2: Exciton and trion PL and SHG tunability by gate under different excitation energies. (A) Tunability of exciton PL (top plot) and SHG (bottom 3 plots) as a function of gate voltage. Excitation energies are shown in the corner of each plot. From top to bottom, the three lower plots correspond to two-photon excitation on exciton, trion, and X^-. (B) Tunability of X^- trion PL (top plot) and SHG (bottom 3 plots) as a function of gate voltage. From top to bottom, the three lower plots correspond to two-photon excitation on exciton, trion, and X^-. [Adapted from [57].]

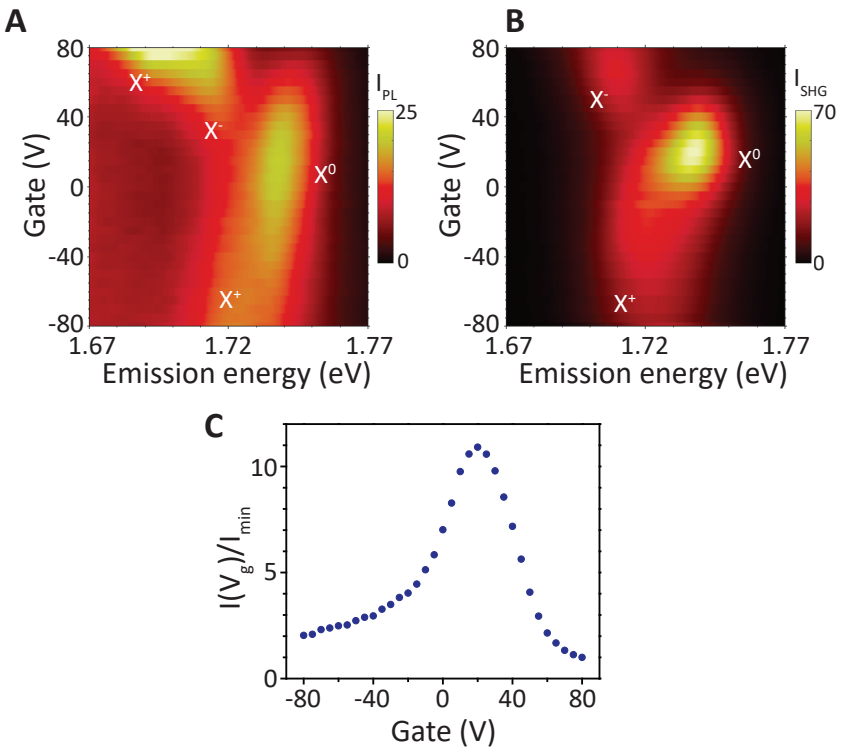

Figure A.3: SHG tunability by bias of a second device (30 K). (A) PL intensity map as a function of gate voltage and emission energy, showing the different exciton species. (B) SHG intensity map showing similar spectral features as Fig. 3.5A. Two-photon excitation energy is centered on X^-. (C) Peak SHG intensity of neutral exciton as a function of gate voltage. [Adapted from [57].]

Appendix B

PHASE-RESOLVED SHG FOR HETEROBILAYER FABRICATION

The ability to precisely stack WSe_2 and $MoSe_2$ monolayers into a heterostructure with a predetermined twist angle is critical for future studies of heterobilayer physics. The broken inversion symmetry of the monolayer honeycomb lattices allows for strong SHG under ultrafast optical excitation, and co-linear polarization-resolved SHG directly reveals the orientation of the armchair axes, as detailed in Chapters 3 and 4. However, because this measurement is not sensitive to the SHG phase, there is ambiguity in the armchair axis direction. This implies the inability to determine whether the heterostructures have AA-like (0° twist angle) or AB-like (60° twist angle) stacking, which may have important differences in their optoelectronic properties. To overcome this limitation, we developed a procedure for phase-sensitive SHG, which we describe below. As an example of its application, this technique was used to determine that spin-valley transfer in $MoSe_2/WSe_2$ heterobilayers only weakly depends on the twisting angle [142].

After identifying high-quality exfoliated monolayers by optical microscopy (Fig. B.1A) and confirming their cleanliness with atomic force microscopy (AFM), we use the standard linear-polarization-resolved SHG to identify the crystal axes of each monolayer (Fig. B.1B) up to 60°. To resolve this armchair direction ambiguity, we perform an SHG spectral interference experiment modelled after Ref. [271–273]. The basic idea is simple. Consider the electric field of two second-harmonic pulses delayed relative to one another by time τ:

$$E(t) = E_1 a(t) e^{-i2\omega t} + E_2 a(t-\tau) e^{-i(2\omega t - \theta)} + c.c., \tag{B.1}$$

where $a(t)$ and $a(t-\tau)$ are the pulse envelopes with amplitude E_1 and E_2, and θ is the relative phase of pulse 2. The Fourier transform is given by

$$E(\Omega) \propto E_1 A(\Omega) + E_2 A(\Omega) e^{i(2\omega\tau + \Omega\tau + \theta)} + c.c., \tag{B.2}$$

so the measured spectral intensity is

$$I(\Omega) \propto |A(\Omega)|^2 \big(E_1^2 + E_2^2 + 2\zeta E_1 E_2 \cos(2\omega\tau + \Omega\tau + \theta)\big), \tag{B.3}$$

where ζ describes the degree of spatial coherence between the two pulses. Therefore, given pulses of comparable intensity at frequency 2ω and delayed by time τ, their spectrum will exhibit inteference fringes with frequency period $2\pi/\tau$. One can then extract the relative between the two pulses, θ, directly from the fringe phase.

In practice, our OPA (Coherent 9800) sends tunable $\sim$200 fs pulses at ω into the setup shown in Fig. B.1C. The excitation is focused onto a z-cut quartz reference, which is oriented to generate horizontally polarized 2ω reference pulses (collinear to and co-polarized with the ω pulses). A time delay (Δt) is generated as the ω and 2ω pulses travel through the dispersive optics in the setup. The pulses are focused by a 50 $\times$ objective (Olympus) onto the sample, generating an additional 2ω sample signal (time-delayed from the 2ω reference). The sample should be oriented with the armchair axis, as determined by the 6-fold pattern (Fig. B.1B), parallel to the 2ω reference and ω polarization. An imaging setup (not shown) and a rotation mount for the sample allow us to position the sample properly. The back-reflected signals are diverted with a 50/50 beamsplitter through a 1 µm short-pass filter, into a spectrometer, and detected by a Si CCD. The time-delayed 2ω sample and reference signals produce spectral interference as shown in Fig. B.1D. The period of the fringes is set by the time delay between the pulses ($\sim$2 ps) and the phase of the interference fringes is determined in part by the phase of SHG generated by the sample. Therefore, this technique can distinguish between armchair axes 60° apart, which shows up as a π phase shift in the interference spectrum. The fringes can be separated from the broad background SHG through Fourier transforms, as shown in Fig. B.1E and F.

As a calibration, we subsequently perform the interference experiment using the front surface of z-cut quartz, which possesses the same allowed second-order susceptibility elements as those of the monolayer MX_2. As with the monolayer experiment, we orient the quartz with its "armchair" axis parallel to the excitation and reference pulses to get a similar interference spectrum (Fig. B.1D, black curve). This is done for two orientations of the quartz, 60° apart. The WSe_2 and $MoSe_2$ interference experiments can then compared with the quartz experiment, allowing determination of the relative crystal orientations of the monolayers. The use of a quartz calibration is important, as it provides a reference for comparing different monolayer interference patterns and makes the experiment robust against laser and optical

setup changes that can affect the absolute phase.

Furthermore, in employing this technique, one needs to be careful about the excitonic resonances, which can introduce additional phase shifts. Thus, we typically measure the phase off-resonance, with the OPA near ∼1440 nm for both $MoSe_2$ and WSe_2. This leads to a good 0° or 180° phase relation between the interference patterns of the MX_2 and the z-front surface.

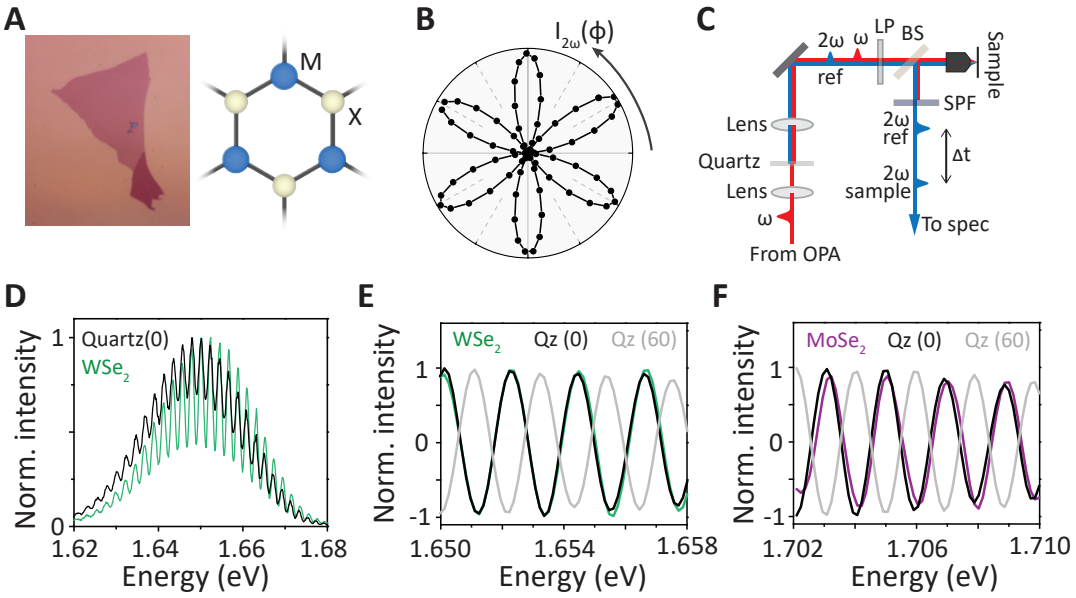

Figure B.1: SHG spectral interferometry. (A) Microscope image of monolayer (left) and top view of crystal structure of single hexagon unit (right). (B) Polarization-resolved SHG intensity polar plot as a function of incident laser polarization. Detected polarization co-linear with excitation. (C) Schematic of phase-resolved SHG setup. LP = linear polarizer, BS = beam splitter, Obj = 50 × IR objective lens, SPF = shortpass filter. (D) SHG interference spectrum between the monolayer in A and a reference SHG signal. (E) Phase-resolved SHG experiment on monolayer WSe_2, compared to quartz (Qz) for two different directions (60° apart). (F) Same as E, but for $MoSe_2$ monolayer. The data in E and F are compared to determine the relative orientation. [Adapted from [142].]

Appendix C

SUPPLEMENTARY MATERIAL FOR VALLEY-POLARIZED INTERLAYER EXCITON STUDIES

The following text provides supporting experiments and theory for Chapter 4, reprinted from the supplementary information of [92].

C.1 Valley polarization in additional heterobilayers

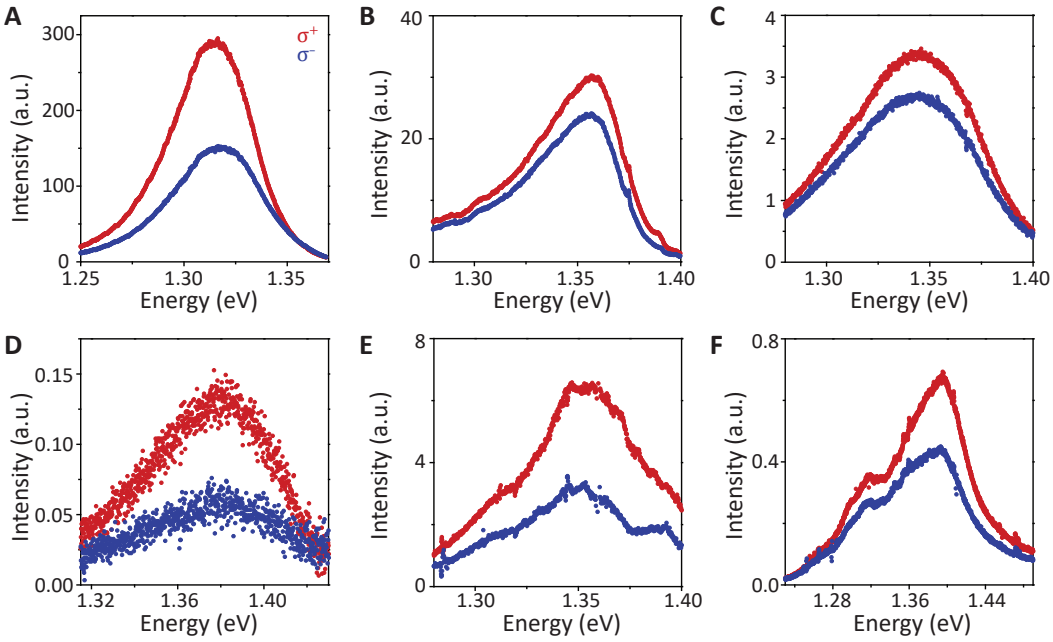

Figure C.1: Valley-polarized interlayer excitons in supplementary heterostructures. Circular polarization-resolved interlayer exciton PL spectra from several heterostructures under σ^+ excitation. Black and red respectively denote σ^+ and σ^- PL emission. The interlayer exciton PL is co-polarized with the helicity of the excitation source for all samples. (A) Device presented in the main text with WSe_2 on top of $MoSe_2$. (B-F) Inverted heterostructures ($MoSe_2$ on WSe_2) displaying similar valley polarization. All data are taken at 30 K. [Adapted from [92].]

C.2 Linear polarization of interlayer excitons

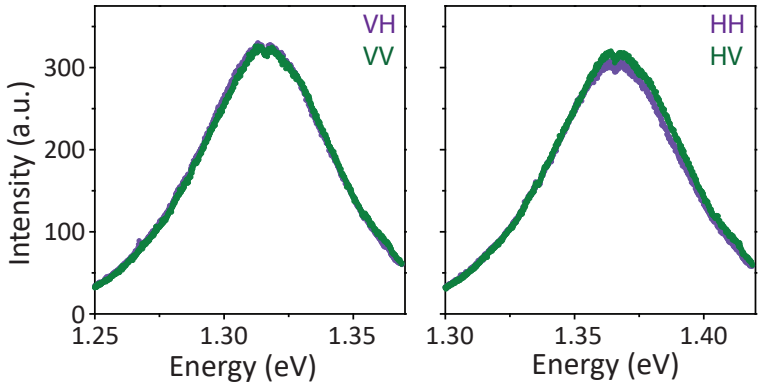

Figure C.2: Linear polarization-resolved interlayer exciton photoluminescence spectra from the device presented in the main text under (A) vertically polarized excitation, and (B) horizontally polarized excitation. Green and purple respectively denote horizontal and vertical PL emission. [Adapted from [92].]

We have also performed polarization-resolved measurements in the linear basis (Fig. C.2). However, the IX does not show appreciable linear polarization. For each valley configuration of the IX, there exist three light cones located at finite center of mass velocities which are related by 120° rotation. These light cones have elliptical polarization which is also related by the 120° rotation. Therefore, when the three light cones are equally populated without mutual quantum coherence, the overall emission can have circularly polarized components, but not linear. A linearly polarized component can potentially be observed when the three light cones have populations that are unbalanced, e.g. in the presence of an excitonic current, which we have not yet achieved. The absence of linear polarization also demonstrates that valley coherence is not preserved during the interlayer exciton formation and relaxation processes prior to radiative recombination.

C.3 Optical pumping of interlayer excitons in heterostructures with AB-like stacking

Here we consider the valley polarization of interlayer excitons in heterostructures with AB-like stacking (twist angle near 60° shown in Fig. C.3). The Brillouin zone of the bottom layer will thus be 180 degree rotation of the top layer (Fig. C.3). In this scenario, the

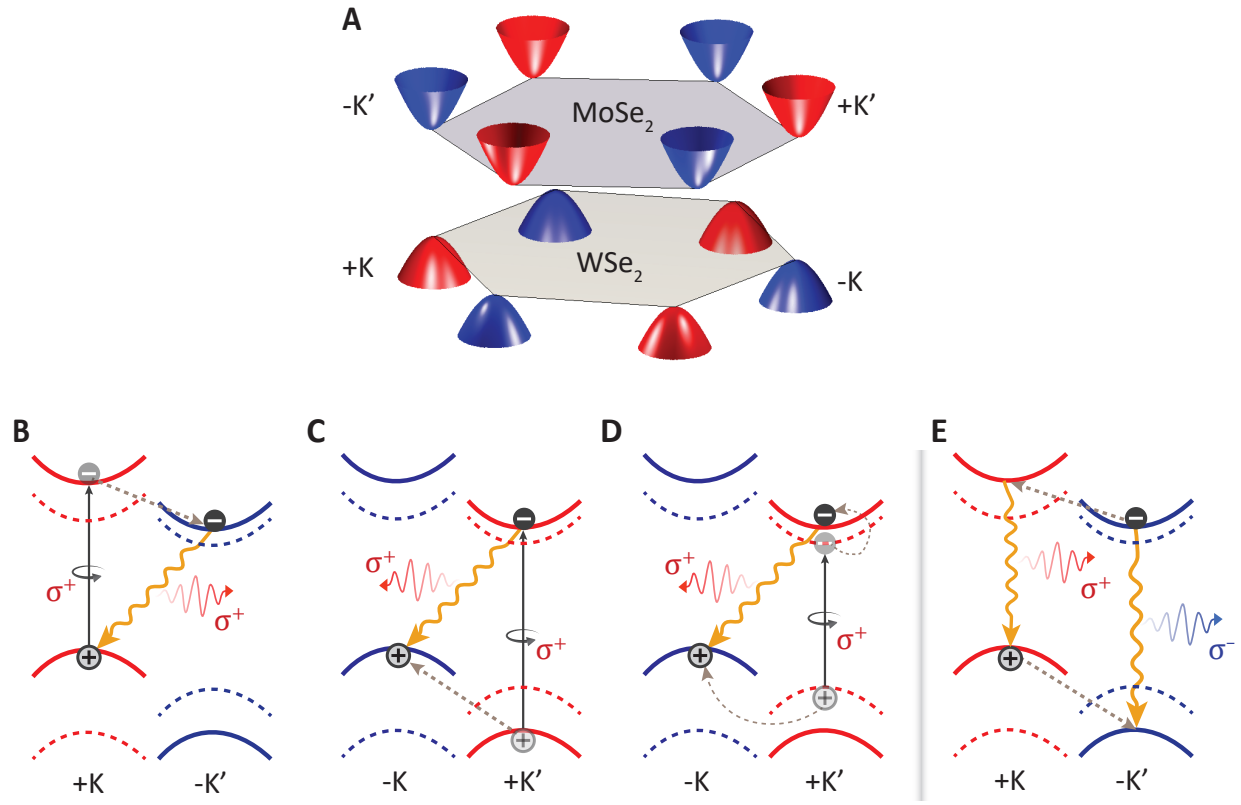

Figure C.3: (A) Side view of AB stacked $MoSe_2/WSe_2$ heterostructure. (B) Illustration of the band edges in the hexagonal Brillouin zone with twisting angle near 60°. There is 180° rotation of the Brillouin zones between the top and bottom layers. (C) Illustration of the two quantum pathways contributing to interlayer exciton recombination: the virtual interlayer hopping of an electron (hole) couples to intralayer excitons in WSe_2 ($MoSe_2$), emitting σ^+ (σ^-) polarized light. Solid (dashed) band indicate spin up (down). (D) Optical pumping with σ^+ polarized light excites the WSe_2 A exciton. Spin-conserving interlayer hopping of the electron (gray dashed arrow) forms the interlayer exciton with electron in $-K'$ valley of $MoSe_2$ and hole in the $+K$ valley of WSe_2. (E) Optical pumping with σ^- polarized light excites the $MoSe_2$ B exciton. Spin-conserving interlayer hopping of the hole (gray dashed arrow) forms the interlayer exciton with electron in $+K'$ valley of $MoSe_2$ and hole in the $-K$ valley of WSe_2. (F) Optical pumping with σ^+ polarized light excites the $MoSe_2$ A exciton. Interlayer hopping requires the hole to change either its spin or valley index. The formation of interlayer exciton through this channel is expected to be inefficient. [Adapted from [92].]

interlayer exciton inherits the valley index $+K$ from one layer and $-K$ from the other. Consider the $X_{-,+}$ interlayer exciton as an example. Here the indices denote an electron in $-K'$ valley of $MoSe_2$ and a hole in $+K$ valley of WSe_2, as shown in Fig. S5C. The

$X_{-,+}$ can radiatively recombine through three quantum pathways. The first pathway is through the virtual intermediate state of an intralayer exciton in the $+Kf$ valley: the electron in $-K'$ conduction band hops to $+K$, followed by intralayer recombination in WSe_2 and subsequent emission of a σ^+ photon at the interlayer exciton energy. The second pathway is through a different virtual intermediate state, the intralayer B exciton in the $-K'$ valley of $MoSe_2$ through the hole interlayer hopping from WSe_2 to $MoSe_2$ (Fig. C.3), and the emitted photon is σ^- polarized. The radiative recombination can also be facilitated by the interlayer transition dipole between the electron and the hole. The interference of the three pathways leads to elliptically polarized emission of the interlayer exciton, with the helicity mainly determined by the relative strength of the electron and hole interlayer hopping rates. When the twisting angle is not exactly 60°, there are three light cones at inequivalent center-of-mass velocities, where the major axes of the elliptical polarization are 120° degree rotation of each other. When the PL is from the incoherent sum of the three light cones, the emission can be circularly polarized. Therefore, valley polarization of interlayer excitons in the AB stacking also corresponds to circularly polarized PL.

With the lack of information on the relative efficiency of the electron and hole interlayer hopping, the absolute emission helicity of a given interlayer exciton valley configuration (say, $X_{-,+}$) is undetermined. Nevertheless, a general argument leads to the expectation that the emission PL has the same helicity as the circularly polarized excitation. This is because the two recombination pathways resulting in co-polarized emission directly correspond to the two most efficient formation channels of bright interlayer excitons by optical pumping (Fig. C.3). Other interlayer exciton formation channels, such as that shown in Fig. C.3, require multiple spin and valley flips of carriers, which are not favored. If the electron interlayer hopping is faster than that of the hole, the formation channel via the A exciton in WSe_2 is more efficient. In such a case, under σ^+ excitation, the interlayer exciton will be polarized in the $X_{-,+}$ valley configuration, from which the PL is expected to be σ^+ polarized. On the other hand, if the formation channels via the B exciton in $MoSe_2$ are more efficient, σ^+ excitation will generate the interlayer exciton polarized in the $X_{+,-}$ valley configuration, from which the PL is also σ^+ polarized. If there is AB-like stacking for the samples we have measured (Fig. C.1), the emitted PL is always co-polarized with the incident light, consistent with the expectation.

C.4 Full gate-dependent interlayer exciton valley polarization

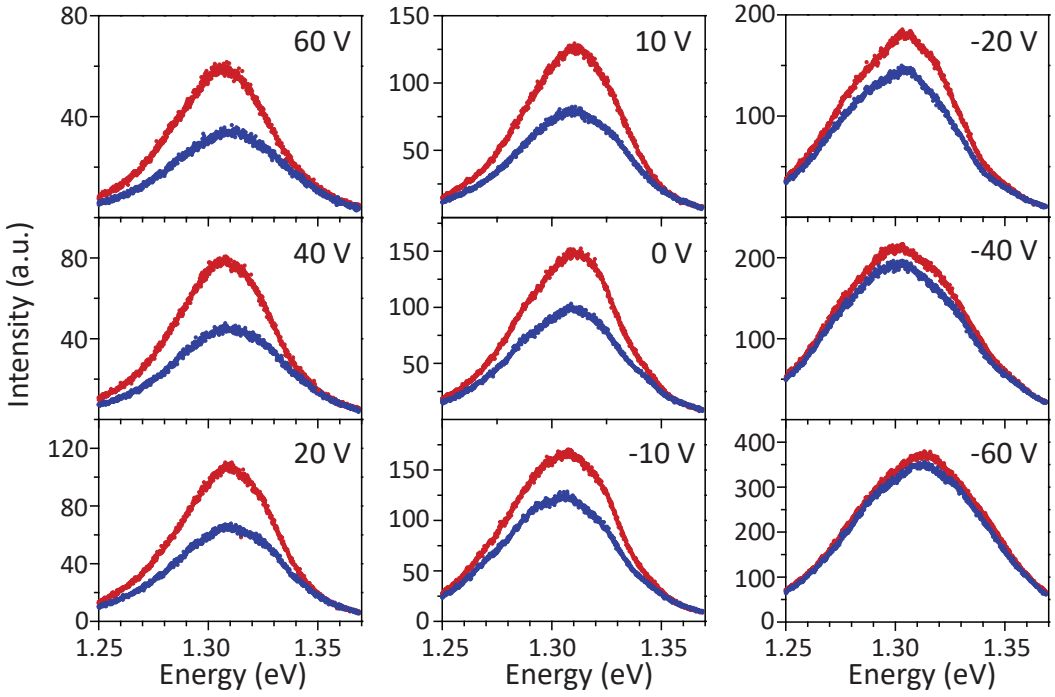

Figure C.4: Gate dependence of interlayer exciton valley polarization. Circular polarization-resolved interlayer exciton PL spectra at various gate voltages for the device presented in the main text. The pulsed laser excitation (5 MHz repetition rate) is σ^+ polarized at 1.72 eV and the co-polarized (black) and cross-polarized (red) components of interlayer exciton PL are detected separately. The degree of valley polarization is largest at high positive gate voltage and becomes nearly negligible at high negative gate voltage. [Adapted from [92].]

C.5 Full gate-dependent valley dynamics

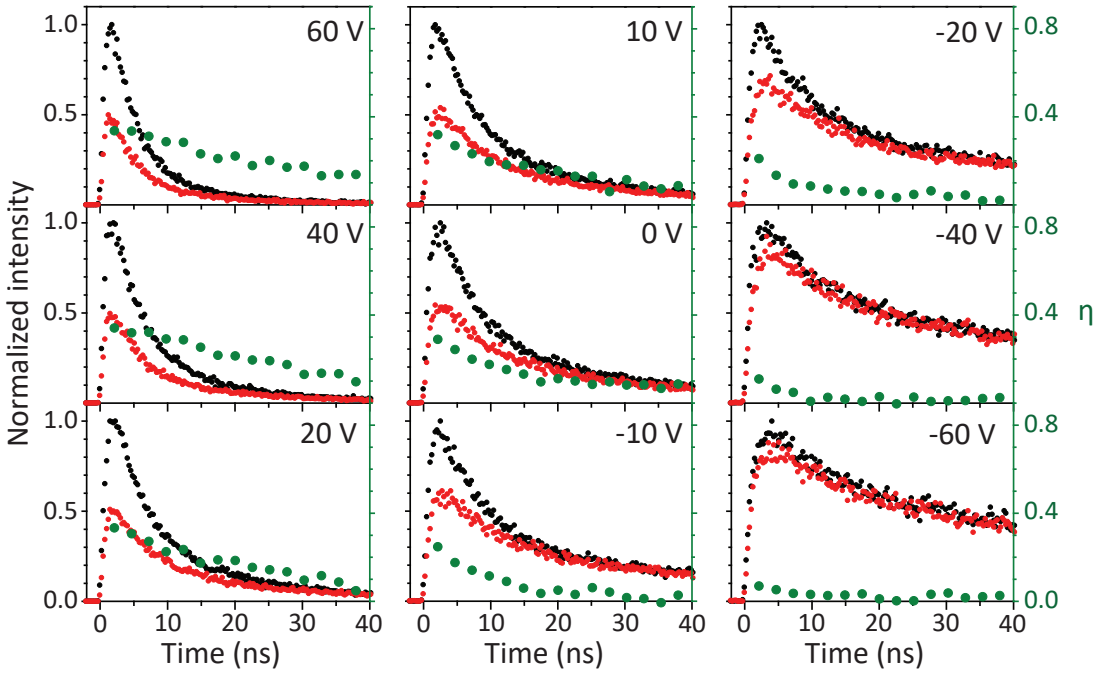

Figure C.5: Gate dependence of polarization dynamics. Time and circular polarization-resolved interlayer exciton PL at various gate voltages under pulsed (100 kHz) σ^+ polarized laser excitation at 1.72 eV for the device in the main text. Co- and cross-polarized emission are shown in black and red, respectively, and the degree of valley polarization is shown in blue. The valley lifetime is longest for large positive gate voltage and decreases with lower gate voltages. At high negative gate voltage, the valley polarization becomes nearly negligible. [Adapted from [92].]

C.6 Valley lifetime in additional heterostructures

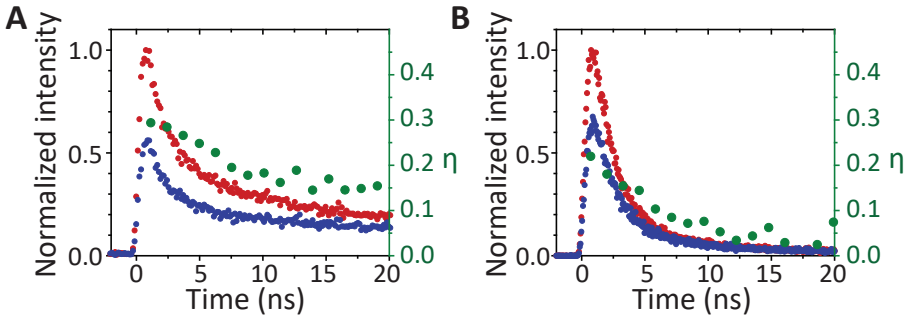

Figure C.6: Valley lifetime in supplementary heterostructures. Time-resolved interlayer exciton PL from two supplementary heterostructures under σ^+ polarized pulsed laser excitation at 1.72 eV. Co-polarized and cross-polarized components of interlayer exciton PL are shown in black and red, respectively, and the degree of valley polarization is shown in blue. The stacking order for these devices is inverted ($MoSe_2$ on WSe_2) compared to the heterostructure in the main text. [Adapted from [92].]

C.7 Exchange and dipole-dipole interactions between interlayer excitons

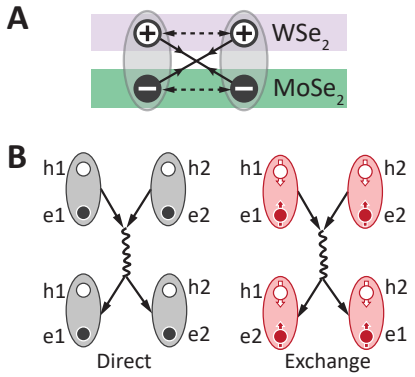

Figure C.7: Interactions between spin-valley polarized interlayer excitons. (A) The interaction between two interlayer excitons. The solid (dashed) double arrows denote the Coulomb attraction (repulsion) between an electron and a hole (two electrons or two holes). (B) Diagram of the valley-independent direct interaction between two excitons (left) and the exchange interaction between two excitons with the same valley indices (right). [Adapted from [92].]

In this section, we discuss the exchange and dipole interactions between interlayer excitons. Following Reference (27), an interlayer exciton in its planewave form with a center-of-mass velocity $\frac{\hbar}{M_0}\mathbf{Q}$ can be expressed in the basis of the free electron-hole Bloch states,

$$\begin{aligned} X_{\tau'\tau,\mathbf{Q}}(\mathbf{r}_e,\mathbf{r}_h) &= \sum_{\Delta\mathbf{Q}} \Phi_I(\Delta\mathbf{Q})\psi_{\tau',\frac{m_e}{M_0}\mathbf{Q}+\Delta\mathbf{Q},c}(\mathbf{r}_e)\psi^*_{\tau,-\frac{m_h}{M_0}\mathbf{Q}+\Delta\mathbf{Q},v}(\mathbf{r}_h) \\ &\approx e^{i\mathbf{Q}\cdot(\frac{m_e}{M_0}\mathbf{r}_e+\frac{m_h}{M_0}\mathbf{r}_h)}\Phi_I(\mathbf{r}_e-\mathbf{r}_h)u_{\tau',0,c}(\mathbf{r}_e)u^*_{\tau,0,v}(\mathbf{r}_h), \end{aligned} \tag{C.1}$$

where $\mathbf{Q}$ is the kinematic momentum of the interlayer exciton and τ (τ') is the electron (hole) valley index. In this expansion, $\psi_{\tau',\Delta\mathbf{Q},c}(\mathbf{r}_e) = e^{i(\tau'\mathbf{K}'+\Delta\mathbf{Q})\cdot\mathbf{r}_e}u_{\tau',\Delta\mathbf{Q},c}(\mathbf{r}_e)$ ($\psi^*_{\tau,\Delta\mathbf{Q},v}(\mathbf{r}_h) = e^{-i(\tau\mathbf{K}+\Delta\mathbf{Q})\cdot\mathbf{r}_h}u^*_{\tau,-\Delta\mathbf{Q},v}(\mathbf{r}_e)$) corresponds to the $\tau'\mathbf{K}'$ ($\tau\mathbf{K}$) valley electron (hole) Bloch function with xy-plane real-space coordinate $\mathbf{r}_e$ ($\mathbf{r}_h$). $\Phi_I(\Delta\mathbf{Q})$ describes the electron-hole relative motion $\Delta\mathbf{Q}$ in momentum space. In the second step above, we have used the envelope approximation $u_{\tau',\Delta\mathbf{Q},c} \approx u_{\tau',\Delta\mathbf{Q}=0,c}$ and $u_{\tau,\Delta\mathbf{Q},v} \approx u_{\tau,\Delta\mathbf{Q}=0,v}$, and a Fourier transform $\Phi_I(\mathbf{r}) \equiv \sum_{\Delta\mathbf{Q}}\Phi_I(\Delta\mathbf{Q})e^{i\Delta\mathbf{Q}\cdot\mathbf{r}}$. In the following discussion, we assume a twisting angle near 0° between the two layers, so X_{++} and X_{--} are spin-allowed optical transitions, while X_{+-} and X_{-+} are spin-forbidden.

Below we consider interlayer excitons in their wave packet forms. Using the wave packet expression one can define the local density that corresponds to the exciton number in an area larger than the wave packet size. We write the real space wavefunction of such an interlayer exciton wave packet

$$\begin{aligned} X_{\tau'\tau,\mathbf{R}}(\mathbf{r}_e,\mathbf{r}_h) &\equiv \sum_{\mathbf{Q}} w_{\mathbf{R}}(\mathbf{Q})X_{\tau'\tau,\mathbf{Q}}(\mathbf{r}_e,\mathbf{r}_h) \\ &\approx w\Big(\frac{m_e}{M_0}\mathbf{r}_e+\frac{m_h}{M_0}\mathbf{r}_h-\mathbf{R}\Big)\Phi_I(\mathbf{r}_e-\mathbf{r}_h)u_{\tau',0,c}(\mathbf{r}_e)u^*_{\tau,0,v}(\mathbf{r}_h). \end{aligned} \tag{C.2}$$

Here $w(\mathbf{r}-\mathbf{R}) \equiv \sum_{\mathbf{Q}} w_{\mathbf{R}}(\mathbf{Q})e^{i\mathbf{Q}\cdot\mathbf{r}}$ describes a real space wavepacket centered at $\mathbf{R}$ whose width W is larger than the interlayer exciton Bohr radius a_B but much smaller than the heterostructure sample size $\sqrt{A}$.

We now consider interactions between two interlayer excitons. The Coulomb interaction between two interlayer excitons is illustrated in Fig. C.7A, where the solid (dashed) double arrows denote attraction (repulsion) between an electron and a hole (two electrons or two holes). We denote the electron (hole) constituent of the n-th exciton as e_n (h_n) with real space coordinate $\mathbf{d}+\mathbf{r}_{e,n}(\mathbf{r}_{h,n})$ and valley index τ'_n (τ_n), where $\mathbf{r}_{e,n}(\mathbf{r}_{h,n})$ lies in the xy-plane and

$\mathbf{d} \equiv d\hat{\mathbf{z}}$ corresponds to the interlayer separation ($\sim$0.7 nm). The exciton-exciton interaction is

$$\hat{V}_{XX} = V(\mathbf{r}_{e1} - \mathbf{r}_{e2}) + V(\mathbf{r}_{h1} - \mathbf{r}_{h2}) + V(\mathbf{d} + \mathbf{r}_{e1} - \mathbf{r}_{h2}) + V(\mathbf{r}_{e2} - \mathbf{r}_{h1}), \tag{C.3}$$

with $V(\mathbf{r})$ being the real space form the Coulomb interaction.

The matrix elements of $\hat{V}_{XX}$ in the two-exciton direct product basis $X_{\tau_1'\tau_1,\mathbf{R}_1}(\mathbf{r}_{e1}, \mathbf{r}_{h1}) \otimes X_{\tau_2'\tau_2,\mathbf{R}_2}(\mathbf{r}_{e2}, \mathbf{r}_{h2})$ can be separated into the dipole-dipole and exchange interaction parts.

Dipole-dipole interaction

First, we consider the dipole-dipole (or direct Coulomb) interaction illustrated in Fig. C.7B, which corresponds to an exciton-exciton scattering process $(e_1, h1) + (e_2, h_2) \rightarrow (e_1, h_1) + (e_2, h_2)$. The direct Coulomb interaction between two interlayer excitons (in wavepacket form) located at $\mathbf{R}_1$ and $\mathbf{R}_2$ is

$$\begin{aligned}
&V_{dd}(\mathbf{R}_1 - \mathbf{R}_2) \\
&\equiv \langle X_{\tau_2'\tau_2,\mathbf{R}_2}(\mathbf{r}_{e2}, \mathbf{r}_{h2}) | \langle X_{\tau_1'\tau_1,\mathbf{R}_1}(\mathbf{r}_{e1}, \mathbf{r}_{h1}) | \hat{V}_{XX} | X_{\tau_1'\tau_1,\mathbf{R}_1}(\mathbf{r}_{e1}, \mathbf{r}_{h1}) \rangle | X_{\tau_2'\tau_2,\mathbf{R}_2}(\mathbf{r}_{e2}, \mathbf{r}_{h2}) \rangle \\
&= \int |u_{\tau_1',0,c}(\mathbf{r}_{e1}) u^*_{\tau_1,0,v}(\mathbf{r}_{h1}) u_{\tau_2',0,c}(\mathbf{r}_{e2}) u^*_{\tau_2,0,v}(\mathbf{r}_{h2}) \\
&\times |w\Big(\frac{m_e}{M_0}\mathbf{r}_{e1} + \frac{m_h}{M_0}\mathbf{r}_{h1} - \mathbf{R}_1\Big) w\Big(\frac{m_e}{M_0}\mathbf{r}_{e2} + \frac{m_h}{M_0}\mathbf{r}_{h2} - \mathbf{R}_2\Big) \Phi_I(\mathbf{r}_{e1} - \mathbf{r}_{h1}) \Phi_I(\mathbf{r}_{e2} - \mathbf{r}_{h2})|^2 \\
&\times (V(\mathbf{r}_{e1} - \mathbf{r}_{e2}) + V(\mathbf{r}_{h1} - \mathbf{r}_{h2}) + V(\mathbf{d} + \mathbf{r}_{e1} - \mathbf{r}_{h2}) + V(\mathbf{r}_{e2} - \mathbf{r}_{h1})) \\
&\times d\mathbf{r}_{e1} d\mathbf{r}_{e2} d\mathbf{r}_{h1} d\mathbf{r}_{h2} \\
&\approx \int |w\Big(\frac{m_e}{M_0}\mathbf{r}_{e1} + \frac{m_h}{M_0}\mathbf{r}_{h1} - \mathbf{R}_1\Big) w\Big(\frac{m_e}{M_0}\mathbf{r}_{e2} + \frac{m_h}{M_0}\mathbf{r}_{h2} - \mathbf{R}_2\Big) \Phi_I(\mathbf{r}_{e1} - \mathbf{r}_{h1}) \Phi_I(\mathbf{r}_{e2} - \mathbf{r}_{h2})|^2 \\
&\times \Big(V(\mathbf{r}_{e1} - \mathbf{r}_{e2}) + V(\mathbf{r}_{h1} - \mathbf{r}_{h2}) + V(\mathbf{d} + \mathbf{r}_{e1} - \mathbf{r}_{h2}) + V(\mathbf{r}_{e2} - \mathbf{r}_{h1})\Big) \\
&\times d\mathbf{r}_{e1} d\mathbf{r}_{e2} d\mathbf{r}_{h1} d\mathbf{r}_{h2}.
\end{aligned} \tag{C.4}$$

Since the width of the interlayer exciton wavefunction is much larger than the interlayer exciton Bohr radius, $W > a_B \gg a$ (a id yhr lattice constant), $w(\mathbf{r} - \mathbf{R})$ and $\Phi_I(\mathbf{r})$ vary slowly with $\mathbf{r}$ compared to $u_{\tau,0,c/v}(\mathbf{r})$. So in the third step above, we approximate $|u_{\tau,0,c/v}(\mathbf{r})|^2$ by its mean value $\int |u_{\tau,0,c/v(\mathbf{r})}(\mathbf{r})|^2 d\mathbf{r} = 1$, and the perioduc part of the Bloch function in the integral can be dropped. For finite interlayer separation $\mathbf{d}$, we can expect $V(\mathbf{r}_{e1} - \mathbf{r}_{e2}) + V(\mathbf{r}_{h1} - \mathbf{r}_{h2}) >$

$V(\mathbf{d}+\mathbf{r}_{e1}-\mathbf{r}_{h2})+V(\mathbf{r}_{e2}-\mathbf{r}_{h1})$ thus $V_{dd}(\mathbf{R}_1-\mathbf{r}_2)>0$ is finite, this is why we call V_{dd} the dipole-dipole interaction between two interlayer excitons. Here we emphasize that V_{dd} is independent of the valley indices of the two excitons.

Exchange interaction

Next, we consider the exchange interactions between two interlayer excitons with the same valley index. From the indistinguishability of Fermions, the two-exciton wavefunction should have an antisymmetrized form

$$\begin{aligned}&\frac{1}{2}\Big(X_{\tau'\tau,\mathbf{R}_1}(\mathbf{r}_{e1},\mathbf{r}_{h1})X_{\tau'\tau,\mathbf{R}_2}(\mathbf{r}_{e2},\mathbf{r}_{h2})-X_{\tau'\tau,\mathbf{R}_1}(\mathbf{r}_{e1},\mathbf{r}_{h2})X_{\tau'\tau,\mathbf{R}_2}(\mathbf{r}_{e2},\mathbf{r}_{h1})\\&-X_{\tau'\tau,\mathbf{R}_1}(\mathbf{r}_{e2},\mathbf{r}_{h1})X_{\tau'\tau,\mathbf{R}_2}(\mathbf{r}_{e1},\mathbf{r}_{h2})+X_{\tau'\tau,\mathbf{R}_1}(\mathbf{r}_{e2},\mathbf{r}_{h2})X_{\tau'\tau,\mathbf{R}_2}(\mathbf{r}_{e1},\mathbf{r}_{h1})\Big)\end{aligned}\tag{C.5}$$

The expectation value $\hat{V}_{XX}$ under this wavefunction then contains two terms. The first term is just the dipole-dipole interaction $V_{dd}(\mathbf{R}_1-\mathbf{R}_2)$ given above, while the second term is

$$\begin{aligned}&V_{ex}(\mathbf{R}_1-\mathbf{R}_2)\\&\quad\equiv-\langle X_{\tau'\tau,\mathbf{R}_2}(\mathbf{r}_{e2},\mathbf{r}_{h1})|\langle X_{\tau'\tau,\mathbf{R}_1}(\mathbf{r}_{e1},\mathbf{r}_{h2})|\hat{V}_{XX}|X_{\tau'\tau,\mathbf{R}_1}(\mathbf{r}_{e1},\mathbf{r}_{h1})\rangle|X_{\tau'\tau,\mathbf{R}_2}(\mathbf{r}_{e2},\mathbf{r}_{h2})\rangle\\&\quad\approx\int\Phi_I(\mathbf{r}_{e1}-\mathbf{r}_{h1})\Phi_I(\mathbf{r}_{e2}-\mathbf{r}_{h2})\Phi_I^*(\mathbf{r}_{e1}-\mathbf{r}_{h2})\Phi_I^*(\mathbf{r}_{e2}-\mathbf{r}_{h1})\\&\quad\times w^*\Big(\frac{m_e}{M_0}\mathbf{r}_{e2}+\frac{m_h}{M_0}\mathbf{r}_{h1}-\mathbf{R}_2\Big)w^*\Big(\frac{m_e}{M_0}\mathbf{r}_{e1}+\frac{m_h}{M_0}\mathbf{r}_{h2}-\mathbf{R}_1\Big)\\&\quad\times w\Big(\frac{m_e}{M_0}\mathbf{r}_{e1}+\frac{m_h}{M_0}\mathbf{r}_{h1}-\mathbf{R}_1\Big)w\Big(\frac{m_e}{M_0}\mathbf{r}_{e2}+\frac{m_h}{M_0}\mathbf{r}_{h2}-\mathbf{R}_2\Big)\\&\quad\times\Big(V(\mathbf{d}+\mathbf{r}_{e1}-\mathbf{r}_{h2})+V(\mathbf{r}_{e2}-\mathbf{r}_{h1})-V(\mathbf{r}_{e1}-\mathbf{r}_{e2})-V(\mathbf{r}_{h1}-\mathbf{r}_{h2})\Big)\\&\quad\times d\mathbf{r}_{e1}d\mathbf{r}_{e2}d\mathbf{r}_{h1}d\mathbf{r}_{h2}.\end{aligned}\tag{C.6}$$

This corresponds to the exciton-exciton scattering process $(e_1,h1)+(e_2,h_2)\rightarrow(e_1,h_2)+(e_2,h_1)$, where either the electron or the hole constituent are exchanged between the two excitons. For two excitons with the same valley indices ($\tau_1'=\tau_2'=\tau$ and $\tau_1=\tau_2=\tau$), this exchange process corresponds to a diagonal energy, i.e. an interaction energy between the excitons. Importantly, we note that V_{ex} is present only between two excitons with the same valley index. This is in contrast to the dipole-dipole interaction V_{dd}, which is valley independent.

The exchange of electrons or holes can happen only when the two interlayer excitons are

in contact with each other, i.e. V_{ex} is only appreciable when the two wave packets have substantial overlap. With a large enough separation between the wave packets ($|\mathbf{R}_1 - \mathbf{R}_2| \gg W$), the exchange interaction decays as $V_{ex}\left(w^*\left(\frac{m_h}{M_0}(\mathbf{R}_1 - \mathbf{R}_2)\right)\right)^2\big(V(\mathbf{d}+\mathbf{R}_1+\mathbf{R}_2) - V(\mathbf{R}_1 - \mathbf{R}_2)\big)$, which is exponentially small.

We note that the Coulomb exchange interaction also results in another process, as shown in Figure S12D: when the two bright interlayer excitons are from different valleys (X_{++} and X_{--}), they will be scattered to become a pair of dark excitons X_{+-} and X_{-+}. This can be phenomenologically described as population decay of the bright excitons and has negligible effect on the spatial pattern of polarization.

Density-dependent energy shift from the exciton-exciton interaction

Here we use the mean field approximation and only consider the diagonal terms for the exciton-exciton interaction. For a heterostructure sample with spatially inhomogeneous X_{++} density $N_+(\mathbf{r})$ and X_{--} density $N_-(\mathbf{r})$, an X_{++} (X_{--}) wavepacket at position $\mathbf{R}$ feels a mean potential from both the dipole-dipole and exchange interactions,

$$\begin{aligned}
\Delta E_\pm(\mathbf{R}) &= \int V_{ex}(\mathbf{R}-\mathbf{r})N_\pm(\mathbf{r})d\mathbf{r} + \int V_{dd}(\mathbf{R}-\mathbf{r})\big(N_+(\mathbf{r}) + N_-(\mathbf{r})\big)d\mathbf{r} \\
&= \left(\frac{\int V_{ex}(\mathbf{R}-\mathbf{r})N_\pm(\mathbf{r})d\mathbf{r}}{\int V_{ex}(\mathbf{R}-\mathbf{r})d\mathbf{r}}\right)\int V_{dd}(\mathbf{R}-\mathbf{r})d\mathbf{r} \\
&+ \left(\frac{\int V_{dd}(\mathbf{R}-\mathbf{r})\big(N_+(\mathbf{r}) + N_-(\mathbf{r})\big)d\mathbf{r}}{\int V_{dd}(\mathbf{R}-\mathbf{r})d\mathbf{r}}\right)\int V_{dd}(\mathbf{R}-\mathbf{r})d\mathbf{r} \\
&\approx N_\pm(\mathbf{R})\overline{V}_{ex} + \big(N_+(\mathbf{R}) + N_-(\mathbf{R})\big)\overline{V}_{dd}.
\end{aligned} \tag{C.7}$$

In the last step above, we have used the fact that $N_\pm(\mathbf{R})$ varies rather slowly with in the typical micron length scale of the experiment, and V_{ex} has a contact nature, so $\frac{\int V_{ex}(\mathbf{R}-\mathbf{r})N_\pm(\mathbf{r})d\mathbf{r}}{\int V_{ex}(\mathbf{R}-\mathbf{r})d\mathbf{r}} \approx \frac{V_{dd}(\mathbf{R}-\mathbf{r})N_\pm(\mathbf{r})d\mathbf{r}}{\int V_{dd}(\mathbf{R}-\mathbf{r})d\mathbf{r}} \approx N_\pm(\mathbf{R})$. $\overline{V}_{ex/dd} \equiv \int V_{ex/dd}(\mathbf{R}-\mathbf{r})d\mathbf{r}$ are two constants independent of $\mathbf{R}$ that will be estimated in the next subsection.

Eq. C.7 above is the central result of the entire section 2.11 which makes clear that for sufficiently dense populations of interlayer excitons, the potential landscape depends on both dipole-dipole and exchange interactions. Since the exchange interactions are only present between excitons in the same valley, in the presence of valley polarization ($N_+(\mathbf{r})$ differs from $N_-(\mathbf{r})$, the spatially dependent potential $\Delta E(\mathbf{R})$ due to the exciton-exciton interaction is different for X_{--} and X_{++}, which then corresponds to a valley-dependent driving force

for the exciton expansion.

Qualitative estimation of the dipole-dipole and exchange interaction

We note that $\overline{V}_{ex/dd} \equiv \int V_{ex/dd}(\mathbf{R}-\mathbf{r})d\mathbf{r}$ corresponds to the interaction between two excitons in planewave forms. For spatially indirect exciton in coupled quantum wells with homogeneous ϵ, references (40-43) have already calculated such $\overline{V}_{ex/dd}$ using the hydrogen model with $1/r$ Coulomb law ($V(\mathbf{r}) = e^2/\epsilon r$). For a qualitative estimation below, we first directly quote their results, then qualitatively discuss the difference between the indirect exciton in coupled quantum wells and the interlayer exciton in transition metal dichalcogenide heterobilayers.

We note that in the hydrogen model the dipole-dipole interaction has the form $V_{dd}(\mathbf{R}) \propto \frac{1}{R} - \frac{1}{\sqrt{R^2+d^2}}$, where $\frac{1}{R}$ comes from the e-e and h-h repulsion while $\frac{-1}{\sqrt{R^2+d^2}}$ is from e-h attraction. When $R \gg d$, $V_{dd}(\mathbf{R}) \propto R^{-3}$ becomes the conventional form for the dipole-dipole interaction. The integral is evaluated as $\overline{V}_{dd} \equiv \int V_{dd}(\mathbf{R})d\mathbf{R} = \frac{e^2}{\epsilon}\int\left(\frac{1}{R} - \frac{1}{\sqrt{R^2+d^2}}\right)RdR = \frac{de^2}{\epsilon}$, which increases linearly with d.

The exchange interaction has a more complicated form and should be evaluated numerically, so we only give an approximate result here: $\overline{V}_{ex} \approx \left(1 - \frac{d}{0.66a_0}\right)\frac{6a_0e^2}{\epsilon}$. It also has an approximately linear dependence on d, where a_0 is the 2D hydrogen model Bohr radius of the intralayer exciton. For small d, V_{ex} is positive which means the exchange interaction is repulsive for two excitons in the same valley. V_{ex} decreases about linearly with d and crosses zero at $d \approx 0.66a_0$.

In the layered structure of transition metal dichalcogenides, however, the dielectric constant ϵ is anisotropic (ϵ in the in-plane direction is much larger than that of the out-of-plane direction), so a simple hydrogen model with $1/r$ Coulomb law is not accurate (44). The exact forms of $\overline{V}_{ex/dd}$ should be more complicated, but nevertheless we can still analyze how they deviate from the above hydrogen model results. Since ϵ in the out-of-plane direction is small, $V(\mathbf{d}+\mathbf{r}_e-\mathbf{r}_h)$ should have a slower decay with d compared to the hydrogen model with isotropic ϵ. This has opposite effects on V_{dd} and V_ex. As shown in the Eq. C.4, in V_{dd}, the electron-hole interaction $V(\mathbf{d}+\mathbf{r}_e-\mathbf{r}_h)$ partially cancels the electron-electron and hole-hole interaction energy. On the other hand, for small d, $V_{ex} > 0$, the repulsive exchange interaction $\overline{V}_{ex}$ mainly originates from the electron-hole interaction $V(\mathbf{d}+\mathbf{r}_e-\mathbf{r}_h)$, as shown in Eq. C.5. Therefore, at given interlayer separation d, the hydrogen model overestimates $\overline{V}_{dd}$ and underestimates $\overline{V}_{ex}$.

Since the layer separation d ($\sim$0.7 nm) is small compared to the Bohr radius of the

intralayer exciton, a_0 ($\sim$1 nm to 3 nm), it only slightly reduces the direct Coulomb interaction between electron and hole that forms the interlayer exciton. For an order of magnitude estimation of $\overline{V}_{ex}$ and $\overline{V}_{dd}$, we assume that the Bohr radius and binding energy of interlayer exciton have the same order of magnitudes as the intralayer excitons in monolayers. From this, we can do an order of magnitude estimation of $\overline{V}_{ex}$ and $\overline{V}_{dd}$, which results in $\overline{V}_{ex} \sim a_0 e^2/\epsilon \sim a_0^2 E_b > 0$, and $0 < \overline{V}_{dd} \lesssim de^2/\epsilon \sim da_0 E_b$, where $E_b \sim e^2/\epsilon a_0 \sim 0.5\,\text{eV}$ is the intralayer exciton binding energy. Therefore, we expect that the exchange and dipole-dipole interactions are both repulsive.

C.8 Interlayer exciton drift-diffusion model and simulation

Consider the heterostructure system with spatial- and time-dependent density X_{++} density $N_+(\mathbf{r},t)$ and X_{--} density $N_-(\mathbf{r},t)$. As described in the previous section, the X_{++} exciton at $\mathbf{r}$ feels a mean potential from both the valley-dependent exchange and valley-independent dipole-dipole interactions, $\overline{V}_{ex}N_+(\mathbf{r},t)+\overline{V}_{dd}(N_+(\mathbf{r},t)+N_-(\mathbf{r},t))$. Similarly, the X_{--} exciton at $\mathbf{r}$ feels a mean potential $\overline{V}_{ex}N_-(\mathbf{r},t) + \overline{V}_{dd}(N_+(\mathbf{r},t) + N_-(\mathbf{r},t))$. The gradient in the density-dependent potential leads to a force on the interlayer excitons, imparting them with a drift velocity $V_{\pm,drift} = -\alpha_0\nabla N_\pm - \beta_0\nabla N_\mp$. Here the parameters $\alpha_0 \equiv \frac{\mu}{e}(\overline{V}_{ex} + \overline{V}_{dd}) \sim \frac{\mu}{e}(a_0+d)a_0E_b$ and $\beta_0 \equiv \frac{\mu}{e}\overline{V}_{dd} \lesssim \frac{\mu}{e}da_0E_b$ based on the previous section. A mobility value of $\mu \sim 50\,\text{cm}^2\,\text{V}^{-1}\,\text{s}^{-1}$ corresponds to $\alpha_0 \sim 10^{-5}\,\mu\text{m}^4\text{ns}^{-1}$. For β_0, currently we only know that $\beta_0 < \alpha_0$, but considering the ambiguity of the α_0 value and the non-hydrogenic corrections discussed in the last section, there could be $\overline{V}_{ex} \gg \overline{V}_{dd}$ and $\alpha_0 \gg \beta_0$. Accordingly, we choose $\alpha_0 = 5\beta_0$ for simulation purposes.

The expansion of the two-valley interlayer excitons under laser generation profile $G_\pm(\mathbf{r},t)$ is described by the drift-diffusion model:

$$\frac{\partial N_\pm}{\partial t} = I_\pm + D\nabla^2 N_\pm + \nabla\cdot\big((\alpha_0\nabla N_\pm + \beta_0\nabla N_\mp)N_\pm\big) - \frac{N_\pm}{\tau} - \frac{N_\pm - N_\mp}{\tau_v}. \tag{C.8}$$

The second term on the right-hand side corresponds to the density-dependent diffusion of the interlayer excitons, and $D = \mu k_B T/e \sim 0.01\,\mu\text{m}^2\,\text{ns}^{-1} = 0.1\,\text{cm}^2\,\text{s}^{-1}$ (at $T \sim 30\,\text{K}$) is the diffusion constant. The third term is of primary interest, as it captures the exchange and dipole-dipole interaction driven drift of the valley interlayer excitons $X_{\pm\pm}$, manifesting the excitonic drift current $-(\alpha_0\nabla N_\pm + \beta_0\nabla N_\mp)N_\pm$. The final two terms capture radiative decay and the valley relaxation, with τ the exciton lifetime and τ_v the valley polarization lifetime.

We note that processes such as biexciton formation, Auger scattering, and the population relaxation between bright and dark excitons are not included in this model, which can be oversimplified for a quantitative comparison with experiment. Nevertheless, the main qualitative features observed (i.e. the ring-like polarization pattern) can be well-reproduced using reasonable parameters, where the valley-dependent exchange and the valley-independent dipole-dipole repulsive interactions are the main causes.

For the pulsed laser with a very short duration, we write the exciton density distribution just after the pulse as $N_+(\mathbf{r}, t = 0) = N_0 e^{-r^2/a^2}$ and $N_-(\mathbf{r}, t = 0) = \delta N_0 e^{-r^2/a^2}$, with N_0 the peak exciton density and a the laser half-width. Let the dimensionless variable $\rho_\pm(\mathbf{r}, t) \equiv N_\pm(\mathbf{r}, t)/N_0$, then the evolution is governed by

$$\frac{\partial \rho_\pm}{\partial t} = D\nabla^2 \rho_\pm + \nabla \cdot \big((\alpha_0 \nabla \rho_\pm + \beta_0 \nabla \rho_\mp)\rho_\pm\big) - \frac{\rho_\pm}{\tau} - \frac{\rho_\pm - \rho_\mp}{\tau_v}. \tag{C.9}$$

In the above, we have written $\alpha \equiv N_0\alpha_0$ and $\beta \equiv N_0\beta_0$. Under a peak density $N_0 \sim 10^{12}$ to $10^{13}\,\mathrm{cm}^{-2}$, $\alpha \sim 0.1$ to $1\,\mu\mathrm{m}^2\,\mathrm{ns}^{-1}$. Simulation results are presented in the following section.

For the simulations, we use $a = 420\,\mathrm{nm}$, $\tau = 10\,\mathrm{ns}$, $\tau_v = 40\,\mathrm{s}$, $\alpha_0 = 10 \times 10^{-6}\,\mu\mathrm{m}^4\mathrm{ns}^{-1}$, $\beta_0 = 2 \times 10^{-6}\,\mu\mathrm{m}^4\mathrm{ns}^{-1}$, $D = 0.005\,\mu\mathrm{m}^2\mathrm{ns}^{-1}$, and $\delta = 0.2$. For Fig. 4.10C, we show the results for excitation powers P_0, $10P_0$, and $60P_0$, which have corresponding densities of $0.0012\,\mathrm{nm}^{-2}$, $0.009\,\mathrm{nm}^{-2}$ and $0.023\,\mathrm{nm}^{-2}$. The densities are estimated from the power-dependent PL intensity in Fig. 4.9, which saturates with power.

Appendix D

SUPPLEMENTARY MATERIAL FOR MOIRÉ INTERLAYER EXCITON EXPERIMENTS

The following section provides supporting experimental data for Chapter 5.

D.1 Interlayer exciton g-factors

As discussed in Chapter 5 (Figs. 5.4A, B), the Zeeman shift of the conduction or valence band edges has three contributions: spin ($\Delta_s = 2s_z\mu_B B$), atomic orbital ($\Delta_a = l_i\mu_B B$), and a valley contribution ($\Delta = \tau\alpha_i\mu_B B$) from the Berry phase effect. Here, $\tau = \pm 1$ is valley index, $s_z = \pm 12$ is electron spin index, μ_B is Bohr magneton. $\alpha_c = m_0/m_e^*$ and $\alpha_v = m_0/m_h^*$ are the valley g-factors for the conduction and valence bands, respectively, according to a simplified 2-band $\mathbf{k}.\mathbf{p}$ description of the band edges [28] with m_e^* (m_h^*) the electron (hole) effective mass and m_0 the free electron mass. The two spin-split conduction bands have close effective masses, so we expect their α_c values to be about the same. $l_c = 0$ and $l_v = 2\tau$ are the magnetic quantum number for the atomic orbitals at the conduction and valence band edges.

For spin-conserved optical transitions, the electron and hole spin contributions to the interlayer exciton Zeeman shift cancel with each other, and only Δ_a and Δ_v are important. For near 0° stacking, the bright interlayer exciton has two configurations with valley pairing $(\tau_c, \tau_v) = (+,+)$ and $(-,-)$, whose Zeeman shifts are $-(2 + \alpha_v - \alpha_c)\mu_B B$ and $(2 + \alpha_v - \alpha_c)\mu_B B$, respectively. For near 60° or 21.8° stacking, the bright interlayer exciton has two configurations with the valley pairing $(\tau_c, \tau_v) = (-,+)$ and $(+,-)$, whose Zeeman shifts are $-(2+\alpha_v+\alpha_c)\mu_B B$ and $(2+\alpha_v+\alpha_c)\mu_B B$, respectively. From the measured exciton g-factors, we have

$$2|2 + \alpha_v - \alpha_c| \approx 6.7, \tag{D.1}$$

$$2|2 + \alpha_v + \alpha_c| \approx 15.9, \tag{D.2}$$

which lead to $\alpha_v \approx 3.65$ in WSe_2 and $\alpha_c \approx 2.3$ in $MoSe_2$.

The sign of the g-factor depends on how the Zeeman splitting is defined. If the Zeeman splitting is defined as the energy of the $(\tau_c, +)$ interlayer exciton minus that of $(-\tau_c, -)$, i.e. according to the hole valley index, then the obtained g-factors should always be negative, i.e., given by $-2(2+\alpha_v-\alpha_c)$ or $-2(2+\alpha_v+\alpha_c)$. However, in the experiments, our observable to distinguish the time-reversal pair of valley configurations is the PL polarization only, so the Zeeman splitting is defined here as the σ^+ PL peak energy minus σ^- PL peak energy. The valley optical selection rule, namely whether $(\tau_c, +)$ emits σ^- or σ^+ photon, then determines the sign of the g-factor.

As pointed out in earlier works [137–140], the circularly polarized valley optical selection rules for interlayer excitons depend on the interlayer registry and hence the location in a moiré supercell. Taking the $(+,+)$ interlayer exciton in a near 0° moiré pattern as an example, it emits a σ^+ (σ^-) photon at the A (B) trapping sites of the moiré potential which has the interlayer registry R_h^h (R_h^X). Here, R_h^μ denotes a 0° lattice-matched stacking, with the μ site of the electron layer vertically aligned with the hexagon center (h) of the hole layer. Interlayer excitons trapped at A and B sites then have g-factors with minus and plus signs, respectively.

For the sample with 57° (2°) twist angle, our measured g-factor of -15.9 (6.7) implies that the PL emission is from interlayer excitons localized at A (B) trapping site of the moiré supercell. The different signs of the g-factors are also consistent with the co-circular PL polarization for 57° and 20° samples and cross-circular polarization for the 2° sample. For example, when exciting at the monolayer exciton resonance in WSe_2 with a σ^+ laser, most of the excited holes will reside in the $+K$ valley. The majority interlayer exciton species is then the $(+,+)$ valley pairing in the 2° sample and $(-,+)$ valley pairing in 57° and 20° samples. At low temperature, the valley-polarized interlayer excitons will relax to the local energy minima, that is, A trapping sites in 57° and 20° samples (B sites in 2° sample), which emit σ^+ (σ^-) circularly polarized PL, i.e. co-polarized (cross-polarized) with the excitation laser, consistent with the experiment.

In the above analysis, we considered only the excitons of the spin-conserved optical transitions, also known as the spin-singlet excitons. In samples with near 0° twist angle, we expect the PL emission is always from the spin-singlet interlayer exciton that is bright and has the lowest energy. However, in samples with near 60° or 21.8° twist angles, the lowest energy interlayer excitons have the spin-triplet configuration due to the $MoSe_2$ conduction band spin alignment. In heterobilayers, despite its spin-flip nature, the optical dipole of the spin-triplet

exciton can be comparable to that of the spin-singlet one [139]. It is therefore possible that the PL emission from these samples arises from the spin-flip optical transitions of the spin-triplet exciton. In such case, the spin contribution to the exciton Zeeman shift are finite, and the total shifts become $-(4+\alpha_v+\alpha_c)\mu_B B$ and $(4+\alpha_v+\alpha_c)\mu_B B$ respectively for $(\tau_c,\tau_v) = (-,+)$ and $(+,-)$. The measured g-factor then gives us the equation: $2|4+\alpha_v+\alpha_c| \approx 15.9$. Combined with $2|2+\alpha_v-\alpha_c| \approx 6.7$ from the 0° samples, these yield $\alpha_v \approx 2.65$ in WSe_2 and $\alpha_c \approx 1.3$ in $MoSe_2$. The spin-triplet interlayer excitons also have circularly polarized valley optical selection rules at the moiré trapping sites as dictated by the rotational symmetry5, and our previous discussion about g-factor signs still applies.

D.2 Heterobilayer moiré pattern for a twist angle close to 21.8°

For two transition metal dichalcogenide layers with the same lattice constant a, a twist angle of 21.8° corresponds to a commensurate pattern with the smallest supercell size ($\sqrt{7}a \times \sqrt{7}a$). Like the 0° or 60° lattice-matched case, here the commensurate 21.8° bilayer also has an interlayer translation degree of freedom, which defines the different stacking configurations. In Figs. D.8A-C, we show three C_3-symmetric stacking at 21.8°. In Fig. D.8A, the stacking corresponds to a metal site (M) in the electron layer overlapped with a metal site in the hole layer. In Fig. D.8B, a hexagon center (h) in the electron layer overlaps with a hexagon center in the hole layer. In Fig. D.8C, a chalcogen site (X) in the electron layer overlaps with a chalcogen site in the hole layer. In the 21.8° heterobilayer of the stacking in (A), (B) and (C), a spin-singlet interlayer exciton with the valley pairing $(\tau_c,\tau_v) = (-,+)$ then has the C_3 quantum numbers $+1$, -1, and 0 respectively [138, 139]. This implies that for the stacking in (A), the $(-,+)$ interlayer exciton can emit a σ^+ circularly polarized photon, whereas for the stacking in (B), it can emit a σ^- circularly polarized photon.

The slight deviation $\delta\theta$ of the twist angle from the commensurate 21.8° will give rise to a concatenated moiré pattern. Different local regions correspond to 21.8° commensurate stacking of different interlayer translation, as shown in Fig. D.8D, where the A, B and C locales correspond to the stacking pattern in (A), (B) and (C), respectively. The moiré periodicity is given by $\frac{a}{\sqrt{7}\delta\theta}$. Meanwhile, the stacking-dependent interlayer hopping can lead to the periodic change of electronic band gaps6, which gives rise to a spatially modulated excitonic potential $E(R)$, where R is the center position of the localized interlayer exciton. At locations A, B or C, the C_3 symmetry requires $\nabla_{\mathbf{R}} E(R) = 0$, which means they correspond to energy extrema. Thus, an interlayer exciton will be localized at A, B or C trapping sites

in near 21.8° moiré pattern.

D.3 Supplementary Figures

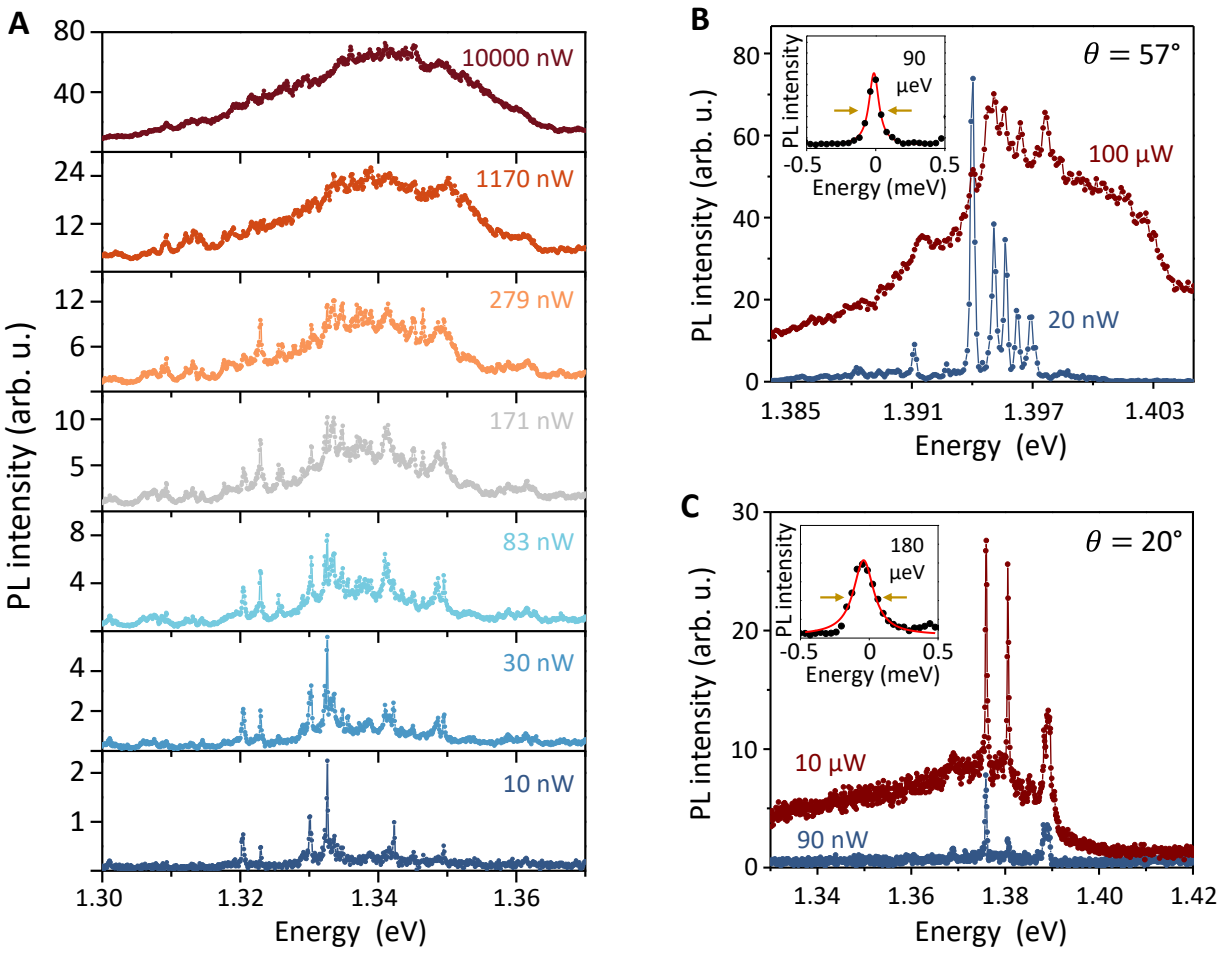

Figure D.1: Supplementary power dependence data. (A) Interlayer exciton PL spectra at selected excitation powers for $\theta = 2°$ sample of device 1. (B), (C), PL spectra at low versus high power (indicated on the figure) for $\theta = 57°$ of device 2 (B) and $\theta = 20°$ of device 1 (C). Insets: Lorentzian fit to representative PL peaks with the indicated linewidths.

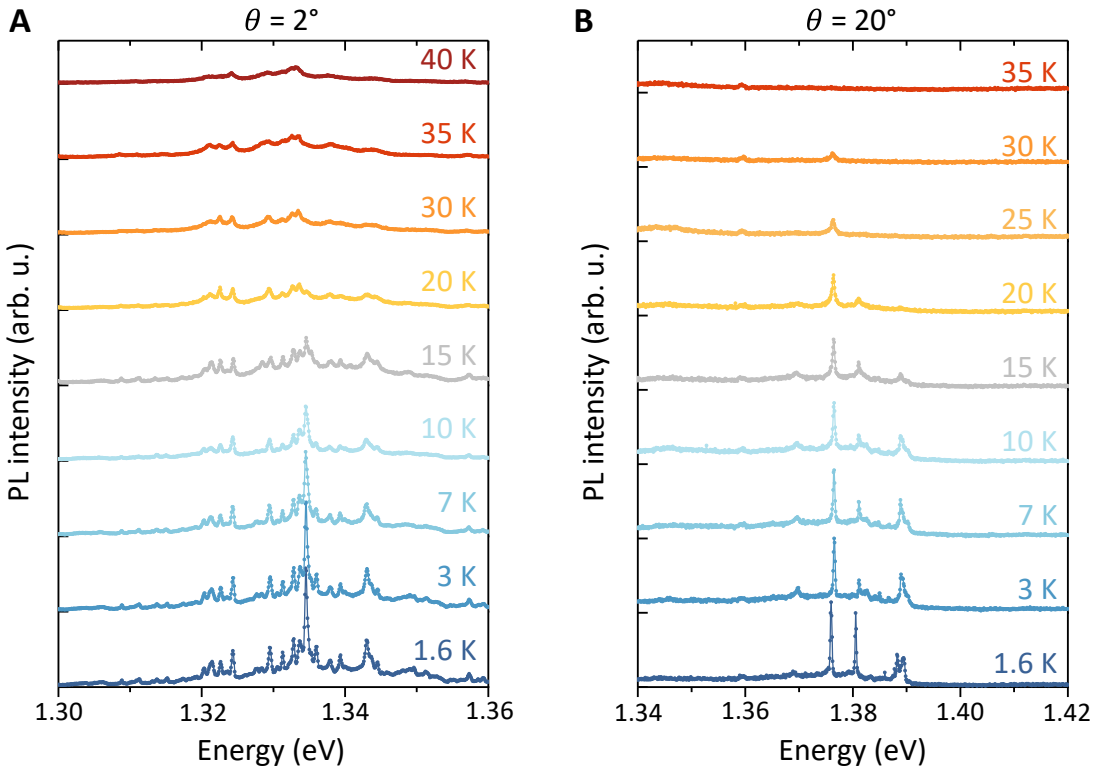

Figure D.2: Temperature-dependent PL. (A), (B), Temperature dependence of the interlayer exciton PL spectra for $\theta = 2°$ (A) and $\theta = 20°$ (B) samples of device 1. The excitation powers were 20 nW (A) and 1 W (B).

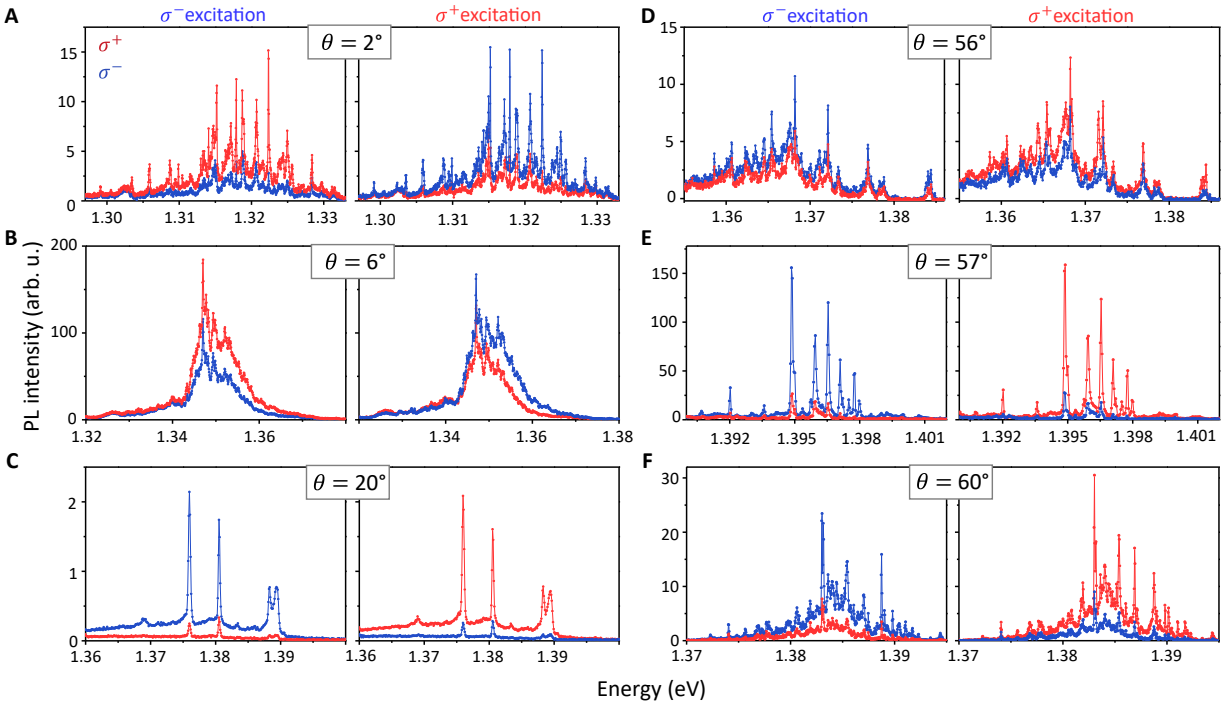

Figure D.3: Supplementary circular-polarization-resolved PL spectra. Each subfigure represents data from a different sample with the indicated twist angle. The left and right columns of each subfigure correspond to σ^- and σ^+ polarized excitation. The red and blue curves indicate σ^+ and σ^- polarized PL components. Spectra from the $\theta = 2°$ and $\theta = 20°$ region of device 1 in the main text are shown in (A) and (C), while $\theta = 6°$ and $\theta = 57°$ from device 2 are shown in (B) and (E). The $\theta = 2°$ spectra in (A) were acquired on a different sample region from that of the spectra in main text, which shows similarly strong polarization reversal. The spectra in (D) and (F) are from additional heterobilayers. The twist angle uncertainty is 1°.

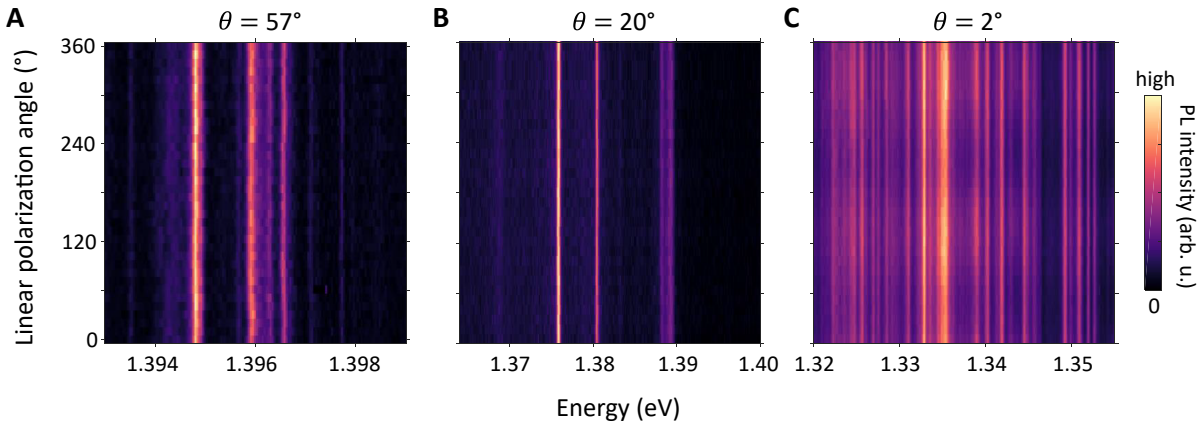

Figure D.4: Linear-polarization-resolved PL. (A)-(C), PL intensity plots as a function of the linear polarization detection angle and photon energy under linearly polarized excitation for $\theta = 57°$ (A), 20° (B), and 2° (C). No linear PL polarization is observed.

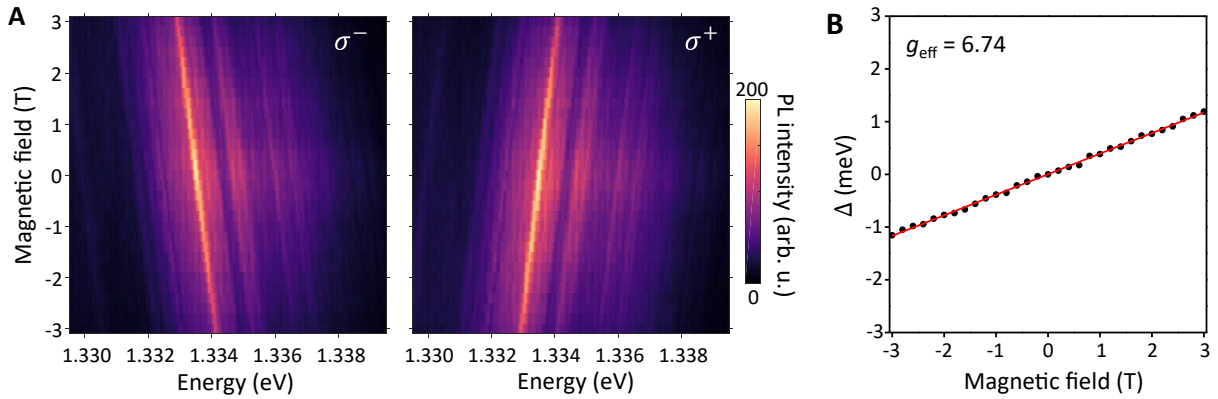

Figure D.5: Free and trapped interlayer exciton g-factor for $\theta \approx 0°$. The data is acquired on the $\theta = 6°$ region of device 2. (A), PL intensity plot of σ^+ (right) and σ^- (left) components as a function of applied magnetic field and photon energy. The broad background (free exciton) clearly shifts with same slope as the sharp trapped interlayer exciton on top. (B), Valley splitting versus applied magnetic field, from which a g-factor of 6.74(5) is extracted from a linear fit to Δ versus B (red solid line).

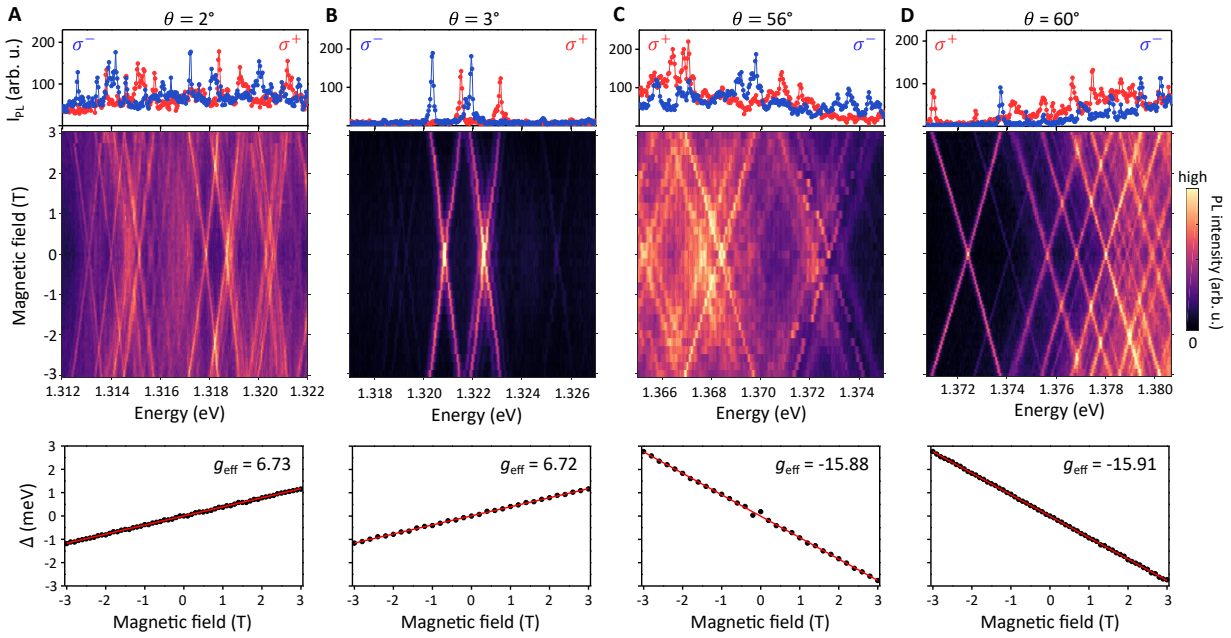

Figure D.6: Uniformity of *g*-factors. (A)-(D), Magneto-PL of 2° (A), 3° (B), 56° (C), and 60° (D) heterobilayers. The data in the 2° heterobilayer (A) was taken at a different spot from the one in the main text. The excitation is linearly polarized. Top row: Circularly polarized PL spectra at 3 T. Middle row: PL intensity as a function of applied magnetic field, which display a clear linear Zeeman shift of the σ^+ and σ^- components. Bottom row: Valley Zeeman splitting versus applied magnetic field. Linear fits (red solid lines) yield effective g-factors of heterobilayers at different twist angle, which are 6.73(2), 6.72(3), −15.88(9), and −15.91(2) for (A)-(D). The data confirm the g-factor uniformity across the same sample as well as different samples with similar twist angle.

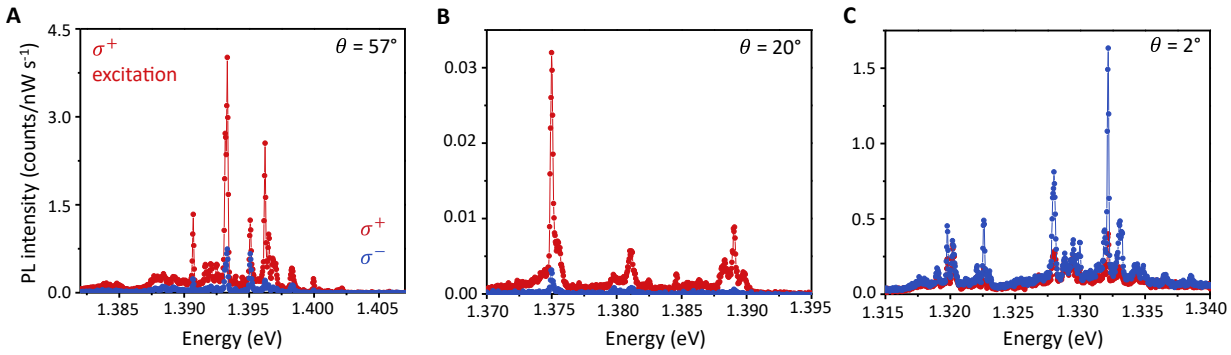

Figure D.7: Calibrated PL spectra to compare PL intensity from heterobilayers with different twist angles. The measurement reveals the PL intensity of $= 2°$ and $57°$ is about 100 times stronger than that of $\theta = 20°$. Excitation powers were 10 nW for (A) and (C) and 100 nW for (B). The PL intensity for $\theta = 20°$ heterobilayer is still in the linear regime for powers less than 100 nW. Aside from the excitation power, the data from all three twist angles were acquired in identical experimental conditions to facilitate their comparison.

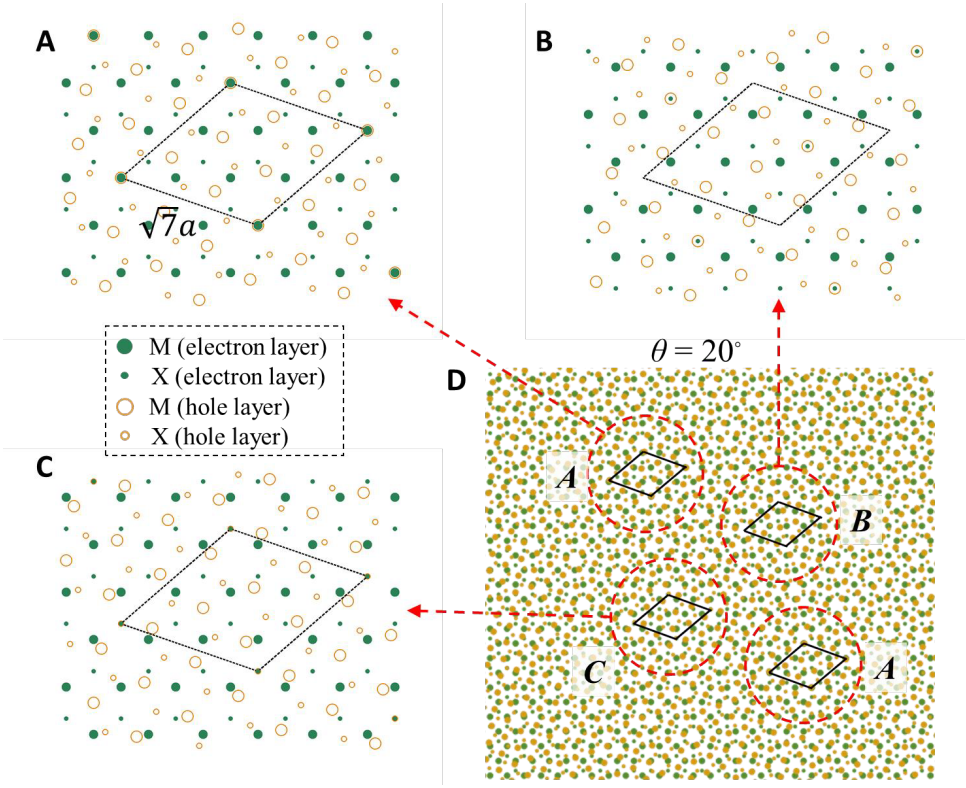

Figure D.8: Heterobilayer moiré pattern for twist angle close to 21.8°**.** (A)-(C), Three high-symmetry stacking patterns under the commensurate 21.8° twist angles for two layers with the same lattice constant a. The dashed diamonds give the smallest supercells, whose periodicity is $\sqrt{7}a$. The large (small) solid green dots denote the metal or M (chalcogen or X) sites in the electron layer, while the large (small) empty orange dots denote the metal or M (chalcogen or X) sites in the hole layer. (A) is the stacking where two M sites in different layers horizontally overlap. (B) is the stacking where two hexagon centers (h sites) in different layers horizontally overlap. (C) is the stacking where two X sites in different layers horizontally overlap. Because M, X and h are the C_3 rotation centers of the monolayers, the stacking in (A), (B) and (C) are all C_3 symmetric. (D) Illustration of the moiré pattern when the twist angle slightly deviates from 21.8° ($\theta = 20^\circ$ here). Red circles marked by A, B and C are the local regions nearly indistinguishable from the 21.8° commensurate pattern in (A), (B) and (C), respectively. The black diamonds are the $\sqrt{7}a \times \sqrt{7}a$ supercells of the local regions.

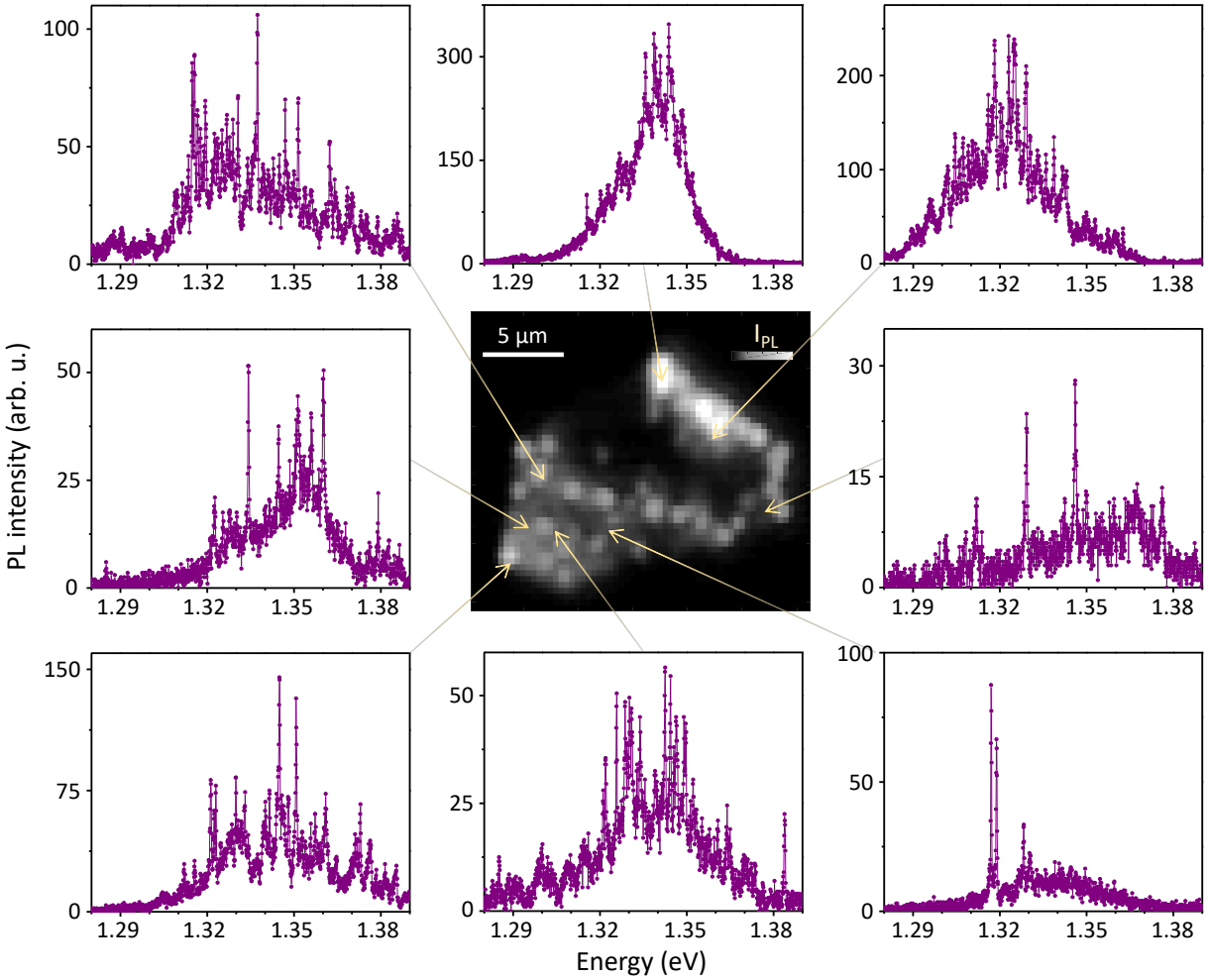

Figure D.9: Spatial homogeneity of interlayer exciton PL. The center image displays a spatial map of the integrated PL for the $\theta = 2°$ heterobilayer and the plots along the outside show selected interlayer exciton PL spectra at different sample locations. The PL is bright across a wide region of the sample, except along one edge of a crack that runs through the sample (note correspondence to sample height map in Fig.5.1C). Narrow-line PL emission is a general feature of the PL spectra across the sample, as seen in the selected spectra from spatially distinct regions of the sample. The number of narrow-line peaks, their intensities, and their energy distribution is inhomogeneous across the sample. The origin of this inhomogeneity is an important topic for further study.

Appendix E

SUPPLEMENTARY MATERIAL FOR CrI_3 EXPERIMENTS

The following text provides supporting experiments and theory for Chapter 6, reprinted from the supplementary information of [172].

E.1 PL from monolayer CrI_3 on SiO_2/Si substrate

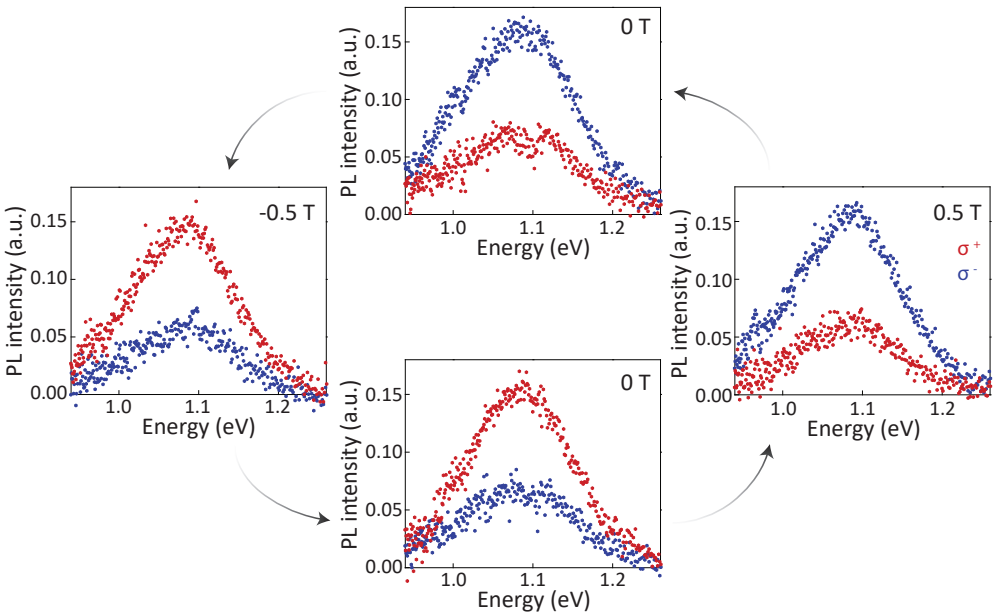

Figure E.1: PL spectra from monolayer CrI_3 on SiO_2/Si substrate for σ^+ (red) and σ^- (blue) circular polarization, acquired at 15 K under linearly polarized excitation and different applied magnetic fields perpendicular to the sample plane. Magnetic field values are shown on the plots and the arrows indicate the magnetic field sweep direction. The results are consistent with those from sapphire substrate (Fig. 6.3). We note that PL from the underlying Si shows up near 1.1 eV. We directly subtracted this PL contribution by using the background spectrum from uncovered SiO_2/Si. To avoid the complication from background Si PL, it is better to study the detailed features of the CrI_3 PL spectrum on transparent substrates. [Adapted from [172].]

E.2 Power dependence of monolayer PL

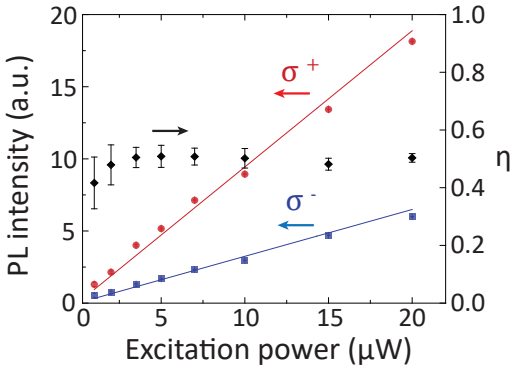

Figure E.2: Power dependence of monolayer CrI_3. Power dependence of σ^+ (red) and σ^- (blue) PL peak intensities and circular polarization (η, black). The data is taken at 0 T after decreasing from -0.5 T (same condition as in Fig. 6.3D). Red and blue lines show a linear fit to the intensity data. We note that the low count rate prohibits accurate measurement of the PL below 1 μW. Furthermore, the power was kept less than or equal to 20 μW to avoid possible sample degradation. Error bars show the standard deviation of the intensities and η at the peak. [Adapted from [172].]

E.3 Bulk CrI_3 differential reflection spectrum

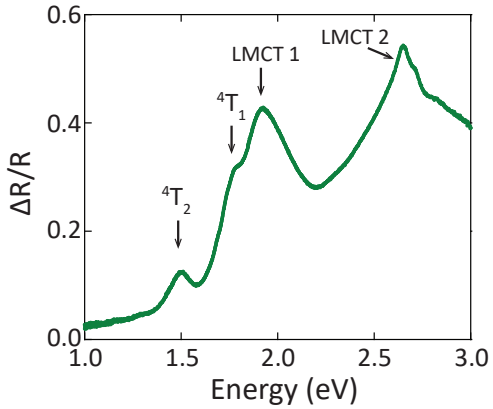

Figure E.3: Differential reflection spectrum for thin bulk CrI_3. Tentative peak assignments are labelled and described in the text. [Adapted from [172].]

Figure E.3 presents the differential reflection spectrum for thin bulk (∼8 layers thick)

CrI_3 at 15 K. The features are consistent with those reported in Ref. [208]. The weak feature at 1.5 eV is the $^4A_2$ to $^4T_2$ transition, which closely matches the monolayer case in Fig. 6.6A. The stronger features consist of a group of two peaks at 1.80 eV and 1.93 eV in addition to another set of peaks at 2.65 eV and 2.7 eV. Based on the connection to prior $CrCl_3$ and $CrBr_3$ experiments [201, 208, 209, 212] and calculations [223, 224], the strong peak at 1.93 eV (LMCT 1) and the 2.7 eV features (LMCT 2) are most likely due to dipole-allowed charge-transfer transitions between the iodine $5p$ orbitals and Cr^{3+} $3d$ orbitals. Specifically, the 1.93 eV peak may arise from the $t_{1u}(\pi)$ or $t_{2u}(\pi)$ to e_g^* transition, and the 2.7 eV peaks from the $t_{1u}(\pi)$ or $t_{2u}(\pi)$ to t_{2g}^* (asterisk denotes anti-bonding orbital). We note that there is less confidence in the specific assignment for the higher energy charge transfer feature, although it is accepted as a $p-d$ LMCT transition (see [223, 224] and references therein). Aside from slight blue-shifts of the peaks in the monolayer limit, we note that the prominent charge-transfer peak at 2.2 eV is not present in the bulk sample, suggesting that interlayer interactions may impact the iodine $5p$ orbitals, which have significant distribution out of the plane. In addition, the 2.65 eV feature is absent in the monolayer limit, leaving only a single peak at 2.7 eV. Detailed thickness- and polarization-dependent absorption measurements, in addition to first-principles calculations, will be necessary to unravel the intriguing structure of the charge transfer transitions.

Appendix F

SUPPLEMENTARY MATERIAL FOR CrI_3/WSe_2 EXPERIMENTS

The following text provides supporting experiments and theory for Chapter 7, reprinted from the supplementary information of [50].

F.1 Electronic structure of CrI_3/WSe_2 bilayer

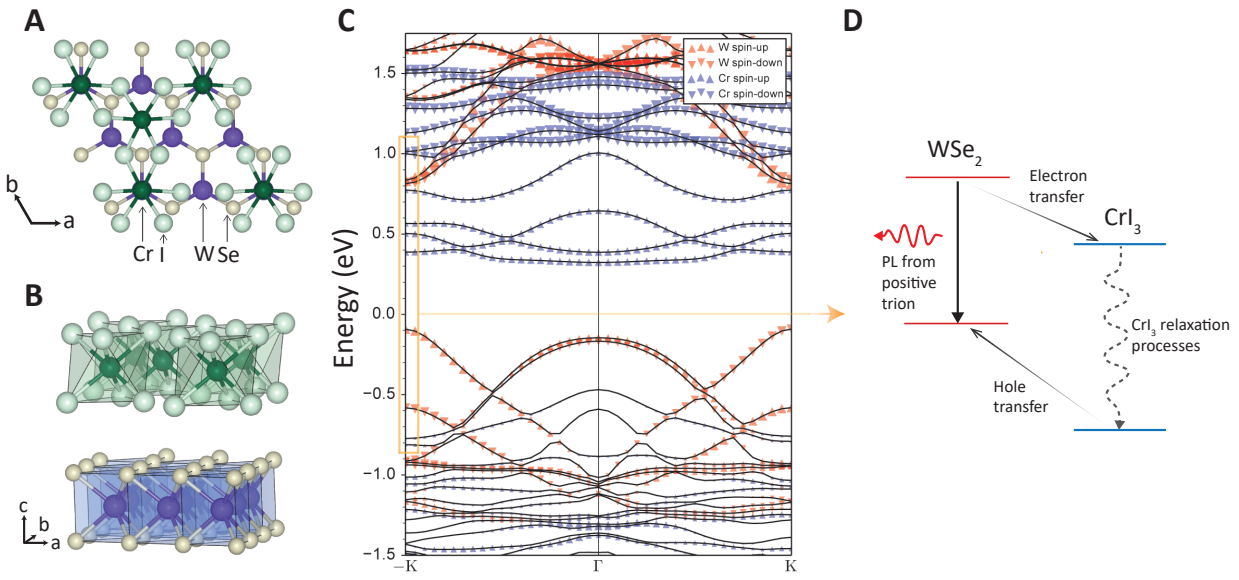

Figure F.1: Atomic structure and the electronic band structure of the WSe_2/CrI_3 bilayer. (A) Top and (B) side view of the WSe_2/CrI_3 bilayer. Dark green, light green, purple and tan spheres represent Cr, I, W and Se atoms, respectively. (C) Electronic structure of the CrI_3-WSe_2 bilayer. The contribution from the W (Cr)-orbitals is shown with red (blue) triangles with the triangles pointing up (down) for up (down)-spins. (D) Schematic of type-II band alignment. Charge transfer to CrI_3 dopes WSe_2 p-type and PL is thus primarily observed from positively charged trions at the WSe_2 $\pm K$ valleys. [Reprinted from [50].]

To determine the band alignment of the CrI_3-WSe_2 heterostructure, we performed first-principles electronic structure calculations for a bilayer made of a monolayer of CrI_3 and a

monolayer of WSe_2. We used the generalized gradient approximation in the parametrization of Perdew, Burke, and Enzerhof [274, 275], as implemented in the QUANTUM ESPRESSO simulation package [276]. A vacuum slab of 15 Å was used. An energy cutoff of 130 Ry and a $12 \times 12 \times 1$ Monkhorst-Pack special k-point mesh for the Brillouin zone integration was found to be sufficient to obtain convergence. To obtain a commensurate heterostructure, 3 % strained 2×2 in-plane superlattice of WSe_2 ($a_0 = 3.32$ Å) was lattice- matched to CrI_3 ($a_0 = 6.84$ Å). This leads to a reduction of the WSe_2 band gap compared to the unstrained monolayers, but it does not affect the type of the band alignment. Structural optimization for the bilayer was performed by fixing the in-plane lattice constants to that of the theoretical bulk CrI_3 lattice constants. Semiempirical Grimme's DFT-D2 method was used to describe van der Waals interactions [277, 278]. The relaxation of the ions was done with the electronic degrees of freedom accurate up to 10^{-6} eV. The results presented here are for a stacking configuration where one of the magnetic Cr^{3+} ions is directly below a W atom (Fig. F.1A and B).

The orbital projected electronic structure of the bilayer is shown in Fig. F.1C. The conduction band minima are mainly made of unoccupied Cr d-orbitals with their spin orientation the same as the occupied Cr d-orbitals. The valence band maxima are mainly made of W d_{xy} and $d_{x^2-y^2}$ orbitals. There is also some hybridization with the I and Se p-orbitals in the conduction and valence bands, respectively (not shown). Thus, the valence and conduction band edges are in the two different monolayers, resulting in a type-II band alignment. Furthermore, we have calculated the work functions for monolayer WSe_2 and monolayer and bilayer CrI_3. Our calculations predict type-II band alignment in both the cases. As the reduction in the band gap from bilayer to bulk CrI_3 is only 0.05 eV, we expect the type-II band alignment to persist even for bulk CrI_3.

F.2 Linear polarization

In the main text, we attribute the main peak around 1.68 eV to the trion peak. Multiple pieces of evidence support this assignment: (1) the type-II band alignment between CrI_3 and WSe_2 (supported by calculations in F.1 and magnetic field dependence of PL in Fig. 7.2) will strongly dope WSe_2 with holes; (2) the shoulder peak on the higher energy side of the main peak implies a weak exciton emission. Another compelling piece of evidence is observed in the absence of linear polarization in the main peak. We excited the sample with a linearly polarized 1.96 eV laser while selectively detecting co- (VV) and cross-linear (VH)

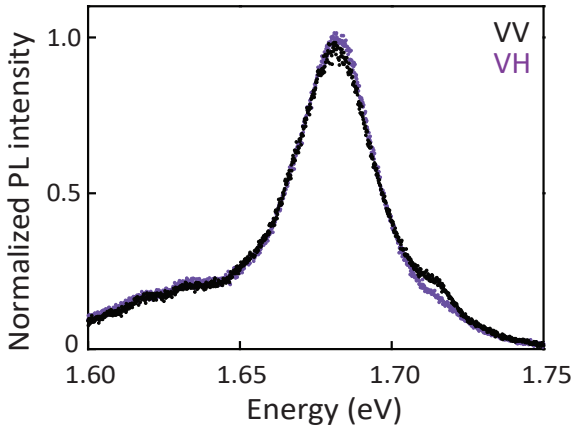

Figure F.2: Linearly polarized excitation and detection. A comparison of PL intensity between VV (black) and VH (purple) polarization, where the first (second) letter represents excitation (detection) polarization. "H" ("V") stands for horizontal (vertical). [Reprinted from [50].]

PL (Fig. F.2). The beam location is chosen where the higher energy shoulder is prominent. The main peak at 1.681 eV has negligible linear polarization, while the shoulder peak on the high-energy side (1.715 eV) shows clear co-linear polarization. In bare WSe_2, while the neutral exciton displays linear polarization due to valley quantum coherence, it is notably absent in the trion emission [46]. Thus, this strongly supports the assignment of the main peak as trion emission. We also note that the energy separation between the shoulder and main peak is 34 meV, which agrees well with the trion binding energy

F.3 Peak parameter extraction

We employ two approaches, weighted average and Gaussian fitting, for extracting the parameters of the PL spectrum and compare their results. For the weighted average, the energy of each data point within the full-width at half maximum (FWHM, shaded region in Fig. F.3A) were weighted by their PL spectral density, $\int Ef(E)dE/\int f(E)dE$, where $f(E)$ is the spectral density and E is the photon energy. The intensity is defined by S/FWHM, where S is the summation of the spectral density within the FWHM.

For the Gaussian fitting, we use multiple Gaussian functions. As shown by the red curve in Fig. F.3A, there are weak spectral features on both sides of the main peak. To achieve the best fits, we fit the main peak and the high-energy peak with Gaussians. The fitting range

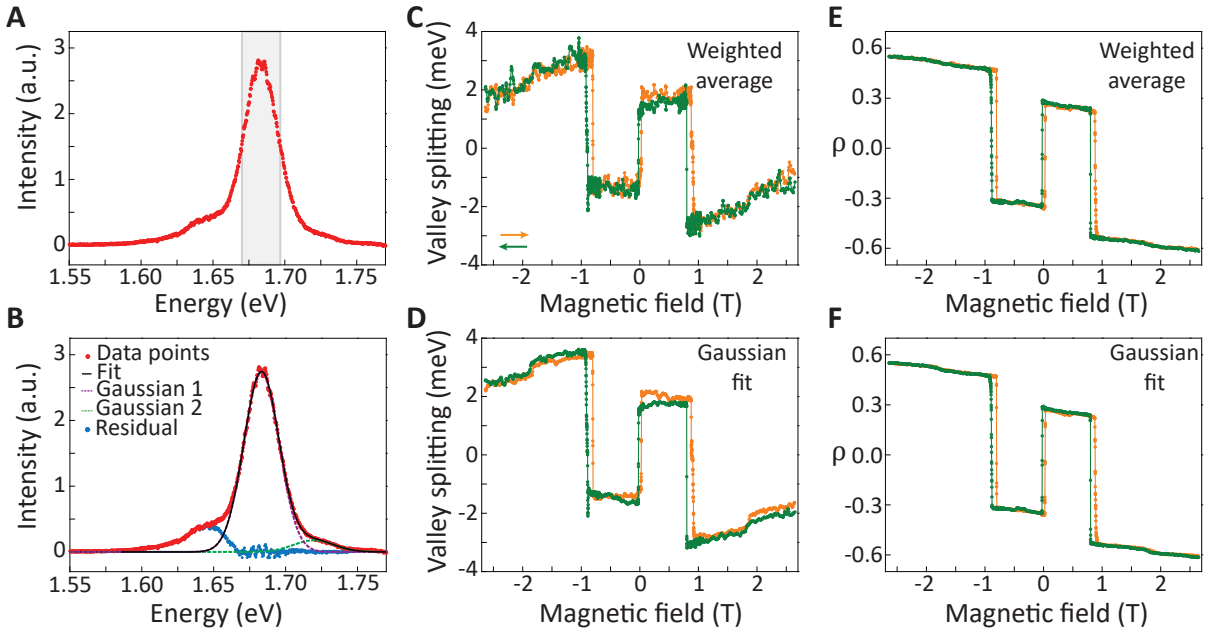

Figure F.3: Peak parameter extraction. (A) PL spectrum of WSe_2/CrI_3. The shaded region indicates the points within the FWHM, which are used to calculate the weighted average. (B) PL spectrum on WSe_2/CrI_3 (red), with Gaussian fits to the main (purple) and high energy (green) peaks. The solid black line represents the total fitted curve and the blue dots give the residual. (C) Valley splitting and (E) ρ obtained by the weighted average method. (D) Valley splitting and (F) ρ obtained by Gaussian fitting. [Reprinted from [50].]

is constrained to 1.665 eV on the low energy end to reduce the influence of the low-energy shoulder, which likely does not have a clear peak shape. The results of this fitting scheme are shown in Fig. F.3B with the black curve. The dashed curves give the individual Gaussian peaks and blue shows the residual. We see the main peak is captured well by this fitting scheme. The wavy residual from 1.67 eV to 1.69 eV is due to slight etaloning from the CCD and does not significantly affect the extracted parameters.

Figures F.3C and D compare the extracted valley splitting by the two approaches. We see that the magnitude of the splitting as a function of applied magnetic field shows good agreement between both parameter extraction methods, while the noise is smaller in the Gaussian fit method compared with the weighted average method. On the other hand, ρ is less sensitive to the fitting approaches, as shown in Figs. F.3E and F. For the magnetic field sweep data (Fig. 7.2 and 7.4) and Fig. F.3E, we adopted the Gaussian fitting method. However, for the spatial maps in Fig. 7.3, we used the weighted average method to extract

ρ. This is because the sample contains both heterostructure and bare monolayer WSe_2 regions, which have different peak shapes. The weighted average approach thus allows a more straightforward comparison over the entire sample region. Furthermore, we note that ρ captures the sign of the CrI_3 magnetization and the valley splitting (Fig. 7.2C and D), and ρ is less noisy, so it allows for higher quality spatially resolved magnetization data than spatially dependent valley splitting (Fig. F.11).

F.4 Power dependence of valley splitting

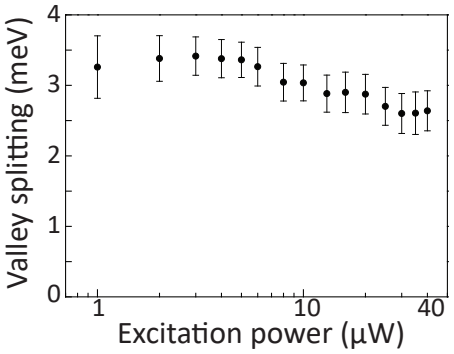

Figure F.4: Power dependence of valley splitting. Valley splitting as a function of excitation power (log scale), performed at zero applied magnetic field, as in Fig. 7.1E. [Reprinted from [50].]

F.5 Voigt geometry

While bulk CrI_3 is known to possess an out-of-plane easy axis [185], the easy axis in very thin samples has not been established experimentally. In Fig. F.5A and B, we show the valley splitting and ρ as a function of applied magnetic field in Voigt geometry (field is parallel to the sample plane). A sharp transition that flips the sign of both the valley splitting and ρ occurs near 2.5 T (-2.5 T) when sweeping the field up (down). In addition, we observe a smaller weaker jump occurs near ± 4 T, followed by a reduction in the splitting and ρ towards zero at high magnetic fields. The zero crossing in the first jump reflects the magnetization flipping from out-of-plane near zero field towards the opposite direction. At high fields, the valley splitting and ρ approach zero, indicating that the CrI_3 magnetization is fully in-plane, aligned with the applied magnetic field. Regardless of the field sweeping direction, the

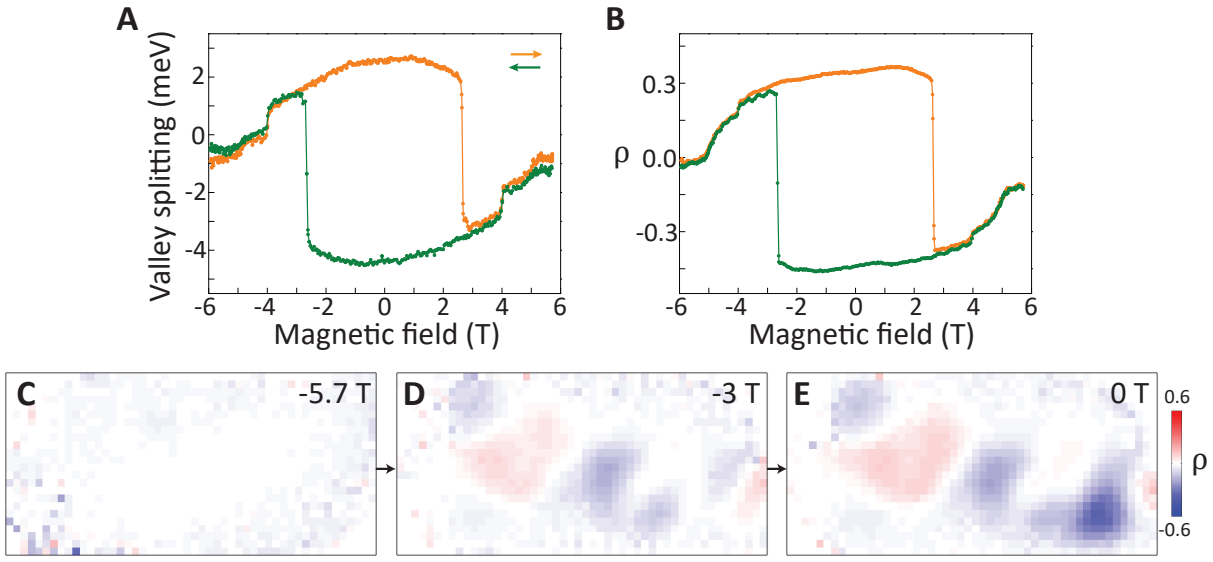

Figure F.5: PL measurements in Voigt geometry. (A) Valley splitting and (B) ρ versus applied magnetic field, obtained by polarized PL in Voigt geometry. The arrows indicate the sweeping direction. Spatial maps of ρ in Voigt geometry at $-5.7\,\mathrm{T}$ (C), $-3\,\mathrm{T}$ (D), and $0\,\mathrm{T}$ (E). [Reprinted from [50].]

non-vanishing value of the valley splitting and ρ at zero field signifies the existence of out-of-plane magnetization, and the vanishing value of the splitting and ρ at high field indicates an in-plane magnetization, which proves an out-of-plane easy axis.

In addition, we present spatial maps of ρ at selected magnetic fields in Voigt geometry. As shown in Fig. F.5C, at $5.7\,\mathrm{T}$, ρ is near zero and no domain structure is visible, consistent with in-plane CrI_3 magnetization. At $-3\,\mathrm{T}$, we see the presence of domains (Fig. F.5D), which increase in strength at zero applied field (Fig. F.5E), demonstrating the rotation of the spins towards their preferred out-of-plane direction.

F.6 Helicity-independent differential reflection at the excitation energy

We performed polarized differential reflection near the excitation energy ($1.96\,\mathrm{eV}$) using a tungsten halogen white light source on device 2 at $5\,\mathrm{K}$. As shown in Fig. F.6, the signal, and correspondingly the optical absorption, is independent of the helicity at these energies. This indicates that initial populations created by σ^+ or σ^- excitation at $1.96\,\mathrm{eV}$ in $+K$ or $-K$, respectively, are equal and independent of the valley splitting. Thus, the difference in PL intensity under σ^+ or σ^- excitation is mainly dominated by valley-dependent non-radiative

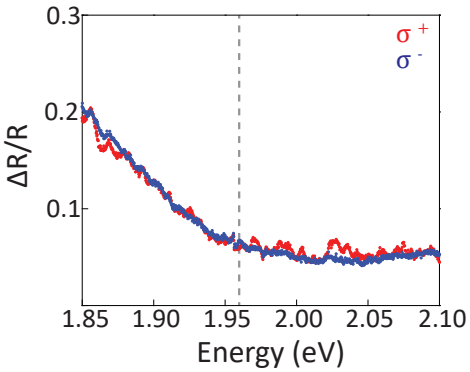

Figure F.6: Differential reflection spectrum of WSe_2/CrI_3. Differential reflection spectrum on WSe_2/CrI_3 for σ^+ (R, red) and σ^- (L, blue) circular excitation. The vertical dashed line indicates the excitation energy of the HeNe laser used in the PL measurements. [Reprinted from [50].]

relaxation channels, as described in the main text.

F.7 Valley polarization and intensity modulation parameter

The valley polarization is determined by the relative emission intensity between $+K$ and $-K$ after exciting both valleys, i.e.. In Fig. F.7A, the valley polarization is plotted versus applied magnetic field. We see that it displays the same major transitions as the quantity ρ, which we defined in the main text as the normalized difference in I_{++} and I_{--} intensity. Near the transition regions, the valley polarization can switch from $\sim$30 % to -30 % for very small changes in applied magnetic field (mT scale).

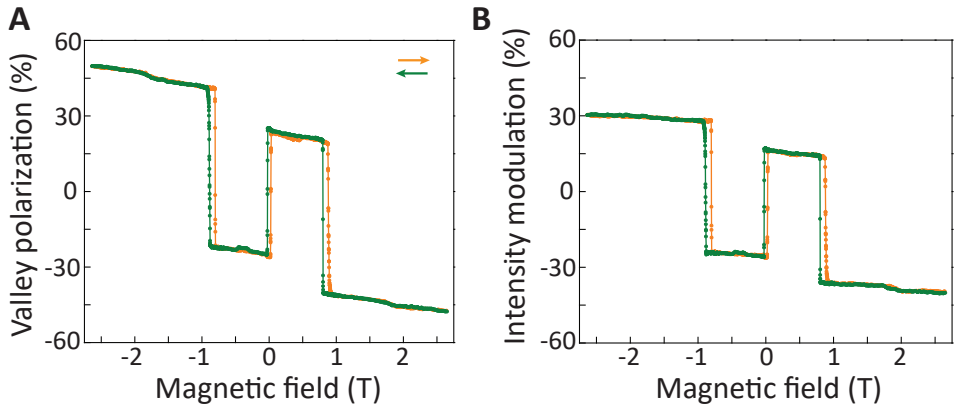

Figure F.7: Valley polarization and intensity modulation parameter. (A) Valley polarization and (B) intensity modulation as a function of applied magnetic field. The arrows indicate the sweeping direction of the applied magnetic field. [Reprinted from [50].]

It is also useful to study the intensity modulation parameter,, which contrasts the total PL intensity after exciting $+K$ or $-K$ (Fig. 7.2). In Fig. F.7B, this parameter is plotted against the applied magnetic field. As discussed in the main text, the highly imbalanced PL after exciting $+K$ or $-K$ reflects the spin-orientation dependent electron transfer to CrI_3 based on its magnetization (Fig. 7.2E). Recently, the phenomenon of spin polarization by spin-dependent charge transfer from a semiconductor to nearby ferromagnetic layer was discovered [247]. In their system, a GaMnAs layer separated from an InGaAs quantum well, they find a spin polarization and intensity modulation of -3 % to 3 % from -60 mT to 60 mT. In contrast, we find that in the WSe_2/CrI_3 system, the effect is dramatically enhanced, giving an order of magnitude larger modulation with an order of magnitude smaller magnetic field range.

F.8 Linewidth difference between polarizations

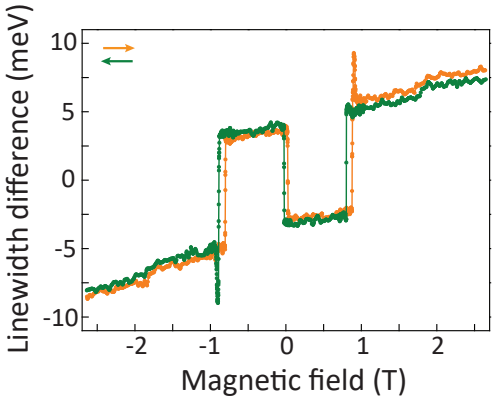

Figure F.8: Linewidth difference between polarizations. (A) Valley polarization and (B) intensity modulation as a function of applied magnetic field. The arrows indicate the sweeping direction of the applied magnetic field. [Reprinted from [50].]

We compare the difference in FWHM between I_{++} and I_{--} spectra as a function of applied magnetic field (Fig. F.8). We see that this quantity follows an opposite trend to ρ (Fig. 7.2D), indicating that the width is large whenever the PL intensity is weak. As noted in the main text, the width difference allows us to estimate the electron hopping rate, which is on the order of 100 fs when CrI_3 is fully magnetized. This nonradiative relaxation channel is an order of magnitude faster than the trion radiative lifetime, and therefore has a significant impact on the PL quantum yield. We note that the spikes near ± 0.9 T highlight the sensitivity of the spin/valley states in WSe_2 to CrI_3 magnetization dynamics, and their origin is an intriguing topic for further study.

F.9 Rapid switching of heterostructure PL

In Fig. F.9, we compare the rate of PL change between plain WSe_2 and WSe_2/CrI_3. Figures F.9A and C are PL spectra maps for I_{--} polarization in plain WSe_2 and the HS, respectively. The magnetic field (sweeping up) ranges from -5.7 T to 5.7 T in Fig. F.9A, whereas it is only plotted around a 40 mT range of the 0.8 T transition in Fig. F.9C. This emphasizes the striking contrast in the rate of PL intensity modulation between bare WSe_2 and the WSe_2/CrI_3 HS. Figures F.9B and D illustrate this further with the spectra at the selected field values. The change in spectral position, in addition to intensity, is clear. In

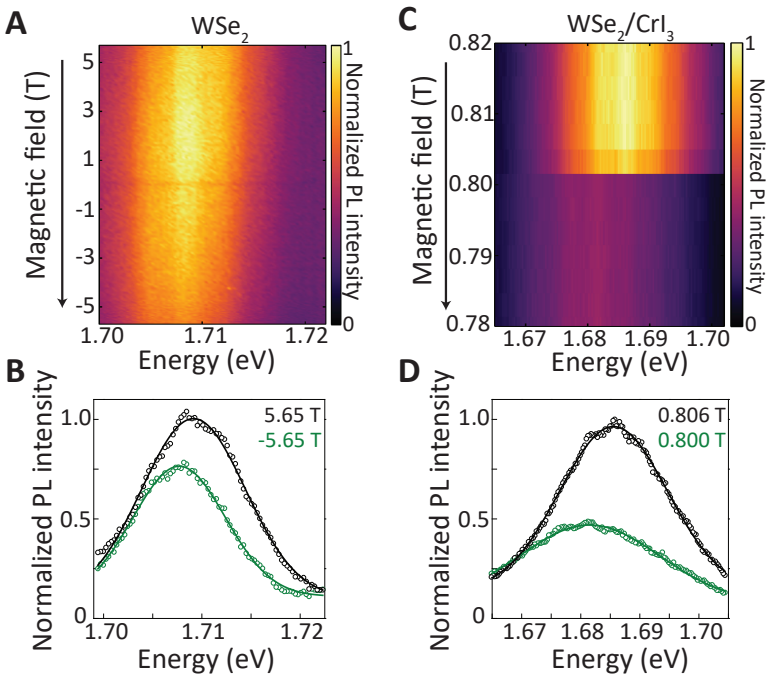

Figure F.9: Rapid switching of heterostructure PL. The difference in FWHM as a function of applied magnetic field. Orange and green curves are data for increasing and decreasing applied magnetic field, respectively. [Reprinted from [50].]

a span of over 11 T, there is a 1.5 meV shift in the trion peak position in plain WSe_2 and 25 % reduction in the PL intensity. For WSe_2 interfaced with CrI_3, we find a 4 meV shift and 50 % reduction in $\leq$6 mT.

F.10 Magnetic field sweep rate dependence

In Fig. F.10, we display the PL intensity (of I_{--} polarization scheme) as a function of decreasing applied magnetic field (from 2.7 T to -2.7 T) for different field sweep rates. The fast sweep data was acquired when sweeping the magnetic field at 8.5 mT s^{-1} over the entire field range. For the slow sweep data, the sweep rate was lowered to 0.95 mT s^{-1} around the critical fields observed in the fast sweep, from 0.96 T to 0.72 T, 0.1 T to -0.1 T, and -0.72 T to -0.96 T. The intensities of the two curves overlap well and the critical fields are within 50 mT of each other (the step size of the fast sweep data), which suggests that the sweep rate does not affect the main results.

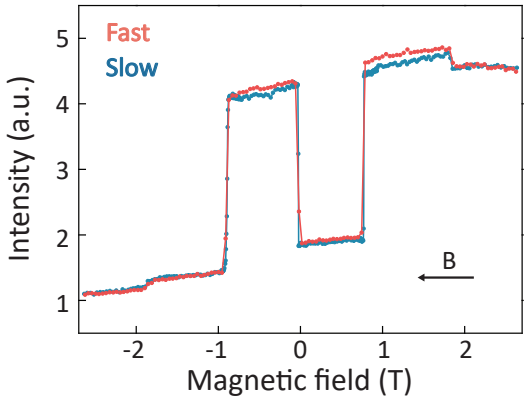

Figure F.10: Magnetic field sweep rate dependence. The difference in FWHM as a function of applied magnetic field. Orange and green curves are data for increasing and decreasing applied magnetic field, respectively. [Reprinted from [50].]

F.11 Spatial maps of valley splitting

In Fig. F.11, we display the valley splitting spatial maps of device 2. These correspond to the same dataset that was used to extract the spatial maps of ρ in Fig. 7.3. To avoid fitting issues due to the variation of PL peaks on and off the HS region, we choose to fit only the data where the HS X^+ emission has the highest intensity and all other splitting values are set to zero. The agreement of the shape in Fig. F.11 to Fig. 7.3 indicates that this fitting scheme captures the HS area well. Furthermore, the size, shape, and sign of the domain patterns match those in Fig. 7.3, further justifying the use of ρ as a good parameter to capture the underlying magnetization. In addition, ρ presents a few noteworthy benefits in the data analysis. To extract the valley splitting with the lowest uncertainty, one must use a fitting scheme, while for ρ, both fitting and weighted averaging work well (as shown in Fig. F.3). Thus, in general, ρ has lower noise than the valley splitting, especially with shorter integration times (1 second per polarization in these spatial maps). Finally, ρ is less sensitive to the peak shapes, allowing extraction of useful results without having to tailor the fits to each pixel.

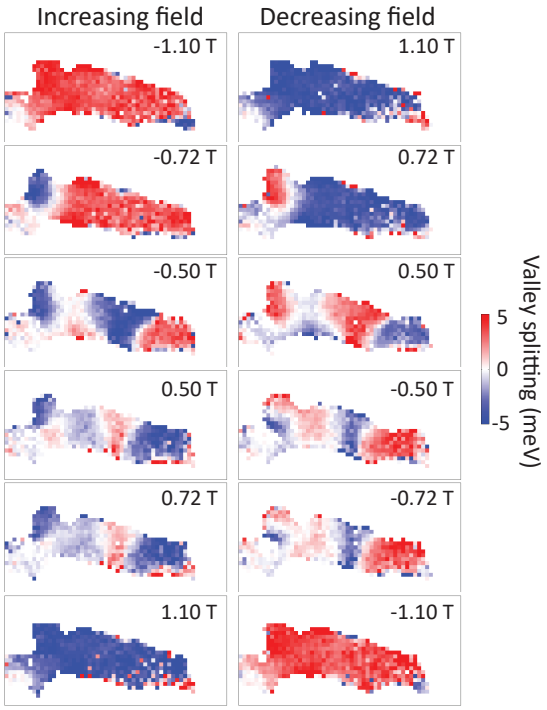

Figure F.11: Spatial maps of valley splitting. The difference in FWHM as a function of applied magnetic field. Orange and green curves are data for increasing and decreasing applied magnetic field, respectively. [Reprinted from [50].]

F.12 Temperature dependence

Temperature dependence of the ρ spatial maps is shown in Fig. F.12. The applied magnetic field is fixed at $-0.15\,\mathrm{T}$ after sweeping up from $-1.1\,\mathrm{T}$. The main feature is the decrease in ρ as temperature increases and its eventual disappearance above 65 K, which suggests that TC in our $\sim$10 nm CrI_3 is comparable to bulk samples ($\sim$61 K) (36). While the domain structure remains mostly unchanged with temperature, there are subtle changes (e.g. in the shape of the large blue domain), which highlights the utility and sensitivity of the scanning PL technique for probing the CrI_3 magnetization.

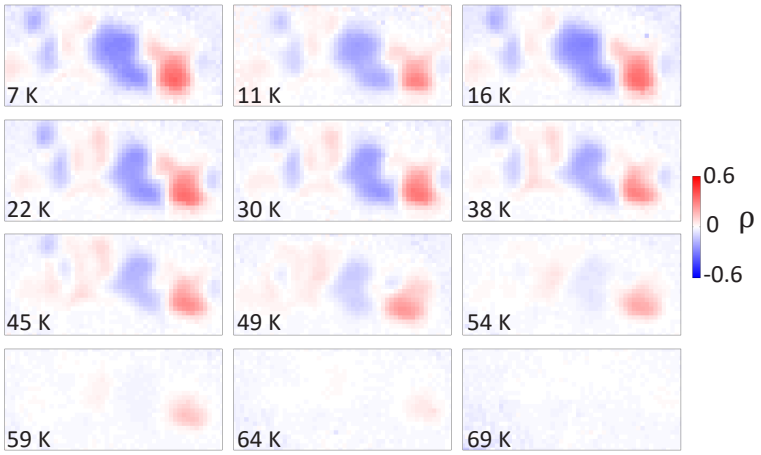

Figure F.12: Temperature dependence. The difference in FWHM as a function of applied magnetic field. Orange and green curves are data for increasing and decreasing applied magnetic field, respectively. [Reprinted from [50].]

Appendix G

SUPPLEMENTARY MATERIAL FOR CRI_3/WSE_2 VALLEY SWITCHING EXPERIMENTS

The following text provides supporting experiments and theory for Chapter 8, reprinted from the supplementary information of [266].

G.1 Magnetic field dependence of domain B

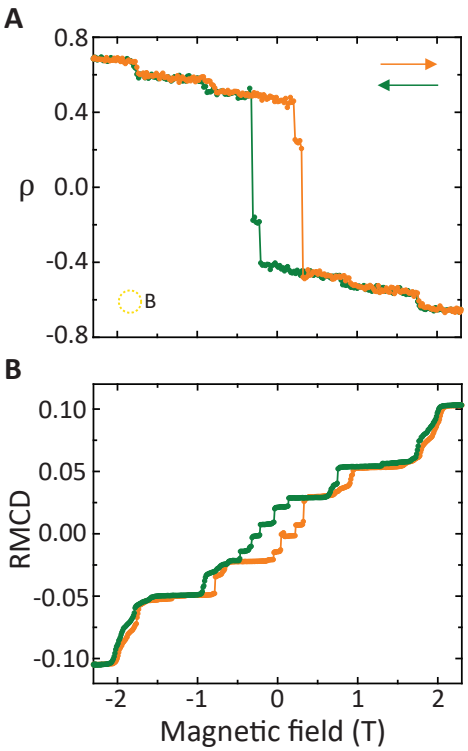

Figure G.1: Magnetic field dependence of domain B. Magnetic field dependence of ρ (A) and RMCD (B) sweeping up (orange curves) and down (green curves) on domain B. The data are taken at the location indicated by the dashed yellow circle in Fig. 8.1D. [Reprinted from [266].]

In Fig. G.1, ρ (Fig. G.1A) and RMCD (Fig. G.1B) are plotted as a function of the applied magnetic field on domain B. The sign of ρ flips only once in each sweep direction, whereas in domain A, ρ flips sign three times. The magnetic field dependence of the RMCD is monotonic with many small step-like jumps. These jumps are a sign of magnetization changes within individual layers of the $\sim$10 nm CrI_3. Since the WSe_2 valley physics is primarily affected by the topmost CrI_3 layer (see further discussion in the main text), we infer that in domain B, the top layer of CrI_3 only flips magnetization once, which leads to single sign flip of ρ in Fig. G.1A. The spin-orientation-dependent charge transfer from WSe_2 to the CrI_3 leads to an opposite sign for the RMCD signal compared to ρ at high magnetic fields. For example, at a high positive magnetic field, the magnetization (and RMCD signal) is positive, which opens access to charge transfer from $|-K,\uparrow\rangle$ electrons from WSe_2, quenches the σ^+ PL, and thus generates negative ρ.

G.2 Power-dependent hysteresis and switching of the valley Zeeman splitting

Figure G.2 provides similar data to Fig. 8.2 in the main text for the valley Zeeman splitting (Δ). It is clear that Δ exhibits the same power-dependent hysteresis loop as ρ (Fig. G.2A). We are thus able to control Δ with the optical excitation power at fixed magnetic fields near the hysteresis loop, as shown in the 2D plot of Δ in Fig. G.2B. The sign of the valley Zeeman splitting is tunable from positive to negative (and the reverse) when the external magnetic field is between $\sim$0.82 T and 0.9 T. The curved white region indicates the critical excitation power that is required to switch the sign of Δ at the different fixed magnetic fields.

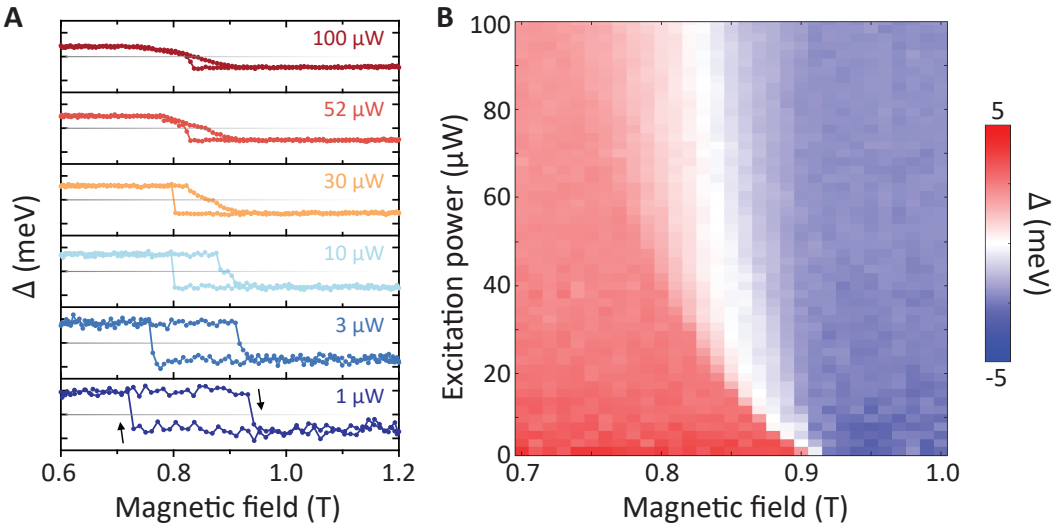

Figure G.2: Power-dependent hysteresis and switching of the valley Zeeman splitting. (A) Magnetic field dependence of valley Zeeman splitting (Δ) from 0.6 to 1.2 to 0.6 T. The gray horizontal lines indicate $\Delta = 0$ and the neighboring y-axis tick marks denote $\Delta = \pm 4$ meV. Black arrows indicate the sweep directions. These data are extracted from the same spectra used in Fig. 8.2A of the main text. (B) Map of the power dependence at different applied magnetic fields for Δ. The magnetic field was first initialized by sweeping up to 0.7 T. A power dependence was then performed from 1 µW to 100 µW at the different fixed magnetic fields from 0.7 µW to 1 µW. These are extracted from the same dataset used in Fig. 8.2B from the main text. [Reprinted from [266].]

G.3 Raw power-dependent PL parameters at 0.88 T

Figure G.3 demonstrates the strong nonlinearity of the PL peak parameters that produces the valley switching effects. For example, in Fig. G.3A, the σ^+ PL intensity power dependence exhibits a kink and its slope decreases above 8 W. This causes the σ^+ and σ^- curves to intersect at 10 µW, which leads to a reversal in the sign of ρ. There is good overlap of the data when the power dependence is performed with increasing and then decreasing power, which shows the reversibility of the phenomenon.

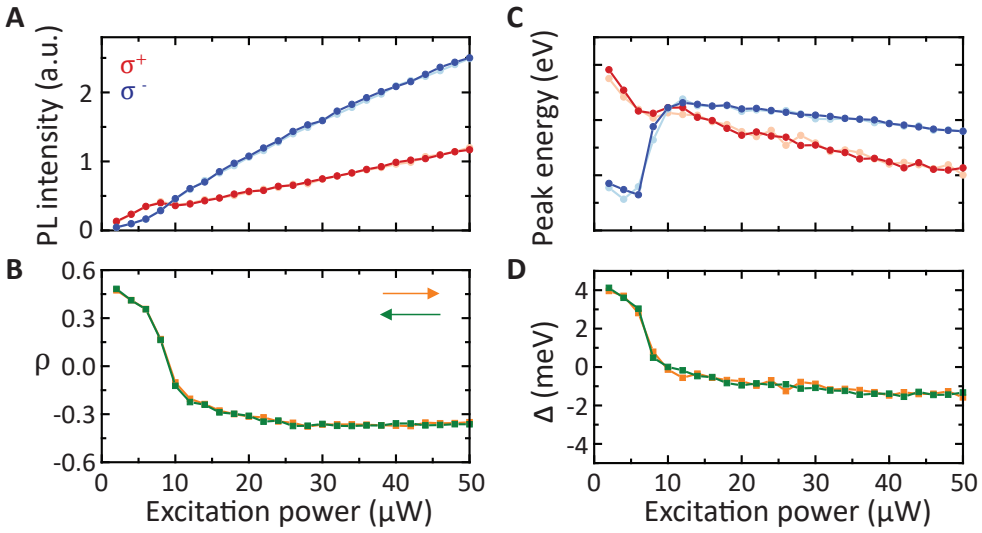

Figure G.3: Raw power-dependent PL parameters at 0.88 T**.** Power dependence of (A) the PL intensity and (c) peak energy for σ^+ (red) and σ^- (blue) excitation and detection polarization. Light (dark) red and blue show the values for increasing (decreasing) power. The corresponding valley parameters ρ and Δ are shown in (B) and (D) respectively for increasing (orange) and decreasing (green) power. The power was swept as high as 100 µW, but we display it up to 50 µW for easier viewing of the low-power nonlinearity. Before the power dependence, the external magnetic field was initialized to 0.88 T by sweeping up from 0.6 T. See Fig. G.5 for the full power dependence of ρ and Δ. [Reprinted from [266].]

G.4 Power-dependent hysteresis and valley switching on a second sample

In Fig. G.4, we provide additional data from a second heterostructure sample of WSe_2/CrI_3. The measurements were acquired at 8 K on a domain where ρ flips three times in a single magnetic field sweep, like domain A in the sample from the main text. The hysteresis loop at 0.8 T exhibits very strong power-dependent coercivity and loop shape (Fig. G.4A), just as with the other sample. We replicate the valley switching effects by fixing the magnetic field at 0.78 T and varying the excitation power. We achieve reversible switching between ±30 % polarization (Fig. G.4B) and around 4 meV to −2 meV valley Zeeman splitting (Fig. G.4C). This change in valley Zeeman splitting corresponds to varying the effective magnetic exchange field from about −15 T to 7 T, via a modest increase in the laser excitation power.

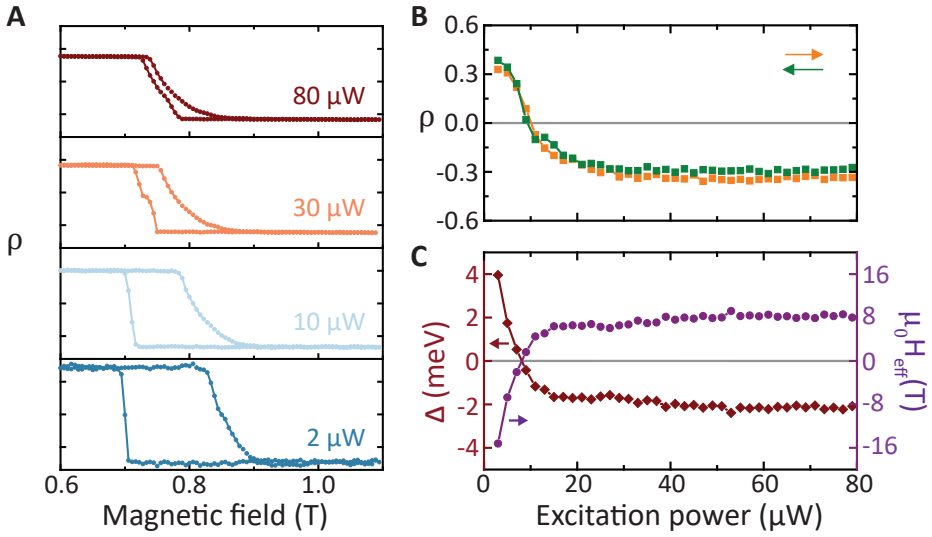

Figure G.4: Power-dependent hysteresis and valley switching on a second sample. (A) Magnetic field sweeps of ρ from 0.6 T to 1.1 T to 0.6 T at selected excitation powers on a second WSe_2/CrI_3 sample. Gray horizontal lines indicate the $\rho = 0$ line and the neighboring tick marks on the y-axis are ± 0.5. Sweep directions are shown by the black arrows. (B) Power dependence of ρ at 0.78 T from 3 μW to 80 μW (orange curve) and subsequently from 80 μW to 3 μW (green curve). (C) Power dependence of Δ (left) at 0.78 T and the corresponding effective magnetic field ($\mu_0 H_{eff}$, right). All data from the second device were acquired at 8 K. [Reprinted from [266].]

G.5 Power dependence of ρ and Δ at selected magnetic fields

In Fig. G.5, we display several power dependences for ρ (Fig. G.5A) and Δ (Fig. G.5B) at different (fixed) applied magnetic fields. They correspond to vertical line cuts in the 2D maps Fig. 8.2 and Fig. G.2B. The indicated magnetic field is first initialized by sweeping up from 0.6 T. Below 0.80 T and above 0.90 T, the signs of ρ and Δ do not change with power. At intermediate magnetic fields, both ρ and Δ flip when the excitation laser reaches a critical power that is determined by the magnetic field. Higher magnetic fields decrease the critical power required for valley switching, but around 0.90 T and above, the system tends towards the high magnetic field state and thus the reversible power dependence is less robust.

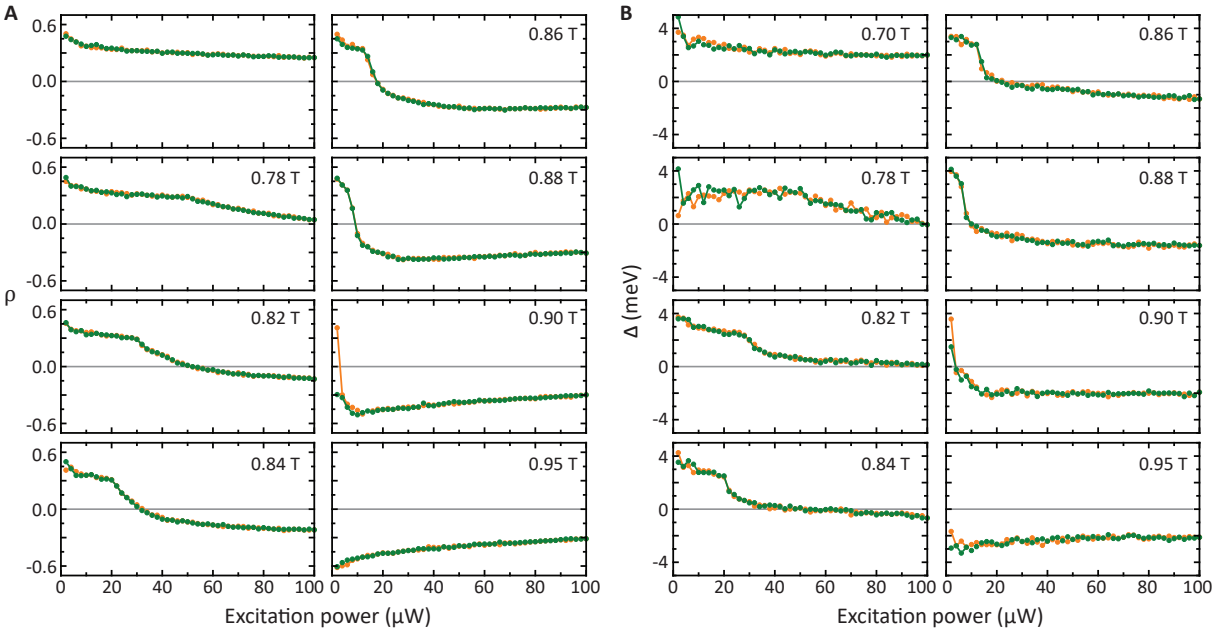

Figure G.5: Power dependence of ρ and Δ at selected magnetic fields. Power dependence of ρ (A) and Δ (B) at selected applied magnetic fields with increasing (orange) and decreasing (green) power. [Reprinted from [266].]

G.6 Comparison between linear and circular excitation

Figure G.6 shows that the valley switching effect occurs under both linear and circular excitation. The linear excitation, circular detection condition allows us to detect the valley polarization that is induced by the magnetic proximity effect. As seen in Fig. G.6A, the valley polarization exhibits very similar power-dependent hysteresis behavior as ρ in Fig. 8.2A, including decreased full-width and increased transition width (the slanted region where ρ reverses) at high powers. We also performed a power dependence under linear (Fig. G.6B) and circular (Fig. G.6C) excitation at 0.84 T. Aside from a $\sim$5 % enhancement, ρ behaves the same as valley polarization. From ρ, we can thus infer the true valley polarization, as reported in the main text. We note that measuring ρ has the benefit of higher PL intensities, which decreases the data integration time required for high-quality spectra. Also, by using circular instead of linear excitation, we avoid the complication of a rotating excitation linear polarization angle with the magnetic field (due to Faraday rotation). Thus, the magnetic field dependence of ρ is robust against possible sample anisotropies. A more detailed explo-

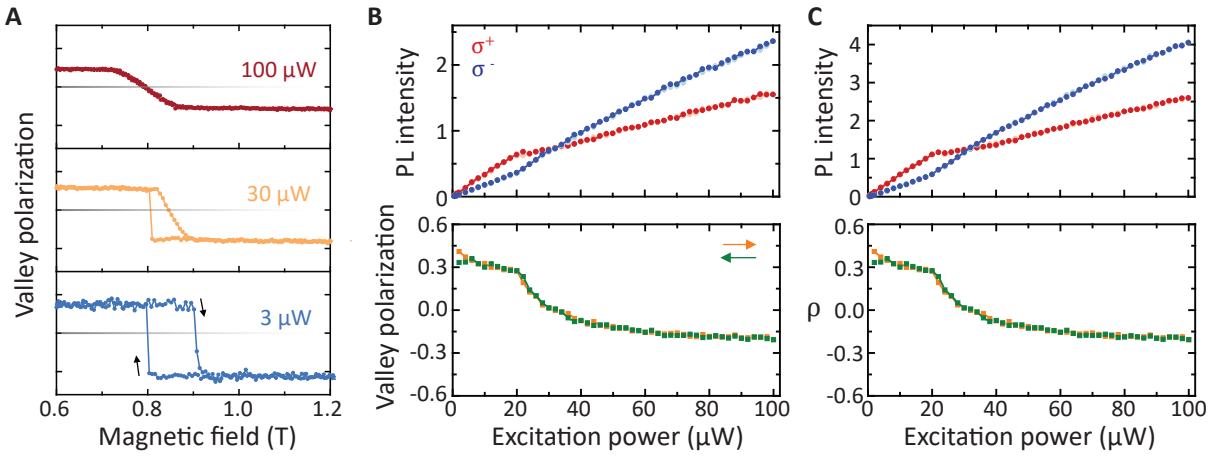

Figure G.6: Comparison between linear and circular excitation. (A) Magnetic field dependence of the valley polarization (circular polarization under linear excitation) at selected excitation powers from 0.6 To 1.2 To 0.6 T. Gray horizontal lines indicate the $\rho = 0$ line and the neighboring tick marks on the y-axis are ± 0.5. Sweep directions are shown by the black arrows. Power dependence of PL intensity and ρ for linear (B) and circular excitation (C) at 0.84 T. [Reprinted from [266].]

ration of linear polarization (excitation and detection) should be performed in the future. Nevertheless, the power-dependent effects we observe here are independent of the excitation polarization and rely only on the total power.

G.7 Magnetic field initialization direction and partial hysteresis

The magnetic field initialization direction affects the power dependence and hysteresis. Figures G.7A and B are power dependences of circularly polarized PL intensities and ρ taken at 0.85 T. Unlike the other power dependences that we show, however, here we initialized the magnetic field by sweeping down from 1.2 T. We thus begin our power dependence in the high-magnetic-field state (which has negative ρ). We first explored the effect of increasing power (orange curve in Fig. G.7B). At ∼14 μW, ρ jumps sharply from negative to positive, and then slowly decreases in magnitude at higher power, eventually flipping back to negative above 25 μW. Upon performing the same power dependence in the reverse direction (decreasing power, green curve), we find a curve very similar to those in Fig. G.5, and there is a mismatch with the orange curve at 14 μW and below. The jump we observe when increasing from 12 μW to 16 μW reflects a sudden transition from the high-magnetic-field state to the

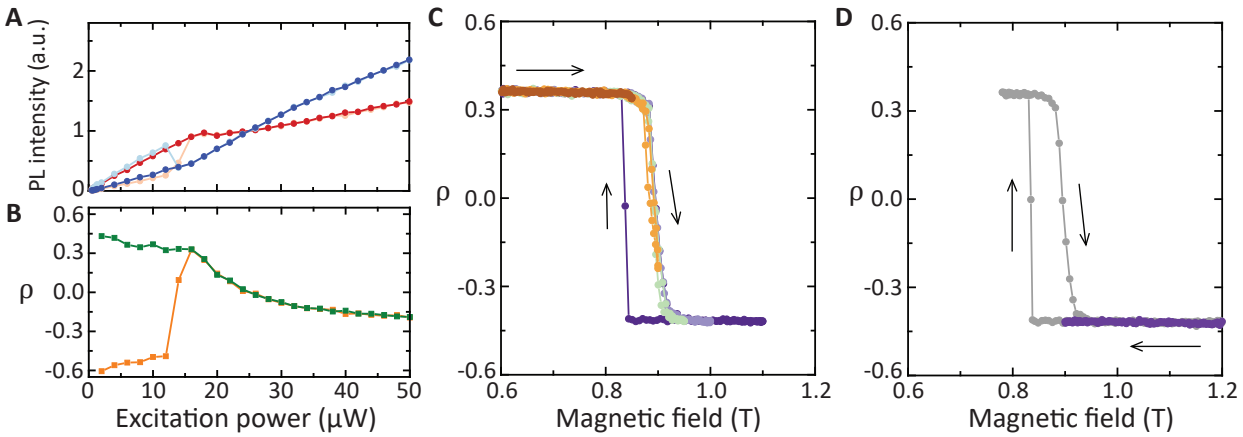

Figure G.7: Magnetic field initialization direction and partial hysteresis. Power dependence of the PL intensity (A) and ρ (B) after initializing the applied magnetic field to 0.85 T by sweeping down from 1.2 T. Light (dark) red and blue curves in (A) show the PL intensity for increasing (decreasing) power. (C) Partial magnetic field sweeps from 0.6 T to different maximum fields and back to 0.6 T. (D) Partial magnetic field sweep from 1.2 T to 0.9 T to 1.2 T (purple) and 1.2 T to 0.78 T to 1.2 T (gray). [Reprinted from [266].]

low-magnetic-field state and indicates that the high-field state is unstable near the hysteresis loop.

Further evidence of the high-field and low-field state stabilities are observed in the partial magnetic field sweeps of ρ. Figure G.7C shows several partial field sweeps where the magnetic field starts at 0.6 T, increases to different maxima, and then decreases back to 0.6 T. Even after ρ has flipped from positive to negative (light purple, green, and orange curves), the sweep down curves closely retrace the sweep up curves with low hysteresis, and the system remains in the low-field state. To observe the full hysteresis loop, the magnetic field must sweep up to over 1.1 T, as shown in the dark purple curve. In contrast, if the partial field sweeps begin in the high-field state at 1.2 T (Fig. G.7D), the system exhibits the full hysteresis as soon as ρ flips sign (gray curve). These data demonstrate the strong stability of the low-field state compared to the high-field state and reveal why the power-dependent valley switching is fully reversible when the system is initialized from low magnetic fields.

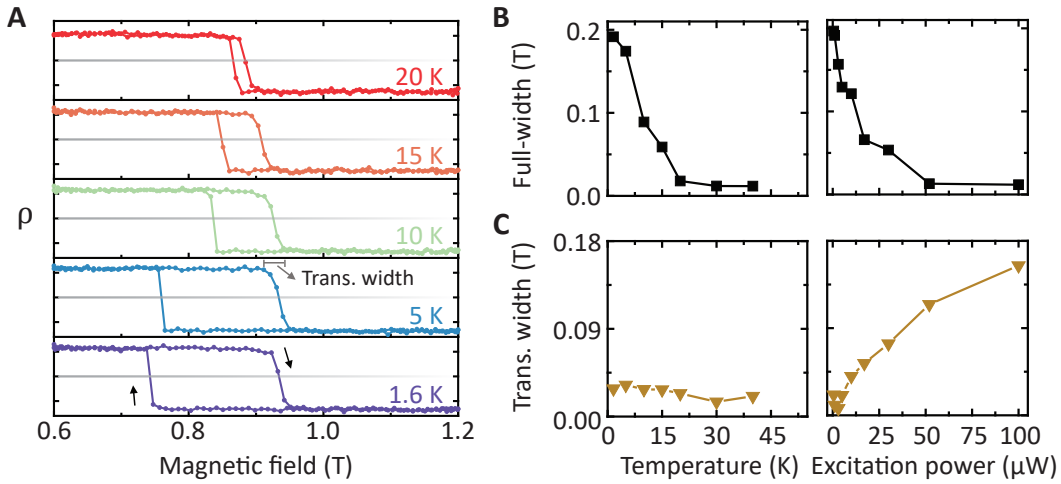

Figure G.8: Temperature dependence. (A) Magnetic field sweeps of ρ as a function of temperature. The excitation power is 1 µW. Horizontal gray lines indicate $\rho = 0$ and the neighboring tick marks on the y-axis are ± 0.5. Black arrows indicate the field sweep directions. (B) Full-width of the hysteresis loop (at $\rho = 0$) versus temperature at 1 µW excitation power (left) and versus excitation power at 1.6 K (right). (C) Transition width versus temperature for 1 µW power (left) and versus excitation power at 1.6 K. See (A) for definition of the transition width. [Reprinted from [266].]

G.8 Temperature dependence

As discussed in the main text, the origin of the optical control of the CrI_3 layer magnetization is an interesting issue for further study. A possible contribution is laser heating of the lattice. As a preliminary test for heating effects, we measured the hysteresis loop of ρ under low power excitation (1 µW) as a function of temperature, as shown in Fig. G.8A. The full-width of the loop decreases with temperature, similar to what occurs at high powers (Fig. G.8B). On the other hand, there is a clear difference in the shape of the hysteresis loop and the magnetic field range of the transition where ρ reverses (i.e., transition width). From 1.6 K to 40 K, the transition width remains small (Fig. G.8C), as is clear from the box-like loop shapes in Fig. G.8A. In contrast, higher power forces a slant in the loop shape (Fig. 8.2A), increasing the transition width. The magnetization thus appears to gradually rotate with the magnetic field at high powers, unlike the rapid spin-flip transition that occurs at lower powers. However, an important point to emphasize is that the focused laser spot ($\sim$1 µm^2) is significantly smaller than the sample. Therefore, in comparing the temperature and power dependences, we must consider the difference between local inhomogeneous laser-induced

heating and the global homogeneous effects of higher bath temperature. In addition, the inhomogeneous distribution of photoexcited carriers from the laser spatial profile can be relevant, as it may provide a spatially dependent magnetic anisotropy across the laser spot that affects the hysteresis behavior. Overall, the evidence suggests that laser heating is an important effect to consider in future analyses. Systematic exploration of these issues as well as other potential opto-magnetic effects should be undertaken in future experiments and theoretical studies.

G.9 Wide magnetic field sweeps at different powers

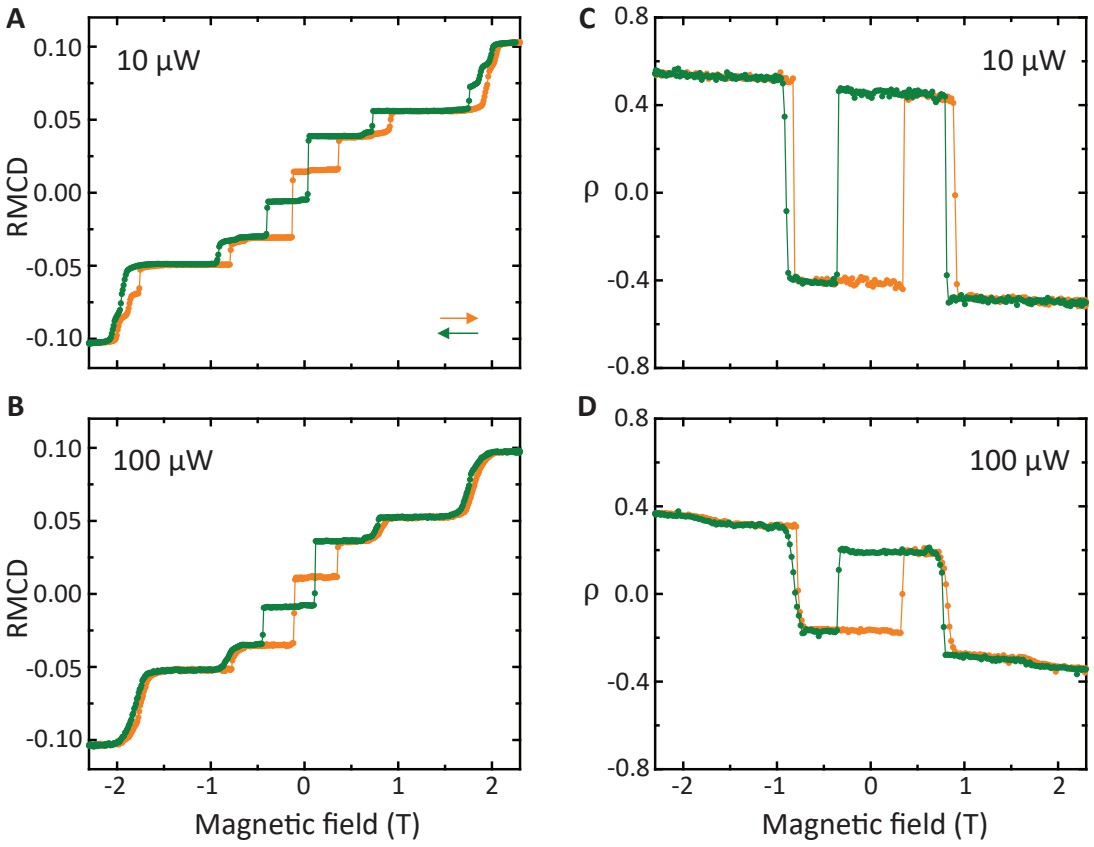

Figure G.9: Wide magnetic field sweeps at different powers. Magnetic field sweeps of RMCD and ρ at different excitation powers. RMCD at 10 μW (A) and 100 μW (B). ρ at 10 μW (C) and 100 μW (D). In the RMCD sweeps, the hysteresis loops at ±0.8 T and ±1.9 T shrink at high power, while the other loops around zero field are largely unchanged. [Reprinted from [266].]

BIBLIOGRAPHY

[1] K. S. Novoselov et al. "2D materials and van der Waals heterostructures". *Science* 353.6298 (2016), aac9439. DOI: 10.1126/science.aac9439.

[2] A. K. Geim and I. V. Grigorieva. "Van der Waals heterostructures". *Nature* 499.7459 (2013), pp. 419–425. DOI: 10.1038/nature12385.

[3] R. P. Feynman. "Plenty of room at the bottom". *Proc. of APS Meeting*. 1959.

[4] F. Xia et al. "Two-dimensional material nanophotonics". *Nat. Photonics* 8.12 (2014), pp. 899–907. DOI: 10.1038/nphoton.2014.271.

[5] C. A. F. Hintze, G. E. Linck, and K. Chudoba. *Handbuch der mineralogie*. Veit, 1904.

[6] M. Chhowalla et al. "The chemistry of two-dimensional layered transition metal dichalcogenide nanosheets". *Nat. Chem.* 5.4 (2013), pp. 263–275. DOI: 10.1038/nchem.1589.

[7] L. F. Mattheiss. "Band structures of transition-metal-dichalcogenide layer compounds". *Phys. Rev. B Condens. Matter* 8.8 (1973), pp. 3719–3740. DOI: 10.1103/PhysRevB.8.3719.

[8] R. G. Dickinson and L. Pauling. "The crystal structure of molybdenite". *J. Am. Chem. Soc.* 45.6 (1923), pp. 1466–1471. DOI: 10.1021/ja01659a020.

[9] K. F. Mak et al. "Atomically thin MoS_2: a new direct-gap semiconductor". *Phys. Rev. Lett.* 105.13 (2010), p. 136805. DOI: 10.1103/PhysRevLett.105.136805.

[10] A. Splendiani et al. "Emerging photoluminescence in monolayer MoS_2". *Nano Lett.* 10.4 (2010), pp. 1271–1275. DOI: 10.1021/nl903868w.

[11] J. A. Wilson and A. D. Yoffe. "The transition metal dichalcogenides discussion and interpretation of the observed optical, electrical and structural properties". *Adv. Phys.* (1969).

[12] G.-B. Liu et al. "Three-band tight-binding model for monolayers of group-VIB transition metal dichalcogenides". *Phys. Rev. B Condens. Matter* 88.8 (2013), p. 085433. DOI: 10.1103/PhysRevB.88.085433.

[13] D. Xiao et al. "Coupled spin and valley physics in monolayers of MoS_2 and other group-VI dichalcogenides". *Phys. Rev. Lett.* 108.19 (2012), p. 196802. DOI: 10.1103/PhysRevLett.108.196802.

[14] Z. Y. Zhu, Y. C. Cheng, and U. Schwingenschlögl. "Giant spin-orbit-induced spin splitting in two-dimensional transition-metal dichalcogenide semiconductors". *Phys. Rev. B Condens. Matter* 84.15 (2011), p. 153402. DOI: 10.1103/PhysRevB.84.153402.

[15] G. Wang et al. "Colloquium: Excitons in atomically thin transition metal dichalcogenides". *Rev. Mod. Phys.* 90.2 (2018), p. 021001. DOI: 10.1103/RevModPhys.90.021001.

[16] Y. Li et al. "Measurement of the optical dielectric function of monolayer transition-metal dichalcogenides: MoS_2, $MoSe_2$, WS_2, and WSe_2". *Phys. Rev. B Condens. Matter* 90.20 (2014), p. 205422. DOI: 10.1103/PhysRevB.90.205422.

[17] N. Saigal, V. Sugunakar, and S. Ghosh. "Exciton binding energy in bulk MoS_2: A reassessment". *Appl. Phys. Lett.* 108.13 (2016), p. 132105. DOI: 10.1063/1.4945047.

[18] D. W. Kim et al. "Measurement of the exciton binding energy in a narrow GaAs-Al_xGa_xAs quantum well by photoluminescence excitation spectroscopy". *Phys. Rev. B Condens. Matter* 47.4 (1993), pp. 2042–2047. DOI: 10.1103/PhysRevB.47.2042.

[19] A. Chernikov et al. "Exciton binding energy and nonhydrogenic Rydberg series in monolayer WS_2". *Phys. Rev. Lett.* 113.7 (2014), p. 076802. DOI: 10.1103/PhysRevLett.113.076802.

[20] D. Y. Qiu, F. H. da Jornada, and S. G. Louie. "Optical spectrum of MoS_2: many-body effects and diversity of exciton states". *Phys. Rev. Lett.* 111.21 (2013), p. 216805. DOI: 10.1103/PhysRevLett.111.216805.

[21] L. V. Keldysh. "Coulomb interaction in thin semiconductor and semimetal films". *Soviet Journal of Experimental and Theoretical Physics Letters* 29 (1979), p. 658.

[22] R. S. Knox. *Theory of excitons*. Vol. 3. Academic Press New York., 1963.

[23] K. F. Mak et al. "Tightly bound trions in monolayer MoS_2". *Nat. Mater.* 12.3 (2013), pp. 207–211. DOI: 10.1038/nmat3505.

[24] J. S. Ross et al. "Electrical control of neutral and charged excitons in a monolayer semiconductor". *Nat. Commun.* 4 (2013), p. 1474. DOI: 10.1038/ncomms2498.

[25] O. Gunawan et al. "Valley susceptibility of an interacting two-dimensional electron system". *Phys. Rev. Lett.* 97.18 (2006), p. 186404.

[26] Y. P. Shkolnikov et al. "Valley splitting of AlAs two-dimensional electrons in a perpendicular magnetic field". *Phys. Rev. Lett.* 89.22 (2002), p. 226805. DOI: 10.1103/PhysRevLett.89.226805.

[27] D. Xiao, W. Yao, and Q. Niu. "Valley-contrasting physics in graphene: magnetic moment and topological transport". *Phys. Rev. Lett.* 99.23 (2007), p. 236809. DOI: 10.1103/PhysRevLett.99.236809.

[28] W. Yao, D. Xiao, and Q. Niu. "Valley-dependent optoelectronics from inversion symmetry breaking". *Phys. Rev. B Condens. Matter* 77.23 (2008), p. 235406. DOI: 10.1103/PhysRevB.77.235406.

[29] S. Pancharatnam. "Generalized theory of interference and its applications". *Proceedings of the Indian Academy of Sciences - Section A* 44.6 (1956), pp. 398–417. DOI: 10.1007/BF03046095.

[30] M. V. Berry. "Quantal phase factors accompanying adiabatic changes". *Proc. R. Soc. Lond. A Math. Phys. Sci.* 392.1802 (1984), pp. 45–57. DOI: 10.1098/rspa.1984.0023.

[31] D. Xiao, M.-C. Chang, and Q. Niu. "Berry phase effects on electronic properties". *Rev. Mod. Phys.* 82.3 (2010), pp. 1959–2007. DOI: 10.1103/RevModPhys.82.1959.

[32] N. Nagaosa et al. "Anomalous Hall effect". *Rev. Mod. Phys.* 82.2 (2010), pp. 1539–1592. DOI: 10.1103/RevModPhys.82.1539.

[33] T. Thonhauser et al. "Orbital magnetization in periodic insulators". *Phys. Rev. Lett.* 95.13 (2005), p. 137205. DOI: 10.1103/PhysRevLett.95.137205.

[34] D. Xiao, J. Shi, and Q. Niu. "Berry phase correction to electron density of states in solids". *Phys. Rev. Lett.* 95.13 (2005), p. 137204. DOI: 10.1103/PhysRevLett.95.137204.

[35] D. Ceresoli et al. "Orbital magnetization in crystalline solids: Multi-band insulators, Chern insulators, and metals". *Phys. Rev. B Condens. Matter* 74.2 (2006), p. 024408. DOI: 10.1103/PhysRevB.74.024408.

[36] J. Shi et al. "Quantum theory of orbital magnetization and its generalization to interacting systems". *Phys. Rev. Lett.* 99.19 (2007), p. 197202. DOI: 10.1103/PhysRevLett.99.197202.

[37] W. Feng et al. "Intrinsic spin Hall effect in monolayers of group-VI dichalcogenides: A first-principles study". *Phys. Rev. B Condens. Matter* 86.16 (2012), p. 165108. DOI: 10.1103/PhysRevB.86.165108.

[38] K. F. Mak et al. "Valleytronics. The valley Hall effect in MoS_2 transistors". *Science* 344.6191 (2014), pp. 1489–1492. DOI: 10.1126/science.1250140.

[39] J. Lee, K. F. Mak, and J. Shan. "Electrical control of the valley Hall effect in bilayer MoS_2 transistors". *Nat. Nanotechnol.* (2016). DOI: 10.1038/nnano.2015.337.

[40] G. Aivazian et al. "Magnetic control of valley pseudospin in monolayer WSe_2". *Nat. Phys.* 11.2 (2015), pp. 148–152. DOI: 10.1038/nphys3201.

[41] G.-B. Liu et al. "Intervalley coupling by quantum dot confinement potentials in monolayer transition metal dichalcogenides". *New J. Phys.* 16.10 (2014), p. 105011. DOI: 10.1088/1367-2630/16/10/105011.

[42] G.-B. Liu et al. "Electronic structures and theoretical modelling of two-dimensional group-VIB transition metal dichalcogenides". *Chem. Soc. Rev.* 44.9 (2014), pp. 2643–2663. DOI: 10.1039/C4CS00301B.

[43] G. Sallen et al. "Robust optical emission polarization in MoS_2 monolayers through selective valley excitation". *Phys. Rev. B: Condens. Matter Mater. Phys.* 86.8 (2012), p. 081301.

[44] G. Sallen et al. "Erratum: Robust optical emission polarization in MoS_2 monolayers through selective valley excitation". *Phys. Rev. B: Condens. Matter Mater. Phys.* 89.7 (2014), p. 079903.

[45] R. A. Bromley, R. B. Murray, and A. D. Yoffe. "The band structures of some transition metal dichalcogenides. III. Group VIA: trigonal prism materials". *J. Phys. C: Solid State Phys.* (1972).

[46] A. M. Jones et al. "Optical generation of excitonic valley coherence in monolayer WSe_2". *Nat. Nanotechnol.* 8.9 (2013), pp. 634–638. DOI: 10.1038/nnano.2013.151.

[47] K. F. Mak et al. "Control of valley polarization in monolayer MoS_2 by optical helicity". *Nat. Nanotechnol.* 7.8 (2012), pp. 494–498. DOI: 10.1038/nnano.2012.96.

[48] T. Cao et al. "Valley-selective circular dichroism of monolayer molybdenum disulphide". *Nat. Commun.* 3 (2012), p. 887. DOI: 10.1038/ncomms1882.

[49] H. Zeng et al. "Valley polarization in MoS_2 monolayers by optical pumping". *Nat. Nanotechnol.* 7.8 (2012), pp. 490–493. DOI: 10.1038/nnano.2012.95.

[50] D. Zhong et al. "Van der Waals engineering of ferromagnetic semiconductor heterostructures for spin and valleytronics". *Sci Adv* 3.5 (2017), e1603113. DOI: 10.1126/sciadv.1603113.

[51] A. Srivastava et al. "Valley Zeeman effect in elementary optical excitations of monolayer WSe_2". *Nat. Phys.* 11.2 (2015), pp. 141–147. DOI: 10.1038/nphys3203.

[52] D. MacNeill et al. "Breaking of valley degeneracy by magnetic field in monolayer $MoSe_2$". *Phys. Rev. Lett.* 114.3 (2015), p. 037401. DOI: 10.1103/PhysRevLett.114.037401.

[53] Y. Li et al. "Valley splitting and polarization by the Zeeman effect in monolayer $MoSe_2$". *Phys. Rev. Lett.* 113.26 (2014), p. 266804. DOI: 10.1103/PhysRevLett.113.266804.

[54] R. Schmidt et al. "Magnetic-field-induced rotation of polarized light emission from monolayer WS_2". *Phys. Rev. Lett.* 117.7 (2016), p. 077402. DOI: 10.1103/PhysRevLett.117.077402.

[55] G. Wang et al. "Control of exciton valley coherence in transition metal dichalcogenide monolayers". *Phys. Rev. Lett.* 117.18 (2016), p. 187401. DOI: 10.1103/PhysRevLett.117.187401.

[56] A. V. Stier et al. "Exciton diamagnetic shifts and valley Zeeman effects in monolayer WS_2 and MoS_2 to 65 Tesla". *Nat. Commun.* 7 (2016). DOI: 10.1038/ncomms10643.

[57] K. L. Seyler et al. "Electrical control of second-harmonic generation in a WSe_2 monolayer transistor". *Nat. Nanotechnol.* 10.5 (2015), pp. 407–411. DOI: 10.1038/nnano.2015.73.

[58] Y. R. Shen. *The principles of nonlinear optics*. adsabs.harvard.edu, 1984.

[59] R. W. Boyd. *Nonlinear optics*. Academic Press, 2003.

[60] R. R. Birss. *Symmetry and magnetism*. North-Holland Pub. Co., 1964.

[61] N. Kumar et al. "Second harmonic microscopy of monolayer MoS_2". *Phys. Rev. B Condens. Matter* 87.16 (2013), p. 161403. DOI: 10.1103/PhysRevB.87.161403.

[62] Y. Li et al. "Probing symmetry properties of few-layer MoS_2 and h-BN by optical second-harmonic generation". *Nano Lett.* 13.7 (2013), pp. 3329–3333. DOI: 10.1021/nl401561r.

[63] L. M. Malard et al. "Observation of intense second harmonic generation from MoS_2 atomic crystals". *Phys. Rev. B Condens. Matter* 87.20 (2013), p. 201401. DOI: 10.1103/PhysRevB.87.201401.

[64] H. Zeng et al. "Optical signature of symmetry variations and spin-valley coupling in atomically thin tungsten dichalcogenides". *Sci. Rep.* 3 (2013), p. 1608. DOI: 10.1038/srep01608.

[65] C. Janisch et al. "Extraordinary second harmonic generation in tungsten disulfide monolayers". *Sci. Rep.* 4 (2014), p. 5530. DOI: 10.1038/srep05530.

[66] W. Wu et al. "Piezoelectricity of single-atomic-layer MoS_2 for energy conversion and piezotronics". *Nature* 514.7523 (2014), pp. 470–474. DOI: 10.1038/nature13792.

[67] H. Zhu et al. "Observation of piezoelectricity in free-standing monolayer MoS_2". *Nat. Nanotechnol.* 10.2 (2015), pp. 151–155. DOI: 10.1038/nnano.2014.309.

[68] X. Yin et al. "Edge nonlinear optics on a MoS_2 atomic monolayer". *Science* 344.6183 (2014), pp. 488–490. DOI: 10.1126/science.1250564.

[69] J. Cheng et al. "Kinetic nature of grain boundary formation in as-grown MoS_2 monolayers". *Adv. Mater.* 27.27 (2015), pp. 4069–4074. DOI: 10.1002/adma.201501354.

[70] K. He et al. "Tightly bound excitons in monolayer WSe_2". *Phys. Rev. Lett.* 113.2 (2014), p. 026803. DOI: 10.1103/PhysRevLett.113.026803.

[71] Z. Ye et al. "Probing excitonic dark states in single-layer tungsten disulphide". *Nature* 513.7517 (2014), pp. 214–218. DOI: 10.1038/nature13734.

[72] B. Zhu, X. Chen, and X. Cui. "Exciton binding energy of monolayer WS_2". *Sci. Rep.* 5 (2015), p. 9218. DOI: 10.1038/srep09218.

[73] G. Wang et al. "Giant enhancement of the optical second-harmonic emission of WSe_2 monolayers by laser excitation at exciton resonances". *Phys. Rev. Lett.* 114.9 (2015), p. 097403. DOI: 10.1103/PhysRevLett.114.097403.

[74] M. Lafrentz et al. "Second-harmonic generation spectroscopy of excitons in ZnO". *Phys. Rev. B Condens. Matter* 88.23 (2013), p. 235207. DOI: 10.1103/PhysRevB.88.235207.

[75] Q. Xu et al. "Micrometre-scale silicon electro-optic modulator". *Nature* 435 (2005), p. 325. DOI: 10.1038/nature03569.

[76] R. W. Terhune, P. D. Maker, and C. M. Savage. "Optical harmonic generation in calcite". *Phys. Rev. Lett.* 8.10 (1962), pp. 404–406. DOI: 10.1103/PhysRevLett.8.404.

[77] C. H. Lee, R. K. Chang, and N. Bloembergen. "Nonlinear electroreflectance in silicon and silver". *Phys. Rev. Lett.* 18.5 (1967), pp. 167–170. DOI: 10.1103/PhysRevLett.18.167.

[78] O. A. Aktsipetrov et al. "Optical second-harmonic generation induced by a dc electric field at the Si–SiO_2 interface". *Opt. Lett.* 19.18 (1994), pp. 1450–1452. DOI: 10.1364/OL.19.001450.

[79] W. Cai, A. P. Vasudev, and M. L. Brongersma. "Electrically controlled nonlinear generation of light with plasmonics". *Science* 333.6050 (2011), pp. 1720–1723. DOI: 10.1126/science.1207858.

[80] L. Kang et al. "Electrifying photonic metamaterials for tunable nonlinear optics". *Nat. Commun.* 5 (2014), p. 4680. DOI: 10.1038/ncomms5680.

[81] B. A. Ruzicka et al. "Second-harmonic generation induced by electric currents in GaAs". *Phys. Rev. Lett.* 108.7 (2012), p. 077403. DOI: 10.1103/PhysRevLett.108.077403.

[82] W. Ding, L. Zhou, and S. Y. Chou. "Enhancement and electric charge-assisted tuning of nonlinear light generation in bipolar plasmonics". *Nano Lett.* 14.5 (2014), pp. 2822–2830. DOI: 10.1021/nl5008294.

[83] C. Sirtori, F. Capasso, D. L. Sivco, et al. "Resonant Stark tuning of second-order susceptibility in coupled quantum wells". *J. Phys. D Appl. Phys.* (1992).

[84] N. Bloembergen and P. S. Pershan. "Light waves at the boundary of nonlinear media". *Phys. Rev.* 128.2 (1962), pp. 606–622. DOI: 10.1103/PhysRev.128.606.

[85] T. Jiang et al. "Valley and band structure engineering of folded MoS_2 bilayers". *Nat. Nanotechnol.* 9.10 (2014), pp. 825–829. DOI: 10.1038/nnano.2014.176.

[86] A. M. Jones et al. "Excitonic luminescence upconversion in a two-dimensional semiconductor". *Nat. Phys.* 12.4 (2015), pp. 323–327. DOI: 10.1038/nphys3604.

[87] Y. Chen et al. "Tunable band gap photoluminescence from atomically thin transition-metal dichalcogenide alloys". *ACS Nano* 7.5 (2013), pp. 4610–4616. DOI: 10.1021/nn401420h.

[88] J. Mann et al. "2-dimensional transition metal dichalcogenides with tunable direct band gaps: $MoS_{2(1-x)}Se_{2x}$ monolayers". *Adv. Mater.* 26.9 (2014), pp. 1399–1404. DOI: 10.1002/adma.201304389.

[89] S. Tongay et al. "Two-dimensional semiconductor alloys: Monolayer $Mo_{1-x}W_xSe_2$". *Appl. Phys. Lett.* 104.1 (2014), p. 012101. DOI: 10.1063/1.4834358.

[90] H. J. Simon and N. Bloembergen. "Second-harmonic light generation in crystals with natural optical activity". *Phys. Rev.* 171.3 (1968), pp. 1104–1114. DOI: 10.1103/PhysRev.171.1104.

[91] R. A. Muniz and J. E. Sipe. "All-optical injection of charge, spin, and valley currents in monolayer transition-metal dichalcogenides". *Phys. Rev. B Condens. Matter* 91.8 (2015), p. 085404. DOI: 10.1103/PhysRevB.91.085404.

[92] P. Rivera et al. "Valley-polarized exciton dynamics in a 2D semiconductor heterostructure". *Science* 351.6274 (2016), pp. 688–691. DOI: 10.1126/science.aac7820.

[93] E. Finkman, M. D. Sturge, and M. C. Tamargo. "X-point excitons in AlAs/GaAs superlattices". *Appl. Phys. Lett.* 49.19 (1986), pp. 1299–1301. DOI: 10.1063/1.97392.

[94] J. Feldmann et al. "Subpicosecond real-space charge transfer in type-II GaAs/AlAs superlattices". *Phys. Rev. Lett.* 62.16 (1989), pp. 1892–1895. DOI: 10.1103/PhysRevLett.62.1892.

[95] H. W. van Kesteren et al. "Fine structure of excitons in type-II GaAs/AlAs quantum wells". *Phys. Rev. B Condens. Matter* 41.8 (1990), pp. 5283–5292. DOI: 10.1103/PhysRevB.41.5283.

[96] Golub et al. "Long-lived spatially indirect excitons in coupled $GaAs/Al_xGa_{1-x}As$ quantum wells". *Phys. Rev. B Condens. Matter* 41.12 (1990), pp. 8564–8567.

[97] G. D. Gilliland et al. "Direct measurement of heavy-hole exciton transport in type-II GaAs/AlAs superlattices". *Phys. Rev. Lett.* 71.22 (1993), pp. 3717–3720. DOI: 10.1103/PhysRevLett.71.3717.

[98] Chen et al. "Effect of electric fields on excitons in a coupled double-quantum-well structure". *Phys. Rev. B Condens. Matter* 36.8 (1987), pp. 4562–4565.

[99] Charbonneau et al. "Transformation of spatially direct to spatially indirect excitons in coupled double quantum wells". *Phys. Rev. B Condens. Matter* 38.9 (1988), pp. 6287–6290.

[100] Fukuzawa, Mendez, and Hong. "Phase transition of an exciton system in GaAs coupled quantum wells". *Phys. Rev. Lett.* 64.25 (1990), pp. 3066–3069.

[101] V. Negoita, D. W. Snoke, and K. Eberl. "Huge density-dependent blueshift of indirect excitons in biased coupled quantum wells". *Phys. Rev. B Condens. Matter* 61.4 (2000), pp. 2779–2783. DOI: 10.1103/PhysRevB.61.2779.

[102] K. Kowalik-Seidl et al. "Long exciton spin relaxation in coupled quantum wells". *Appl. Phys. Lett.* 97.1 (2010), p. 011104. DOI: 10.1063/1.3458703.

[103] L. V. Butov, A. C. Gossard, and D. S. Chemla. "Macroscopically ordered state in an exciton system". *Nature* 418.6899 (2002), pp. 751–754. DOI: 10.1038/nature00943.

[104] D. Snoke et al. "Long-range transport in excitonic dark states in coupled quantum wells". *Nature* 418.6899 (2002), pp. 754–757. DOI: 10.1038/nature00940.

[105] J. R. Leonard et al. "Spin transport of excitons". *Nano Lett.* 9.12 (2009), pp. 4204–4208. DOI: 10.1021/nl9024227.

[106] L. V. Keldysh and A. N. Kozlov. "Collective properties of excitons in semiconductors". *Sov. Phys. JETP* 27.3 (1968), p. 521.

[107] L. V. Butov. "Cold exciton gases in coupled quantum well structures". *J. Phys. Condens. Matter* 19.29 (2007), p. 295202. DOI: 10.1088/0953-8984/19/29/295202.

[108] A. A. High et al. "Control of exciton fluxes in an excitonic integrated circuit". *Science* 321.5886 (2008), pp. 229–231. DOI: 10.1126/science.1157845.

[109] Z. Vörös et al. "Trapping excitons in a two-dimensional in-plane harmonic potential: experimental evidence for equilibration of indirect excitons". *Phys. Rev. Lett.* 97.1 (2006), p. 016803. DOI: 10.1103/PhysRevLett.97.016803.

[110] A. A. High et al. "Indirect excitons in elevated traps". *Nano Lett.* 9.5 (2009), pp. 2094–2098. DOI: 10.1021/nl900605b.

[111] A. A. High et al. "Trapping indirect excitons in a GaAs quantum-well structure with a diamond-shaped electrostatic trap". *Phys. Rev. Lett.* 103.8 (2009), p. 087403. DOI: 10.1103/PhysRevLett.103.087403.

[112] A. A. High et al. "Condensation of excitons in a trap". *Nano Lett.* 12.5 (2012), pp. 2605–2609. DOI: 10.1021/nl300983n.

[113] M. Hagn et al. "Electric-field-induced exciton transport in coupled quantum well structures". *Appl. Phys. Lett.* 67.2 (1995), pp. 232–234. DOI: 10.1063/1.114677.

[114] J. Rudolph, R. Hey, and P. V. Santos. "Long-range exciton transport by dynamic strain fields in a GaAs quantum well". *Phys. Rev. Lett.* 99.4 (2007), p. 047602. DOI: 10.1103/PhysRevLett.99.047602.

[115] A. G. Winbow et al. "Electrostatic conveyer for excitons". *Phys. Rev. Lett.* 106.19 (2011), p. 196806. DOI: 10.1103/PhysRevLett.106.196806.

[116] H. Terrones, F. López-Urías, and M. Terrones. "Novel hetero-layered materials with tunable direct band gaps by sandwiching different metal disulfides and diselenides". *Sci. Rep.* 3 (2013), p. 1549. DOI: 10.1038/srep01549.

[117] J. Kang et al. "Band offsets and heterostructures of two-dimensional semiconductors". *Appl. Phys. Lett.* 102.1 (2013), p. 012111. DOI: 10.1063/1.4774090.

[118] K. Kośmider and J. Fernández-Rossier. "Electronic properties of the MoS_2-WS_2 heterojunction". *Phys. Rev. B Condens. Matter* 87.7 (2013), p. 075451. DOI: 10.1103/PhysRevB.87.075451.

[119] H.-P. Komsa and A. V. Krasheninnikov. "Electronic structures and optical properties of realistic transition metal dichalcogenide heterostructures from first principles". *Phys. Rev. B Condens. Matter* 88.8 (2013), p. 085318. DOI: 10.1103/PhysRevB.88.085318.

[120] C.-H. Lee et al. "Atomically thin p-n junctions with van der Waals heterointerfaces". *Nat. Nanotechnol.* 9.9 (2014), pp. 676–681. DOI: 10.1038/nnano.2014.150.

[121] M. M. Furchi et al. "Photovoltaic effect in an electrically tunable van der Waals heterojunction". *Nano Lett.* 14.8 (2014), pp. 4785–4791. DOI: 10.1021/nl501962c.

[122] R. Cheng et al. "Electroluminescence and photocurrent generation from atomically sharp WSe_2/MoS_2 heterojunction p-n diodes". *Nano Lett.* 14.10 (2014), pp. 5590–5597. DOI: 10.1021/nl502075n.

[123] M.-H. Chiu et al. "Determination of band alignment in the single-layer MoS_2/WSe_2 heterojunction". *Nat. Commun.* 6 (2015), p. 7666. DOI: 10.1038/ncomms8666.

[124] D. Jariwala et al. "Van der Waals materials for atomically-thin photovoltaics: promise and outlook". *ACS Photonics* 4.12 (2017), pp. 2962–2970. DOI: 10.1021/acsphotonics.7b01103.

[125] P. Rivera et al. "Observation of long-lived interlayer excitons in monolayer $MoSe_2$–WSe_2 heterostructures". *Nat. Commun.* 6 (2015), ncomms7242. DOI: 10.1038/ncomms7242.

[126] X. Hong et al. "Ultrafast charge transfer in atomically thin MoS_2/WS_2 heterostructures". *Nat. Nanotechnol.* 9.9 (2014), pp. 682–686. DOI: 10.1038/nnano.2014.167.

[127] F. Ceballos et al. "Ultrafast charge separation and indirect exciton formation in a MoS_2–$MoSe_2$ van der Waals heterostructure". *ACS Nano* 8.12 (2014), pp. 12717–12724. DOI: 10.1021/nn505736z.

[128] B. Peng et al. "Ultrafast charge transfer in MoS_2/WSe_2 p–n heterojunction". *2D Mater.* 3.2 (2016), p. 025020. DOI: 10.1088/2053-1583/3/2/025020.

[129] H. Wang et al. "The role of collective motion in the ultrafast charge transfer in van der Waals heterostructures". *Nat. Commun.* 7 (2016), p. 11504. DOI: 10.1038/ncomms11504.

[130] H. Chen et al. "Ultrafast formation of interlayer hot excitons in atomically thin MoS_2/WS_2 heterostructures". *Nat. Commun.* 7 (2016), ncomms12512. DOI: 10.1038/ncomms12512.

[131] H. Zhu et al. "Interfacial charge transfer circumventing momentum mismatch at two-dimensional van der Waals heterojunctions". *Nano Lett.* (2017). DOI: 10.1021/acs.nanolett.7b00748.

[132] H. Fang et al. "Strong interlayer coupling in van der Waals heterostructures built from single-layer chalcogenides". *Proc. Natl. Acad. Sci. U. S. A.* 111.17 (2014), pp. 6198–6202. DOI: 10.1073/pnas.1405435111.

[133] G. Moody, J. Schaibley, and X. Xu. "Exciton dynamics in monolayer transition metal dichalcogenides". *J. Opt. Soc. Am. B, JOSAB* 33.7 (2016), pp. C39–C49. DOI: 10.1364/JOSAB.33.000C39.

[134] J. S. Ross et al. "Interlayer exciton optoelectronics in a 2D heterostructure p–n junction". *Nano Lett.* 17.2 (2017), pp. 638–643. DOI: 10.1021/acs.nanolett.6b03398.

[135] K. Sivalertporn et al. "Direct and indirect excitons in semiconductor coupled quantum wells in an applied electric field". *Phys. Rev. B Condens. Matter* 85.4 (2012), p. 045207. DOI: 10.1103/PhysRevB.85.045207.

[136] N. R. Wilson et al. "Determination of band offsets, hybridization, and exciton binding in 2D semiconductor heterostructures". *Sci Adv* 3.2 (2017), e1601832. DOI: 10.1126/sciadv.1601832.

[137] H. Yu et al. "Anomalous light cones and valley optical selection rules of interlayer excitons in twisted heterobilayers". *Phys. Rev. Lett.* 115.18 (2015), p. 187002. DOI: 10.1103/PhysRevLett.115.187002.

[138] H. Yu et al. "Moiré excitons: From programmable quantum emitter arrays to spin-orbit–coupled artificial lattices". *Science Advances* 3.11 (2017), e1701696. DOI: 10.1126/sciadv.1701696.

[139] H. Yu, G.-B. Liu, and W. Yao. "Brightened spin-triplet interlayer excitons and optical selection rules in van der Waals heterobilayers". *2D Mater.* 5.3 (2018), p. 035021. DOI: 10.1088/2053-1583/aac065.

[140] F. Wu, T. Lovorn, and A. H. MacDonald. "Theory of optical absorption by interlayer excitons in transition metal dichalcogenide heterobilayers". *Phys. Rev. B Condens. Matter* 97.3 (2018), p. 035306. DOI: 10.1103/PhysRevB.97.035306.

[141] C. Zhang et al. "Interlayer couplings, Moiré patterns, and 2D electronic superlattices in $MoS2_2WSe_2$ hetero-bilayers". *Science Advances* 3.1 (2017), e1601459. DOI: 10.1126/sciadv.1601459.

[142] J. R. Schaibley et al. "Directional interlayer spin-valley transfer in two-dimensional heterostructures". *Nat. Commun.* 7 (2016), p. 13747. DOI: 10.1038/ncomms13747.

[143] P. J. Zomer et al. "Fast pick up technique for high quality heterostructures of bilayer graphene and hexagonal boron nitride". *Appl. Phys. Lett.* 105.1 (2014), p. 013101. DOI: 10.1063/1.4886096.

[144] Q. Wang et al. "Valley carrier dynamics in monolayer molybdenum disulfide from helicity-resolved ultrafast pump-probe spectroscopy". *ACS Nano* 7.12 (2013), pp. 11087–11093. DOI: 10.1021/nn405419h.

[145] C. Mai et al. "Many-body effects in valleytronics: direct measurement of valley lifetimes in single-layer MoS_2". *Nano Lett.* 14.1 (2014), pp. 202–206. DOI: 10.1021/nl403742j.

[146] C. R. Zhu et al. "Exciton valley dynamics probed by Kerr rotation in WSe_2 monolayers". *Phys. Rev. B Condens. Matter* 90.16 (2014), p. 161302. DOI: 10.1103/PhysRevB.90.161302.

[147] C. R. Dean et al. "Hofstadter's butterfly and the fractal quantum Hall effect in moiré superlattices". *Nature* 497.7451 (2013), pp. 598–602. DOI: 10.1038/nature12186.

[148] B. Hunt et al. "Massive Dirac fermions and Hofstadter butterfly in a van der Waals heterostructure". *Science* 340.6139 (2013), pp. 1427–1430. DOI: 10.1126/science.1237240.

[149] L. A. Ponomarenko et al. "Cloning of Dirac fermions in graphene superlattices". *Nature* 497.7451 (2013), pp. 594–597. DOI: 10.1038/nature12187.

[150] Y. Cao et al. "Correlated insulator behaviour at half-filling in magic-angle graphene superlattices". *Nature* 556.7699 (2018), pp. 80–84. DOI: 10.1038/nature26154.

[151] G. Chen et al. "Gate-tunable Mott insulator in trilayer graphene-boron nitride moiré superlattice". *arXiv preprint arXiv:1803. 01985* (2018).

[152] Y. Cao et al. "Unconventional superconductivity in magic-angle graphene superlattices". *Nature* 556.7699 (2018), pp. 43–50. DOI: 10.1038/nature26160.

[153] C. Jin et al. "Imaging of pure spin-valley diffusion current in WS_2-WSe_2 heterostructures". *Science* 360.6391 (2018), pp. 893–896. DOI: 10.1126/science.aao3503.

[154] P. Nagler et al. "Giant magnetic splitting inducing near-unity valley polarization in van der Waals heterostructures". *Nat. Commun.* 8.1 (2017), p. 1551. DOI: 10.1038/s41467-017-01748-1.

[155] C. Jiang et al. "Microsecond dark-exciton valley polarization memory in two-dimensional heterostructures". *Nat. Commun.* 9.1 (2018), p. 753. DOI: 10.1038/s41467-018-03174-3.

[156] W.-T. Hsu et al. "Negative circular polarization emissions from WSe_2/$MoSe_2$ commensurate heterobilayers". *Nat. Commun.* 9.1 (2018), p. 1356. DOI: 10.1038/s41467-018-03869-7.

[157] P. Nagler et al. "Interlayer exciton dynamics in a dichalcogenide monolayer heterostructure". *2D Mater.* 4.2 (2017), p. 025112. DOI: 10.1088/2053-1583/aa7352.

[158] B. Miller et al. "Long-lived direct and indirect interlayer excitons in van der Waals heterostructures". *Nano Lett.* (2017). DOI: 10.1021/acs.nanolett.7b01304.

[159] I. Bloch. "Ultracold quantum gases in optical lattices". *Nat. Phys.* 1.1 (2005), pp. 23–30. DOI: 10.1038/nphys138.

[160] Y.-M. He et al. "Single quantum emitters in monolayer semiconductors". *Nat. Nanotechnol.* 10.6 (2015), pp. 497–502. DOI: 10.1038/nnano.2015.75.

[161] A. Srivastava et al. "Optically active quantum dots in monolayer WSe_2". *Nat. Nanotechnol.* 10.6 (2015), pp. 491–496. DOI: 10.1038/nnano.2015.60.

[162] M. Koperski et al. "Single photon emitters in exfoliated WSe_2 structures". *Nat. Nanotechnol.* 10.6 (2015), pp. 503–506. DOI: 10.1038/nnano.2015.67.

[163] C. Chakraborty et al. "Voltage-controlled quantum light from an atomically thin semiconductor". *Nat. Nanotechnol.* 10.6 (2015), pp. 507–511. DOI: 10.1038/nnano.2015.79.

[164] T. T. Tran et al. "Quantum emission from hexagonal boron nitride monolayers". *Nat. Nanotechnol.* (2015). DOI: 10.1038/nnano.2015.242.

[165] A. T. Hanbicki et al. "Double indirect interlayer exciton in a $MoSe_2$/WSe_2 van der Waals heterostructure". *ACS Nano* 12.5 (2018), pp. 4719–4726. DOI: 10.1021/acsnano.8b01369.

[166] J. Kunstmann et al. "Momentum-space indirect interlayer excitons in transition-metal dichalcogenide van der Waals heterostructures". *Nature Physics* (2018), p. 1. DOI: 10.1038/s41567-018-0123-y.

[167] C. Chakraborty et al. "3D localized trions in monolayer WSe_2 in a charge tunable van der Waals heterostructure". *Nano Lett.* (2018). DOI: 10.1021/acs.nanolett.7b05409.

[168] S. Zhang et al. "Defect structure of localized excitons in a WSe_2 monolayer". *Phys. Rev. Lett.* 119.4 (2017), p. 046101. DOI: 10.1103/PhysRevLett.119.046101.

[169] C. Palacios-Berraquero et al. "Large-scale quantum-emitter arrays in atomically thin semiconductors". *Nat. Commun.* 8 (2017), p. 15093. DOI: 10.1038/ncomms15093.

[170] A. Branny et al. "Deterministic strain-induced arrays of quantum emitters in a two-dimensional semiconductor". *Nat. Commun.* 8 (2017), p. 15053. DOI: 10.1038/ncomms15053.

[171] F. Wu, T. Lovorn, and A. H. MacDonald. "Topological exciton bands in moiré heterojunctions". *Phys. Rev. Lett.* 118.14 (2017), p. 147401. DOI: 10.1103/PhysRevLett.118.147401.

[172] K. L. Seyler et al. "Ligand-field helical luminescence in a 2D ferromagnetic insulator". *Nat. Phys.* 14 (2018), pp. 277–281. DOI: 10.1038/s41567-017-0006-7.

[173] N. D. Mermin and H. Wagner. "Absence of ferromagnetism or antiferromagnetism in one- or two-dimensional isotropic heisenberg models". *Phys. Rev. Lett.* 17.22 (1966), pp. 1133–1136. DOI: 10.1103/PhysRevLett.17.1133.

[174] P. C. Hohenberg. "Existence of long-range order in one and two dimensions". *Phys. Rev.* 158.2 (1967), pp. 383–386. DOI: 10.1103/PhysRev.158.383.

[175] N. W. Ashcroft and N. D. Mermin. *Solid State Physics*. Brooks Cole, 1976.

[176] L. J. de Jongh and A. R. Miedema. "Experiments on simple magnetic model systems". *Adv. Phys.* (1974).

[177] L. J. de Jongh, ed. *Magnetic Properties of Layered Transition Metal Compounds*. Kluwer Academic Publishers, 1990.

[178] C. L. Fu, A. J. Freeman, and T. Oguchi. "Prediction of strongly enhanced two-dimensional ferromagnetic moments on metallic overlayers, interfaces, and superlattices". *Phys. Rev. Lett.* 54.25 (1985), pp. 2700–2703. DOI: 10.1103/PhysRevLett.54.2700.

[179] B. Heinrich et al. "Ferromagnetic-resonance study of ultrathin bcc Fe(100) films grown epitaxially on fcc Ag(100) substrates". *Phys. Rev. Lett.* 59.15 (1987), pp. 1756–1759. DOI: 10.1103/PhysRevLett.59.1756.

[180] N. C. Koon et al. "Direct evidence for perpendicular spin orientations and enhanced hyperfine fields in ultrathin Fe(100) films on Ag(100)". *Phys. Rev. Lett.* 59.21 (1987), pp. 2463–2466. DOI: 10.1103/PhysRevLett.59.2463.

[181] W. Dürr et al. "Magnetic phase transition in two-dimensional ultrathin Fe films on Au(100)". *Phys. Rev. Lett.* 62.2 (1989), pp. 206–209. DOI: 10.1103/PhysRevLett.62.206.

[182] U. Gradmann. "Magnetism in ultrathin transition metal films". *Handbook of Magnetic Materials*. Vol. 7. Elsevier, 1993, pp. 1–96. DOI: 10.1016/S1567-2719(05)80042-3.

[183] Y. Li and K. Baberschke. "Dimensional crossover in ultrathin Ni(111) films on W(110)". *Phys. Rev. Lett.* 68.8 (1992), pp. 1208–1211. DOI: 10.1103/PhysRevLett.68.1208.

[184] F. Huang et al. "Magnetism in the few-monolayers limit: A surface magneto-optic Kerr-effect study of the magnetic behavior of ultrathin films of Co, Ni, and Co-Ni alloys on Cu(100) and Cu(111)". *Phys. Rev. B Condens. Matter* 49.6 (1994), pp. 3962–3971. DOI: 10.1103/PhysRevB.49.3962.

[185] M. A. McGuire et al. "Coupling of crystal structure and magnetism in the layered, ferromagnetic insulator CrI_3". *Chem. Mater.* 27.2 (2015), pp. 612–620. DOI: 10.1021/cm504242t.

[186] J. L. Lado and J. Fernández-Rossier. "On the origin of magnetic anisotropy in two dimensional CrI_3". 3 (2017), p. 035002. DOI: 10.1088/2053-1583/aa75ed.

[187] B. Huang et al. "Layer-dependent ferromagnetism in a van der Waals crystal down to the monolayer limit". 7657 (2017), pp. 270–273. DOI: 10.1038/nature22391.

[188] J.-U. Lee et al. "Ising-type magnetic ordering in atomically thin $FePS_3$". *Nano Lett.* 16.12 (2016), pp. 7433–7438. DOI: 10.1021/acs.nanolett.6b03052.

[189] C. Gong et al. "Discovery of intrinsic ferromagnetism in two-dimensional van der Waals crystals". *Nature* 546.7657 (2017), pp. 265–269. DOI: 10.1038/nature22060.

[190] Z. Fei et al. "Two-dimensional itinerant Ising ferromagnetism in atomically thin Fe_3GeTe_2" (2018).

[191] Y. Deng et al. "Gate-tunable room-temperature ferromagnetism in two-dimensional Fe_3GeTe_2" (2018).

[192] M. Bonilla et al. "Strong room-temperature ferromagnetism in VSe_2 monolayers on van der Waals substrates". *Nat. Nanotechnol.* 13.4 (2018), pp. 289–293. DOI: 10.1038/s41565-018-0063-9.

[193] D. J. O'Hara et al. "Room temperature intrinsic ferromagnetism in epitaxial manganese selenide films in the monolayer limit" (2018).

[194] J. L. Snoek. *New developments in ferromagnetic materials*. Vol. 19. Elsevier Publishing Company, 1949.

[195] I. Tsubokawa. "On the magnetic properties of a $CrBr_3$ single crystal". *J. Phys. Soc. Jpn.* 15.9 (1960), pp. 1664–1668. DOI: 10.1143/JPSJ.15.1664.

[196] P. Wachter. "The optical electrical and magnetic properties of the europium chalcogenides and the rare earth pnictides". *Crit. Rev. Solid State Mater. Sci.* 3.2 (1972), pp. 189–241. DOI: 10.1080/10408437208244865.

[197] P. K. Baltzer, H. W. Lehmann, and M. Robbins. "Insulating ferromagnetic spinels". *Phys. Rev. Lett.* 15.11 (1965), pp. 493–495. DOI: 10.1103/PhysRevLett.15.493.

[198] J. K. Furdyna. "Diluted magnetic semiconductors". *J. Appl. Phys.* 64.4 (1988), R29–R64. DOI: 10.1063/1.341700.

[199] H. Ohno et al. "Magnetotransport properties of p-type (In,Mn)As diluted magnetic III-V semiconductors". *Phys. Rev. Lett.* 68.17 (1992), pp. 2664–2667. DOI: 10.1103/PhysRevLett.68.2664.

[200] H. Ohno et al. "(Ga,Mn)As: A new diluted magnetic semiconductor based on GaAs". *Appl. Phys. Lett.* 69.3 (1996), pp. 363–365. DOI: 10.1063/1.118061.

[201] J. F. Dillon, H. Kamimura, and J. P. Remeika. "Magneto-optical properties of ferromagnetic chromium trihalides". *J. Phys. Chem. Solids* 27.9 (1966), pp. 1531–1549. DOI: 10.1016/0022-3697(66)90148-X.

[202] K. S. Burch, D. D. Awschalom, and D. N. Basov. "Optical properties of III-Mn-V ferromagnetic semiconductors". *J. Magn. Magn. Mater.* 320.23 (2008), pp. 3207–3228. DOI: 10.1016/j.jmmm.2008.08.060.

[203] P. A. Miles, W. B. Westphal, and A. Von Hippel. "Dielectric spectroscopy of ferromagnetic semiconductors". *Rev. Mod. Phys.* 29.3 (1957), pp. 279–307. DOI: 10.1103/RevModPhys.29.279.

[204] T. Dietl and H. Ohno. "Dilute ferromagnetic semiconductors: Physics and spintronic structures". *Rev. Mod. Phys.* 86.1 (2014), pp. 187–251. DOI: 10.1103/RevModPhys.86.187.

[205] J. F. Dillon, H. Kamimura, and J. P. Remeika. "Magnetic rotation of visible light by ferromagnetic $CrBr_3$". *Phys. Rev. Lett.* 9.4 (1962), pp. 161–163. DOI: 10.1103/PhysRevLett.9.161.

[206] D. L. Wood et al. "Crystal-field spectra of $d^{3,7}$ ions. III. spectrum of Cr^{3+} in various octahedral crystal fields". *J. Chem. Phys.* 39.4 (1963), pp. 890–898. DOI: 10.1063/1.1734388.

[207] W. Jung. "Dielectric constant and magneto-optical Kerr rotation of ferromagnetic chromium tribromide above the absorption band edge". *J. Appl. Phys.* 36.8 (1965), pp. 2422–2426. DOI: 10.1063/1.1714503.

[208] P. M. Grant and G. B. Street. "Optical properties of chromium trihalides in the region 1-11 eV". *Bull. Am. Phys. Soc.* 13. 1968, p. 415.

[209] I. Pollini and G. Spinolo. "Intrinsic optical properties of $CrCl_3$". *phys. stat. sol. (b)* 41.2 (1970), pp. 691–701. DOI: 10.1002/pssb.19700410224.

[210] G. Pedroli, I. Pollini, and G. Spinolo. "Specific magnetic rotation spectra and crystal field calculation in $CrBr_3$ and $CrCl_3$". *J. Phys. C: Solid State Phys.* 8.14 (1975), p. 2317. DOI: 10.1088/0022-3719/8/14/013.

[211] G. Guizzetti et al. "Reflectance and thermoreflectance studies of $CrCl_3$, $CrBr_3$, $NiCl_2$, and $NiBr_2$ crystals". *Phys. Rev. B Condens. Matter* 14.10 (1976), pp. 4622–4629. DOI: 10.1103/PhysRevB.14.4622.

[212] V. M. Bermudez and D. S. McClure. "Spectroscopic studies of the two-dimensional magnetic insulators chromium trichloride and chromium tribromide—I". *J. Phys. Chem. Solids* 40.2 (1979), pp. 129–147. DOI: 10.1016/0022-3697(79)90030-1.

[213] V. M. Bermudez and D. S. McClure. "Spectroscopic studies of the two-dimensional magnetic insulators chromium trichloride and chromium tribromide—II". *J. Phys. Chem. Solids* 40.2 (1979), pp. 149–173. DOI: 10.1016/0022-3697(79)90031-3.

[214] L. Nosenzo et al. "Influence of the magnetic transition on the optical properties of $CrBr_3$". *Solid State Commun.* 29.11 (1979), pp. 793–795. DOI: 10.1016/0038-1098(79)90163-7.

[215] A. Borghesi et al. "Magneto-optical effects in the paramagnetic and ferromagnetic phases of $CrBr_3$". *Phys. Rev. Lett.* 47.7 (1981), pp. 538–541. DOI: 10.1103/PhysRevLett.47.538.

[216] L. Nosenzo, G. Samoggia, and I. Pollini. "Effect of magnetic ordering on the optical properties of transition-metal halides: $NiCl_2$, $NiBr_2$, $CrCl_3$, and $CrBr_3$". *Phys. Rev. B Condens. Matter* 29.6 (1984), pp. 3607–3616. DOI: 10.1103/PhysRevB.29.3607.

[217] B. N. Figgis and M. A. Hitchman. *Ligand field theory and its applications*. Wiley-VCH, 2000.

[218] Y. Cao et al. "Quality heterostructures from two-dimensional crystals unstable in air by their assembly in inert atmosphere". *Nano Lett.* 15.8 (2015), pp. 4914–4921. DOI: 10.1021/acs.nanolett.5b00648.

[219] J. D. E. McIntyre and D. E. Aspnes. "Differential reflection spectroscopy of very thin surface films". *Surf. Sci.* 24.2 (1971), pp. 417–434. DOI: 10.1016/0039-6028(71)90272-X.

[220] I. H. Malitson. "Refraction and dispersion of synthetic sapphire". *J. Opt. Soc. Am., JOSA* 52.12 (1962), pp. 1377–1379. DOI: 10.1364/JOSA.52.001377.

[221] K. F. Mak and J. Shan. "Photonics and optoelectronics of 2D semiconductor transition metal dichalcogenides". *Nat. Photonics* 10.4 (2016), pp. 216–226. DOI: 10.1038/nphoton.2015.282.

[222] T. Low et al. "Polaritons in layered two-dimensional materials". *Nat. Mater.* 16.2 (2016), pp. 182–194. DOI: 10.1038/nmat4792.

[223] K. Shinagawa et al. "Charge-transfer transitions in chromium trihalides". *J. Phys. Condens. Matter* 8.44 (1999), p. 8457. DOI: 10.1088/0953-8984/8/44/002.

[224] L. F. McAven et al. "The Kerr magneto-optic effect in ferromagnetic $CrBr_3$". *J. Phys. B At. Mol. Opt. Phys.* 32.3 (1999), p. 563. DOI: 10.1088/0953-4075/32/3/002.

[225] W.-B. Zhang et al. "Robust intrinsic ferromagnetism and half semiconductivity in stable two-dimensional single-layer chromium trihalides". *J. Mater. Chem.* 3.48 (2015), pp. 12457–12468. DOI: 10.1039/C5TC02840J.

[226] B. Henderson and G. Frank Imbusch. *Optical spectroscopy of inorganic solids*. Clarendon Press, 2006.

[227] J. F. Dillon Jr and C. E. Olson. "Magnetization, resonance, and optical properties of the ferromagnet CrI_3". *J. Appl. Phys.* 36.3 (1965), pp. 1259–1260. DOI: 10.1063/1.1714194.

[228] R. Knochenmuss et al. "Broadband near-infrared luminescence of Cr^{+3} in the elpasolite lattices $Cs_2NaInCl_6$, Cs_2NaYCl_6, and Cs_2NaYBr_6". *J. Chem. Phys.* 85.8 (1986), pp. 4280–4289. DOI: 10.1063/1.451801.

[229] M. Moreno, M. T. Barriuso, and J. A. Aramburu. "The Huang-Rhys factor S(a_{1g}) for transition-metal impurities: a microscopic insight". *J. Phys. Condens. Matter* 4.47 (1999), p. 9481. DOI: 10.1088/0953-8984/4/47/027.

[230] T. J. Barton and R. C. Slade. "Chemical significance of ligand-field parameters in chromium(III) complexes of quadrate symmetry". *J. Chem. Soc. Dalton Trans.* 8 (1975), pp. 650–657. DOI: 10.1039/DT9750000650.

[231] E. J. Sie et al. "Valley-selective optical Stark effect in monolayer WS_2". *Nat. Mater.* 14.3 (2015), pp. 290–294. DOI: 10.1038/nmat4156.

[232] E. J. Sie et al. "Large, valley-exclusive Bloch-Siegert shift in monolayer WS_2". *Science* 355.6329 (2017), pp. 1066–1069. DOI: 10.1126/science.aal2241.

[233] Z. Ye, D. Sun, and T. F. Heinz. "Optical manipulation of valley pseudospin". *Nat. Phys.* 13.1 (2016), pp. 26–29. DOI: 10.1038/nphys3891.

[234] M. D. Stiles. "Interlayer exchange coupling". *J. Magn. Magn. Mater.* 200.1–3 (1999), pp. 322–337. DOI: 10.1016/S0304-8853(99)00334-0.

[235] W. H. Meiklejohn. "Exchange anisotropy—a review". *J. Appl. Phys.* 33.3 (1962), pp. 1328–1335. DOI: 10.1063/1.1728716.

[236] M. N. Baibich et al. "Giant magnetoresistance of (001) Fe/(001) Cr magnetic superlattices". *Phys. Rev. Lett.* 61.21 (1988), p. 2472.

[237] G. Binasch et al. "Enhanced magnetoresistance in layered magnetic structures with antiferromagnetic interlayer exchange". *Phys. Rev. B Condens. Matter* 39.7 (1989), pp. 4828–4830.

[238] J.-G. (Zhu and C. Park. "Magnetic tunnel junctions". *Mater. Today* 9.11 (2006), pp. 36–45. DOI: 10.1016/S1369-7021(06)71693-5.

[239] A. I. Buzdin. "Proximity effects in superconductor-ferromagnet heterostructures". *Rev. Mod. Phys.* 77.3 (2005), pp. 935–976. DOI: 10.1103/RevModPhys.77.935.

[240] C. Lee et al. "Direct measurement of proximity-induced magnetism at the interface between a topological insulator and a ferromagnet". *Nat. Commun.* 7 (2016), p. 12014. DOI: 10.1038/ncomms12014.

[241] F. Katmis et al. "A high-temperature ferromagnetic topological insulating phase by proximity coupling". *Nature* 533.7604 (2016), pp. 513–516. DOI: 10.1038/nature17635.

[242] A. H. MacDonald, P. Schiffer, and N. Samarth. "Ferromagnetic semiconductors: moving beyond (Ga,Mn)As". *Nat. Mater.* 4.3 (2005), pp. 195–202. DOI: 10.1038/nmat1325.

[243] G. A. Prinz. "Hybrid ferromagnetic-semiconductor structure". *Science* 250.4984 (1990), pp. 1092–1097. DOI: 10.1126/science.250.4984.1092.

[244] J. Fabian et al. "Semiconductor spintronics". *Acta Physica Slovaca. Reviews and Tutorials* 4-5 (2007), p. 75313. DOI: 10.2478/v10155-010-0086-8.

[245] R. I. Dzhioev et al. "Detection of the magnetization of a ferromagnetic film in a Ni/GaAs structure from the polarization of electrons of the semiconductor". *C/C OF PIS'MA V* (1994).

[246] R. C. Myers, A. C. Gossard, and D. D. Awschalom. "Tunable spin polarization in III-V quantum wells with a ferromagnetic barrier". *Phys. Rev. B Condens. Matter* 69.16 (2004), p. 161305. DOI: 10.1103/PhysRevB.69.161305.

[247] V. L. Korenev et al. "Dynamic spin polarization by orientation-dependent separation in a ferromagnet–semiconductor hybrid". *Nat. Commun.* 3 (2012), p. 959. DOI: 10.1038/ncomms1957.

[248] V. L. Korenev et al. "Long-range *p-d* exchange interaction in a ferromagnet-semiconductor hybrid structure". *Nat. Phys.* (2015). DOI: 10.1038/nphys3497.

[249] H. X. Yang et al. "Proximity effects induced in graphene by magnetic insulators: first-principles calculations on spin filtering and exchange-splitting gaps". *Phys. Rev. Lett.* 110.4 (2013), p. 046603. DOI: 10.1103/PhysRevLett.110.046603.

[250] H. Haugen, D. Huertas-Hernando, and A. Brataas. "Spin transport in proximity-induced ferromagnetic graphene". *Phys. Rev. B Condens. Matter* 77.11 (2008), p. 115406. DOI: 10.1103/PhysRevB.77.115406.

[251] B. Scharf et al. "Magnetic proximity effects in transition-metal dichalcogenides: converting excitons". *Phys. Rev. Lett.* 119.12 (2017), p. 127403. DOI: 10.1103/PhysRevLett.119.127403.

[252] Z. Qiao et al. "Quantum anomalous Hall effect in graphene from Rashba and exchange effects". *Phys. Rev. B Condens. Matter* 82.16 (2010), p. 161414. DOI: 10.1103/PhysRevB.82.161414.

[253] Z. Qiao et al. "Quantum anomalous Hall effect in graphene proximity coupled to an antiferromagnetic insulator". *Phys. Rev. Lett.* 112.11 (2014), p. 116404. DOI: 10.1103/PhysRevLett.112.116404.

[254] J. Qi et al. "Giant and tunable valley degeneracy splitting in $MoTe_2$". *Phys. Rev. B Condens. Matter* 92.12 (2015), p. 121403. DOI: 10.1103/PhysRevB.92.121403.

[255] Q. Zhang et al. "Large spin-valley polarization in monolayer $MoTe_2$ on top of EuO(111)". *Adv. Mater.* (2015). DOI: 10.1002/adma.201502585.

[256] W. Han et al. "Graphene spintronics". *Nat. Nanotechnol.* 9.10 (2014), pp. 794–807. DOI: 10.1038/nnano.2014.214.

[257] P. Wei et al. "Strong interfacial exchange field in the graphene/EuS heterostructure". *Nat. Mater.* (2016). DOI: 10.1038/nmat4603.

[258] Z. Wang et al. "Proximity-induced ferromagnetism in graphene revealed by the anomalous Hall effect". *Phys. Rev. Lett.* 114.1 (2015), p. 016603. DOI: 10.1103/PhysRevLett.114.016603.

[259] Y. Ye et al. "Electrical generation and control of the valley carriers in a monolayer transition metal dichalcogenide". *Nat. Nanotechnol.* 11.7 (2016), pp. 598–602. DOI: 10.1038/nnano.2016.49.

[260] O. L. Sanchez et al. "Valley polarization by spin injection in a light-emitting van der Waals heterojunction". *Nano Lett.* (2016). DOI: 10.1021/acs.nanolett.6b02527.

[261] J. Zhang et al. "Robust quantum anomalous Hall effect in graphene-based van der Waals heterostructures". *Phys. Rev. B Condens. Matter* 92.16 (2015), p. 165418. DOI: 10.1103/PhysRevB.92.165418.

[262] X. Xu et al. "Spin and pseudospins in layered transition metal dichalcogenides". *Nat. Phys.* 10.5 (2014), pp. 343–350. DOI: 10.1038/nphys2942.

[263] G. Wang et al. "Magneto-optics in transition metal diselenide monolayers". *2D Mater.* 2.3 (2015), p. 034002. DOI: 10.1088/2053-1583/2/3/034002.

[264] O. Hellwig et al. "A new phase diagram for layered antiferromagnetic films". *Nat. Mater.* 2.2 (2003), pp. 112–116. DOI: 10.1038/nmat806.

[265] O. Hellwig, A. Berger, and E. E. Fullerton. "Domain walls in antiferromagnetically coupled multilayer films". *Phys. Rev. Lett.* 91.19 (2003), p. 197203. DOI: 10.1103/PhysRevLett.91.197203.

[266] K. L. Seyler et al. "Valley manipulation by optically tuning the magnetic proximity effect in WSe_2/CrI_3 heterostructures". *Nano Lett.* 18.6 (2018), pp. 3823–3828. DOI: 10.1021/acs.nanolett.8b01105.

[267] K. Sato. "Measurement of magneto-optical Kerr effect using piezo-birefringent modulator". *Jpn. J. Appl. Phys.* 20.12 (1981), p. 2403. DOI: 10.1143/JJAP.20.2403.

[268] G. V. Astakhov et al. "Nonthermal photocoercivity effect in a low-doped (Ga,Mn)As ferromagnetic semiconductor". *Phys. Rev. Lett.* 102.18 (2009), p. 187401. DOI: 10.1103/PhysRevLett.102.187401.

[269] B. P. Zakharchenya and V. L. Korenev. "Integrating magnetism into semiconductor electronics". *Phys.-Usp.* 48.6 (2007), p. 603. DOI: 10.1070/PU2005v048n06ABEH002200.

[270] A. Oiwa, T. Słupinski, and H. Munekata. "Control of magnetization reversal process by light illumination in ferromagnetic semiconductor heterostructure p-(In, Mn)As/GaSb". *Appl. Phys. Lett.* 78.4 (2001), pp. 518–520. DOI: 10.1063/1.1343497.

[271] L. Lepetit, G. Chériaux, and M. Joffre. "Linear techniques of phase measurement by femtosecond spectral interferometry for applications in spectroscopy". *J. Opt. Soc. Am. B, JOSAB* 12.12 (1995), pp. 2467–2474. DOI: 10.1364/JOSAB.12.002467.

[272] K. J. Veenstra et al. "Phase-sensitive detection technique for surface nonlinear optics". *Phys. Rev. B Condens. Matter* 58.24 (1998), R16020–R16023. DOI: 10.1103/PhysRevB.58.R16020.

[273] P. T. Wilson et al. "Frequency-domain interferometric second-harmonic spectroscopy". *Opt. Lett.* 24.7 (1999), pp. 496–498. DOI: 10.1364/OL.24.000496.

[274] J. P. Perdew, K. Burke, and M. Ernzerhof. "Generalized gradient approximation made simple". *Phys. Rev. Lett.* 77.18 (1996), pp. 3865–3868. DOI: 10.1103/PhysRevLett.77.3865.

[275] J. P. Perdew, K. Burke, and M. Ernzerhof. "Generalized gradient approximation made simple". *Phys. Rev. Lett.* 78.7 (1997), pp. 1396–1396. DOI: 10.1103/PhysRevLett.78.1396.

[276] P. Giannozzi et al. "QUANTUM ESPRESSO: a modular and open-source software project for quantum simulations of materials". *J. Phys. Condens. Matter* 21.39 (2009), p. 395502. DOI: 10.1088/0953-8984/21/39/395502.

[277] S. Grimme. "Semiempirical GGA-type density functional constructed with a long-range dispersion correction". *J. Comput. Chem.* 27.15 (2006), pp. 1787–1799. DOI: 10.1002/jcc.20495.

[278] V. Barone et al. "Role and effective treatment of dispersive forces in materials: Polyethylene and graphite crystals as test cases". *J. Comput. Chem.* 30.6 (2009), pp. 934–939. DOI: 10.1002/jcc.21112.